Effects of Tool Positions on Borehole Acoustic Measurements: a Stretched Grid Finite Difference Approach

by

Xiaojun Huang

B.S. in Physics, Nanjing University (1993)
M.S. in Electrical Engineering, Nanjing University (1996)

Submitted to the Department of Earth, Atmospheric, and Planetary Sciences
in partial fulfillment of the requirements for the degree of

Doctor of Philosophy

at the

MASSACHUSETTS INSTITUTE OF TECHNOLOGY

April 2003

Author .....
Department of Earth, Atmospheric, and Planetary Sciences
April 29, 2003

Certified by .....
M. Nafi Toksöz
Professor of Geophysics
Thesis Supervisor

Accepted by .....
Ronald G. Prinn
Department Chair

Effects of Tool Positions on Borehole Acoustic Measurements: a Stretched Grid Finite Difference Approach

by

Xiaojun Huang

Submitted to the Department of Earth, Atmospheric, and Planetary Sciences
on April 29, 2003, in partial fulfillment of the
requirements for the degree of
Doctor of Philosophy

Abstract

This dissertation made three contributions to numerical simulation and borehole acoustic logging.

The first one is a novel finite difference time domain algorithm that features non-uniform grid, wavelet-based difference operator and anisotropic perfectly matched layer. This algorithm reduces numerical reflections and wave distortions introduced by grid change to a minimum by sampling the physical space with gradually varying mesh. By coordinate stretching, the algorithm discretizes the physical space with variable grid, while solving the wave equation on a uniform mesh. That approach helps retain the advantages pertaining to uniform mesh. Further improvement in efficiency is achieved without losing accuracy by the development of a wavelet-based difference operator. By using a family of compactly supported wavelet function, the wavelet-based finite difference time domain algorithm allows less grid point per wavelength. Coordinate stretching is also employed in deriving an anisotropic perfectly matched layer, superior to currently available perfectly matched layer formulation which requires field splitting, a process that results in more computer memory requirement for the storage of extra variables. Validations of the algorithm include comparison with analytical solutions, uniform grid FDTD solutions and discrete wavenumber results.

The second contribution is a time domain investigation of wave propagations in the logging while drilling situation. Logging while drilling is an emerging downhole acoustic acquisition method. The investigation is focused on soft formations where formation shear velocity is slower than borehole fluid velocity, because shear velocity measurement, one of the key measurements that acoustic logging is designed to acquire, is the most problematic in soft formations. Special attention is paid to mode excitations, with respect to frequencies, tool positions and source types, in the hope to shed some light on some highly debated questions regarding tool design and data interpretation. The stretched grid finite difference algorithm is applied.

The third contribution is the development of an inversion method to estimate stress magnitudes and directions from borehole acoustic measurements. It is predicted in theory that a crossover in flexural dispersion is an indicator of stress-induced

anisotropy dominating over other sources of intrinsic anisotropy. The prediction is subsequently verified in a scaled-borehole experiment. We are the first ones that observe flexural dispersion crossover in field data. Using the flexural crossover as a stress signature on the borehole acoustic data, we are able to isolate stressed zones. The maximum horizontal stress direction coincides with the polarization direction of far field fast shear. The stress magnitude is related to velocity changes in the stressed state from the zero stress or hydrostatically balanced state, through a perturbation theory developed in the late 1990's. Stress directions estimated in this dissertation are consistent with focal mechanism and borehole breakout data present in the world stress map database.

Thesis Supervisor: M. Nafi Toksöz
Title: Professor of Geophysics

Acknowledgments

I wish to thank many people during my six and half years of studying at the Earth Resource Laboratory. Firstly, my advisor Nafi Toksöz. Besides his scientific guidance that has been reflected in many places of this thesis, he has inspired me to think independently and critically which will benefit the rest of my scientific career. I would also like to thank Dan Burns and Rama Rao for their always-ready-to-give support, both spiritually and technically.

I have received a great deal of technical help as well as friendship from many former and current ERL students and staff members who have created a stimulating research environment at ERL. They are Roger Turpening, Bill Rodi, Liz Henderson, Sue Turbak, Weiqun Shi, Jie Zhang, Yingping Li, Matthijs Haartsen, Matthias Imhof, Bertram Nolte, Felix Herrmann, Johnathan Kane, Mark Willis, Koich Hayashi, Mary Krasovec, Kuleli Sadi, Abdulfattah Al-Dajani, Youshun Sun, Xu Li, Edmund Sze, Victoria Briggs, Samantha Grandi, Lisa Lassener, Sudipta Sarkar and Joongmoo Byun. Many thanks to Linda Meinke and Scott Blomquist, a lot of my computer intensive works would have not gone smoothly had not been their timely effort of maintaining ERL computer facilities. I am grateful to Zhenya Zhu for his endless care that helped me adjust to the new environment smoothly. I thank Arthur Cheng for his care and help on my thesis and career, and Xiaoming Tang for sharing his knowledge in borehole acoustic logging.

I would like to thank Dale Morgan for sharing his insights on how to think, write and present in the context of scientific research. I appreciate that besides Nafi and Dale, several faculty members like Rob Van De Hilst, Tom Jordan and Chris Marone had taken the time to share their thoughts on the career of academic research.

I also would acknowledge several people outside MIT. Bakashi Sinha at Schlumberger Doll and Brian Hornby at ARCO (now BP-Amaco) each took me as a summer intern and shared with me their valuable experience with real data. Bakashi has kept giving me advice ever since and co-authored the paper of stress inversion which constitutes the last chapter of this thesis . I am grateful to ChevronTexco for providing

the logging data, particularly Gopa De who made it possible and gave me invaluable advices. Halliburton kindly offered their computer cluster to host several computations before ERL's own cluster came into place. My appreciation also goes to Joakim Blanch at SensorWise and Jennifer Market of Halliburton-SperrySun for their timely help whenever I bugged them with questions regarding to real data, tools, *etc.*

I would like to take the opportunity to thank many of my friends around the globe. Their letters, emails, phone calls and virtual chats have generated this strange yet heart-warming delusion that living in a foreign country is really the continuance of the good old days. There is no doubt that MIT life was stressful, but thanks to my old friends and new ones at MIT, it had been fulfilling and colorful. I had my tech-geek mafia, movie/symphony/ballet/ski/dinner-going gang, singing group, social service league and die-hard entrepreneur club, all of which had supplemented my academic life and made the educational course comprehensive. I had believed and still believe that the very key to succeed a career, no matter in science, technology or business, is creativity. But creativity is not something that one can merely learn from pre-arranged curricular. Learning from people, from a diversified group coming from various backgrounds and with a whole spectrum of perspectives, is the most efficient way to creativity. Thanks to MIT's tremendous efforts in providing an open and diversified atmosphere on campus, I walk away from MIT with a true team spirit, appreciation to different cultures, better understanding of the background where I came from and hopefully creativity.

I owe a great debt to my family for their endless support and encouragement. My husband, Yibing Zheng, who is currently a postdoc at ERL and contributed the non-splitting perfectly matched layer to my finite difference algorithm, has kindly and patiently stood by me through all the ups and downs in this journey. I am particularly indebted to my mother, a successful professional who fearlessly steered her career through the most drastic economic transformation in Chinese history, setting me an example that every step forward in life depends on determination, self-confidence and perseverance. My deepest gratitude goes to my step father whose unconditional love soothed the pain of losing my beloved father when I was 13.

I would dedicate the dissertation to my father, a physicist who led me to the door of science, for giving me wisdoms that have shaped who I am and saved my self-esteem and self-confidence throughout the stressful life at MIT.

This research was supported by the Borehole Acoustics and Logging Consortium at MIT.

Contents

List of Figures

List of Tables

Chapter 1

Introduction

The essence of geophysics is about acquiring data and extracting information from data about the earth. The ever aggressive effort to explore the inner earth, together with the advancement in areas like sensor technology, material science and information technology, has brought geophysical data acquisition into an era of innovation. To understand the data and extract meaningful information out of it, on the other hand, still relies on the old wisdom: modeling and inversion. This study deals with modeling and analysis of data acquired in boreholes through acoustic logging with wireline or logging while drilling tools.

The dissertation starts with the development of a novel finite difference time domain approach that features non-uniform grid, wavelet-based difference operator and anisotropic perfectly matched layers. It can be applied to simulate wave propagations in a broad spectrum of earth models. With the finite difference algorithm, the dissertation then sets out to understand a novel downhole data acquisition system (logging while drilling tool), specifically to identify modal arrivals in various logging situations. The dissertation closes with a novel inversion scheme for formation stresses using borehole acoustic measurements.

1.1 A Stretched Grid Finite Difference Time Domain Scheme

There have been two dominant approaches to investigate wave propagations in a fluid-filled borehole: eigenvalue based wavenumber integral method and finite difference method. While it is fast and accurate, the wavenumber integration method requires some form of symmetry in the physical model in order to solve the eigenvalue problem (Kurkjian, 1985; Bouchon and Schmitt, 1989; Ellefsen, 1990; Randall, 1990, 1991a; Norris and Sinha, 1993). The finite difference method, on the other hand, is able to handle fairly general spatial variations of elastic properties (Virieux, 1986; Stephen et al., 1985; Randall, 1991b; Chen, 1994; Liu and Sinha, 2000). The main approach that the dissertation takes to study wave propagations in the logging while drilling (LWD) situation is the finite difference time domain (FDTD) method. Apart from the normal criteria to satisfy a stable and accurate simulation, the nature of the particular models discussed in the dissertation poses extra requirements: ability to handle wave propagations in fluid, solid layers and multiple scales of physical dimension at reasonable computational costs. We address those requirements from three perspectives: the mesh scheme, the difference operator and the numerical absorbing boundary.

1.1.1 Variable Grid

To avoid excessive numbers of calculations, while still obtaining a high degree of resolution in some particular regions, a non-uniform grid system may be used with a fine grid in the borehole area with small features or large changes and coarse grid over the rest of the areas that are smooth. To illustrate why it is necessary for a highly efficient mesh in the LWD case, let's suppose along one dimension, a is the percentage of the region has small features that requires a fine grid size, $\Delta x_{\min}$, while the rest can use a grid size of $\Delta x_{\max}$. Let $\alpha = \Delta x_{\max}/\Delta x_{\min}$. It can save memory by (1- $1/\alpha$)(1-a/100) percent by using non-uniform grid as opposed to the uniform grid

in one dimension. Memory saving grows geometrically as dimension goes from 1 to 3. Figure 1-1 illustrate memory saving rate with respect to the grid ratio α for different values of a. Figure 1-2 illustrates the cross-section of a fluid-filled borehole with an LWD tool inside. The thin annulus between the steel pipe and the formation may be as small as several millimeters, about 1/100 of the primary shear wavelength (for a 2 kHz source) in the formation. If the annulus is to be sampled with 3 grids, as the rule of thumb normally requires, the formation is then at least $20 \sim 30$ times oversampled in one coordinate dimension, which means we can chose the grid ratio to be at least 20. If the whole borehole area is sampled with small grid, which only makes up around $1\% \sim 2\%$ of the whole cross-section, at least 95% of memory saving can be achieved by using non-uniform grid. A computer needs to have several hundreds giga bytes of memory to deal with an LWD model using uniform grid. For that reason, finite difference time domain study for the LWD situation has been a difficult task due to the limitations of computer capacities.

While efficiency can be achieved by sampling the physical space adaptively with variable grid, that benefit may be offset by other problems introduced by the change in grid size. The formal truncation error and the stability of the system may be adversely affected by the change in grid size (Crowder and Dalton, 1971). There may also be wave distortion or numerical reflections due to a phase change at the interface of two grids (Browning et al., 1973). Hayashi (1999) developed a 4th order 2D variable grid FDTD algorithm by using discontinuous grids, which involves interpolation of the wave field on more than one plane. Special formulae are used at the interface of the two grids. Pitarka (1999) developed a 3D 4th order FDTD algorithm that uses continuous non-uniform spacing grids. Pitarka's approach reduces both numerical reflection and wave distortion. However, memory overhead of this approach is high and it requires solving a linear system before conducting the FDTD calculation. The linear system has to be re-solved when the difference operator needs a change (*e.g.* from 4th order to 8th order).

We apply coordinate stretching to discretize the physical space with gradually varying grid, while solving the wave equation on a uniform mesh. That results in a

significant improvement in efficiency while ensuring numerical advantages pertaining to uniform mesh. Numerical reflection and wave distortion are reduced to the similar level as Pitarka's method. Its advantages over Pitarka's approach include less memory requirement (no overhead), no need to solve a linear system, flexibility with difference operators and implementation friendly.

1.1.2 Wavelet-based Difference Operator

The difference operator that approximates the spatial derivatives also affects efficiency and accuracy of an algorithm. By approximating derivatives with differences, the finite difference scheme converts PDEs with linear algebraic equations. The discrepancy between the finite difference solution and the PDE solution consists of two contributions: the discretization error that causes grid dispersion and anisotropy, and the error due to cutting the infinite long operator into a finite length. Techniques for obtaining a more accurate numerical solution using FDTD has been focused on reducing those two effects, such as using higher-order difference approximations (Dablain, 1986) and staggered grids (Virieux, 1986). None conventional difference operators were also proposed to improve reflection and transmission accuracy at sharp boundaries (Cunha, 1993).

In recent years, several successful applications are reported using wavelet-based FDTD schemes in computing electrodynamics (Krumpholz and Katehi, 1996; Fujii and Hoefer, 2001). Comparing to conventionally used Taylor's expansion based method, the wavelet-based algorithm approximates derivatives with a better interpolation function, thus it generates considerably less numerical dispersion than the Taylor's expansion based method.

The wavelet formulation of the FDTD method thus far has not been studied solving the elastic wave equations. We formulate the wavelet based FDTD algorithm for elastodynamics, and find it shows more linear dispersion property than the 4th and the 2nd order schemes, allowing coarser sampling at a given accuracy. In addition, the wavelet based scheme yields more accurate reflection and transmission coefficients at a discontinuity, especially when combined with variable griding.

1.1.3 Perfectly Matched Layer

In most cases, we need to simulate wave propagations in a boundless medium, hence the medium is truncated into a finite size. This requires a numerical implementation of an absorbing boundary layer surrounding the computational domain to reduce reflections off the numerical boundary. An inefficient absorbing boundary layer results in a less accurate or computationally more costly algorithm.

Berenger (1994) first proposed the perfectly matched layer (PML) concept for electrodynamics using the FDTD method. Different from most traditional or differential equation-based absorbing boundaries, the PML satisfies all continuity conditions at the interface between the computational domain and the PML. Therefore, it has proven to be the most efficient mechanism to absorb wave energies outside the computational domain (Taflove, 1998). Liu formulated the PML for elastic waves using the field-splitting method which requires 27 independent unknowns for a general 3-D problem (9 velocity components and 18 stress components), three times the original 9 variables in ordinary elastic wave equations (Liu, 1999). Zheng and Huang formulated an anisotropic PML without using field splitting that only requires 12 independent unknowns for a general 3-D problem, and showed superior results using the finite element method (Zheng et al., 2002). In this study, we show that 18 independent unknowns are required for a stable FDTD PML, 1/3 less than that of the field-splitting method. More importantly, our formulation unites the non-uniform grid scheme with the non-splitting PML, allowing much simpler implementation.

1.1.4 2.5-D Formulation

3-D finite difference computations are often performed in the (x,y,z,t) domain. For the particular problems that this dissertation is to address, namely, wave propagations in a fluid-filled borehole, properties in the axial direction (z direction) are often assumed homogeneous. That means a plane wave propagating in the z direction does not change, therefore the wave equation can be Fourier transformed to and solved by a finite difference approach in the (x,y,k_z,t) domain to further increase computational

efficiency, as model properties are assumed homogeneous along the z axis throughout the dissertation. k_z represents the axial wavenumber. The final solution of the 3-D wave equation in the (x,y,z,t) domain is obtained by an inverse Fourier transform. Such finite difference approach is referred as 2.5-D (Randall, 1991b). There are two major benefits of using the 2.5-D formula over a 3-D formula for the applications in the scope of the thesis: 1) significant memory saving; 2) can be completely parallelized with respect to k_z.

The resulting finite difference time domain algorithm developed in the dissertation is able to finish most LWD simulations within a day on a 24-CPU PC cluster. Also the mesh scheme and the difference operators proposed in the dissertation can be adapted to solve other forms of partial differential equations. The method is described in chapter2 and chapter 3.

1.2 Modal Excitations in LWD

A review of the borehole acoustic logging history would help understand the motivation and significance of the LWD study.

Borehole acoustic logging has been a highly specialized technology in exploration for natural resources for decades. It works as an extension of surface seismology (*i.e.*, check shots and depth calibration of travel times), and as a method for characterizing lithologies *in situ*. It started as a simple device to measure the time required for acoustic waves to travel along a given length of formation adjacent to the borehole, and then invert for the *in situ* compressional velocity, v_p (Summers and Broding, 1952). Figure 1-3 shows the schematic illustration of acoustic logging in a fluid-filled borehole. More than a decade later, with the development of AD/DA (analog to digital and digital to analog) technology, waveforms were digitized and recorded, marking the start of *full waveform* acoustic logging era. Shear arrivals was subsequently detected in the waveform at times after the first compressional arrivals and the formation shear velocity v_s is then determined (Willis and Toksoz, 1983). Up then, the source had a uniform radiation pattern and both compressional and shear

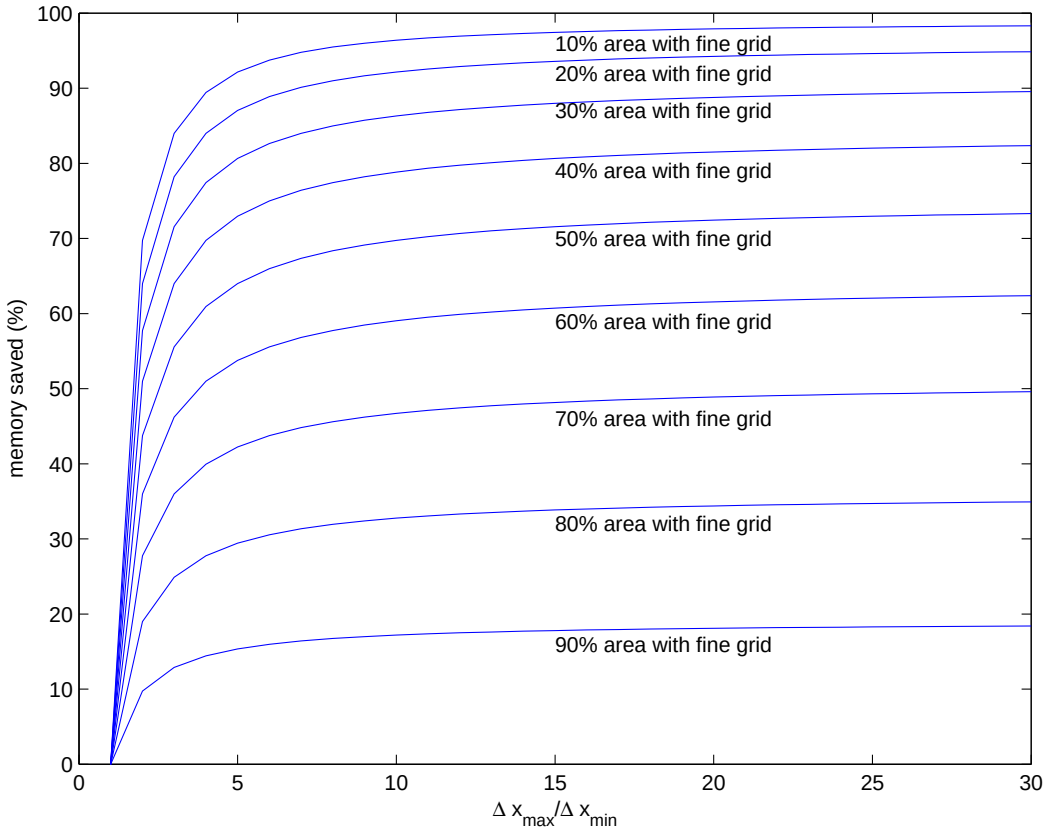

Figure 1-1: Memory saving rate by using a non-uniform spacing mesh with respect to the ratio of the coarsest grid size over the finest one. Each line represents models that has $a\%$ of the volume that requires fine grid.

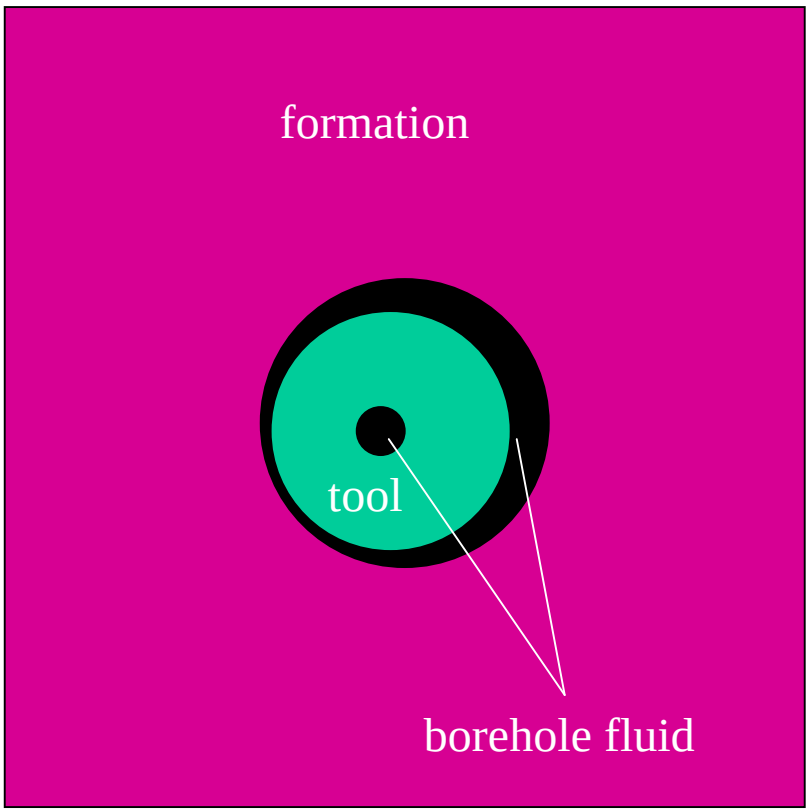

Figure 1-2: A cross-section of a fluid-filled borehole with an LWD tool. The tool is off-centered. Typically, the borehole diameter is around 20 cm, the outer diameter of the tool is about 18 cm. The fluid annulus could be as small as several millimeters.

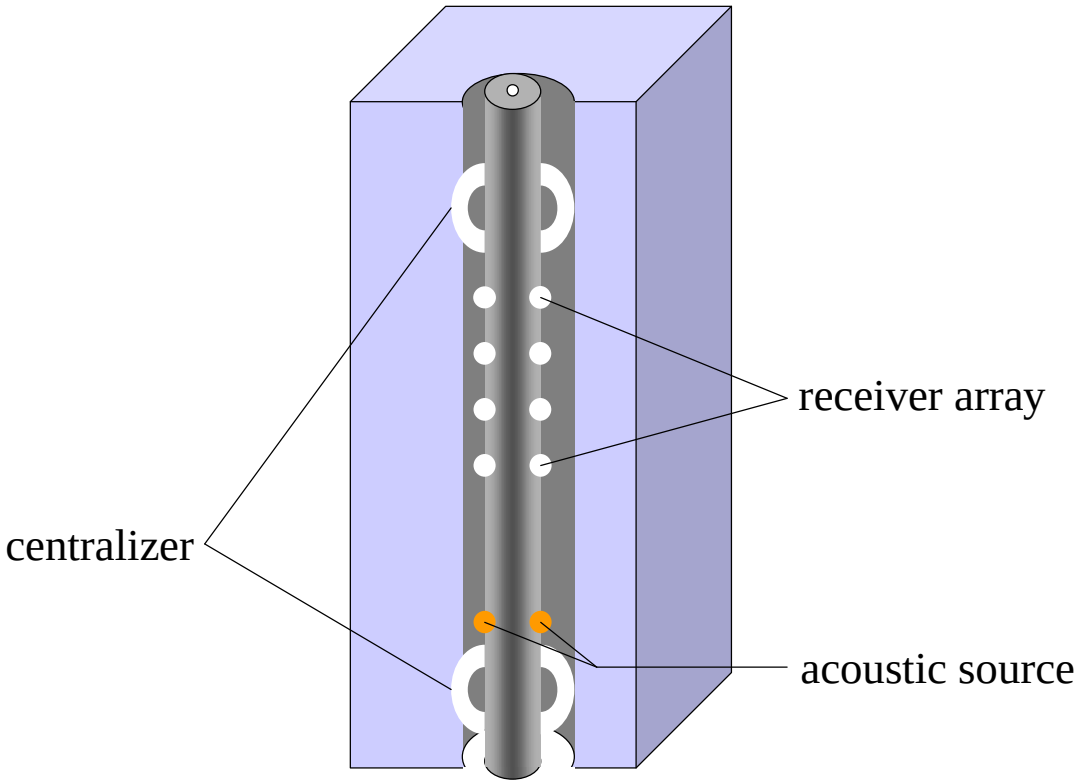

Figure 1-3: A schematic illustration of acoustic logging in a fluid-filled borehole.

measurements come from critically refracted head waves. Although ideas of using multipole (mainly dipole and quadrupole) source and receivers in the acoustic logging was proposed in the 1960's (White, 1967), dipole logging did not get attention until later. As demonstrated in later analysis, multipole shear logging tool is not measuring the shear velocity directly, rather it is measuring the flexural mode, trapped by the fluid-filled borehole (Kurkjian and Chang, 1986; Winbow, 1988; Schmitt, 1988).

Along the way, number of studies had shown that the fluid-filled borehole acts as a waveguide, eigenvalues of which are determined by the specific borehole geometry, velocity contrasts between the borehole fluid and the formation, and frequencies excited by the logging source (Biot, 1952; Peterson, 1974; Tsang and Rader, 1979; Cheng and Toksoz, 1981). Each eigenvalue of the waveguide represents a mode and

determines a certain dispersion relation (velocity *vs* frequency) of that mode. Modes differ from each other by number of pressure (or velocity) nodes in both azimuthal and radial direction. For identification purpose, a mode is labeled by (n, m), representing the n-th order azimuthal variation (with 2n nodes azimuthally) and m-th order radial variation (with m nodes radially). Monopole mode refers to any mode that does not vary azimuthally, *i.e.* n=0, where (0,0) mode is conventionally named as Stoneley mode. Dipole mode refers to any one in the (1,m) family, where (1,0) mode is conventionally named as flexural mode. Figure 1-4 shows dispersion curves of 8 modes in both hard and soft formations.

Up to the 1990's, acoustic logging had been carried out after the borehole is drilled. As the tool needs a cable to be sent down the hole, it is referred as wireline tool. The radius of a typical wireline tool is at least half less than that of the borehole. Effects of the tool on borehole modes are small so that they have been neglected or adjusted with simple corrections in both modeling studies or data processings. The list of formation properties that the acoustic logging is able to measure has been progressively longer, from v_p and v_s values to formation anisotropy and permeability.

Logging while drilling (LWD) tools emerged in the 1990's and are gaining momentum due to their engineering and economical advantages (Minear et al., 1995, 1996; Heysse et al., 1996; Tang et al., 2002). Formation properties are measured simultaneously while drilling avoiding problems such as "mud cake" and reducing the rig time, compared to their wireline counterparts. LWD measurements may also enable a real-time evaluation of formation properties which leads to significant potential for "look-ahead of the bit" and better control of well trajectories.

LWD tool differs from its wireline counterpart only by geometry. Thus it looked reasonable for LWD tool designers to borrow the wealth of wisdoms in the wireline logging literature. However, with its sources and receivers more close to the borehole wall and substantially larger cross-section of the tool taking up majority space in the fluid-filled borehole, LWD is found to differ considerably from its wireline counterpart. It has significant effects on borehole modes (Rao et al., 1999). That gives rise the difficulties to identify modal arrivals, a crucial step to estimate formation v_p and v_s

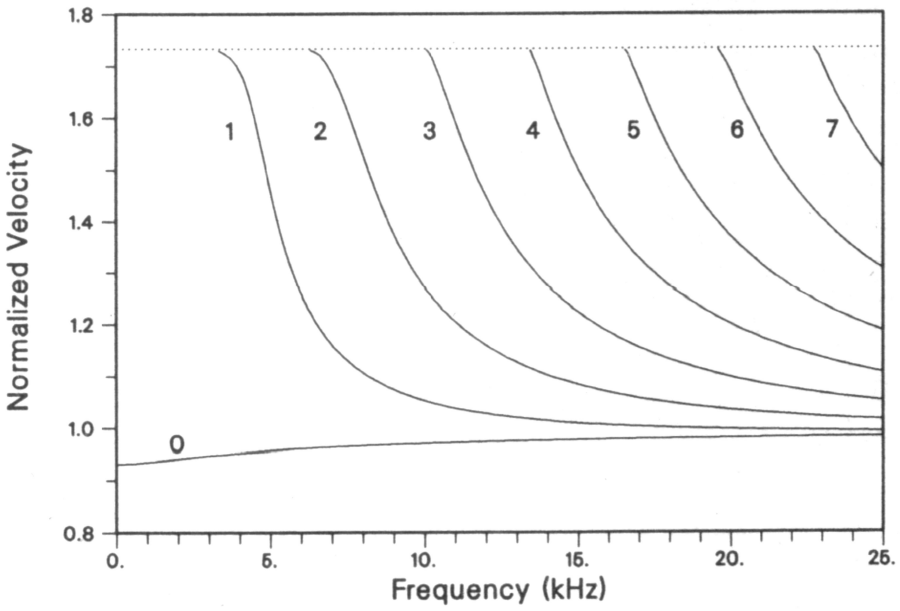

(a) hard formation

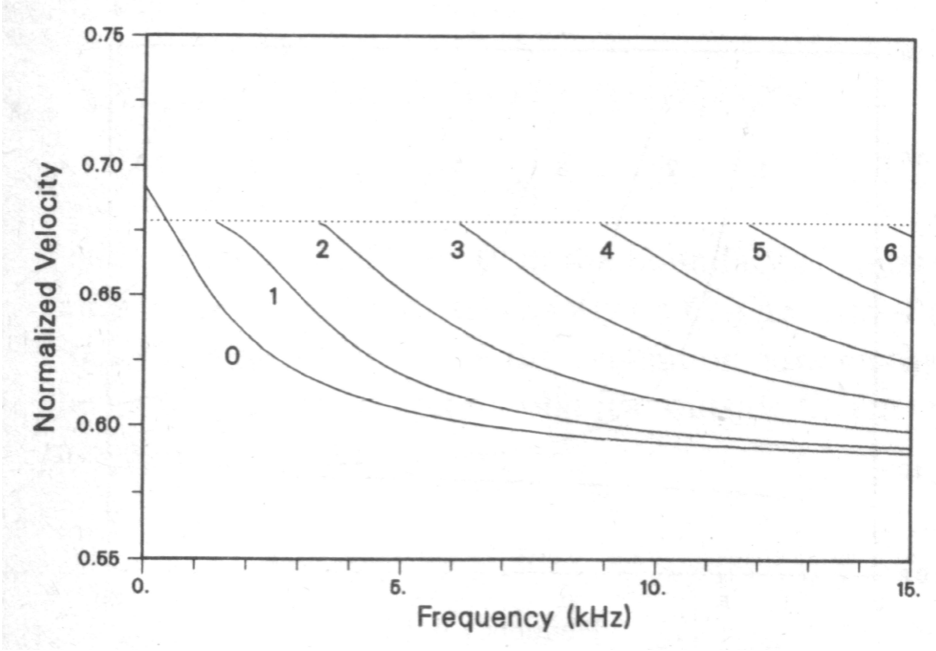

(b) soft formation

Figure 1-4: Dispersion curves of borehole modes (n=0-7, m=0) of a 10-cm radius borehole in a hard and soft formation. Phase velocities are normalized by the compressional velocity of the borehole fluid. Curves are labeled by the azimuthal order n. Dotted horizontal line is the formation shear velocity. .

values.

In this thesis, the author conducts a comprehensive study of LWD with focus on modal excitations with respect to frequencies, tool positions, source type and formation type (chapter 4 and chapter 5). Its findings may lead to new designs that take advantages of LWD situation. Also understanding characteristics of LWD will provide some insights to data interpretion.

1.3 Measuring Formation Stress from Acoustic Logging Data

The dissertation comes in the middle of another ongoing efforts in the borehole acoustic logging area, which is to extract formation stresses from acoustic logging data.

As lithospheric plates interact with each other, complicated stresses patterns develop within each plate. Mapping formation stress may help understand plate tectonics. To the petroleum industry, knowledge of formation stresses would aid in enhanced recovery of hydrocarbons, prevention of sand production and borehole instability (Gaarenstroom et al., 1993; Dore and Lundin, 1996; Finkbeiner et al., 1998; Wiprut, 2001). Stresses in the earth also plays an important role in assessment of long term stability of underground waste disposal. Currently, large scale stress orientations are estimated from geological or geophysical data including earthquake focal mechanisms, fault slips and volcanic alignments (Zoback, 1992). For exploration and engineering purposes, earthquake and volcanic data lack the necessary resolution, not mentioning the fact that they may not occur over the desired area. At local scale, techniques like borehole breakouts and *in-situ* stress measurements such as hydraulic fracturing and overcoring, are commonly used. Breakouts in vertical boreholes may help locate stress orientations fairly accurately, but provide little information for estimating stress magnitudes (Zoback et al., 1985). By far the most accurate, also the most expensive, technique to measure the formation stress is hydraulic fracturing, where the formation stress is assumed to be completely balanced by a controlled

water pressure when a shear failure happens to the borehole wall. However, that assumption often breaks in realistic measurements (Haimson, 1988).

All the above mentioned stress estimating methods are under the framework of static mechanics, where formation stresses are considered being balanced by other processes or forces. Therefore, to accurately estimate formation stresses, an exhaustive and accurate analysis of all processes and forces is essential. However in those analysis often the number of unknowns is large.

We choose to estimate formation stresses indirectly from seismic or acoustic measurements based on the belief that the problem may be better constrained. It has been well established from experiments that stresses introduce anisotropy and velocity changes to a formation (Nur and Simmons, 1969; Lo et al., 1986). While it is difficult in seismic data to differentiate stress induced anisotropy from intrinsic anisotropy caused by such things like fractures and thin-layered bedding, it is not so in borehole acoustic data. To satisfy the boundary conditions at the circular wall, an originally uniform stress field deforms and concentrates around a borehole. In a vertical borehole, the maximum compressional stress around the borehole aligns with the direction of the minimum regional horizontal stress. As borehole flexural mode is sensitive to the far-field stress at low frequencies and to the near-field stress at high frequencies, a crossover in borehole flexural dispersion occurs, indicating stress-induced anisotropy dominating over other sources of intrinsic anisotropy. That was predicted theoretically by Sinha and Kostek (1996). The prediction was subsequently verified in a scaled-borehole experiment (Winkler et al., 1998).

In chapter 6, a multi-frequency inversion method is developed to estimate stress magnitudes and directions from borehole acoustic measurements. We are the first ones that observe flexural dispersion crossover in field data(Nolte et al., 1997; Huang et al., 1999). Using the flexural crossover as a stress signature in the borehole acoustic data, we are able to isolate stressed zones. The maximum horizontal stress direction coincides with the polarization direction of far field fast shear. The stress magnitude is related to velocity changes in the stressed state from the zero stress or hydrostatically balanced state, through a perturbation theory, which is used in the multi-frequency

inversion method developed here to estimate stress magnitude. Our method is applied to a set of field data collected in an oil field near San Andreas fault. The estimated stress directions are consistent with focal mechanism and borehole breakout data present in the world stress map database (Zoback, 1992).

Chapter 7 summarizes the dissertation and outlines some future work.

Chapter 2

A Stretched Coordinate Formulation of Finite Difference Time Domain Scheme with Non-Uniform Spacing Grids and Anisotropic Perfectly Matched Layers

ABSTRACT

A novel finite difference time domain formulation is developed to solve the elastic wave equations. By coordinate stretching, the algorithm discretizes the physical space with gradually varying grid, while solving the wave equation on a uniform mesh. That results in a significant improvement in efficiency while ensuring numerical advantages pertaining to uniform mesh. Further improvement in efficiency is achieved without losing accuracy by the development of a wavelet-based difference operator, allowing less grid point per wavelength. Coordinate stretching is also employed in deriving an

anisotropic perfectly matched layer, superior to currently available perfectly matched layer formulation which requires field splitting, a process that results more computer memory requirement for the storage of extra variables. Validations of the algorithm include comparison with analytical solutions and uniform grid FDTD solutions.

2.1 Introduction

The FDTD method has been one of the most widely used tools to simulate wave propagations in 2-D and 3-D elastic media with fairly general spatial variations of elastic properties. In recent years, applications to highly inhomogeneous models have made it necessary to sample the physical model adaptively with non-uniform grid.

While it is obvious that efficiency can be achieved by sampling the physical space adaptively with variable grid, that benefit may be offset by other problems introduced by the change in grid size. The formal truncation error and the stability of the system may be adversely affected by the change in grid size (Crowder and Dalton, 1971). There may also be wave distortion or numerical reflections due to a phase change at the interface of two grids (Browning et al., 1973). Hayashi (1999) developed a 4th order 2D variable grid FDTD algorithm by using discontinuous grids, which involves interpolation of the wave field on more than one plane. Special formulae are used at the interface of the two grids. Pitarka (1999) developed a 3D 4th order FDTD algorithm that uses continuous non-uniform spacing grids. Pitarka's approach reduces both numerical reflection and wave distortion. However, memory overhead of this approach is high and it requires solving a linear system before conducting the FDTD calculation. The linear system has to be re-solved when the difference operator needs a change (*e.g.* from 4th order to 8th order).

We develop an FDTD scheme using non-uniform spacing grids. Numerical reflection and wave distortion are reduced to the similar level as Pitarka's method. Its advantages over Pitarka's approach include less memory requirement (no overhead), no need to solve a linear system, flexibility with difference operators and implementation friendly. More importantly, our formulation unites the non-uniform grid scheme

with the non-splitting (anisotropic) perfectly matched layer (PML), a numerical absorbing mechanism proven to be the most effective of its kind (Berenger, 1994; Shlager and Schneider, 1998). The key component in our formulation is a coordinate transformation, or more specifically, stretching along both the real and imaginary of axes of each coordinate directions. The stretching along the real axes in three coordinate directions leads to an effective variable gridding in the physical domain while uniform gridding in the transformed domain. An important benefit of doing so is that the formal truncation error and the stability properties of the finite difference computation are preserved because the computation is carried out on a uniform grid. The stretching along the imaginary axes in three coordinate directions introduces a highly efficient attenuation in the absorbing layer.

The difference operator that approximate the spatial derivatives also affects efficiency and accuracy of an algorithm. There have been several efforts of constructing higher order or non-conventional difference operators to reduce numerical dispersion and improve accuracy, especially at discontinuities (Dablain, 1986; Cunha, 1993; Vossen et al., 2002). In recent years, several successful applications have been reported using wavelet-based FDTD schemes in computing electrodynamics (Krumpholz and Katehi, 1996; Fujii and Hoefer, 2001). Unlike the conventionally used Taylor's expansion based method, wavelet-based algorithm approximate derivatives without truncation by using compactly supported wavelet-functions, and it generates considerably less numerical dispersion than the Taylor's expansion based method. The wavelet formulation of the FDTD method thus far has not been studied solving the elastic wave equations. We formulate the wavelet based FDTD algorithm for elastodynamics and find it shows more linear dispersion property than the 4th and the 2nd order schemes, allowing coarser sampling at a given accuracy. In addition, the wavelet based scheme yields more accurate reflection and transmission coefficients at a discontinuity, especially when combined with variable gridding.

2.2 Coordinate Stretching

Equations governing the elastic wave propagation can be written as two coupled first order equations 2.1 and 2.2, where $c_{\alpha j\gamma\beta}$ denotes the elastic tensor and ρ the mass density. Solving the wave equation numerically is to compute all three components of particle velocities v_j and all 6 components of stress tensors $\tau_{\alpha j}$ at every time t and spatial position $\vec{r} = [x_1, x_2, x_3] = [x, y, z]$. All indices ($\eta$, j, γ and β) take values of 1, 2 and 3, representing three orthogonal coordinate directions. Einstein's summation convention applies to the subscript indices.

$$\rho v_{j,t} = \tau_{\eta j,\eta}, \tag{2.1}$$

$$\tau_{\eta j,t} = c_{\eta j\gamma\beta} v_{\gamma,\beta}. \tag{2.2}$$

We choose the grid size in the physical domain, Δx_i, equal to the grid size in the transformed domain, $\Delta\tilde{x}_i$, times a smoothly varying function $\epsilon^i(\tilde{x})$ that takes values between 1 and α^i, where α^i can be any positive real number, *i.e.* $\alpha^i \in \mathbf{R}^+$,

$$\Delta x_i = \epsilon^i(\tilde{x}_i)\Delta\tilde{x}_i. \tag{2.3}$$

$\epsilon^i(\tilde{x}_i)$ can be functions of the user's choice. We construct the smoothly varying function in each of the coordinate directions, $\epsilon^i(\tilde{x}_i)$, as the following

$$\epsilon^i(\tilde{x}_i) = \begin{cases} 1 & \tilde{x}_i \leqslant \tilde{x}_i^0 \\ 1 + (\alpha^i - 1)\sin\frac{\pi}{2L^i}(\tilde{x}_i - \tilde{x}_i^0) & \tilde{x}_i^0 \leqslant \tilde{x}_i \leqslant \tilde{x}_i^0 + L^i \\ \alpha^i & \tilde{x}_i \geqslant \tilde{x}_i^0 + L^i \end{cases} \tag{2.4}$$

Thus the grid size in the stretched domain is uniform, and varies gradually from $\Delta\tilde{x}_i$ to $\alpha^i\Delta\tilde{x}_i$ in the physical domain. α^i controls the ratio of the grid size between the coarsest and the finest ones in x_i direction. It is called as the stretching factor. Notice that $\epsilon^i(\tilde{x}_i)$ is defined in the transformed domain. Figure 2-1(a) shows the shape of ϵ^i with different α^i, the corresponding grid spacing is shown in figure 2-1(b).

When the grid size is small enough, equation 2.3 also represents the relationship

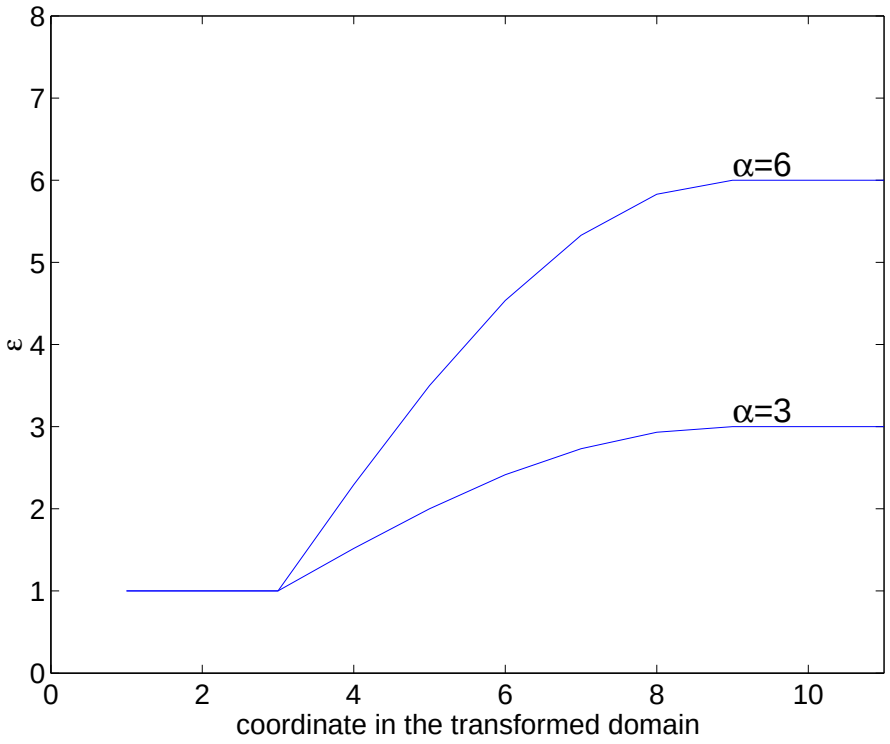

(a) stretching function

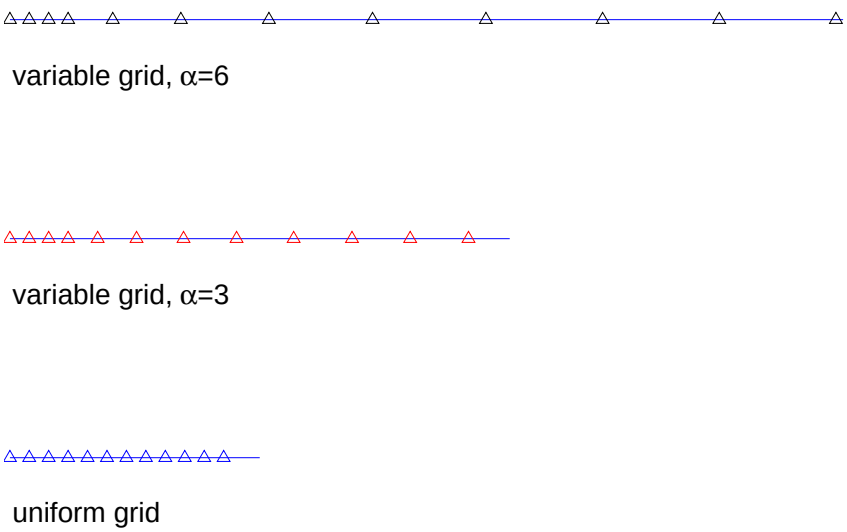

(b) grid scheme

Figure 2-1: a. The stretching function $\epsilon(\tilde{x})$ for different stretching parameters, α. b. Uniform grid in the transformed domain and non-uniform grid in the physical domain corresponding to stretching functions in figure a.

between the differential operations in the two domains, i.e., $\Delta x_i \rightarrow dx_i$ and $\Delta \tilde{x}_i \rightarrow d\tilde{x}_i$, the integration of which in three respective coordinate directions are the mapping functions between the two domains, $x_i = f_i(\tilde{x}_i)$ shown in equation 2.5.

$$x_i = \begin{cases} \tilde{x}_i & \tilde{x}_i \leqslant \tilde{x}_i^0 \\ \tilde{x}_i + (\alpha^i - 1)\frac{2L^i}{\pi}\{1 - \cos\frac{\pi}{2L^i}(\tilde{x}_i - \tilde{x}_i^0)\} & \tilde{x}_i^0 \leqslant \tilde{x}_i \leqslant \tilde{x}_i^0 + L^i \\ (1-\alpha^i)(\tilde{x}_i^0 + L^i - \frac{2L^i}{\pi}) + \alpha^i \tilde{x}_i & \tilde{x}_i \geqslant \tilde{x}_i^0 + L^i \end{cases} \tag{2.5}$$

Transforming all field variables from (x_1, x_2, x_3, t) domain to ($\tilde{x}_1$, $\tilde{x}_2$, $\tilde{x}_3$, t) domain by mapping functions $\tilde{x}_i = f_i^{-1}(x)$, the spatial derivative of a field variable, g(x_1,x_2,x_3,t), becomes,

$$\partial_{x_i} g(x_1, x_2, x_3, t) = \frac{\partial_{\tilde{x}_i}}{\partial x_i} \partial_{\tilde{x}_i} g(\tilde{x}_1, \tilde{x}_2, \tilde{x}_3, t) = \frac{1}{\epsilon^i(\tilde{x}_i)} \partial_{\tilde{x}_i} g(\tilde{x}_1, \tilde{x}_2, \tilde{x}_3, t) \tag{2.6}$$

Equations 2.1 and 2.2 then become,

$$\rho v_{j,t} = \frac{1}{\epsilon^\eta(\tilde{x}_\eta)} \tau_{\eta j,\eta} \tag{2.7}$$

$$\tau_{\eta j,t} = c_{\eta j \gamma \beta} \frac{1}{\epsilon^\beta(\tilde{x}_\beta)} v_{\gamma,\beta}. \tag{2.8}$$

Discretizing the above equations with uniform grid in the transformed domain is equivalent to a non-uniform grid in the physical domain that has been stretched by a factor of ϵ^i in each coordinate direction. Note that along each coordinate direction, the elastic impedence remains unchanged after the coordinate stretching; therefore, in theory, there should be no reflection introduced by stretching. Using a smooth stretching function is to ensure low numerical reflection.

When implementing the stretched grid FDTD algorithm, positions of discontinuous points, lines and surfaces as well as sources and receivers in the physical domain are transformed to the stretched domain by the mapping functions before a uniform discretization is performed in the transformed domain. Final results are then mapped back to the physical domain.

Equation 2.4 is not a complete function that controls the coordinate stretching

at the vicinity where the change in grid size takes place. Depending on the physical model, a complete stretching function of the total physical domain requires piecing together different versions of equation 2.4, either by being flipped or taking different values of $\tilde{x}_i^0$, L^i or α^i. Take a fluid-filled borehole as an example, finer sampling is needed inside and at the neighborhood of the borehole wall. So both stretching functions at the x_1 and x_2 directions may be built as shown in figure 2-2. The cross section of the resulting gridding scheme is illustrated in figure 2-3 for the physical domain and figure 2-4 for the transformed domain, respectively. In the transformed domain where the FDTD computation is performed, the model size is smaller and the grid size is uniform. The area reduction reflects the amount of memory saving achieved by using the variable grid versus using the uniform grid where the grid size equals to the smallest grid size in the variable grid.

2.3 Absorbing Boundary: Anisotropic Perfectly Matched Layer (PML)

In most cases, we need to simulate wave propagations in an unbounded medium, hence the medium is truncated into a finite size. This requires numerically implementing an absorbing boundary layer surrounding the computational domain to reduce reflections off the numerical boundary. An inefficient absorbing boundary layer results in a less accurate and less efficient algorithm.

Berenger (1994) first proposed the perfectly matched layer (PML) concept for electrodynamics using the FDTD method. Different from most traditional or differential equation-based absorbing boundaries, the PML satisfies all continuity conditions at the interface between the computational domain and the PML. Therefore, it has proven to be the most efficient mechanism to absorb wave energies outside the computational domain (Taflove, 1998). Liu formulated the PML for elastic waves using the field-splitting method which requires 27 independent unknowns for a general 3-D problem (9 velocity components and 18 stress components), three times the original

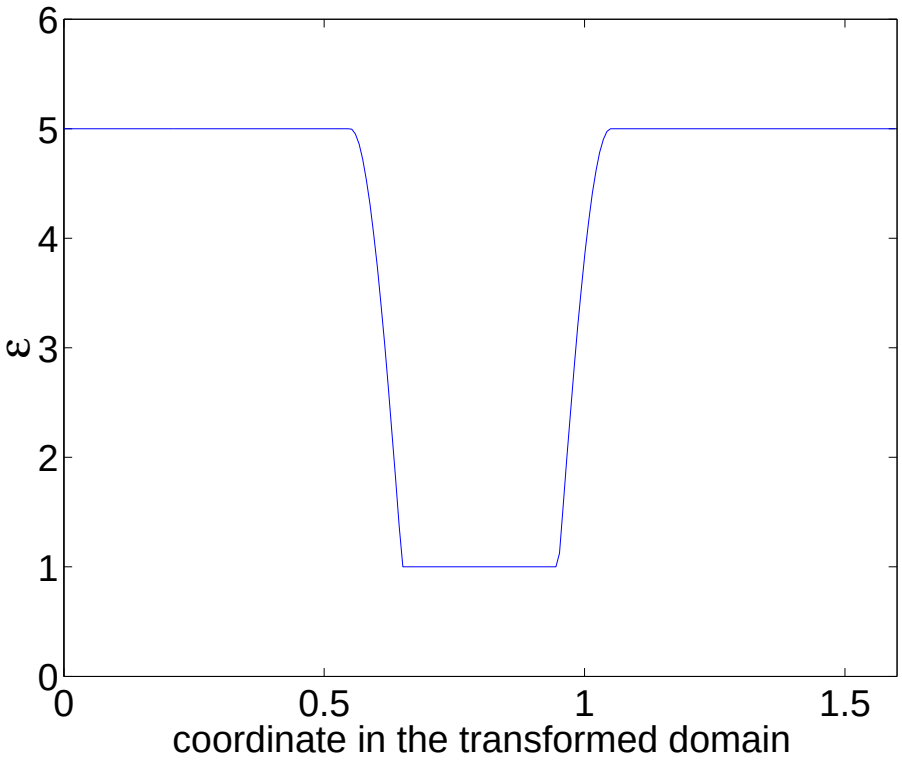

Figure 2-2: The complete stretching function $\epsilon^1(\tilde{x_1})$ or $\epsilon^2(\tilde{x_2})$. All numerical examples in this paper use the same stretching function. Only the stretching factor α and the transition length L may vary from case to case.

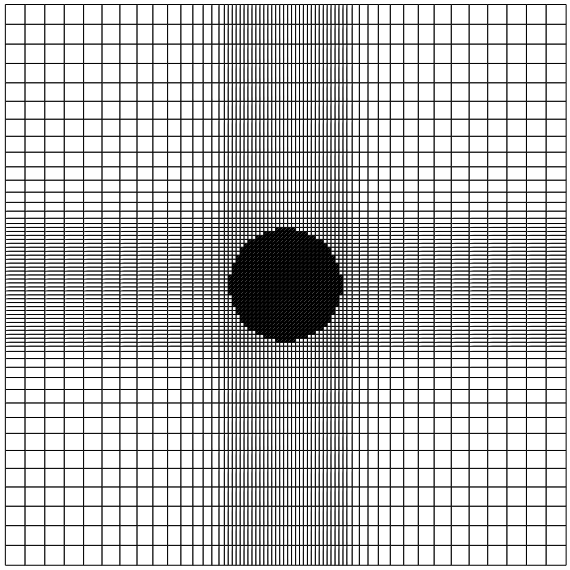

Figure 2-3: The variable gridding scheme of a fluid filled borehole in the physical domain. The stretching ratio is 5.

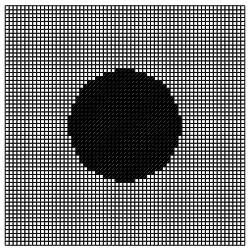

Figure 2-4: Same model as shown in figure 2-3 in the transformed domain with uniform gridding. Comparing to figure 2-3, the model space becomes smaller, directly reflecting a saving in memory.

9 variables in ordinary elastic wave equations (Liu, 1999).

Based on the concept of coordinate stretching along the imaginary axes, an anisotropic PML without using field splitting is formulated which only requires 12 independent unknowns for a general 3-D problem, and showed superior results using the finite element method (Zheng, 2002). Further study shows that 18 independent unknowns are required for a stable FDTD PML (Zheng et al., 2003), 1/3 less than the field-splitting formulae. Besides the advantage of non-splitting and requiring less variables, Zheng's PML is stable and has the same format for both isotropic and anisotropic media. It ultimately shares the same formulae as for the stretched grid approach describe in the previous section. In the vector and tensor format, Zheng's PML are expressed in equation 2.9 and 2.10.

$$\rho\epsilon_1\epsilon_2\epsilon_3\partial_t\vec{v} = \nabla\cdot\tau \tag{2.9}$$

$$\mathbf{e}\partial_t\tau = \mathbf{c} : \epsilon_1\epsilon_2\epsilon_3\mathbf{e}^{-1}\nabla\vec{v} \tag{2.10}$$

where

$$\mathbf{e} = \begin{bmatrix} \epsilon_1 & 0 & 0 \\ 0 & \epsilon_2 & 0 \\ 0 & 0 & \epsilon_3 \end{bmatrix} \tag{2.11}$$

and vector $\vec{v} = [v_x, v_y, v_z]^T = [v_1, v_2, v_3]^T$ represents particle velocities, $\mathbf{c}$ is the elasticity tensor and the stress tensor τ is defined as

$$\tau = \begin{bmatrix} \tau_{xx} & \tau_{xy} & \tau_{xz} \\ \tau_{yx} & \tau_{yy} & \tau_{yz} \\ \tau_{zx} & \tau_{zy} & \tau_{zz} \end{bmatrix} \tag{2.12}$$

ϵ_j in equations 2.9 and 2.10 controls the coordinate stretching along the imaginary axes of three coordinate directions in the PML and is chosen as $1-i\frac{\beta_j}{\omega}$, where ω is the angular frequency. Fourier transforming equations 2.9 and 2.10 by replacing ∂_t with $i\omega$ and substituting ϵ_j with $1-i\frac{\beta_j}{\omega}$, then inverse Fourier transforming the equations

back to the time domain, the general 3D wave equations in the PML that need to be numerically solved in the stretched coordinate are obtained. Their individual components are listed in the following where orthorhombic anisotropy is assumed for the formation.

$$\partial_t B_{xx} + \beta_x B_{xx} = \frac{1}{\rho}\left(\frac{1}{\epsilon^x(\tilde{x})}\partial_{\tilde{x}}\tau_{xx} + \frac{1}{\epsilon^y(\tilde{y})}\partial_{\tilde{y}}\tau_{yx} + \frac{1}{\epsilon^z(\tilde{z})}\partial_{\tilde{z}}\tau_{zx}\right) \tag{2.13}$$

$$\partial_t B_{xy} + \beta_x B_{xy} = \frac{1}{\rho}\left(\frac{1}{\epsilon^x(\tilde{x})}\partial_{\tilde{x}}\tau_{xy} + \frac{1}{\epsilon^y(\tilde{y})}\partial_{\tilde{y}}\tau_{yy} + \frac{1}{\epsilon^z(\tilde{z})}\partial_{\tilde{z}}\tau_{zy}\right) \tag{2.14}$$

$$\partial_t B_{xz} + \beta_x B_{xz} = \frac{1}{\rho}\left(\frac{1}{\epsilon^x(\tilde{x})}\partial_{\tilde{x}}\tau_{xz} + \frac{1}{\epsilon^y(\tilde{y})}\partial_{\tilde{y}}\tau_{yz} + \frac{1}{\epsilon^z(\tilde{z})}\partial_{\tilde{z}}\tau_{zz}\right) \tag{2.15}$$

$$\partial_t B_{yx} + \beta_y B_{yx} = \frac{1}{\rho}\left(\frac{1}{\epsilon^x(\tilde{x})}\partial_{\tilde{x}}\tau_{xx} + \frac{1}{\epsilon^y(\tilde{y})}\partial_{\tilde{y}}\tau_{yx} + \frac{1}{\epsilon^z(\tilde{z})}\partial_{\tilde{z}}\tau_{zx}\right) \tag{2.16}$$

$$\partial_t B_{yy} + \beta_y B_{yy} = \frac{1}{\rho}\left(\frac{1}{\epsilon^x(\tilde{x})}\partial_{\tilde{x}}\tau_{xy} + \frac{1}{\epsilon^y(\tilde{y})}\partial_{\tilde{y}}\tau_{yy} + \frac{1}{\epsilon^z(\tilde{z})}\partial_{\tilde{z}}\tau_{zy}\right) \tag{2.17}$$

$$\partial_t B_{yz} + \beta_y B_{yz} = \frac{1}{\rho}\left(\frac{1}{\epsilon^x(\tilde{x})}\partial_{\tilde{x}}\tau_{xz} + \frac{1}{\epsilon^y(\tilde{y})}\partial_{\tilde{y}}\tau_{yz} + \frac{1}{\epsilon^z(\tilde{z})}\partial_{\tilde{z}}\tau_{zz}\right) \tag{2.18}$$

$$\partial_t B_{zx} + \beta_z B_{zx} = \frac{1}{\rho}\left(\frac{1}{\epsilon^x(\tilde{x})}\partial_{\tilde{x}}\tau_{xx} + \frac{1}{\epsilon^y(\tilde{y})}\partial_{\tilde{y}}\tau_{yx} + \frac{1}{\epsilon^z(\tilde{z})}\partial_{\tilde{z}}\tau_{zx}\right) \tag{2.19}$$

$$\partial_t B_{zy} + \beta_z B_{zy} = \frac{1}{\rho}\left(\frac{1}{\epsilon^x(\tilde{x})}\partial_{\tilde{x}}\tau_{xy} + \frac{1}{\epsilon^y(\tilde{y})}\partial_{\tilde{y}}\tau_{yy} + \frac{1}{\epsilon^z(\tilde{z})}\partial_{\tilde{z}}\tau_{zy}\right) \tag{2.20}$$

$$\partial_t B_{zz} + \beta_z B_{zz} = \frac{1}{\rho}\left(\frac{1}{\epsilon^x(\tilde{x})}\partial_{\tilde{x}}\tau_{xz} + \frac{1}{\epsilon^y(\tilde{y})}\partial_{\tilde{y}}\tau_{yz} + \frac{1}{\epsilon^z(\tilde{z})}\partial_{\tilde{z}}\tau_{zz}\right) \tag{2.21}$$

$$\partial_t \tau_{xx} + \beta_x \tau_{xx} = c_{11}\frac{1}{\epsilon^x(\tilde{x})}\partial_{\tilde{x}}B_{xx} + c_{12}\frac{1}{\epsilon^y(\tilde{y})}\partial_{\tilde{y}}B_{yy} + c_{13}\frac{1}{\epsilon^z(\tilde{z})}\partial_{\tilde{z}}B_{zz} \tag{2.22}$$

$$\partial_t \tau_{xy} + \beta_x \tau_{xy} = c_{66}\left(\frac{1}{\epsilon^x(\tilde{x})}\partial_{\tilde{x}}B_{xy} + \frac{1}{\epsilon^y(\tilde{y})}\partial_{\tilde{y}}B_{yx}\right) \tag{2.23}$$

$$\partial_t \tau_{xz} + \beta_x \tau_{xz} = c_{55}\left(\frac{1}{\epsilon^x(\tilde{x})}\partial_{\tilde{x}}B_{xz} + \frac{1}{\epsilon^z(\tilde{z})}\partial_{\tilde{z}}B_{zx}\right) \tag{2.24}$$

$$\partial_t \tau_{yx} + \beta_y \tau_{yx} = c_{66}\left(\frac{1}{\epsilon^x(\tilde{x})}\partial_{\tilde{x}}B_{xy} + \frac{1}{\epsilon^y(\tilde{y})}\partial_{\tilde{y}}B_{yx}\right) \tag{2.25}$$

$$\partial_t \tau_{yy} + \beta_y \tau_{yy} = c_{12}\frac{1}{\epsilon^x(\tilde{x})}\partial_{\tilde{x}}B_{xx} + c_{22}\frac{1}{\epsilon^y(\tilde{y})}\partial_{\tilde{y}}B_{yy} + c_{23}\frac{1}{\epsilon^z(\tilde{z})}\partial_{\tilde{z}}B_{zz} \tag{2.26}$$

$$\partial_t \tau_{yz} + \beta_y \tau_{yz} = c_{44}\left(\frac{1}{\epsilon^y(\tilde{y})}\partial_{\tilde{y}}B_{yz} + \frac{1}{\epsilon^z(\tilde{z})}\partial_{\tilde{z}}B_{zy}\right) \tag{2.27}$$

$$\partial_t \tau_{zx} + \beta_z \tau_{zx} = c_{55}\left(\frac{1}{\epsilon^x(\tilde{x})}\partial_{\tilde{x}}B_{xz} + \frac{1}{\epsilon^z(\tilde{z})}\partial_{\tilde{z}}B_{zx}\right) \tag{2.28}$$

$$\partial_t \tau_{zy} + \beta_z \tau_{zy} = c_{44}\left(\frac{1}{\epsilon^y(\tilde{y})}\partial_{\tilde{y}}B_{yz} + \frac{1}{\epsilon^z(\tilde{z})}\partial_{\tilde{z}}B_{zy}\right) \tag{2.29}$$

$$\partial_t \tau_{zz} + \beta_z \tau_{zz} = c_{13}\frac{1}{\epsilon^x(\tilde{x})}\partial_{\tilde{x}}B_{xx} + c_{23}\frac{1}{\epsilon^y(\tilde{y})}\partial_{\tilde{y}}B_{yy} + c_{33}\frac{1}{\epsilon^z(\tilde{z})}\partial_{\tilde{z}}B_{zz} \tag{2.30}$$

where B_{ij} represents modified particle velocity and defined as

$$B_{xx} = \epsilon_y\epsilon_z v_x \quad B_{xy} = \epsilon_y\epsilon_z v_y \quad B_{xz} = \epsilon_y\epsilon_z v_z \tag{2.31}$$

$$B_{yx} = \epsilon_x\epsilon_z v_x \quad B_{yy} = \epsilon_x\epsilon_z v_y \quad B_{yz} = \epsilon_x\epsilon_z v_z \tag{2.32}$$

$$B_{zx} = \epsilon_x\epsilon_y v_x \quad B_{zy} = \epsilon_x\epsilon_y v_y \quad B_{zz} = \epsilon_x\epsilon_y v_z \tag{2.33}$$

In the model domain where no absorption occurs, β_j is set to be zero. Thus B_{ij} has only 3 independent components that equal to v_x, v_y and v_z and in addition, equations 2.13 dim 2.30 degenerate into normal wave equations without attenuation. When it comes to implementation, there is no need to keep all 18 variables (B_{ij} and τ_{ij}) inside the model domain, instead, only 9 (v_x, v_y, v_z, τ_{xx}, τ_{xy}, τ_{xz},τ_{yy}, τ_{yz} and τ_{zz}) are necessary due to symmetry. Discretization of the full 3D wave equations in the transformed domain and strategies to choose β_j are discussed in chapter 3.

2.4 Discretization Using Taylor's Expansion-Based And Wavelet-based Difference Schemes

The most commonly used and studied FDTD schemes are formulated based on the Taylor's expansion. References on this subject may be found in a wealth of finite difference literatures. The wavelet based formulae have been developed for electrodynamics based on the method of moments (Harrington, 1993). This method projects wave field components (particle velocities and stress components) to a complete set of orthonormal basis functions, then solves the partial differential equation in the projected domain iteratively. It was shown that the Taylor's expansion based staggered grid FDTD scheme can be derived using the method of moments with pulse functions making up the orthonormal basis functions (Krumpholz and Russer, 1993, 1994). By choosing the Battle-Lemarie scaling and wavelet functions as basis functions for spatial expansions and the Harr scaling functions for the temporal expansion, the wavelet based FDTD scheme exhibits highly linear numerical dispersion characteristics, allowing coarser grid spacing (Krumpholz and Katehi, 1996). Because the Battle-Lemarie basis functions do not satisfy the interpolation property, the expansion coefficients do not represent direct wave field values. Hence it becomes necessary to reconstruct the physical field by taking a weighted sum of neighboring coefficients, resulting in a complicated algorithm and a large computational overhead. Fujii and Hoefer (2001) avoid the step of reconstruction by building the spatial basis functions

	2nd order	4th order	6th order	8th order
a_1	1	9/8	75/64	1225/1024
a_2		-1/24	-25/384	-245/3072
a_3			3/640	49/5120
a_4				-5/7168
discretization error	$O(\Delta x^2)$	$O(\Delta x^4)$	$O(\Delta x^6)$	$O(\Delta x^8)$

Table 2.1: Coefficients of the 2nd, 4th, 6th and 8th order finite differencing operators.

with the Deslauriers-Dubuc interpolating functions (Dubuc, 1986; Deslauriers and Dubuc, 1989).

Thus far the wavelet formulation of the FDTD scheme has not been studied solving elastic wave equations. We derive the formulae, and as an initial investigation, limit our discussion to the scaling functions of the Deslauriers-Dubuc interpolating functions. Incorporating wavelet functions may possibly yield higher resolution schemes. We employ staggered grid for the wavelet based FDTD as it proves to be more stable and accurate (Virieux, 1986).

2.4.1 Taylor's expansion based FDTD schemes

The order of a Taylor's expansion based differencing operator, N, represents the order of the inherent error (Δx^N) of the difference approximation to derivatives. For a 1-D case, the first order derivative of a continuous function $f_{,x}$ at $x = x_0$ may be approximated in the discreet format by the following differencing operation

$$f_{,x}|_{x_0} = \frac{df}{dx}|_{x_0} = D_x^N f|_m + O(\Delta x^N), \tag{2.34}$$

where Δx is the grid spacing and $x_0 = m\Delta x$. The differencing operator, $D_x^N f|_m$ is defined as

$$D_x^N f|_m = \frac{1}{\Delta x} \sum_{l=1}^{N/2} a_l (f_{m+(l-1/2)} - f_{m-(l-1/2)}), \tag{2.35}$$

where coefficients a_l are listed in table 2.1 for N equal to 2, 4, 6 and 8.

Without losing generality, we show only FDTD formulae for 1-D case. Using the 2nd order differencing operator explicitly to approximate temporal derivatives and the N-th order for spatial derivatives, the 1-D wave equations in the stretched coordinate domain, equations 2.7 and 2.8, can be solved numerically by the following finite difference equations

$$v^{\tilde{x}}_{i;n+1/2} = v^{\tilde{x}}_{i;n-1/2} + \frac{\Delta t}{\epsilon_i \rho_i} D^N_{\tilde{x}} \tau^{\tilde{x}\tilde{x}}|_{i;n}, \tag{2.36}$$

$$\tau^{\tilde{x}\tilde{x}}_{i+1/2;n+1} = \tau^{\tilde{x}\tilde{x}}_{i+1/2;n} + c_{11}^{i+1/2} \frac{\Delta t}{\epsilon_{i+1/2}} D^N_{\tilde{x}} v^{\tilde{x}}|_{i+1/2;n+1/2}. \tag{2.37}$$

2.4.2 A wavelet based FDTD scheme

To construct the wavelet based FDTD scheme, field components such as particle velocities and stresses are expanded to the spatial and temporal functions basis. The spatial function basis is composed of the Deslauriers-Dubuc interpolating functions and the temporal function basis is composed of the Harr scaling functions.

The Deslauriers-Dubuc interpolating function $\phi(x)$ of order $2p-1$ is the autocorrelation function of Daubechies compactly supported orthogonal scaling function $\phi_0(x)$ of p vanishing moments (Mallat, 1997),

$$\phi(x) = \int_{-\infty}^{\infty} \phi_0(u)\phi_0(u-x)du. \tag{2.38}$$

ϕ is compactly supported, has a minimum support of $[-2p+1, 2p-1]$ and is able to reproduce polynomials of order $2p-1$. In addition, being an autocorrelation function, $\phi(x)$ is symmetric. Figures 2-5 and 2-6 illustrate Daubechies scaling function and Deslauriers-Dubuc interpolating function. Note that $\phi(x)$ is orthogonal to its integer shift; functions being expanded to a family of $\phi(x)$ do not require extra computation to be reconstructed, in other words, the expansion coefficients coincide with the field values. $\phi(x)$ satisfies the so called two-scale relation or dilation relation which means

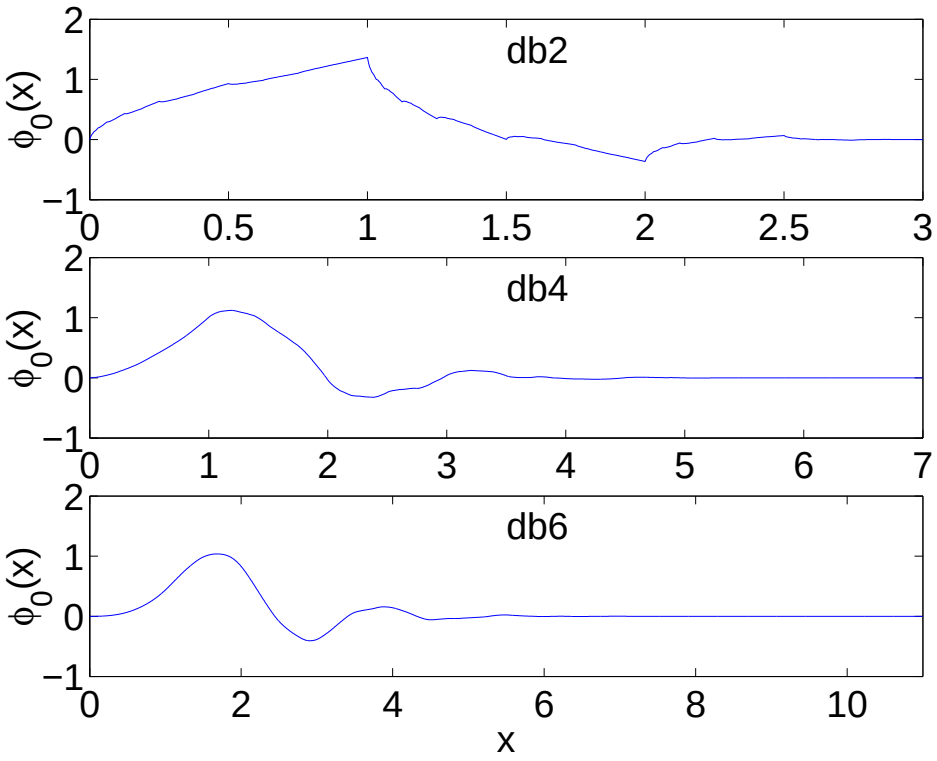

Figure 2-5: Daubechies compactly supported scaling function ϕ_0 of 2, 4, and 6 vanishing moments.

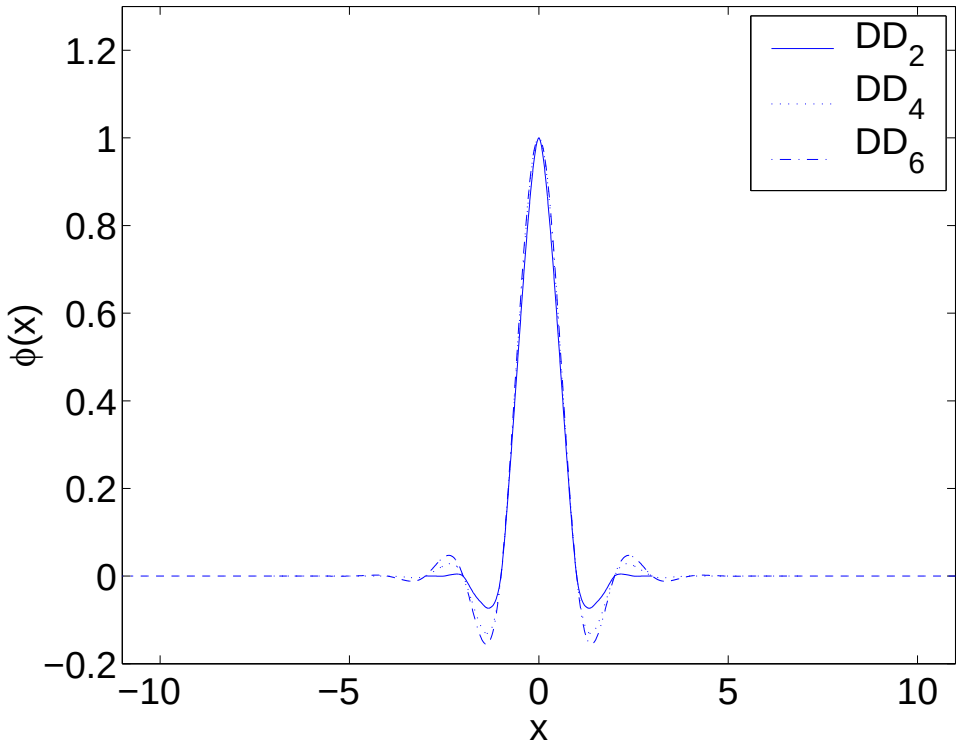

Figure 2-6: Deslauriers-Dubuc compactly supported interpolating functions, DD_2, DD_4 and DD_6. They are autocorrelation functions of Daubechies compactly supported scaling function of order 2, 4 and 6, respectively.

k	p=2	p=4	p=6
0	1.00000000	1.00000000	1.00000000
1	0.56250000	0.59814453	0.61016818
2	0.00000000	0.00000000	0.00000000
3	-0.06250000	-0.11962891	-0.14539719
4		0.00000000	0.00000000
5		0.02392578	0.04361916
6		0.00000000	0.00000000
7		-0.00244141	-0.01038551
8			0.00000000
9			0.00161552
10			0.00000000
11			-0.00012016

Table 2.2: Filter coefficients h_k^* in equation 2.39.

that it can be written as a sum of scaled and translated copies of itself, i.e.,

$$\phi(x) = \sum_{k=-\infty}^{+\infty} h_k^* \phi(2x - k). \tag{2.39}$$

Coefficients h_k^* are obtained by taking the autocorrelation of Daubechies wavelet filter h_k (Daubechies, 1988). Values of h_k^* for $p = 2$,4, and 6 are listed in table 2.2. In this paper, because only the scaling functions are chosen as the basis function, h_k is the coefficient of the low-pass decomposition filter of Daubechies wavelet family. Results of electrodynamics show that using merely the scaling function itself still leads to savings in the number of grids due to the highly linear dispersion property of the resulting scheme (Fujii and Hoefer, 2001).

Dirac delta function $\delta(x)$ is chosen to be the dual function of $\phi(x)$, as they satisfy the biorthogonal relation in equation 2.41. Suppose $f(x)$ represent $\phi(x)$ and its dual function $\delta(x)$, the discretization of $f(x)$ is obtained by

$$f_j(x) = f(\frac{x}{\Delta x} - j), \tag{2.40}$$

where Δx is the grid spacing. Because $f(x)$ is orthogonal to its integer shift, $f_j(x)$

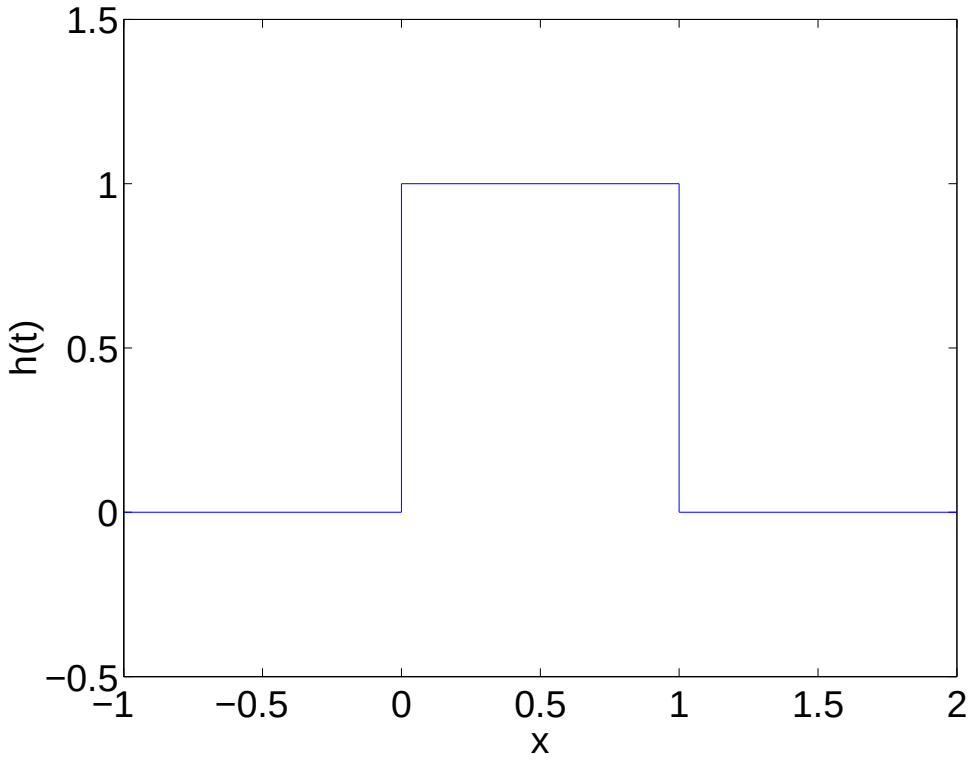

Figure 2-7: Harr scaling function $h(t)$.

is orthogonal to shifts equal to integer times of Δx. The inner product of $\phi_i(x)$ and $\delta_j(x)$ satisfies the following biorthogonal relation

$$< \phi_i, \delta_j >= \delta_{ij} \tag{2.41}$$

where δ_{ij} is the Kronecker delta function.

The Harr scaling function $H(t)$ is illustrated in figure 2-7. It is also orthogonal to its integer shift. In order to construct a staggered-grid scheme, the discretized Harr scaling function is left shifted by $\frac{1}{2}$. The corresponding discretization is then defined as

$$H_n(t) = H(\frac{t}{\Delta t} - n + \frac{1}{2}) \tag{2.42}$$

where Δt is the temporal spacing or time step. Similar to $f_j(x)$, $H_n(t)$ is orthogonal to shifts equal to integer times of Δt. All orthogonality conditions are listed below

l	p=2	p=4
0	1.2291666667	1.3110340773
1	-0.0937500000	-0.1560100710
2	0.0104166667	0.0419957460
3		-0.0086543236
4		0.0008308695
5		0.0000108999
6		-0.0000000041

Table 2.3: a_l in equation 2.46. $a_{-l} = -a_{l-1}$.

explicitly,

$$\int_{x=-\infty}^{+\infty} \phi_i(x)\delta_{i'}(x)dx = \delta_{i,i'}\Delta x, \tag{2.43}$$

$$\int_{t=-\infty}^{+\infty} H_n(t)H_{n'}(t)dt = \delta_{n,n'}\Delta t, \tag{2.44}$$

$$\int_{t=-\infty}^{+\infty} \partial_t H_{n+1/2}(t)H_{n'}(t)dt = \delta_{n,n'} - \delta_{n+1,n'}, \tag{2.45}$$

$$\int_{x=-\infty}^{+\infty} \partial_x \phi_{i+1/2}(x)\delta_{i'}(x)dx = \frac{d\phi(x)}{dx}|_{x=i'-i-\frac{1}{2}} \equiv a_l, \quad l = i - i'. \tag{2.46}$$

Coefficients a_l in equation 2.46 are evaluated numerically and are listed in Table 2.3 for $p = 2$ and 4.

Equations 2.47 and 2.48 show expansions of the normal stress $\tau_{xx}(x,t)$ and particle velocity $v_x(x,t)$ with a family of discretized Deslauriers-Dubuc interpolating functions $\phi_j(x)$ in space and Harr scaling functions $H_n(t)$ in time:

$$\tau_{xx}(x,t) = \sum_{i,n=-\infty}^{+\infty} \tau^{xx}_{i+1/2;n}\phi_{i+1/2}(x)H_n(t), \tag{2.47}$$

$$v(x,t) = \sum_{i,n=-\infty}^{+\infty} v^{x}_{i;n+1/2}\phi_i(x)H_{n+1/2}(t). \tag{2.48}$$

Substituting the expanded $\tau_{xx}(x,t)$ and $v_x(x,t)$ into the wave equations in the stretched coordinate (Eqs 2.7 and 2.8), taking the inner product of both sides with testing functions $\delta_{i'}(\tilde{x})$ and $H_{n'}(t)$, and applying the orthogonality conditions in equa-

tions 2.43 $\sim$ 2.46, we obtain the wavelet based time domain formula, the 1-D case of which is written in below,

$$v^x_{i';n'+1/2} = v^x_{i';n'-1/2} + \frac{\Delta t}{\rho_{i'}\Delta x}\sum_{l=0}^{Ls-1} a_l(\tau^{xx}_{i'+l-1/2;n'} - \tau^{xx}_{i'-l+1/2;n'}), \tag{2.49}$$

$$\tau^{xx}_{i'+1/2;n'+1} = \tau^{xx}_{i'+1/2;n'} + c_{11}^{i'+1/2}\frac{\Delta t}{\Delta x}\sum_{l=0}^{L_s-1} a_l(v^x_{i'+l;n'+1/2} - v^x_{i'+1-l;n'+1/2}). \tag{2.50}$$

Where $L_s = 2p-1$, the effective support of the basis function $\phi(x)$.

2.4.3 Numerical dispersion and stability condition

Due to the discretization in space and time, all FDTD schemes exhibits deviations from the linear dispersion behavior as predicted by theory. Linear dispersion means that both compressional and shear velocities are independent of frequency or wavelength in a homogeneous medium. If numerical errors increase over time iteration, the FDTD scheme is not stable. To apply an FDTD algorithm efficiently at a given accuracy, it is important to analyze numerical dispersion and the stability condition. Without losing generality, a 1-D scaler wave equation is solved by various FDTD schemes and their accuracy and efficiency are compared with one another.

We define a generalized spatial differencing operator in the stretched coordinate for all differencing schemes, $D_{\tilde{x}}$, for the convenience of easier and more structurized numerical implementation as well as simpler mathematical expressions.

$$D_{\tilde{x}}f|_m = \frac{1}{\epsilon^1_m\Delta\tilde{x}}\sum_{l=0}^{Q_s} a_l(f_{m+(l-1/2)} - f_{m-(l-1/2)}), \tag{2.51}$$

where $Q_s = N/2$ and $a_l = 0$ for Taylor's expansion based formula of order N. For the wavelet based formula, $Q_s = L_s - 1$. Then all FDTD schemes mentioned in this paper may be written in the following general form

$$v^{\tilde{x}}_{i;n+1/2} = v^{\tilde{x}}_{i;n-1/2} + \frac{\Delta t}{\rho_i}D_{\tilde{x}}\tau^{\tilde{x}\tilde{x}}|_{i;n}, \tag{2.52}$$

$$\tau^{\tilde{x}\tilde{x}}_{i+1/2;n+1} = \tau^{\tilde{x}\tilde{x}}_{i+1/2;n} + c_{11}^{i+1/2}\Delta t D_{\tilde{x}}v^{\tilde{x}}|_{i+1/2;n+1/2}. \tag{2.53}$$

We are interested in the numerical dispersion produced by various FDTD schemes, i.e., the deviation of the numerical velocity from the true medium velocity at different frequency. We set the grid size to be uniform, i.e., $\epsilon(\tilde{x}) = 1$ so that $\tilde{x} = x$.

Let V_p and V_p^{num} denote the compressional velocity and the associated numerical velocity, respectively, and λ the wavelength. For convenience, we define the following three variables:$q_p = V_p^{\text{num}}/V_p$, $\xi = V_p\Delta t/\Delta x$ and $H = \Delta x/\lambda$, where Δx and Δt represent spatial and temporal spacings.

Substituting the plane wave solution which is proportional to $e^{i\frac{2\pi}{\lambda}(V_p^{\text{num}}t-x)}$ to the difference equations 2.52 and 2.53, yields the numerical dispersion relation of all FDTD schemes,

$$\frac{1}{\xi} = \frac{\sum_{l=0}^{Q_s} a_l \sin[(2l-1)\pi H]}{\sin(\pi H \xi q_p)}. \tag{2.54}$$

As $|\sin(\pi H\xi q_p)|$ is no larger than 1, a sufficient stability condition is obtained from the numerical dispersion relation above, when

$$\xi \leq \frac{1}{\sum_{l=0}^{Q_s} |a_l|} = \xi_{\max}. \tag{2.55}$$

The stability condition puts an upper bound on ξ, which means the information can not be propagated across the mesh faster than the mesh velocity $\Delta\tilde{x}/\Delta t$. Note that $\xi_{\max}$ varies with different FDTD schemes, with $\xi_{\max}^{\text{2nd}}$ the largest, followed in order with $\xi_{\max}^{\text{4th}}$, $\xi_{\max}^{\text{6th}}$, $\xi_{\max}^{\text{8th}}$, $\xi_{\max}^{DD_2}$ and $\xi_{\max}^{DD_4}$. DD_2 and DD_4 denote that the order of Daubechies scaling function p is equal to 2 and 4, respectively. In general, the larger ξ is chosen, the shorter the running time of any FDTD algorithm.

Figure 2-8 shows the normalized numerical dispersion relations of various FDTD schemes when ξ of each scheme takes the same value that varies from $\xi_{\max}^{DD_4}$ to 1% of that value. In order to obtain a numerical solution without too much numerical dispersion, the grid spacing Δx and time step Δt should be chosen such that the numerical dispersion curve is inside the flat regime. The 6th and 8th order Taylor's expansion based FDTD schemes exhibit highly linear dispersion behavior compared with others; therefore for the same accuracy, they allows at least twice coarser mesh than the normally used 4th order scheme and that saves 8 times of memory and twice

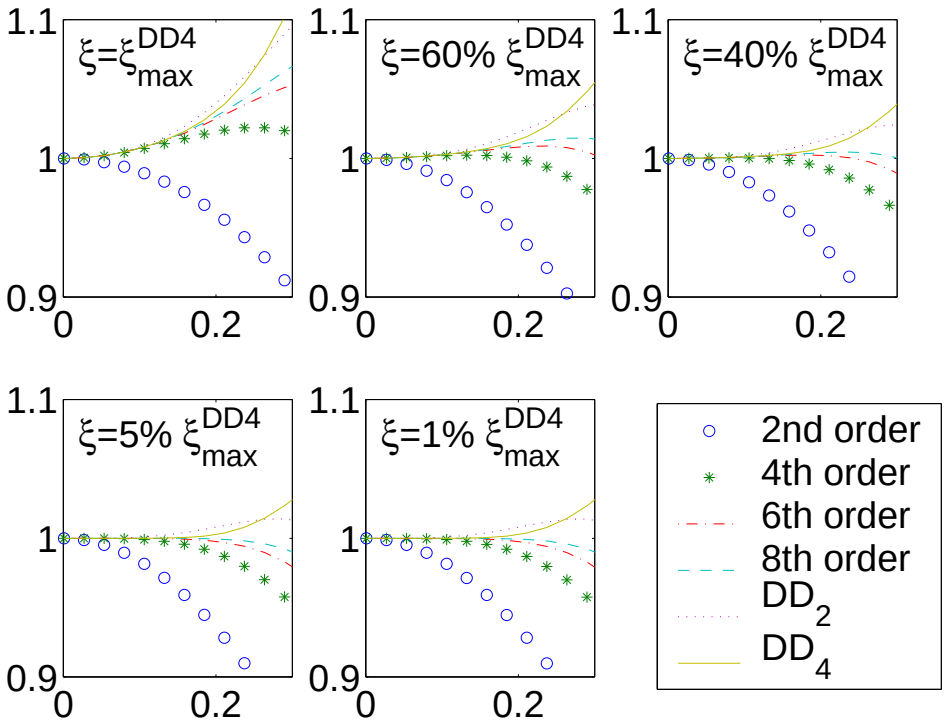

Figure 2-8: Numerical dispersion relations of various FDTD schemes, including 2nd, 4th, 6th and 8th order Taylor's expansion based and wavelet based ones, with $p = 2$ and 4. ξ of each scheme has been chosen from $\xi_{\max}^{DD_4}$ to 1% of that value. In each figure, the horizontal and the vertical axes denote the normalized grid size $H = \Delta x/\lambda$ and the normalized numerical velocity $q_p = V_p^{\text{num}}/V_p$.

the running time as Δt can be twice larger for a 3-D model. However, 4th order scheme is the most efficient scheme when a solution with relatively low accuracy is needed ($\xi = \xi_{\max}$). Numerical dispersion of DD_2 and DD_4 schemes are slightly better than the 4th order scheme. For the 2nd order scheme, 15 to 20 grid points per wavelength is required to suppress serious numerical dispersion.

2.4.4 Reflection and transmission at a sharp boundary

For modeling wave propagation in surface seismic exploration or acoustic logging configurations, it is of significance to find a scheme that can handle wave reflections and transmissions at sharp boundaries. We use each scheme to solve wave propagation in a 1-D model. The model consists two layers with the impedance ratio of 1 : 2, therefore the reflection and transmission coefficients should be 1/3 and 2/3, respectively. We chose the following parameters for all the FDTD simulations: the center frequency, 10 Hz; the grid spacing, 7, 10 and 20 grid points per smallest wavelength; ξ, $0.4\xi_{\max}^{DD_4}$. Numerical reflection and transmission coefficients are computed from Fourier transformed waveforms obtained from FDTD computations. Errors in those coefficients for each scheme are shown in figures 2-9$\sim$ 2-11. For the 2nd order scheme, there are some noticeable dispersions in the waveforms even with 20 grid points per smallest wavelength. It produces the least accurate reflection and transmission at the sharp boundary compared with results from higher order method, contrary to what is discussed in previous work (Cunha, 1993). For the rest of the FDTD schemes, all of them produce similar results with a fine grid, except that errors in the reflection coefficients are much greater than in the transmission coefficients. With a coarse grid (Fig 2-9), the DD_2 method performs slightly better for reflections while much less error for transmissions than the others. In order, the performance of DD_4 follows that of DD_2, then is followed by that of 8th, 6th and 4th order schemes. Note that with 7 grid points per smallest wavelength, the 4th order scheme generates some noticeable dispersion in the reflected waveform while higher order and wavelet based methods do not. By reducing grid size 3 times, errors in reflection and transmission coefficients for all schemes are reduced 5 to 10 times.

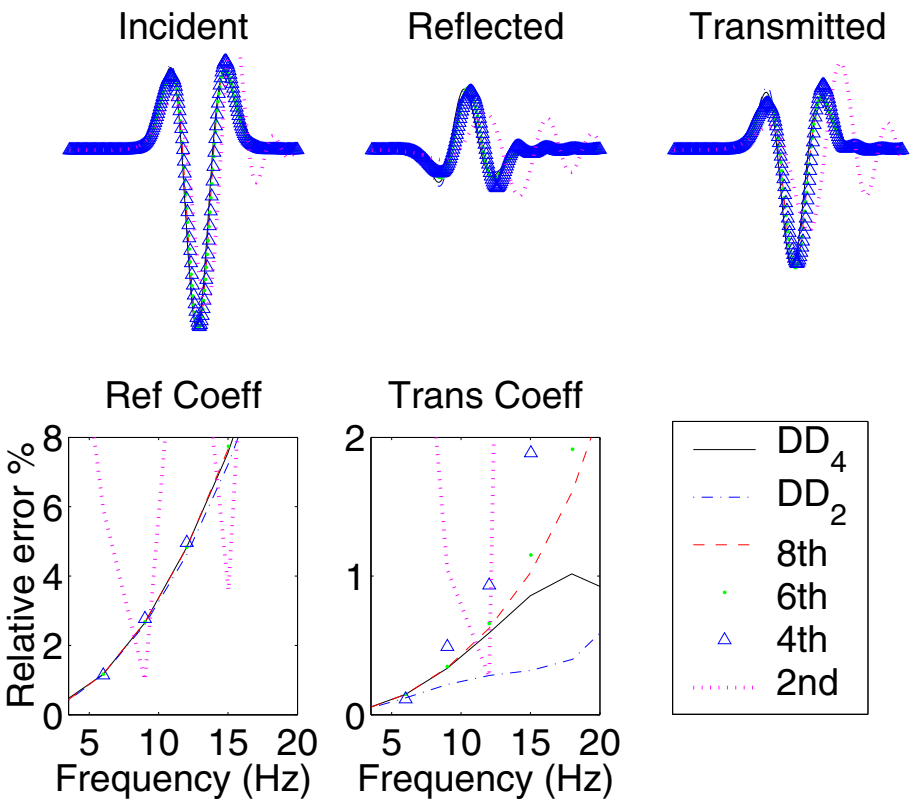

Figure 2-9: The incident, reflected and transmitted waves that propagate in a 2-layer model and are obtained from 6 FDTD computations using uniform grid. The grid size is 1/7 of the smallest wavelength. Both 2nd order and 4th order solutions show noticeable numerical dispersions. The reflection and transmission coefficients are computed from those waves. Their relative errors to the analytical answer are plotted in the frequency domain.

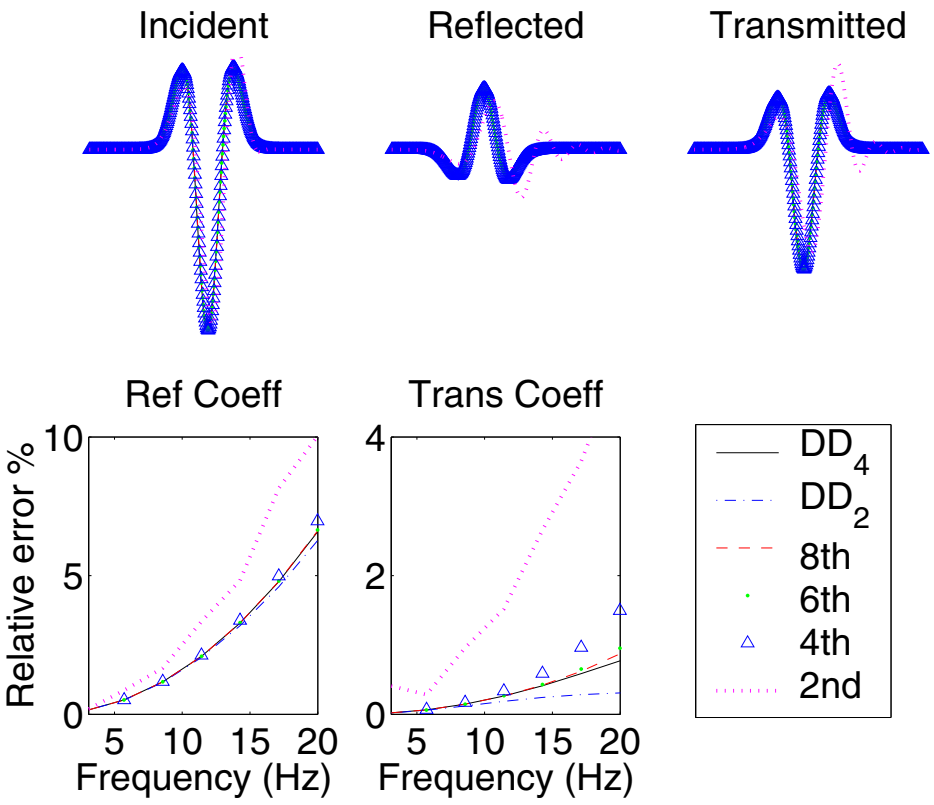

Figure 2-10: Same as figure 2-9 except that the grid size is 1/10 of the smallest wavelength.

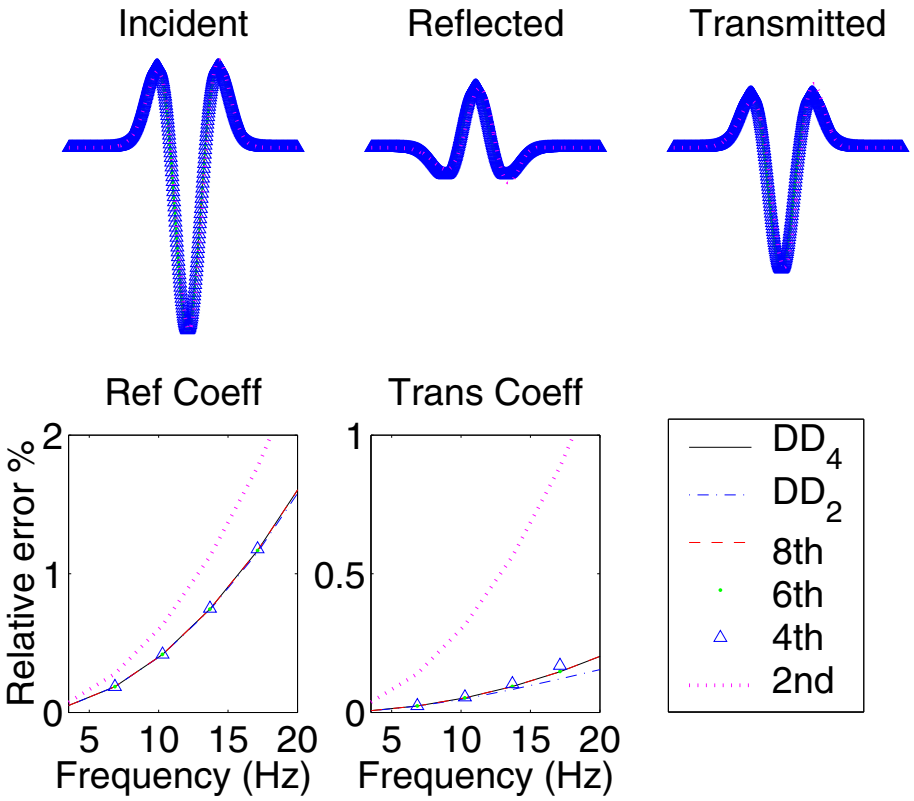

Figure 2-11: Same as figure 2-9 except that the grid size is about 3 times smaller while errors in reflection and transmission coefficients drop more than 5 times. With little numerical dispersion, the 2nd order scheme does not produce the most accurate reflections and transmissions as some studies suggested.

2.5 Numerical Results

To investigate if the stretched grid causes any artificial grid reflections or wave distortions that are normally associated with variable grids, it is important to design the test case such that few other numerical or physical effects are present and the case is well understood. A 2-D homogeneous medium with a monopole source is ideal as a test case for grid reflections and wave distortion.

2.5.1 2-D homogeneous medium

The model is 50 m X 50 m in dimension. The mesh grid is variable in both x_1 and x_2 directions produced by using the stretching function shown in figure 2-2. Both stretching ratios, α^1 and α^2, are chosen to be 2. The compressional velocity is 3000 m/s, the density 2000 kg/m^3 and the center frequency 500 Hz. The smallest grid size is equivalent to 12 grid points per smallest wavelength. The 8th order FDTD scheme is selected as it has the most linear numerical dispersion relation which allows the coarsest sampling among all aforementioned schemes. The source is put inside the medium in a manner that it is not in the symmetry center of the grid. Figure 2-12 shows a snapshot plotting on top of the mesh grid. At this time step, some part of the wave is still inside the finer grid area, some part is at the transaction zone between the fine and coarse grid and some part has already propagated into the coarse grid area. The snapshot shows no numerical distortion as the wave front remains the expected circular shape. There is no observable artificial reflections off the grid boundary either. A series of snapshots show the progressive development of the wave in figure 2-13. There is no sign of numerical reflection or distortion during the numerical propagation of the wave. Figure 2-14 shows waveforms at 9 locations from both FDTD and analytical solutions. All 9 receivers are evenly placed along the line in x_2 or y direction across the model, which is 20 meters away from the source. The perfect match between the analytical and FDTD solution proves again there is no wave distortion induced by the stretched grid, nor any observable reflections.

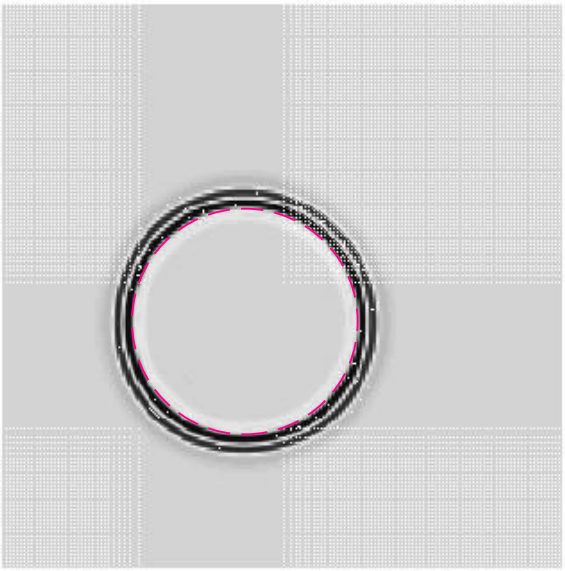

Figure 2-12: One snapshot of a wave propagating in a homogeneous medium which is discretized with a variable grid. The source is not in the symmetry center of the mesh which is shown at the background. A dashed lined circle is plotted at the wave end to benchmark the wavefront. The perfect circular shape of the wavefront suggests little phase distortion introduced by variable grids. No numerical reflection is observed either.

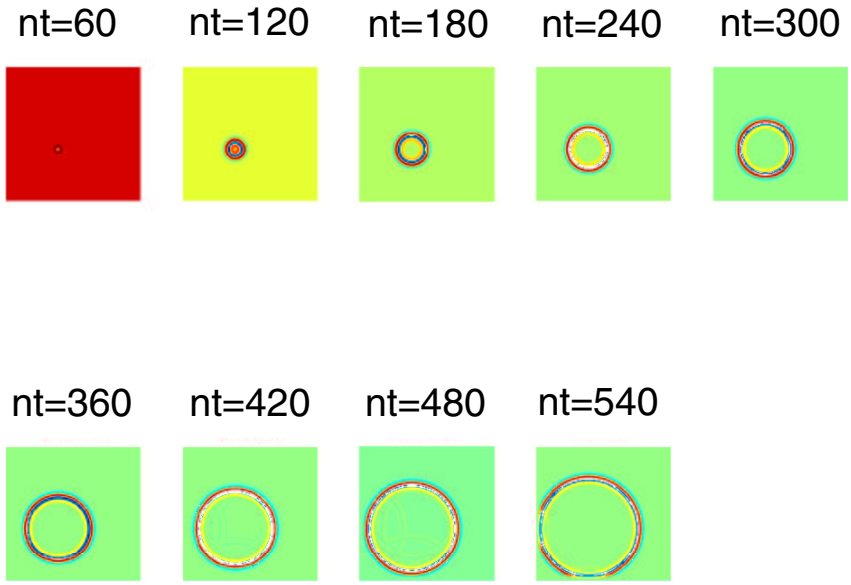

Figure 2-13: The progressive development of the wave shown in figure 2-12. The wavefront keeps its circular shape, suggesting no phase distortion, throughout its propagation across the medium and there is no noticeable numerical reflections observed.

2.5.2 1-D layered model

Surface seismology requires accurate amplitude and phase information of waves reflected from subsurface boundaries. It was shown in the previous section that reducing the grid size improves more effectively the accuracy of wave propagating across a sharp boundary, as opposed to to selecting an operator out of the 4th, 6th, 8th order or wavelet based schemes (Followed by the 8th order scheme, DD_2 slightly outperforms others). For efficiency, we only refine the grid size in the neighborhood of the discontinuity using the proposed gridding scheme in this paper. Results of a 1-D model with a sharp boundary illustrates the improvement in efficiency without much a loss in accuracy by using the stretched grid. The wave equations are solved with both DD_2 and 8th order methods.

We conduct 4 numerical computations for the same 1-D model as in previous section. The 4 computations include three cases using 8th order scheme: case I, a fine uniform grid (40 grid points per smallest wavelength); case II, a coarse uniform

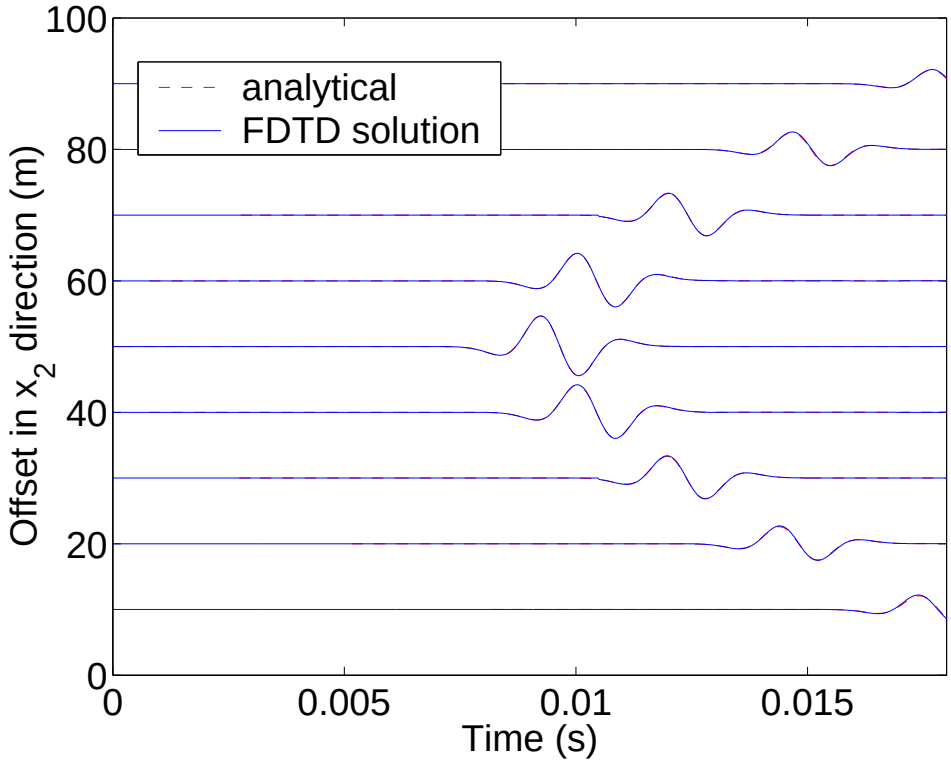

Figure 2-14: Waveforms from both the FDTD and analytical solution are plotted against one another. All 9 receivers are placed inside the fine grid region, the transition zone between fine and coarse grid, and the coarse grid region. The perfect match between two solutions suggest there is no amplitude and phase distortions introduced by the variable grid. No numerically reflected wave is recorded.

grid (6 times coarser than the fine grid) and case III, a variable grid. The variable grid is constructed using the stretching function shown in figure 2-2 with the stretching ratio α equal to 6. Thus the size of the fine grid in the vicinity of the boundary equals to the grid size of the fine uniform grid in case I while the coarse grid in the homogeneous region equals to the grid size of the coarser uniform grid in case II. In case III, both receivers for the reflected and the transmitted waves are put in the coarse grid region. Case IV is the same as case III except that the FDTD scheme is DD_2.

The resulting errors in reflection and transmission coefficients of each case are shown in figure 2-15. Two significant improvements are achieved by locally refining the grid mesh in the neighborhood of the boundary: 1) both reflection and transmission coefficients decrease greatly; 2) those coefficients become much less frequency dependent as should be the case by theory. Note that the reduction in error is more so for the reflection coefficient so that errors in both coefficients are at the same level as oppose to the uniform grid case. The DD_2 solution for the stretched wave equation is more accurate than the 8th order one as is in the uniform grid case.

2.5.3 2-D layered model

The dimension of the 2-D layered model is 7 m X 7 m, with an interface at x=4 m. One layer is water, with the density being 1000 kg/m^3 and compressional velocity v_p being 1500 m/s. The second layer is a soft formation, where the density is 2200 kg/m^3, v_p 3000 m/s and v_s 1200 m/s. The source is a point source at location (3.2 m, 3.2 m) with a center frequency of 2000 Hz. Δy is chosen to be 0.04 m, and $\Delta\tilde{x}$ is 0.01 m and the stretching factor α_1=4. The model and the variable mesh is shown in figure 2-16. 10 grid points are used for PML. For the uniform grid, Δy=Δx=0.01 m, so that the number of grid points is 13 times more than that of the variable grid. Figures 2-17 $\sim$ 2-22 show snapshots of the wave field computed by the variable grid and the uniform grid. The same color scale is applied to all figures. Both the stretched grid and uniform grid solutions match with each other very well. From the last snapshot where part of wave front is outside the computational domain 2-

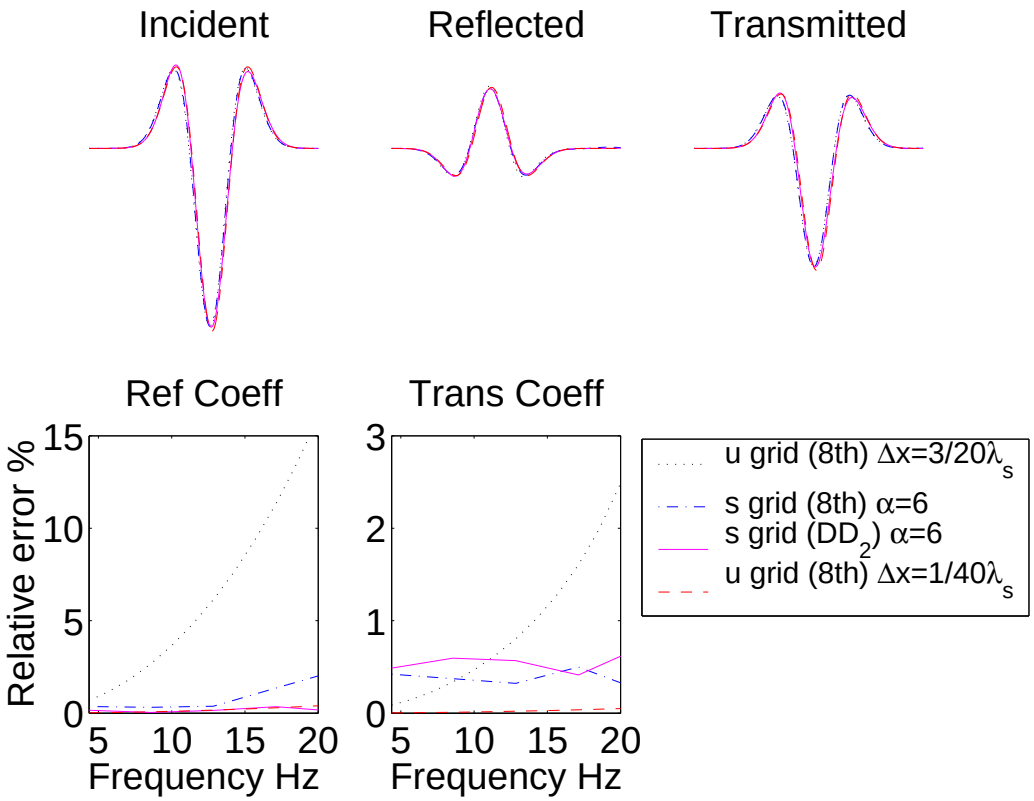

Figure 2-15: The incident, reflected and transmitted waves that propagate in the same 2-layer model as in figure 2-9. The model is discretized by 3 scenarios: A. uniform coarse grids with the grid size small enough to suppress numerical dispersion; B. uniform fine grids with the grid size 6 times smaller than the coarse grids; C. variable grids with the grid size in the neighborhood of the boundary equal to the grid size in scenario B and the grid size in the rest areas equal to that in scenario A. At a computational cost slightly higher than in scenario A, scenario C gives the results with an accuracy close to that of scenario B which is at least 6 times more costly than scenario A for 1D case. DD_2 outperforms 8th order method in reflection while ties with 8th order method in transmission. Incorporating the wavelet functions may improve the accuracy of DD_2 further.

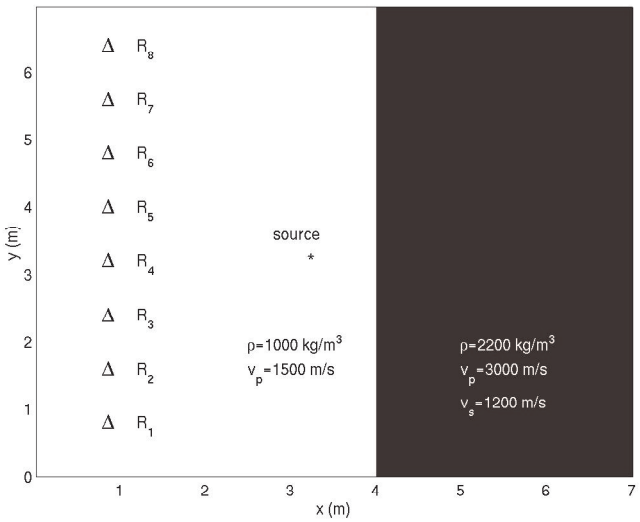

(a) survey layout

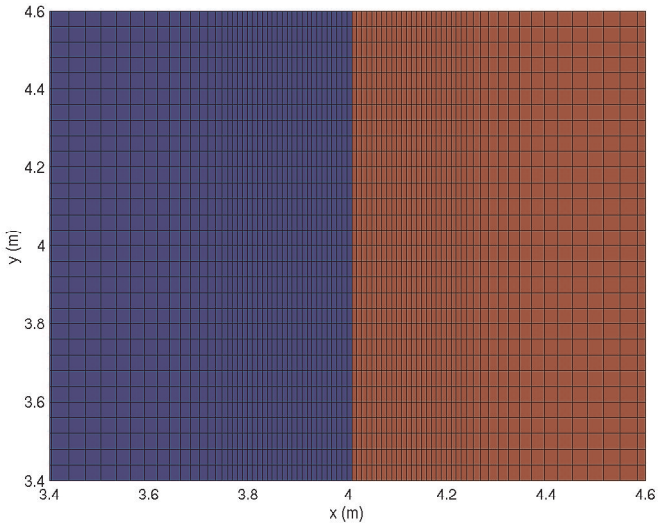

(b) mesh

Figure 2-16: The 2-D layered model and the variable mesh. Efficiency is improved 13 times. The source is located at (x,y)= (3.2, 3.2). Eight receivers are placed at (0.8, 0.8), (0.8, 1.6), (0.8, 2.4), (0.8, 3.2), (0.8, 4.0), (0.8, 4.8), (0.8, 5.6), (0.8, 6.4). All values are in meters.

22, two slices are taken to evaluate the performance of the PML. The numerical reflection off the PML boundary is less than 0.4%, indicating a super performance of the PML. Figures 2-24, 2-25 and 2-26 show the trace by trace comparison of the pressure, x direction particle velocity and y direction particle velocity at different receiver locations, between the oversampled uniform grid case and the variable grid case. The agreement between the two cases is good.

2.6 Discussions and Conclusions

Simulating wave propagation in the earth with the FDTD method is a common practice among the geophysics community. However, it is important to do it in an accurate and efficient fashion as the models that we are dealing with become more and more complex. The paper shows two effective ways to achieve this goal. One is to discretize the model space adaptively, namely, to employ a variable gridding scheme. The other way is to use higher order (6th or 8th) or wavelet based difference schemes.

Variable grids samples the model with finer grids only at places where it is necessary to save computational cost while retaining accuracy in the solution. The proposed stretched grid scheme in this paper samples the physical space with gradually varying grid while solving the wave equations in the transformed domain where the grid size is uniform. Benefits of our method include 1) reducing numerical reflections which are often associated with abrupt changes in grid size; 2) eliminating wave distortions and preserving the formal truncation error and the stability of the system; 3) easy numerical implementation. The second and third benefit are hard to accomplish if the FDTD solution is directly computed in the physical domain that is discretized with a variable mesh. Numerical results from different models show that the proposed stretched grid approach works quite well.

We also formulate a wavelet based FDTD algorithm for elastodynamics with Deslauriers- Dubuc interpolating functions, avoiding reconstruction of the wave field, a problem associated with many other wavelet based formulae. The dispersion analysis shows that at same accuracy, using wavelet based or higher order Taylor's expan-

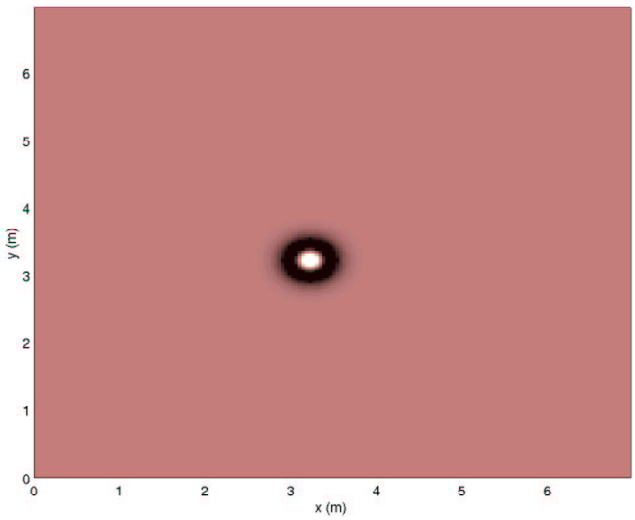

(a) uniform grid

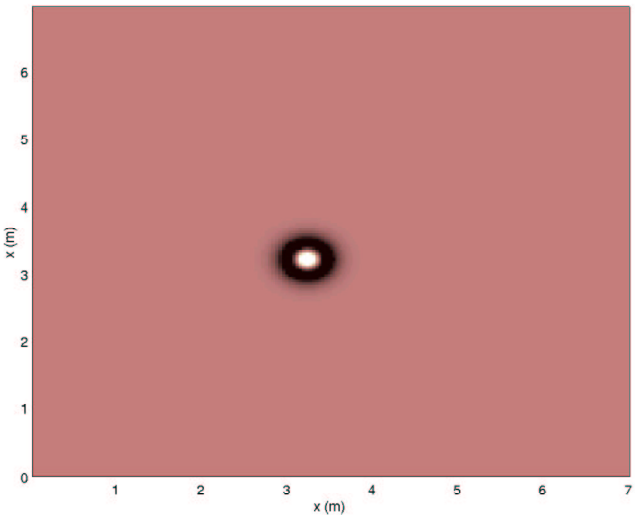

(b) stretched grid

Figure 2-17: Snapshots of the wave field in the 2-layer model.

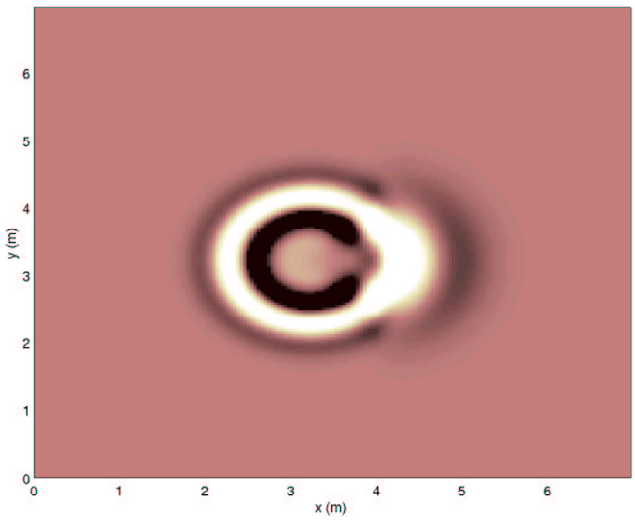

(a) uniform grid

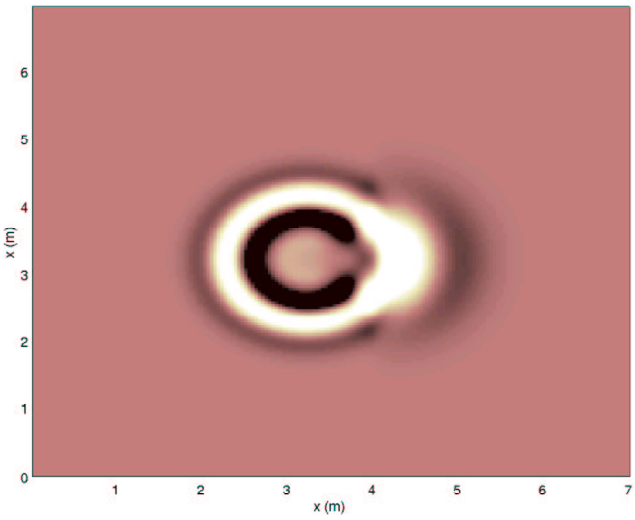

(b) stretched grid

Figure 2-18: Snapshots of the wave field in the 2-layer model.

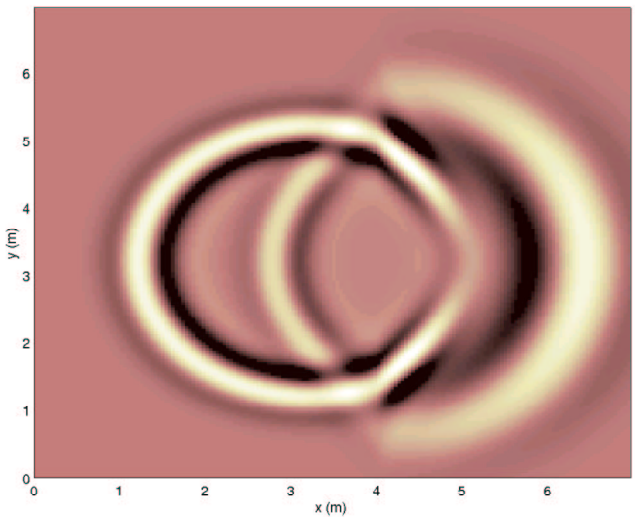

(a) uniform grid

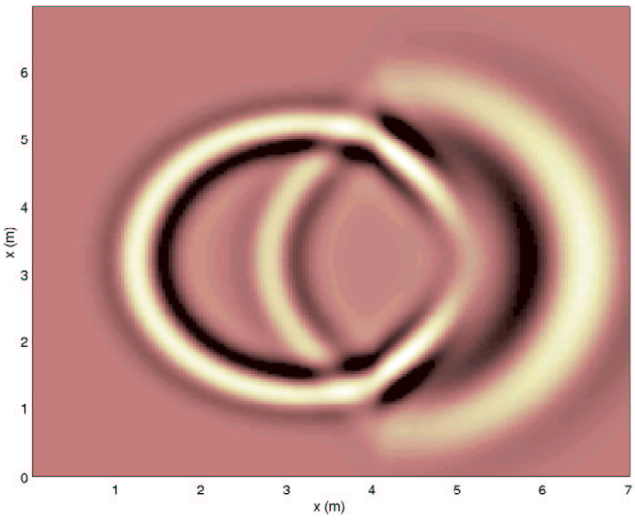

(b) stretched grid

Figure 2-19: Snapshots of the wave field in the 2-layer model.

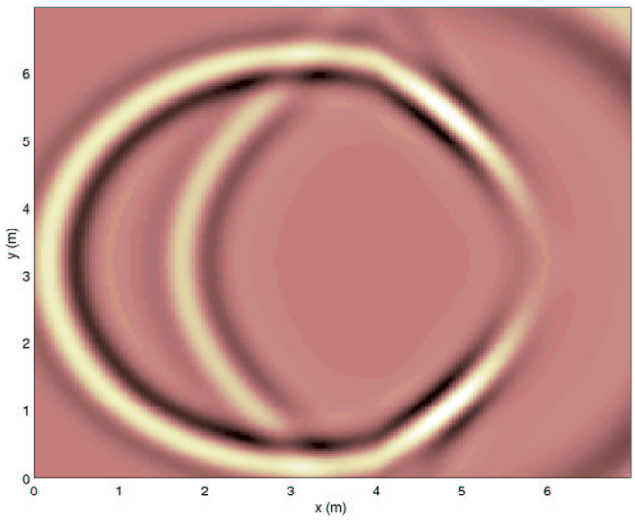

(a) uniform grid

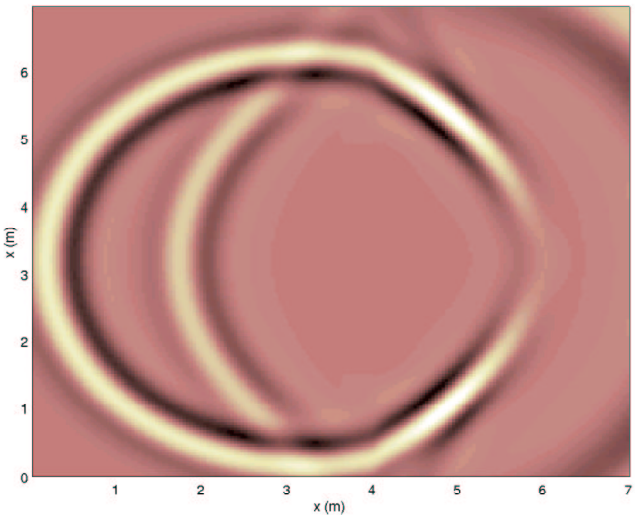

(b) stretched grid

Figure 2-20: Snapshots of the wave field in the 2-layer model.

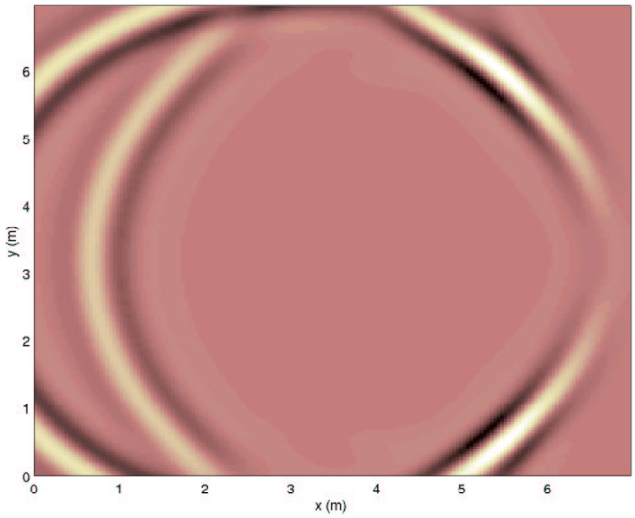

(a) uniform grid

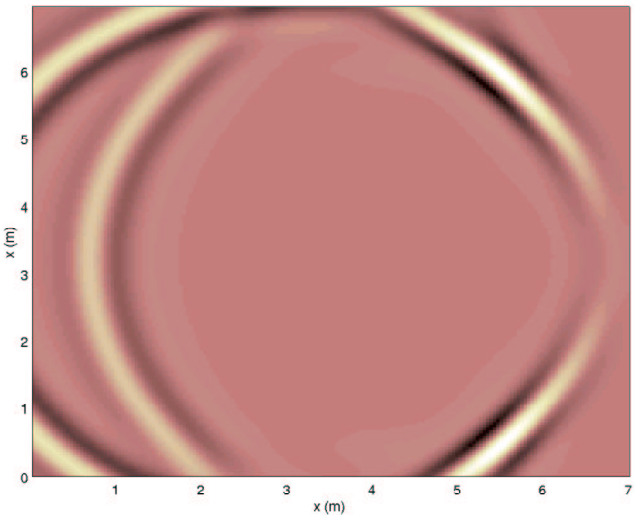

(b) stretched grid

Figure 2-21: Snapshots of the wave field in the 2-layer model.

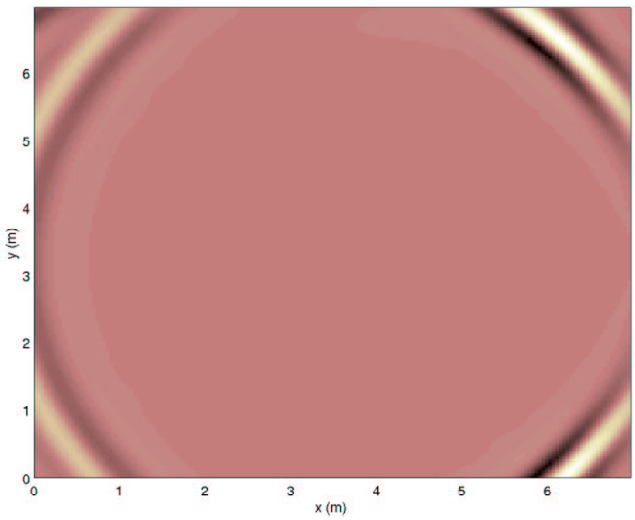

(a) uniform grid

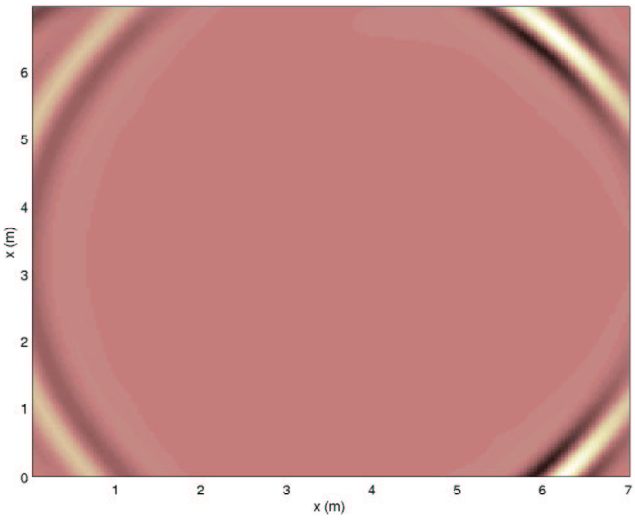

(b) stretched grid

Figure 2-22: Snapshots of the wave field in the 2-layer model.

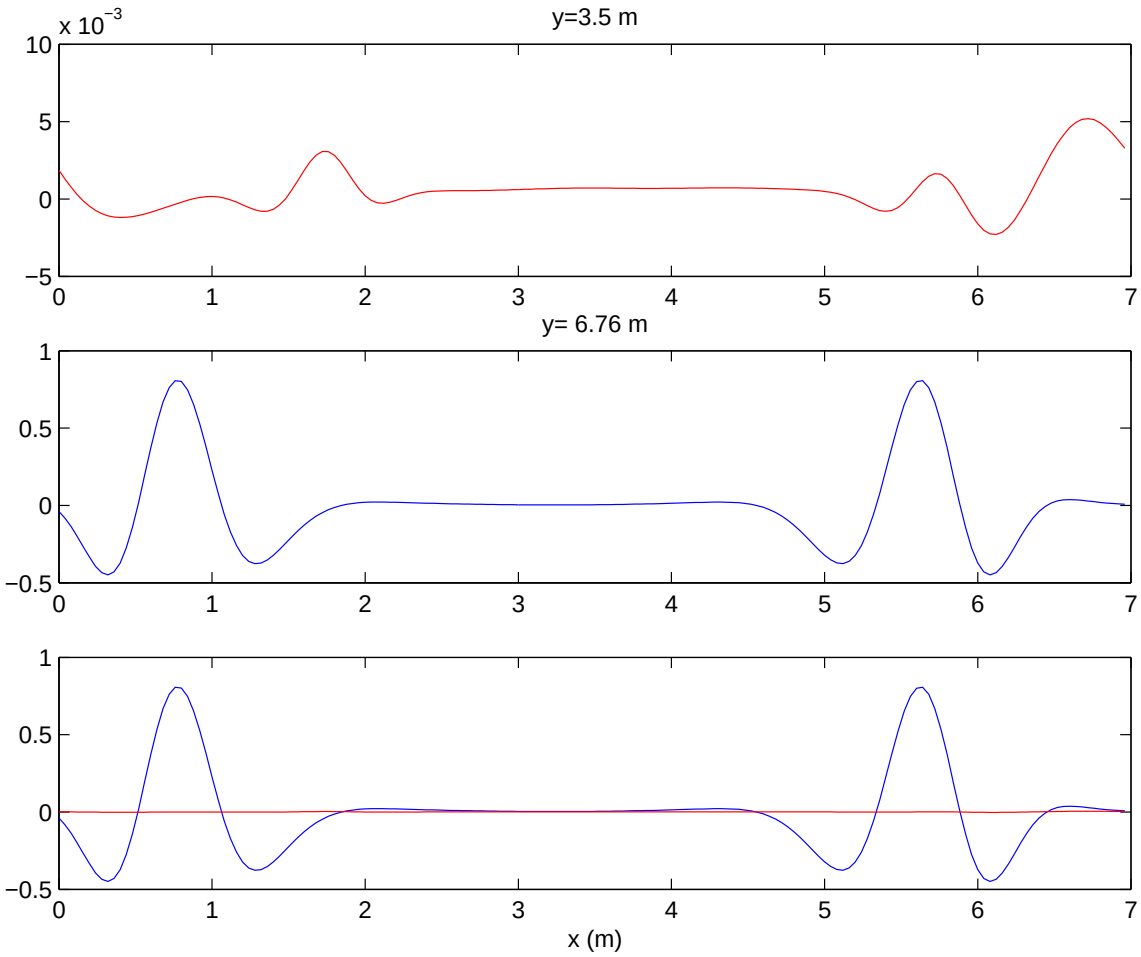

Figure 2-23: From the last snapshot where part of wave front is outside the computational domain 2-22, two slices are taken to evaluate the performance of the PML. One is taken at y=3.5 m where the wave front is already outside the computational domain so that the remaining energy is caused by numerical reflection off the PML; the other is taken at y=6.76 m where the wave front energy is a good estimate of the incident energy. The numerical reflection off the PML boundary is less than 0.4%, indicating a super performance of the PML.

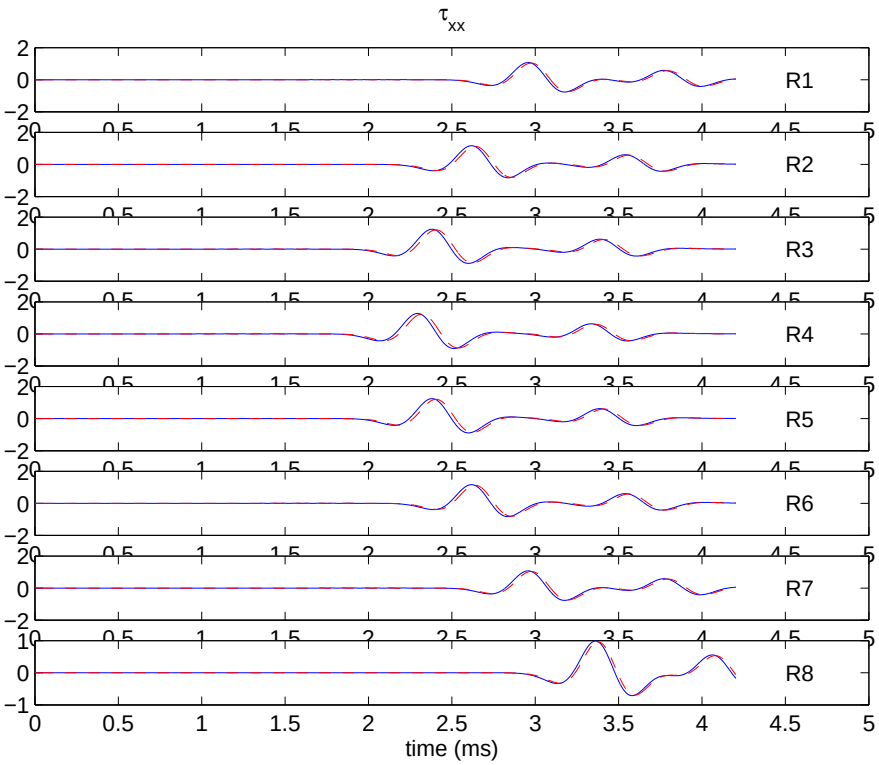

Figure 2-24: Trace by trace comparison of the pressure component, τ_{xx}, between the oversampled uniform grid solution and the variable grid solution of the 2-D layered model. Solid line: uniform grid; Dash line: variable grid.

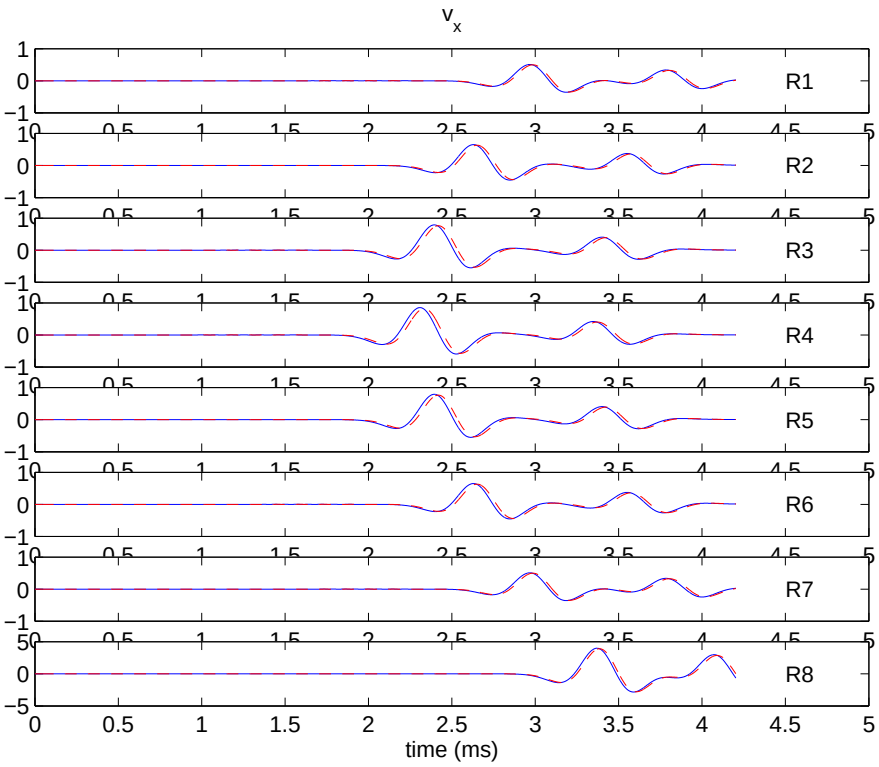

Figure 2-25: Trace by trace comparison of the particle velocity component, v_x, between the oversampled uniform grid solution and the variable grid solution of the 2-D layered model. Solid line: uniform grid; Dash line: variable grid.

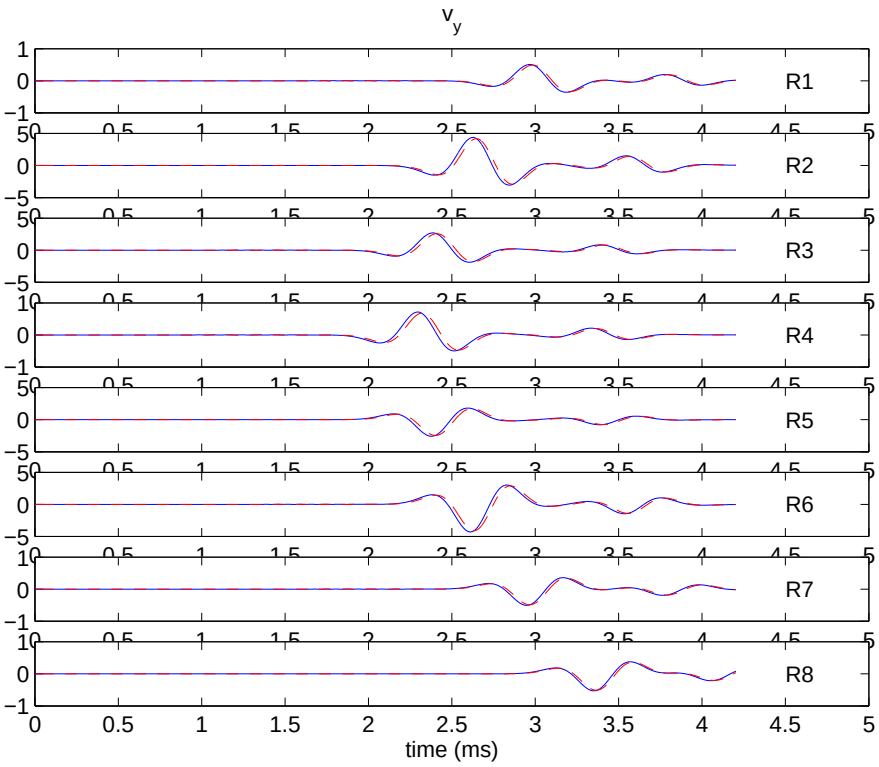

Figure 2-26: Trace by trace comparison of the particle velocity component, v_y, between the oversampled uniform grid solution and the variable grid solution of the 2-D layered model. Solid line: uniform grid; Dash line: variable grid.

sion based differencing schemes for spatial derivatives reduces the universal sampling rate in one coordinate direction by a factor of 2, comparing to the widely applied 4th order method. That reduces 8 times the memory requirements for 3D applications. The reason for the saving is that these schemes produce much less numerical dispersions. The wavelet based DD_2 scheme yields more accurate reflection and transmission coefficients at sharp boundaries, specially when combined with variable grids in the neighborhood of a discontinuity. Only the scaling functions of the Deslauriers-Dubuc interpolating family has been used in this paper. Further accuracy/efficiency may be obtained by incorporating the wavelet functions.

Chapter 3

2.5-D Stretched Grid FDTD Formula and A Non-splitting Perfectly Matched Layer

3.1 Introduction

3-D finite difference computations are often performed in the (x,y,z,t) domain. For the particular problems that this dissertation is to address, namely, LWD tool effects on wave propagations along a fluid-filled borehole, properties in the axial direction (z direction) are assumed homogeneous to avoid additional complexity and to further save computational cost. Whne the model property is invariant in the axial direction, a plane wave propagating in the z direction does not change, therefore the wave equation can be Fourier transformed to and solved by a finite difference approach in the (x,y,k_z,t) domain to further increase computational efficiency, as model properties are assumed homogeneous along the z axis throughout the dissertation. k_z represents the axial wavenumber. The final solution of the 3-D wave equation in the (x,y,z,t) domain is obtained by an inverse Fourier transform. Such finite difference approach is referred as 2.5-D (Randall, 1991b). There are two major benefits of using the 2.5-D formula over a 3-D formula for the applications in the scope of the thesis: 1)

significant memory saving; 2) can be completely parallelized with respect to k_z.

The non-split perfectly matched layer (PML), anisotropic PML, developed in chapter 2 is used to minimize the reflection at boarders of the computational domain. Advantages of the anisotropic PML includes high absorbing rate, less memory requirement and universal formulation for both isotropic and anisotropic media, as well as the variable grid scheme in chapter 2.

The 2.5-D stretched grid FDTD algorithm is tested by a 3-D homogeneous model and a fluid-filled borehole with a monopole source.

3.2 Staggered Grid FDTD Formula with General Spatial Difference Operator on A Stretched Mesh

Wave equations 2.13 $\sim$ 2.30 are the general wave equation in the stretched coordinate both for the computational and PML regimes. They are Fourier transformed from the ($\tilde{x}$, $\tilde{y}$, z, t) domain into the ($\tilde{x}$, $\tilde{y}$, k_z, t) domain. Note that there is no need to stretch the z coordinate in this case. The finite difference solution of the wave equation is obtained in the ($\tilde{x}$,$\tilde{y}$,k_z,t) domain and transformed back to the (x,y,z,t) domain in the end. Derivatives with respect to z, ∂_z, are then replaced by $-ik_z$ (equation 3.3), instead of using finite difference approximation. Because only $\partial_{\tilde{x}}$ and $\partial_{\tilde{y}}$ are computed using finite difference, this type of solution is called 2.5 dimensional solution. As less grid points are needed in the k_z domain than in the z domain, the 2.5-D FDTD formulation results in a reduction in memory requirement by several times. Since solutions for each k_z are independent, efficient parallelization can be achieved trivially.

The 3-D wave equations in the transformed domain are discretized in a 2-D staggered-grid (Figure 3-1). To avoid confusions in notations, Fourier and its inverse transformations are explicitly written in equations 3.1 and 3.2.

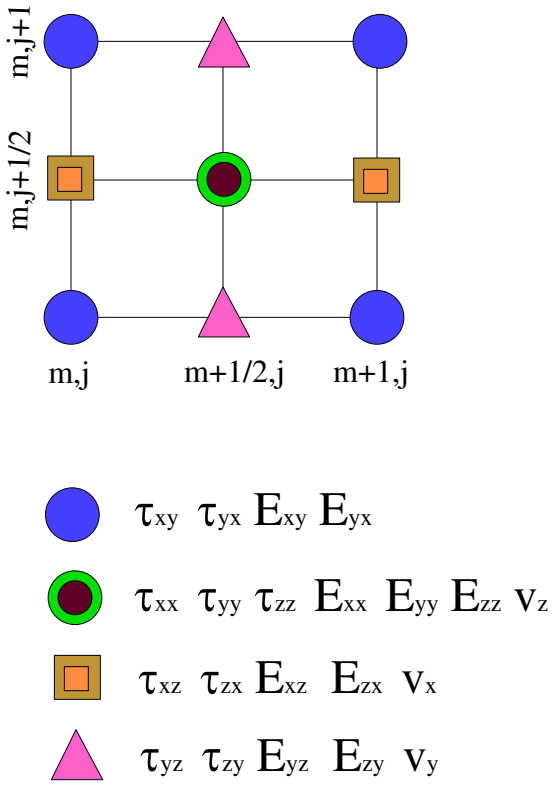

Figure 3-1: Schematics of staggered-grids for 2.5D schemes.

$$\tilde{f}(k_z) = \frac{1}{2\pi}\int_{-\infty}^{+\infty} f(z)e^{ik_z z}dz, \tag{3.1}$$

$$f(z) = \int_{-\infty}^{+\infty} \tilde{f}(k_z)e^{-ik_z z}dk_z \tag{3.2}$$

$$\text{Fourier Transform}\{\partial_z f(\tilde{x},\tilde{y},z)\} = -ik_z\tilde{f}(\tilde{x},\tilde{y},k_z) \tag{3.3}$$

The first order temporal derivative is approximated by the 2nd order center difference operator for Taylor's expansion based method or the Harr scaling function for the wavelet-based method. Spatial derivatives are approximated by a generalized operator representing the 2nd, 4th, 6th and 8th Taylor's expansion based and the wavelet based differencing operator (chapter 2). With reference to equation 2.51, generalized spatial differencing operators in the 2.5-D stretched coordinate, $D_{\tilde{x}}f|_{m,j,k}$ and $D_{\tilde{y}}f|_{m,j,k}$, representing numerical evaluations at location ($m\Delta\tilde{x}$, $j\Delta\tilde{y}$, $k\Delta k_z$), of the first order derivatives of $\tilde{f}$ with respect to $\tilde{x}$ and $\tilde{y}$, are defined as follows:

$$D_{\tilde{x}}f|_{m,j,k} = \frac{1}{\epsilon^1(m,:)\Delta\tilde{x}}\sum_{l=0}^{Q_s} a(l)(f_{m+(l-1/2),j,k} - f_{m-(l-1/2),j,k}) \tag{3.4}$$

$$D_{\tilde{y}}f|_{m,j,k} = \frac{1}{\epsilon^2(:,j)\Delta\tilde{y}}\sum_{l=0}^{Q_s-1} a(l)(f_{m,j+(l-1/2),k} - f_{m,j-(l-1/2),k}) \tag{3.5}$$

where $\epsilon^1(m,:)$ represents discretized the stretching function in the x direction for all possible values of j.

Wave equations 2.13 $\sim$ 2.30 are discretized after being Fourier transformed into the k_z domain. Take B_{xx} component as an example (equation 2.13), the discretized expression is

$$\begin{aligned} & \rho_{m,j+1/2}\frac{B^{xx}_{m,j+1/2,k;n+1/2} - B^{xx}_{m,j+1/2,k;n-1/2}}{\Delta t} \\ + \quad & \beta^1_{m,j+1/2}\frac{B^{xx}_{m,j+1/2,k;n+1/2} + B^{xx}_{m,j+1/2,k;n-1/2}}{2} \\ = \quad & D_{\tilde{x}}\tau^{xx}|_{m,j+1/2,k;n} + D_{\tilde{y}}\tau^{yx}|_{m,j+1/2,k;n} - ik\Delta k_z\tau^{zx}_{m,j+1/2,k;n}. \end{aligned} \tag{3.6}$$

Solving for $B^{xx}_{m,j+1/2,k;n+1/2}$ from equation 3.6, we obtain the time iteration formula (equation 3.9) to update $B^{xx}(m\Delta\tilde{x},(j+1/2)\Delta\tilde{y},k\Delta k_z)$, at time step $n+1/2$, i.e.

$t = (n + 1/2)\Delta t$, from their previous time step values. $\gamma^{i+}_{m,j}$ and $\gamma^{i-}_{m,j}$ are defined as

$$\gamma^{i+}_{m,j} = \frac{1}{\Delta t} + \frac{\beta^{i}_{m,j}}{2} \tag{3.7}$$

$$\gamma^{i-}_{m,j} = \frac{1}{\Delta t} - \frac{\beta^{i}_{m,j}}{2} \tag{3.8}$$

$$\begin{aligned} B^{xx}_{m,j+1/2,k;n+1/2} &= \frac{1}{\gamma^{1+}_{m,j+1/2}}\{\gamma^{1-}_{m,j+1/2} B^{xx}_{m,j+1/2,k;n-1/2} \\ &+ \frac{1}{\rho_{m,j+1/2}}(D_{\tilde{x}}\tau^{xx}|_{m,j+1/2,k;n} + D_{\tilde{y}}\tau^{yx}|_{m,j+1/2,k;n} \\ &- ik\Delta k_z \tau^{zx}_{m,j+1/2,k;n})\} \end{aligned} \tag{3.9}$$

Similarly, particle velocities can be updated from their previous time step values by equations 3.10 $\sim$ 3.17, respectively.

$$\begin{aligned} B^{xy}_{m+1/2,j,k;n+1/2} &= \frac{1}{\gamma^{1+}_{m+1/2,j}}\{\gamma^{1-}_{m+1/2,j} B^{xy}_{m+1/2,j,k;n-1/2} \\ &+ \frac{1}{\rho_{m+1/2,j}}(D_{\tilde{x}}\tau^{xy}|_{m+1/2,j,k;n} + D_{\tilde{y}}\tau^{yy}|_{m+1/2,j,k;n} \\ &- ik\Delta k_z \tau^{zy}_{m+1/2,j,k;n})\} \end{aligned} \tag{3.10}$$

$$\begin{aligned} B^{xz}_{m+1/2,j+1/2,k;n+1/2} &= \frac{1}{\gamma^{1+}_{m+1/2,j+1/2}}\{\gamma^{1-}_{m+1/2,j+1/2} B^{xz}_{m+1/2,j+1/2,k;n-1/2} \\ &+ \frac{1}{\rho_{m+1/2,j+1/2}}(D_{\tilde{x}}\tau^{xz}|_{m+1/2,j+1/2,k;n} + D_{\tilde{y}}\tau^{yz}|_{m+1/2,j+1/2,k;n} \\ &- ik\Delta k_z \tau^{zz}_{m+1/2,j+1/2,k;n})\} \end{aligned} \tag{3.11}$$

$$\begin{aligned} B^{yx}_{m,j+1/2,k;n+1/2} &= \frac{1}{\gamma^{2+}_{m,j+1/2}}\{\gamma^{2-}_{m,j+1/2} B^{yx}_{m,j+1/2,k;n-1/2} \\ &+ \frac{1}{\rho_{m,j+1/2}}(D_{\tilde{x}}\tau^{xx}|_{m,j+1/2,k;n} + D_{\tilde{y}}\tau^{yx}|_{m,j+1/2,k;n} \\ &- ik\Delta k_z \tau^{zx}_{m,j+1/2,k;n})\} \end{aligned} \tag{3.12}$$

$$
\begin{aligned}
B^{yy}_{m+1/2,j,k;n+1/2} &= \frac{1}{\gamma^{2+}_{m+1/2,j}}\{\gamma^{2-}_{m+1/2,j}B^{yy}_{m+1/2,j,k;n-1/2} \\
&+ \frac{1}{\rho_{m+1/2,j}}(D_{\tilde{x}}\tau^{xy}|_{m+1/2,j,k;n} + D_{\tilde{y}}\tau^{yy}|_{m+1/2,j,k;n} \\
&- ik\Delta k_z\tau^{zy}_{m+1/2,j,k;n})\} \qquad (3.13)
\end{aligned}
$$

$$
\begin{aligned}
B^{yz}_{m+1/2,j+1/2,k;n+1/2} &= \frac{1}{\gamma^{2+}_{m+1/2,j+1/2}}\{\gamma^{2-}_{m+1/2,j+1/2}B^{yz}_{m+1/2,j+1/2,k;n-1/2} \\
&+ \frac{1}{\rho_{m+1/2,j+1/2}}(D_{\tilde{x}}\tau^{xz}|_{m+1/2,j+1/2,k;n} + D_{\tilde{y}}\tau^{yz}|_{m+1/2,j+1/2,k;n} \\
&- ik\Delta k_z\tau^{zz}_{m+1/2,j+1/2,k;n})\} \qquad (3.14)
\end{aligned}
$$

$$
\begin{aligned}
B^{zx}_{m,j+1/2,k;n+1/2} &= \frac{1}{\gamma^{3+}_{m,j+1/2}}\{\gamma^{3-}_{m,j+1/2}B^{zx}_{m,j+1/2,k;n-1/2} \\
&+ \frac{1}{\rho_{m,j+1/2}}(D_{\tilde{x}}\tau^{xx}|_{m,j+1/2,k;n} + D_{\tilde{y}}\tau^{yx}|_{m,j+1/2,k;n} \\
&- ik\Delta k_z\tau^{zx}_{m,j+1/2,k;n})\} \qquad (3.15)
\end{aligned}
$$

$$
\begin{aligned}
B^{zy}_{m+1/2,j,k;n+1/2} &= \frac{1}{\gamma^{3+}_{m+1/2,j}}\{\gamma^{3-}_{m+1/2,j}B^{zy}_{m+1/2,j,k;n-1/2} \\
&+ \frac{1}{\rho_{m+1/2,j}}(D_{\tilde{x}}\tau^{xy}|_{m+1/2,j,k;n} + D_{\tilde{y}}\tau^{yy}|_{m+1/2,j,k;n} \\
&- ik\Delta k_z\tau^{zy}_{m+1/2,j,k;n})\} \qquad (3.16)
\end{aligned}
$$

$$
\begin{aligned}
B^{zz}_{m+1/2,j+1/2,k;n+1/2} &= \frac{1}{\gamma^{3+}_{m+1/2,j+1/2}}\{\gamma^{3-}_{m+1/2,j+1/2}B^{zz}_{m+1/2,j+1/2,k;n-1/2} \\
&+ \frac{1}{\rho_{m+1/2,j+1/2}}(D_{\tilde{x}}\tau^{xz}|_{m+1/2,j+1/2,k;n} + D_{\tilde{y}}\tau^{yz}|_{m+1/2,j+1/2,k;n} \\
&- ik\Delta k_z\tau^{zz}_{m+1/2,j+1/2,k;n})\} \qquad (3.17)
\end{aligned}
$$

Inside the computational regime, β_i are set to be zero and only three B_{ij}, *e.g.* $B_{xx} = v_x$, $B_{xy} = v_y$ and $B_{xz} = v_z$ need to be computed and stored in the memory as the rest are equal to one of them (equation 2.31 $\sim$ 2.33). As the PML is very efficient in absorption, small number of grid points are required for the PML; therefore the

increment in memory requirement by the introduction of 6 more variables in the PML regime is negligible. Typically 10 PML grid points can reduce the numerical reflection to 0.1%. Also working in the discrete k_z domain, periodicity is assume in the z direction, therefore numerical absorbing is not necessary along the z direction. β_3 is set to zero.

Discretizing equations 2.22 $\sim$ 2.30 in the stretching coordinate leads to the time iteration equations to update each stress component.

$$\begin{aligned}
\tau^{xx}_{m+1/2,j+1/2,k;n+1} &= \frac{1}{\gamma^{1+}_{m+1/2,j+1/2}}(\gamma^{1-}_{m+1/2,j+1/2}\tau^{xx}_{m+1/2,j+1/2,k;n} \\
&+ d^{11}_{m+1/2,j+1/2}D_{\tilde{x}}v^x|_{m+1/2,j+1/2,k;n+1/2} \\
&+ d^{12}_{m+1/2,j+1/2}D_{\tilde{y}}v^y|_{m+1/2,j+1/2,k;n+1/2} \\
&- d^{13}_{m+1/2,j+1/2}ik\Delta k_z v^z_{m+1/2,j+1/2,k;n+1/2}) \qquad (3.18)
\end{aligned}$$

$$\begin{aligned}
\tau^{xy}_{m,j,k;n+1} &= \frac{1}{\gamma^{1+}_{m,j}}(\gamma^{1-}_{m,j}\tau^{xy}_{m,j,k;n} \\
&+ d^{41}_{m,j}D_{\tilde{y}}v^x|_{m,j,k;n+1/2} \\
&+ d^{42}_{m+1/2,j+1/2}D_{\tilde{x}}v^y|_{m,j,k;n+1/2}) \qquad (3.19)
\end{aligned}$$

$$\begin{aligned}
\tau^{xz}_{m,j+1/2,k;n+1} &= \frac{1}{\gamma^{1+}_{m,j+1/2}}(\gamma^{1-}_{m,j+1/2}\tau^{xz}_{m,j+1/2,k;n} \\
&- d^{61}_{m,j+1/2}ik\Delta k_z v^x_{m,j+1/2,k;n+1/2} \\
&+ d^{63}_{m,j+1/2}D_{\tilde{x}}v^z|_{m,j+1/2,k;n+1/2}) \qquad (3.20)
\end{aligned}$$

$$\begin{aligned}
\tau^{yx}_{m,j,k;n+1} &= \frac{1}{\gamma^{2+}_{m,j}}(\gamma^{2-}_{m,j}\tau^{yx}_{m,j,k;n} \\
&+ d^{51}_{m,j}D_{\tilde{y}}v^x|_{m,j,k;n+1/2} \\
&+ d^{52}_{m+1/2,j+1/2}D_{\tilde{x}}v^y|_{m,j,k;n+1/2}) \qquad (3.21)
\end{aligned}$$

$$\begin{aligned}
\tau^{yy}_{m+1/2,j+1/2,k;n+1} &= \frac{1}{\gamma^{2+}_{m+1/2,j+1/2}}(\gamma^{2-}_{m+1/2,j+1/2}\tau^{yy}_{m+1/2,j+1/2,k;n} \\
&+ d^{21}_{m+1/2,j+1/2}D_{\tilde{x}}v^x|_{m+1/2,j+1/2,k;n+1/2} \\
&+ d^{22}_{m+1/2,j+1/2}D_{\tilde{y}}v^y|_{m+1/2,j+1/2,k;n+1/2} \\
&- d^{23}_{m+1/2,j+1/2}ik\Delta k_z v^z_{m+1/2,j+1/2,k;n+1/2}) \qquad (3.22)
\end{aligned}$$

$$\begin{aligned}
\tau^{yz}_{m+1/2,j,k;n+1} &= \frac{1}{\gamma^{2+}_{m+1/2,j}}(\gamma^{2-}_{m+1/2,j}\tau^{yz}_{m+1/2,j,k;n} \\
&- d^{82}_{m+1/2,j}ik\Delta k_z v^y_{m+1/2,j,k;n+1/2} \\
&+ d^{83}_{m+1/2,j}D_{\tilde{y}}v^z|_{m+1/2,j,k;n+1/2}) \qquad (3.23)
\end{aligned}$$

$$\begin{aligned}
\tau^{zx}_{m,j+1/2,k;n+1} &= \tau^{zx}_{m,j+1/2,k;n} \\
&+ \Delta t(-d^{71}_{m,j+1/2}ik\Delta k_z v^x_{m,j+1/2,k;n+1/2} \\
&+ d^{73}_{m,j+1/2}D_{\tilde{x}}v^z|_{m,j+1/2,k;n+1/2}) \qquad (3.24)
\end{aligned}$$

$$\begin{aligned}
\tau^{zy}_{m+1/2,j,k;n+1} &= \tau^{zy}_{m+1/2,j,k;n} \\
&+ \Delta t(-d^{92}_{m+1/2,j}ik\Delta k_z v^y_{m+1/2,j,k;n+1/2} \\
&+ d^{93}_{m+1/2,j}D_{\tilde{y}}v^z|_{m+1/2,j,k;n+1/2}) \qquad (3.25)
\end{aligned}$$

$$\begin{aligned}
\tau^{zz}_{m+1/2,j+1/2,k;n+1} &= \tau^{zz}_{m+1/2,j+1/2,k;n} \\
&+ \Delta t(d^{31}_{m+1/2,j+1/2}D_{\tilde{x}}v^x|_{m+1/2,j+1/2,k;n+1/2} \\
&+ d^{32}_{m+1/2,j+1/2}D_{\tilde{y}}v^y|_{m+1/2,j+1/2,k;n+1/2} \\
&- d^{33}_{m+1/2,j+1/2}ik\Delta k_z v^z_{m+1/2,j+1/2,k;n+1/2}) \qquad (3.26)
\end{aligned}$$

In the PML regime, $T_{ij} \neq T_{ji}$, introducing 3 extra variables. Again they only need to be computed and restored in the PML regime, resulting little increment in memory requirement. Also note that the spatial difference operator can be chosen at the

user's choice, including the wavelet based scheme and the 2nd, 4th, 6th and 8th order Taylor's expansion based ones. Definition of spatial difference operators are defined in chapter 2.

When considering wave propagation in an elastic medium without residual stresses, the stress tensor is symmetric, i.e., $\tau_{\alpha\beta} = \tau_{\beta\alpha}$ and $d_{p\alpha}$ denotes the elasticity of the medium. It is widely acknowledged that orthorhombic anisotropy is sufficient to describe the general anisotropy for the solid earth. For orthorhombic anisotropy, the elasticity matrix of the medium is

$$[d_{p\alpha}] = \begin{bmatrix} c_{11} & c_{12} & c_{13} \\ c_{12} & c_{22} & c_{23} \\ c_{13} & c_{23} & c_{33} \\ c_{66} & c_{66} & 0 \\ c_{66} & c_{66} & 0 \\ c_{55} & 0 & c_{55} \\ c_{55} & 0 & c_{55} \\ 0 & c_{44} & c_{44} \\ 0 & c_{44} & c_{44} \end{bmatrix} \tag{3.27}$$

Material properties (density and elasticity) are defined at (m+1/2,j+1/2), properties at (m+1/2,j), (m, j+1/2) and (m, j) are obtained through the following averaging

formulae:

$$\rho_{m+1/2,j} = \frac{1}{2}(\rho_{m+1/2,j-1/2} + \rho_{m+1/2,j+1/2}) \tag{3.28}$$

$$\rho_{m,j+1/2} = \frac{1}{2}(\rho_{m-1/2,j+1/2} + \rho_{m+1/2,j+1/2}) \tag{3.29}$$

$$\begin{aligned} \rho_{m,j} &= \frac{1}{4}(\rho_{m-1/2,j+1/2} + \rho_{m+1/2,j+1/2} \\ &+ \rho_{m-1/2,j-1/2} + \rho_{m+1/2,j-1/2}) \end{aligned} \tag{3.30}$$

$$d^{p\alpha}_{m+1/2,j} = 2/(1/d^{p\alpha}_{m+1/2,j-1/2} + 1/d^{p\alpha}_{m+1/2,j+1/2}) \tag{3.31}$$

$$d^{p\alpha}_{m,j+1/2} = 2/(1/d^{p\alpha}_{m-1/2,j+1/2} + 1/d^{p\alpha}_{m+1/2,j+1/2}) \tag{3.32}$$

$$\begin{aligned} d^{p\alpha}_{m,j} &= 4/(1/d^{p\alpha}_{m-1/2,j+1/2} + 1/d^{p\alpha}_{m+1/2,j+1/2} \\ &+ 1/d^{p\alpha}_{m-1/2,j-1/2} + 1/d^{p\alpha}_{m+1/2,j-1/2}) \end{aligned} \tag{3.33}$$

All FDTD equations are derived in the stretching coordinate. Depending on the shape of stretching functions $\epsilon^1(\tilde{x})$ and $\epsilon^2(\tilde{y})$, grid size in the physical domain is variable. Following the same approach as for the 1-D case in chapter 2, we may obtain the stability condition for the variable grid 2.5-D FDTD scheme,

$$\xi \leq \frac{1}{\sum_{l=0}^{Q_s} |a(l)|}(2 + \frac{k^2_{z_{\max}}\Delta^2}{4})^{-\frac{1}{2}} \tag{3.34}$$

For simplicity, let $\Delta\tilde{x} = \Delta\tilde{y} = \Delta$.

The upper limit of axial wavenumber, $k_z^{\max}$, is chosen as

$$k_z^{\max} = 1.5\frac{\omega_{\max}}{v_z^{\min}} \tag{3.35}$$

where $v_z^{\min}$ represents the slowest phase velocity in the axial direction. $k_z^{\max}$ also implies the resolution in the z direction, i.e., $\Delta z = \frac{2\pi}{k_z^{\max}}$. The spacing in k_z direction, Δk_z, is determined by the desired computational dimension in the z direction. Suppose the computational range in the z direction is $[-L_z, L_z]$, then $\Delta k_z = \frac{\pi}{L_z}$.

The numerical source can be one or many point or dipole sources. The source time function is a Kelly wavelet (Stephen et al., 1985).

3.3 Working With the Anisotropic Perfectly Matched Layer

Let the stretching parameter along the imaginary axes, β^j in equations 2.9 and 2.10 vary gradually in the x_j direction, otherwise a reflection may happen at the boarder of the computational domain due to a sudden change in β_j. Figure 3-2 illustrates how β_1 and β_2 are arranged for the 2.5D algorithm. β_j is zero in the computational domain and quadratically increasing toward the outer boundary inside the PML. x_1, x_2 and x_3 denote x, y and z directions, respectively.

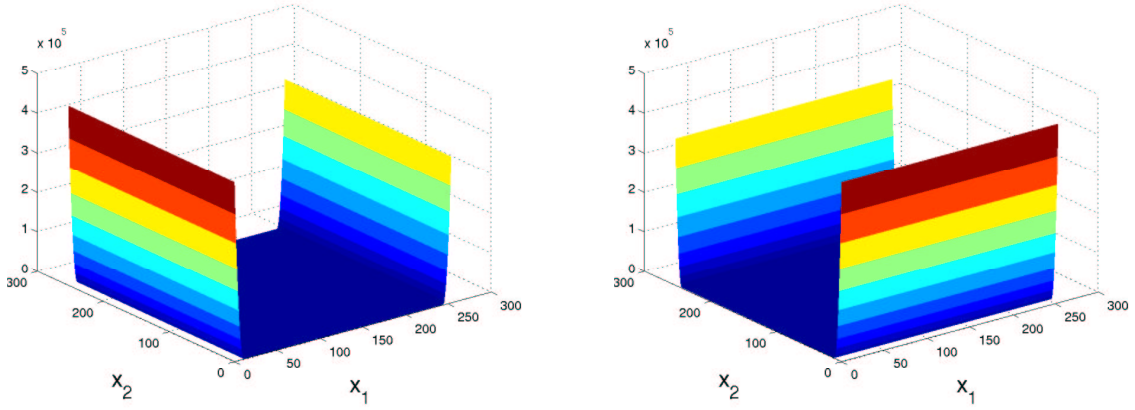

(a) β_1 (b) β_2

Figure 3-2: Distribution of the absorbing parameter β_1 and β_2 for a 2-D computation. β_j is zero in the computational domain and quadratically increasing toward the outer boundary inside the PML.

3.4 Numerical Results

The variable grid scheme and the performance of PML in 2-D case has been tested in chapter 2. Here the numerical test is focused on the 2.5-D algorithm and the PML in the 2.5-D situation. Both kinematics and amplitudes of the numerical solution are to be compared with analytical solutions. The artifacts of the 2.5-D algorithm (Randall, 1991b; Liu and Sinha, 2000) and ways to get rid of them are shown. The remaining

energy due to the imperfection of the PML is calculated. Because the FDTD algorithm will be used to simualate wave propagations in a fluid-filled borehole in the following chapters, the stretched grid 2.5-D FDTD solution is compared with those from a discrete wavenumber computation and a uniform grid algorithm.

3.4.1 3-D Homogeneous Model

The testing model is 50 m by 50 m by 50 m in size with a compressional velocity equal to 3000 m/s. Being discrete in the k_z domain implies the 2.5D solution is periodic with respect to x_3 or the z direction. The period is equal to $2\pi/\Delta k_z$. Therefore Δk_z should not exceed $2\pi/50 = \pi/25$. In this case, Δk_z is chosen to be $\pi/50$. A point source with a center frequency of 500 Hz is placed at (25, 25, 0). The upper half-power frequency of the source is 678 Hz (Stephen et al., 1985), thus the maximum k_z is chosen to be 2.8. The 2.5-D scheme in this case requires less than half the grid points of a 3-D scheme for the same resolution. The DD_2 is selected as the spatial differencing operator. A 10 point PML is placed around the computational domain, with the maximum β_1 and β_2 being 20000. Further investigation shows that with the same number of PML grid points and absorbing rate, β_j should be increased with the increment of the source center frequency and the highest velocity of the physical model.

Figure 3-7 shows 3-D snapshots of the spherical wave propagating in the homogeneous medium at various time steps. The PML works very well. The maximum amplitude in figure 3-7(l) is 0.2% that in figure 3-7(j). The wavefront is able to maintain its spherical shape, except a strong artifact along the z direction at or nearly the source location at initial time steps. The artificial disturbance propagates only in the x_1 and x_2 plane, not along the x_3 or the z direction. The cause of this artifact is that the inverse Fourier transform in equation 3.2 does not converge when k_z is zero. As the artifact does not propagate in the x_3 direction, which means it is constant along the x_3 direction, a pure artifact at each time step can be recorded far from the wavefront and be taken away from the wavefield completely. Figure 3-8 shows snapshots of the spherical wave after the artifact is taken out.

Figure 3-9(b) shows both FDTD and analytical waveforms recorded by a receiver array (figure 3-9(a)) along the x_2 direction. The FDTD solution agrees extremely well with the analytical solution both in kinematics and amplitude. Figure 3-9(b) also demonstrates that PML absorbs most of the propagating energy, because the recording time is long enough for the reflected wave to show up if they have not been absorbed by the PML.

For the receiver array along the x_3 direction (figure 3-10(a)), comparison of waveforms of both the FDTD and the analytical solutions is shown in figure 3-10. As the receiver array is close to the source location in the x_1 and x_2 plane, there are artifacts prior to the wave arrivals in figure 3-10(b). They can be taken away by subtracting a well isolated artifact (such as the one at the far end receiver) from the waveforms. The waveforms without artifacts are shown in figure 3-10(c). Again the FDTD solution agrees extremely well with its analytical counterpart both in kinematics and amplitudes.

3.4.2 A monopole source in a fluid-filled borehole

To show that variable grids are able to represent more efficiently an inhomogeneous model, such as a fluid-filled borehole, the model is discretized as shown in figure 2-3. The stretched wave equations (Eq 2.7 and 2.8) are solved with the 2.5-D FDTD algorithm. As we are interested in possible improvement in the numerical computation by representing the circular borehole more smoothly, we only show simulations for a monopole source and 8 monopole receivers at the center of the borehole. Parameters for the simulation are listed in Table 3.1. Results from the stretched grid FDTD computation are compared with those from a discrete wavenumber computation and a uniform grid algorithm. The cross section of the uniformly discretized model is illustrated in figure 3-3, where the grid size of equals to the coarse grid size in the stretched mesh.

The cross section slice of snapshots computed by the 2.5-D FDTD algorithm on a uniform grid and a stretched grid at a similar time are shown in figures 3-4 and 3-5, respectively. In the uniform grid case, the wavefront can hardly hold its

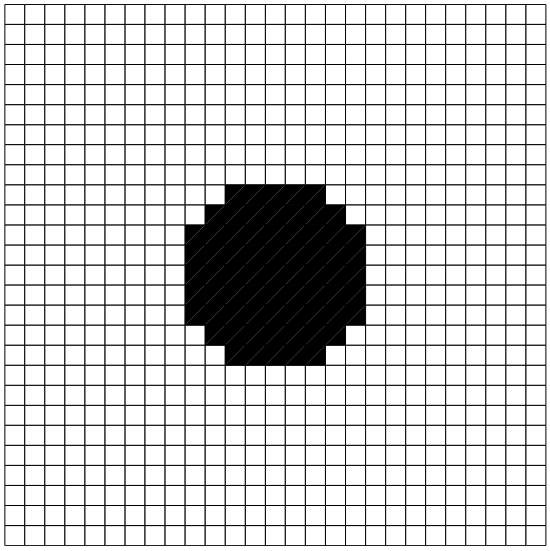

Figure 3-3: The same borehole as in figure 2-3 except being discretized using a uniform grid. The grid size equals to the coarse grid size in the stretched mesh.

water	ρ V_p	1000 1500
formation	ρ V_p V_s	2000 3000 2000
borehole radius	r	0.1
source 1st receiver offset	z_0	3.3528
receiver spacing	dz	0.1524
number of receivers	nrec	8
source center frequency	f_c (Hz)	8000
grid size in the stretched domain	$\Delta\tilde{x}$	0.007
stretching factor	α^1 & α^2	3
differencing scheme		DD_2

Table 3.1: Model parameters for FDTD simulations. All in *S.I.* units.

circular shape due to the poor representation of the circular borehole. That is in sharp contrast to its counterpart in the case of the stretched grid. Waveforms at all 8 receivers from both FDTD computation are plotted against results from a discrete wavenumber algorithm (Bouchon and Schmitt, 1989) in figure 3-6. The stretched grid FDTD result agrees with the discrete wave number result very well, given the different nature of the two method; whereas both the phase and amplitude of the uniform grid FDTD waveform deviates from the discrete wave number solution from early on.

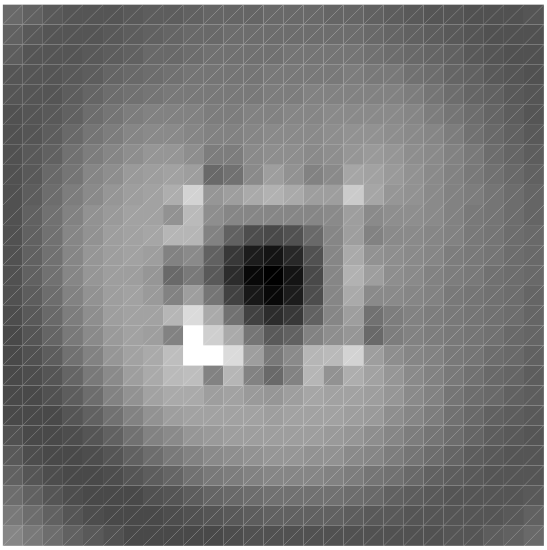

Figure 3-4: A cross-section slice of the snapshot computed on the uniform grid. The wave front loses its circular shape due to poor representation of the circular borehole.

3.5 Discussions and Conclusions

A 2.5-D variable grid FDTD algorithm has been implemented with the anisotropic PML. It has options of choosing between the 2nd, 4th, 6th, 8th and the wavelet based (DD_2 and DD_4) differencing operators.

The non-splitting anisotropic PML is able to absorb as much as 99.8% of the total wave energy with 10 grid points. The proposed PML shares the same formula as the

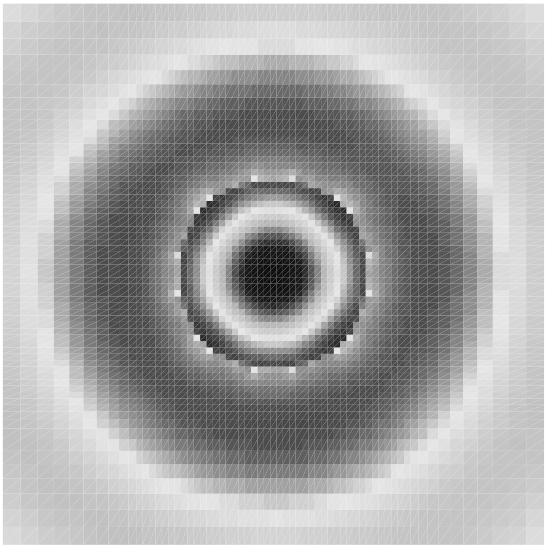

Figure 3-5: A cross-section slice of the snapshot computed on the stretched grid. The wave front keeps a better circular shape comparing the uniform grid case.

variable grid scheme introduced in chapter 2, allowing an easy and modular implementation for both isotropic and anisotropic media. The anisotropic PML requires less field variables than the formula that employs field splitting.

Although introducing some strong artifacts near the source location, the 2.5D solution yields accurate results in both kinematics and amplitudes. Artifacts can be easily removed as they do not vary in the x_3 direction.

Numerical simulations of wave propagating along a fluid-filled borehole demonstrate considerable improvement in the solution by refining grid size around the borehole.

To illustrate the amount of computational savings made by the variable mesh and 2.5D implementation, we can take a logging while drilling model as an example. Model parameters are listed in table 3.2. The center frequency is 2 kHz. The model dimension is 4.6 m by 4.6 m by 3.8910 m. When the tool is off-centered, the annulus between the formation and the tool can be as thin as 0.006 m. At least 4 points are needed inside the annulus and that requires a grid size as small as 0.0015 m. If a 3-D uniform grid FDTD is applied, the model requires a total of 2.5×10^{10}

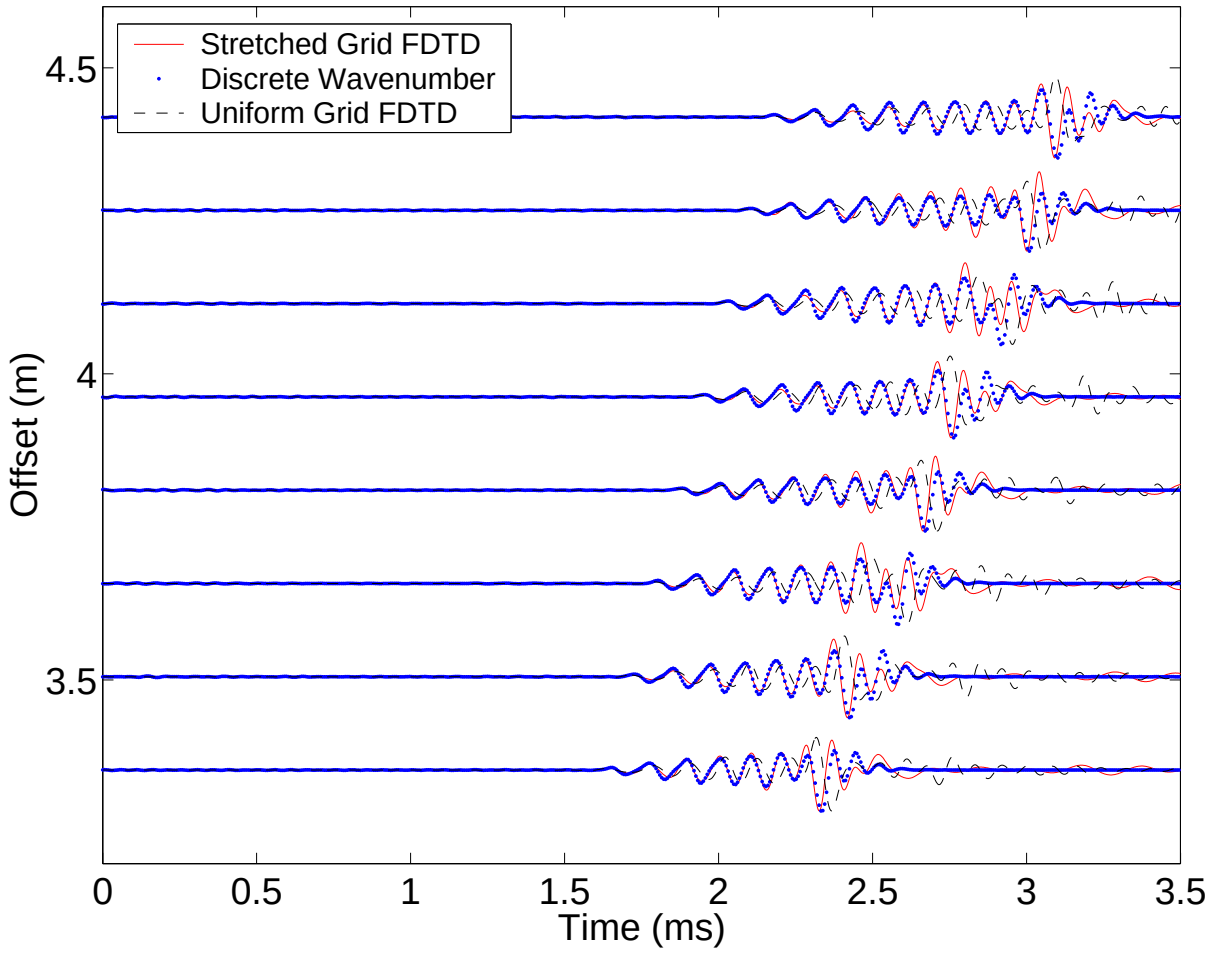

Figure 3-6: Waveforms received at axial locations in a fluid-filled borehole.

	density (kg/m^3)	v_p (m/s)	v_s (m/s)
borehole fluid	1000	1500	0
steel tool	7800	5860	3130
formation (soft)	2200	3000	1200

Table 3.2: Model parameters of a fluid-filled borehole with a steel tool.

grid points which leads to a minimum (isotropic case) memory requirement of 2500 Gbytes, far beyond the capacity of a normal parallel supercomputer or cluster, not mentioning the significant delay caused by massive communication required between nodes. Applying the variable grid scheme, the grid size inside the formation can be 26 times that inside the borehole, plus a coarser sampling rate in the k_z domain when using the 2.5-D formula, a total number of grid points now reduces to 10^7, 2500 times less. The memory requirement now reduces to 1 or a couple of Gbytes, enabling a desktop computer or multiple nodes cluster to compute. Moreover, the 2.5-D solution in k_z domain needs no communication between nodes, allowing a complete parallelization with no communication induced latency.

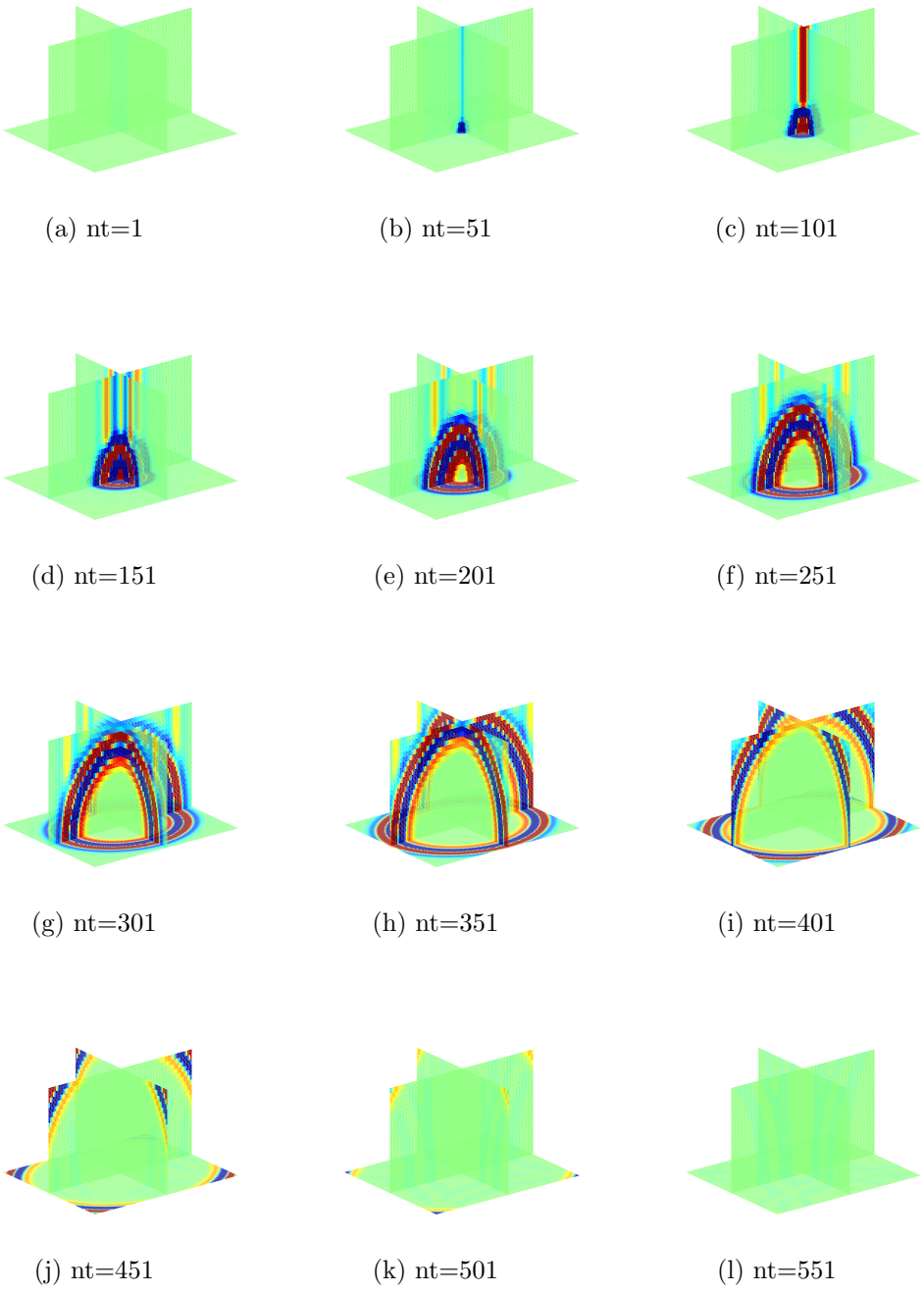

(a) nt=1 (b) nt=51 (c) nt=101

(d) nt=151 (e) nt=201 (f) nt=251

(g) nt=301 (h) nt=351 (i) nt=401

(j) nt=451 (k) nt=501 (l) nt=551

Figure 3-7: 3-D snapshots of a spherical wave, generated by a point source, propagating in a homogeneous medium.

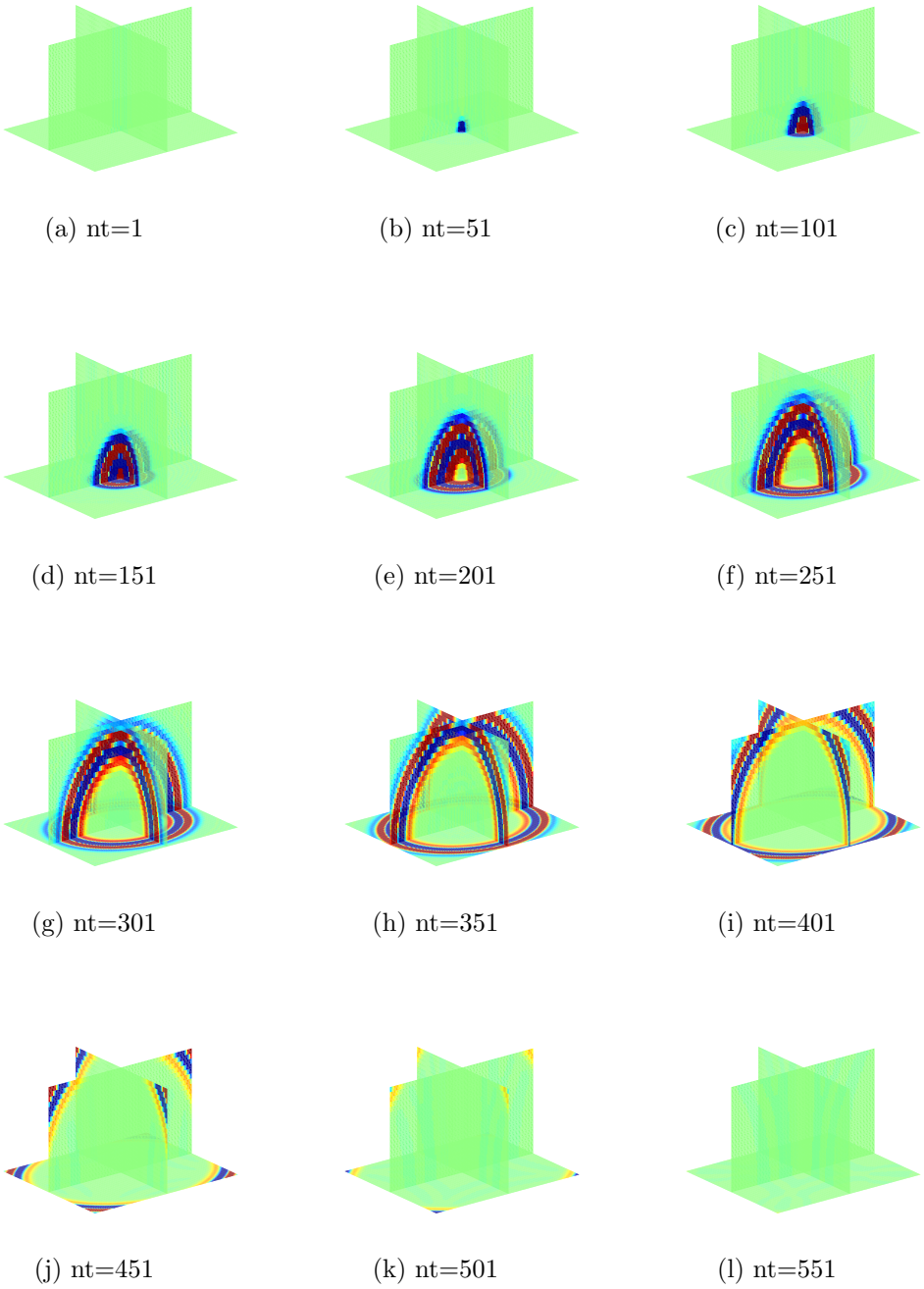

(a) nt=1 (b) nt=51 (c) nt=101

(d) nt=151 (e) nt=201 (f) nt=251

(g) nt=301 (h) nt=351 (i) nt=401

(j) nt=451 (k) nt=501 (l) nt=551

Figure 3-8: 3-D snapshots of the same spherical wave as in figure 3-7 after the artifact is taken out.

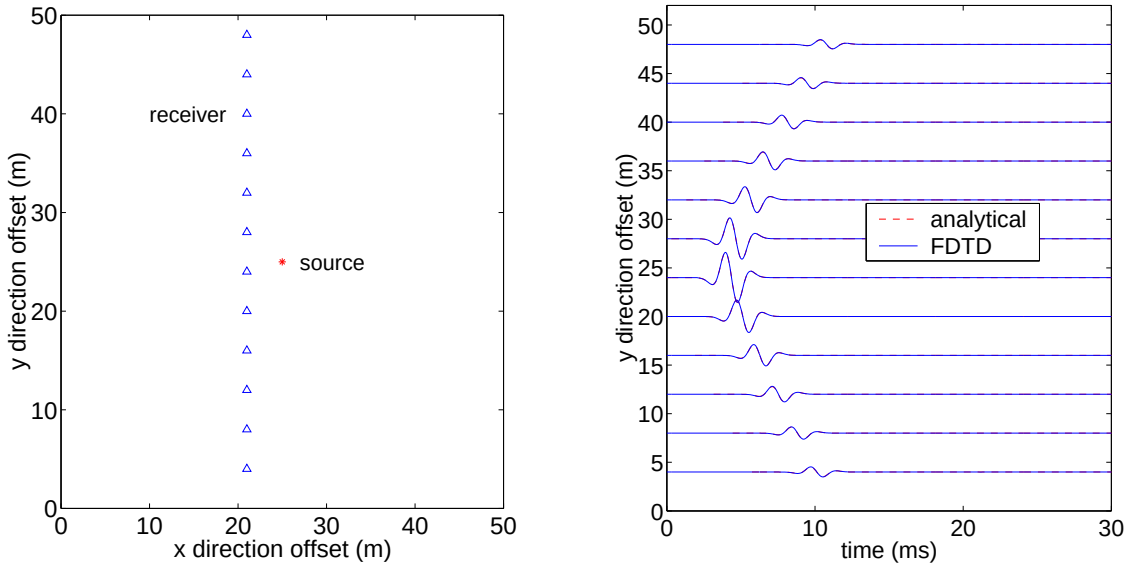

(a) Source and receiver array along x_2 direction

(b) Waveform comparison

Figure 3-9: FDTD and analytical waveforms recorded by a receiver array (figure 3-9(a) along the y direction. The FDTD solution agrees extremely well with the analytical solution. Figure 3-9(b) also demonstrates that PML absorbs most of the propagating energy, because the recording time is long enough for the reflected wave to show up had they not been absorbed by the PML.

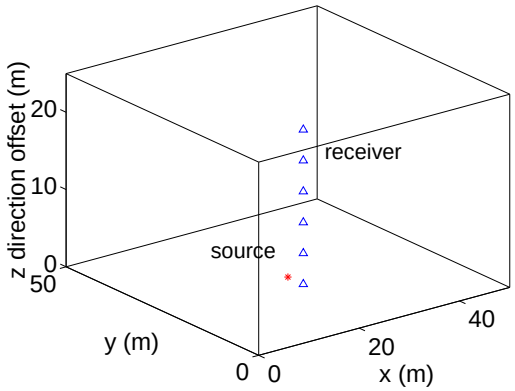

(a) Source and receiver array along z direction

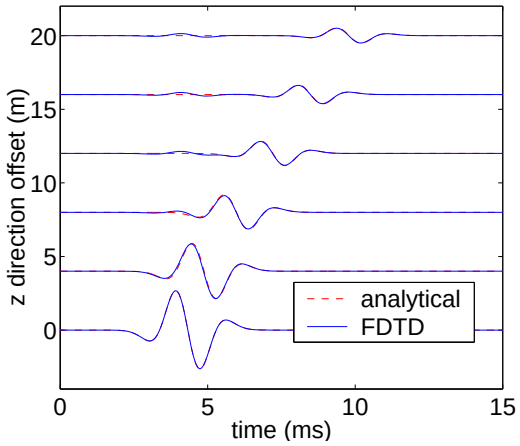

(b) Waveform comparison (with artifacts)

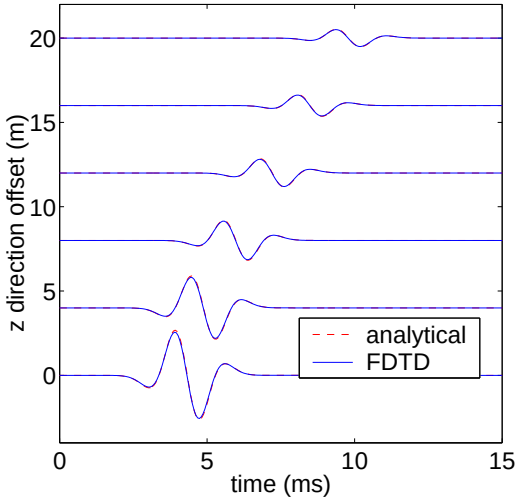

(c) Waveform comparison (without artifacts)

Figure 3-10: Waveforms of both the FDTD and the analytical solutions for the receiver array shown in figure 3-10(a). There are artifacts prior to the wave arrivals in figure 3-10(b). Same artifacts are found in the snapshots of figure 3-7. As artifacts do not vary along the z direction, they can be taken away by subtracting a well isolated artifact (such as the one at the far end receiver) from the waveforms. The waveforms without artifacts are shown in figure 3-10(c).

Chapter 4

Wave Propagation Studies on Acoustic Logging While Drilling – Centered Tool

ABSTRACT

Acoustic waveforms recorded in a fluid-filled borehole in soft formation with a logging while drilling tool are computed by a non-uniform grid finite difference algorithm. The tool is at the center of the fluid-filled borehole. At low frequencies (the source center frequency is chosen to be 2 kHz), monopole, dipole and quadrupole LWD logging tools are simulated. A clear direct shear arrival is observed in the dipole and monopole case, providing a good cross-check for modal based shear measurements. Quadrupole mode asymptotically approaches formation shear velocity at low frequencies, which may serve as a good candidate to measure formation shear velocity. Dipole, monopole and quadrupole excitations are efficiently achieved by two out of phase point sources, four in phase point sources and four alternate phase point sources. Dipole logging operating at higher frequencies (the source center frequency is chosen to be 8 kHz and 15 kHz) is also investigated. At higher frequencies, the borehole flexural arrival is well separated from the tool flexural arrival, and it is less dispersive. However, higher

mode (*e.g.* n=3) is excited, which may complicate data interpretation. To identify and take higher mode into account in data processing, frequency domain dispersion analysis is essential. Numerical results agrees with eigenvalue based solutions.

4.1 Introduction

Logging while drilling (LWD) tools emerged in the 1990's and are gaining momentum due to their engineering and economical advantages (Aron et al., 1994; Minear et al., 1995, 1996; Heysse et al., 1996; Market et al., 2002; Tang et al., 2002). Formation properties are measured simultaneously while drilling avoiding problems such as "mud cake" and reducing the rig time, compared to their wireline counterparts. LWD measurements may also enable a real-time evaluation of formation properties which leads to significant potential for "look-ahead of the bit" and better control of well trajectories.

LWD tool differs from its wireline counterpart only by geometry. Thus it looked reasonable for LWD tool designers to borrow the wealth of wisdom in the wireline logging literature. However, with its sources and receivers closer to the borehole wall and substantially larger cross-section of the tool taking up majority space in the fluid-filled borehole, LWD is found to differ considerably from its wireline counterpart. It has significant effects on borehole modes. That gives rise to difficulties to identify modal arrivals, a crucial step to estimate formation v_p and v_s values.

Current LWD tools can measure shear velocity in hard formation and compressional velocity in both hard and soft formation with some level of confidence. Shear velocity measurements in soft formations could be problematic. In order to improve ways to measure formation shear velocity in soft formations, it is essential to understand modal excitations and wave propagation characteristics in the LWD situation. A frequency domain modal study has shown that tool modes affect dispersion properties of important borehole modes like the flexural (1,0) mode that is used to measure formation shear velocity in the wireline case (Rao et al., 1999). Time domain investigation, will complement the frequency domain analysis and understand amplitude

responses of all arrivals, guided modes, refracted arrivals and even leaky modes.

Finite difference time domain method has been extensively used to study time domain wave propagations in the wireline situation (Stephen et al., 1985; Chen, 1994; Randall, 1991b; Liu and Sinha, 2000), for its flexibility to handle not only symmetric borehole model, but also asymmetric ones such as off-centered tool and non-circular borehole shapes which are otherwise difficult to solve with wavenumber integral methods (Kurkjian, 1985; Bouchon and Schmitt, 1989; Ellefsen, 1990; Randall, 1990, 1991a; Norris and Sinha, 1993). Time domain studies in LWD have been hampered because of the large memory requirements for a typical model using uniform grid spacing. With the development of the stretched grid FDTD algorithm (chapter 2 and 3), wave propagation in the LWD can be simulated even with mid-sized PC-clusters.

Numerical results are limited to soft formation, as shear velocity measurement is the most problematic in soft formations. Discussions include modal excitations with respect to various sources types (such as monopole, dipole and quadrupole) and source frequencies. In this chapter, discussions are limited to centered tools.

4.2 Dispersion Curves of Various Borehole Modes in LWD

Both wireline and LWD acoustic logging tools consist a steel pipe with one or a pair of sources and several pairs of receivers mounted to it. Typical offset between the source and the first receiver pair is about 11 ft for wireline and 4.5 ft for LWD tools. Receivers always align with the source in both radial and azimuthal positions. Figure 4-1 shows a schematic diagram of an LWD tool. Both the fluid-filled borehole and the LWD tool pipe act as waveguides. At a certain frequency, only waves traveling with certain phase velocities propagate efficiently along the axial direction. Those waves are known as borehole modes. While their dispersion properties had been investigated (Rao et al., 1999), a brief discussion of various borehole modes in a typical LWD tool is useful to establish a context for the time domain study.

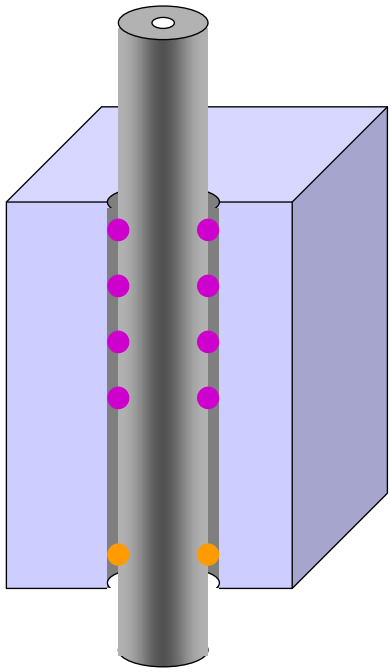

Figure 4-1: A schematic diagram of an LWD tool.

Discussion is limited to azimuthal orders of 0, 1,and 2, referred as the monopole, dipole and quadrupole cases. The frequency range is 0-20 kHz. Formation and tool properties are listed in Table 4.1.

4.2.1 Monopole Modes (n=0)

In the frequency range of 0-20 kHz, Stoneley wave is the only borehole mode in the monopole case. It is trapped in the fluid annulus between the steel pipe and the formation. The dispersion curves of Stoneley mode with and without the LWD tool are shown in figure 4-2. The Stoneley mode becomes localized at the borehole wall as frequency increases, and its phase velocity approaches that of the Schölte fluid-solid interface wave. Without the LWD tool, the low-frequency limit of the Stoneley phase velocity is the "tube wave" speed given by $c_T = c_f(1 + B/\mu)$, where c_f is the fluid p velocity, B the bulk modulus of the fluid and μ the shear modulus of the formation (Paillet and Cheng, 1991). The introduction of a steel pipe in the borehole

fluid reduces the low-frequency limit of the Stoneley phase velocity considerably. Figure 4-3 shows both phase and group velocities of the borehole Stoeneley in the LWD situation.

4.2.2 Dipole Modes (n=1)

The dispersion curves for the dipole case are shown in figure 4-4. Only the tool and borehole flexural modes are shown, because other modes are of little consequence in the LWD operation. Without the LWD tool, the borehole flexural mode asymptotically approaches the formation shear velocity at low-frequency limit. When the tool is inside an infinite fluid volume, the tool flexural phase velocity approaches to 0 at low-frequency limit. It increases with frequency. When the LWD tool is inside the fluid-filled borehole, the tool flexural mode interacts with the borehole flexural mode at low frequencies. As a result, the borehole flexural mode keeps its dispersion property at high frequencies and exchanges dispersion property at low frequencies with the tool flexural mode. The low-frequency limit of the phase velocity of the borehole flexural mode is no longer the formation shear velocity. Figure 4-5 shows both phase and group velocities of borehole and tool flexural modes.

4.2.3 Quadrupole Modes (n=2)

The dispersion curves for the quadrupole case are shown in figure 4-6. The borehole quadrupole mode asymptotically approaches the formation shear at low frequencies regardless of the existence of an LWD tool. Because of this property, Tang et al. (2002) reported using the quadrupole mode to measure formation shear velocities. Figure 4-5 shows both phase and group velocities of borehole quadrupole modes.
On top of the aforementioned borehole modes, it is well established that compressional velocities in both formations and shear velocities in hard formation can be measured by refracted arrivals.

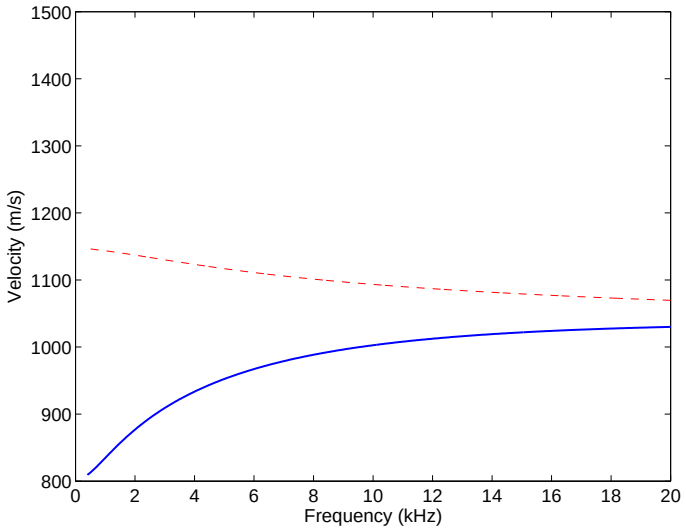

Figure 4-2: Dispersion of borehole Stoneley modes (monopole) with or without the LWD tool. Solid line: with LWD tool; Dash line: without LWD tool.

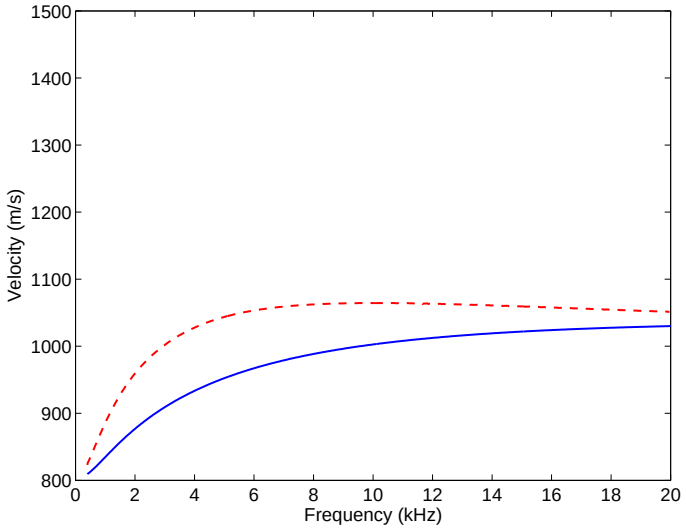

Figure 4-3: Phase and group velocities of the borehole Stoneley mode. Solid line: phase velocity; Dash line: group velocity. Formation properties: v_p=3000 m/s, v_s=1200 m/s, ρ=2200 kg/m^3. Fluid properties: v_p=1500 m/s, ρ=1000 kg/m^3. Tool properties: v_p=5860 m/s, v_s=3130 m/s and ρ=7800 kg/m^3.

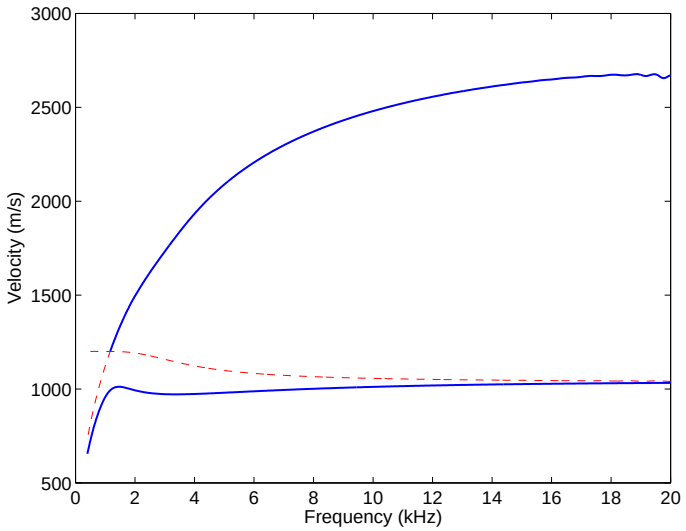

Figure 4-4: Dispersion of dipole modes. The faster mode is the tool flexural. The dash line represents tool flexural mode when the tool is in an infinite fluid volume. The solid line represents the tool flexural mode when the tool is inside a fluid-filled borehole. They lay on top of each other at higher frequencies. The slower mode is the borehole flexural. The dash line shows its dispersion behavior without the LWD tool. The solid line shows the borehole flexural dispersion that has interacted with the tool flexural mode at low frequencies.

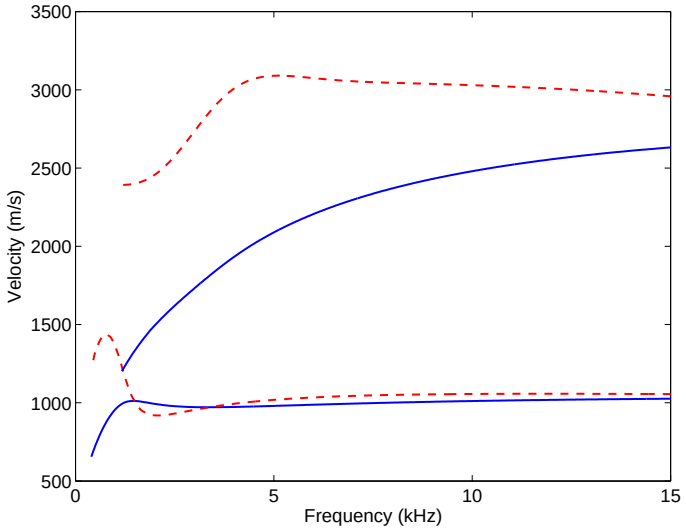

Figure 4-5: Phase and group velocities of borehole and tool flexural modes. Solid line: phase velocity; Dash line: group velocity. Formation properties: v_p=3000 m/s, v_s=1200 m/s, ρ=2200 kg/m^3. Fluid properties: v_p=1500 m/s, ρ=1000 kg/m^3. Tool properties: v_p=5860 m/s, v_s=3130 m/s and ρ=7800 kg/m^3.

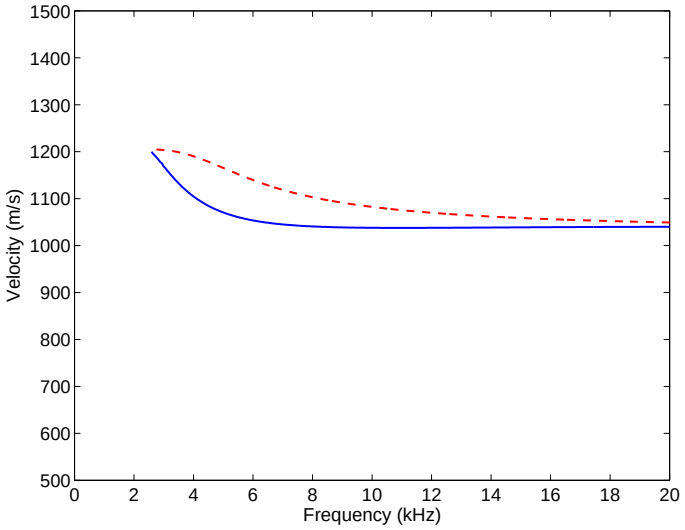

Figure 4-6: Dispersion of quadrupole modes. Solid line: with LWD tool; Dash line: without LWD tool. Formation properties: v_p=3000 m/s, v_s=1200 m/s, ρ=2200 m/s. Fluid properties: v_p=1500 m/s, ρ=1000 kg/m^3. Tool properties: v_p=5860 m/s, v_s=3130 m/s and ρ=7800 kg/m^3.

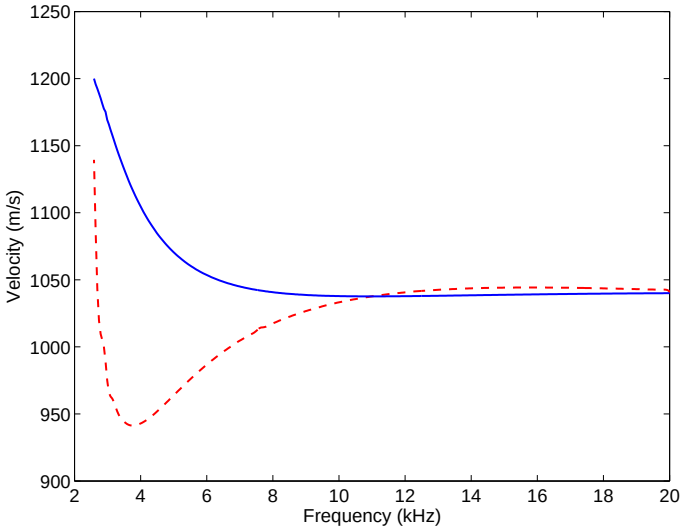

Figure 4-7: Phase and group velocities of the borehole quadrupole mode. Solid line: phase velocity; Dash line: group velocity.

	formation	tool	borehole fluid
v_p (m/s)	3000	5860	1500
v_s (m/s)	1200	3130	0
ρ (kg/m^3)	2200	7800	1000
a (tool inner radius) (m)	0.02413		
b (tool outer radius) (m)	0.092075		
c (borehole radius) (m)	0.109375		

Table 4.1: Model parameters of a fluid-filled borehole with a steel tool.

4.3 Wave Propagations in Logging While Drilling Situation

In this section, the stretched grid FDTD algorithm is used to study characteristics of wave propagations in the LWD situation. We shall discuss monopole, dipole and quadrupole loggings at low frequencies (0-5 kHz) and dipole logging at high frequencies (0-30 kHz).

The dominant wavelengths in the formation are $\lambda_p = v_p/f_c$ and $\lambda_s = v_s/f_c$, where f_c is the source center frequency. To reduce boundary effects, dimension of the numerical model is chosen to be $2\lambda_p$ by $2\lambda_p$ in x and y, because the radial penetration depth into the formation of each mode is around one wavelength(Paillet and Cheng, 1991). $kz_{\max}$ is determined by equation 3.35. $\Delta\tilde{x}$ and $\Delta\tilde{y}$ are chosen such that the smallest structure in the model, which is the thin annulus between the steel pipe and the formation, can have at least 4 sampling grid points. Stretching factors α_1 and α_2 are determined by the criteria that the maximum grid sizes, $\alpha_1\Delta\tilde{x}$ and $\alpha_2\Delta\tilde{y}$, will guarantee 8 sampling points per smallest wavelength in the formation. 10 grid points are used for PML. The absorption parameter, β_1 and β_2, are chosen to ensure the numerical reflections at the outer boundaries of the computational domain are less than 0.4% (80000 for low frequency excitation and 800000 for high frequency excitation). Figure 4-8 shows the mesh scheme of the borehole cross-section with an LWD tool at the center of the borehole. The monopole, dipole and quadrupole sources consist two or four point sources (figure 4-9). A dipole ring source that consists

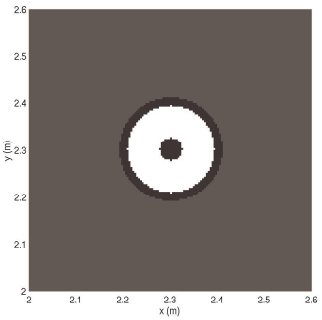

Figure 4-8: The mesh scheme of the borehole cross-section with a centered tool.

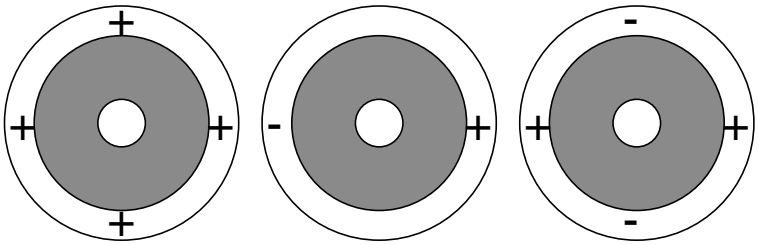

(a) monopole (b) dipole (c) quadrupole

Figure 4-9: A schematic diagram of a monopole, dipole and quadrupole source of LWD tool. It is made of two or four point sources. Plus and minus signs illustrate opposite phase.

of 72 point sources around a circle (figure 4-10) is also used. All point sources are placed inside the annulus, 5 mm away from the steel pipe. The source function is a Kelly wavelet (Stephen et al., 1985), shown in figure 4-11(a). Three center frequencies, 2 kHz, 8 kHz and 15 kHz, are chosen for the Kelly wavelet. Figure 4-11 shows source spectra.

4.4 Numerical Results

Numerical results are presented in the sequence of dipole, monopole and quadrupole logging with low frequency excitations, and dipole logging with high frequency excitation.

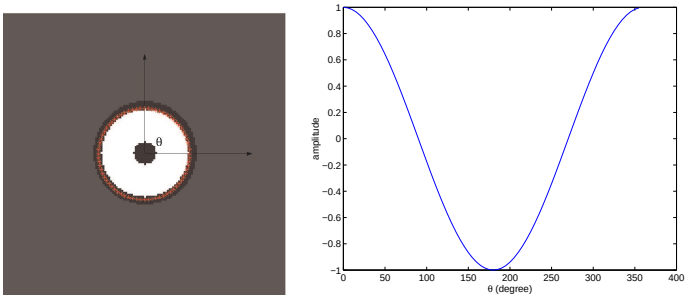

(a) ring source location

(b) ring source amplitude

Figure 4-10: The fluid-filled borehole cross-section with a dipole ring source. Each * represents a point source. The magnitude of each point source is proportional to $cos\theta$, and θ is the azimuthal angle with respect to the x axis.

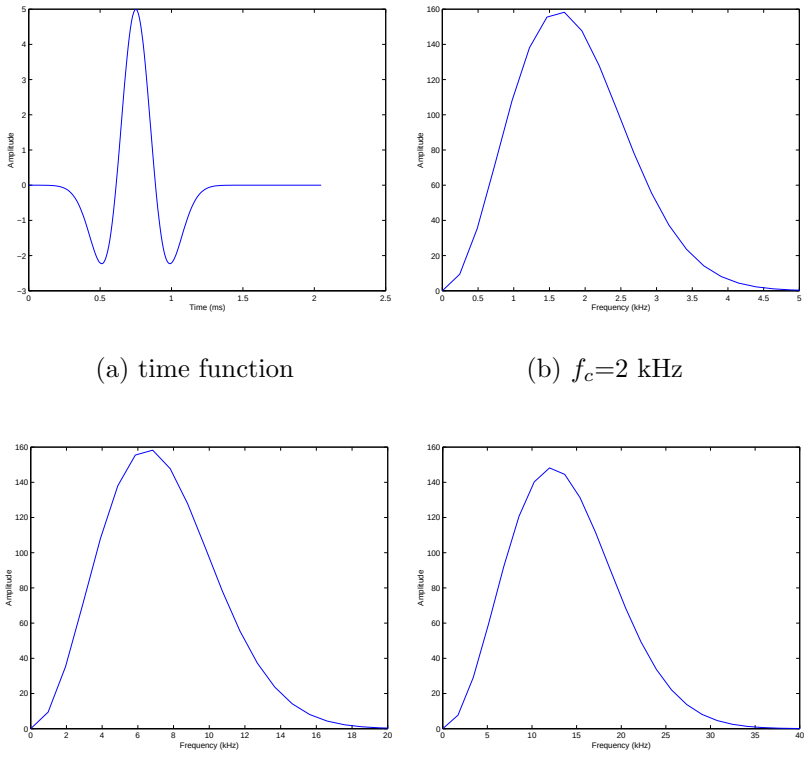

(a) time function

(b) f_c=2 kHz

(c) f_c=8 kHz

(d) f_c=15 kHz

Figure 4-11: Source time function and spectra with different center frequencies (f_c).

Figure 4-8 shows the zoomed in cross-section of the borehole model (x-y plane) and the numerical mesh. The annulus between the formation and the pipe is 17.3 mm. The smallest grid is chosen to be 4 mm. The grid stretching factor in both x and y direction is 10 for low frequency excitation and 1.5 for high frequency excitation.

Dipole Source (n=1)– Two Point Sources

Dispersion curves in figure 4-4 show that the borehole flexural mode and the tool flexural mode exchange dispersion properties at low frequencies, with the tool flexural asymptotes to formation shear velocity at low frequencies. So we fire the source at low frequency in the hope to excite a mode that propagates with a speed close to formation shear velocity.

Like a real LWD tool, two point sources are put in the fluid annulus at 0^o (front) and 180^o (back) with respect to the x axis and at z=0, to simulate a dipole source. The source is described in figure 4-9(b). In order to study azimuthal variations or modal orders, receivers are placed in the annulus at 8 axial (from $z_{\min}$=1.44876 m to $z_{\max}$=2.51724 m with dz=0.15264) and 10 azimuthal (θ=$0^o \sim 180^o$, $\Delta\theta$=20^o) positions. The model is perfectly axial symmetric about the x axis, and so is the wavefield.

Pressure waveforms are plotted in figures 4-12 by common θ gather. Amplitude in each individual figure is normalized by the maximum amplitude recorded at the first axial receivers with $\theta = 0^o$, 20^o, 40^o, 60^o and 80^o, respectively. For a pure dipole excitation, waveform pairs recorded at θ and $180^o + \theta$ should be identical to each other except 180^o shift in phase. Waveforms show that the dipole assumption holds quite well in this case.

In the real logging situation, dipole mode is obtained by subtracting the two out of phase waveforms recorded at $\theta = 0^o$ (front) and 180^o (back) receivers. Figure 4-13(a) and 4-13(b) shows the resulting waveforms and spectra. Energy span in the frequency domain is 0-5 kHz. The waveform shows there are three distinctive arrivals traveling roughly at 1600 m/s, 1200 m/s and 1000 m/s, respectively, each with different frequency content. Accurate velocity of each arrival is analyzed by semblance,

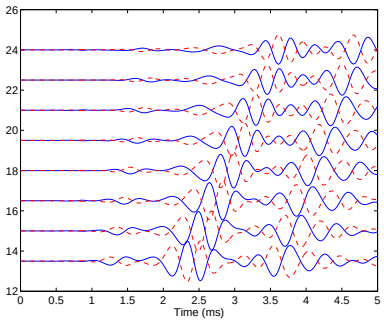

(a) $\theta = 0^o$ and 180^o

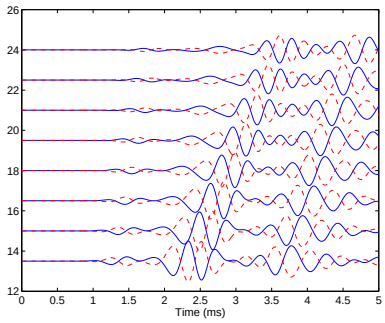

(b) $\theta = 20^o$ and 200^o

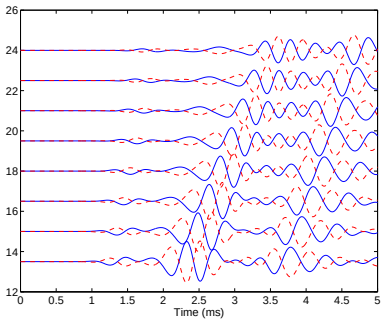

(c) $\theta = 40^o$ and 220^o

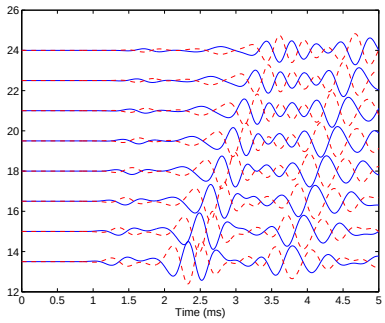

(d) $\theta = 60^o$ and 240^o

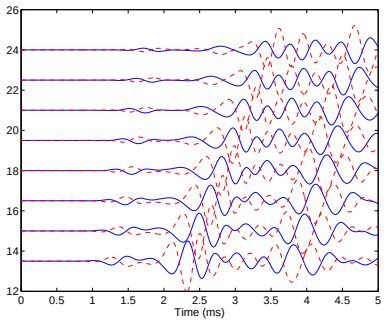

(e) $\theta = 80^o$ and $\theta = 260^o$

Figure 4-12: Dipole result. The center frequency is 2 kHz. Common θ gather of waveforms recorded at different axial positions (τ_{xx} component). Solid lines represent receivers at the $0^o \sim 90^o$ quadrant and the dash lines represent receivers at $180^o \sim 270^o$ quadrant. Waveforms at locations being 180^o apart show perfectly out of phase, indicating dipole characteristics.

a process that separates each arrivals in the velocity-time domain. Semblance was originally used for velocity estimation from seismic reflection data (Yilmaz, 1987). The underlining procedure includes two steps. First, assume a velocity and correct the travel time of waveforms at each receiver back to a reference receiver (the first one in this thesis) ; the second step is to stack across receivers. Figure 4-13(c) shows the normalized semblance energy. Velocities of the three arrivals are 1560 m/s, 1200 m/s and 990 m/s. In order to pinpoint each arrivals, the group and phase velocity curves of tool and borehole flexural modes in figure 4-5 are mapped to the semblance image. Time delay is obtained by dividing the source-receiver offset (1.44876 m) with the group velocity. The three arrivals are then identified as the tool mode arrival, the leaky shear arrival and the borehole flexural arrival. Both source and receivers are placed in the fluid, in other words, they are completely decoupled from the tool. So it is not surprising that the tool mode is weak. In reality, the source and receivers are mounted to the steel pipe with some attenuating materials to decouple them from the tool. Therefore, the numerical results presented here represent the results that one can expect with the ideal technical implementations.

The second arrival travels at the shear velocity and is known as leaky shear (Kurkjian, 1985). In the wireline case, leaky shear is so weak in soft formation that it is often times drowned out by noise or other arrivals. Dipole acoustic logging was developed to measure shear velocities using borehole flexural mode in soft formation because of that in the first place. The shear arrival in the LWD case is still weak, but much more observable. It may serve as a cross check for modal arrival based shear measurement.

Next, the dispersion curve is extracted from the waveform data so as to compare with the analytical solutions (Rao et al., 1999). One commonly used technique to accomplish this task is Prony's method (Lang et al., 1987). A disadvantage of this method is that it often generates spurious estimates (Ellefsen et al., 1993). We introduced a simple, yet efficient technique that does not suffer the disadvantage of Prony's method and is referred to as back-propagation method in this thesis (Nolte et al., 1997). The technique is outlined briefly in Appendix A.

The dispersion curve of the dipole waveform is shown in figure 4-13(d) and it is plotted against the analytical solution of the flexural mode. The extracted dispersion curve agrees with the analytical result very well, especially at 2.5-5 kHz.

Similar to real LWD source, the dipole source used in the above simulation consists two out of phase sources. The quality of a dipole source simulated by a two-point-source system is determined by $k\delta$, where k is the wavenumber in the borehole fluid and δ the distance between the two point sources, which is more than the outer diameter of the LWD tool. The smaller the $k\delta$ value is, the better the dipole quality is (Kurkjian and Chang, 1986). In the LWD case, $k\delta$ is at least twice larger than it is in the wireline case. When the dipole quality is low, borehole modes with other azimuthal orders will be excited. A pure dipole excitation means that at any time, amplitude of the wave field at angle θ is proportional to $cos\theta$. Figure 4-14(a) shows the recorded waveforms (at $z = z_{\min}$) in the θ domain, with each line representing one time sample. Figure 4-14(b) shows the same figure, except amplitude at each time step is normalized by the maximum amplitude along the azimuthal direction, and the line width is proportional to the normalization factor. The dashed lines are what it should be for a pure dipole excitation. Now it can be seen that the dipole excitation is not pure and other modes must have been excited.

Although in the above case, the dipole mode is efficiently obtained by subtracting waveforms received at 0^o and 180^o from each other, evidenced by both the dispersion curve (figure 4-13(d)) and opposite phase waveform pairs (figure 4-12), quantifying multipole excitations may help estimate signal to noise ratio, with the noise being non-dipole modes here. To accomplish that, wave field is decomposed into the cylindrical coordinates. For the pressure component p(r, θ, z, t) inside the annulus, a complete decomposition is

$$p(r,\theta,z,t) = \int_{-\infty}^{\infty} S(\omega) \sum_{n=0}^{\infty} [A_n Z_n(k_r^{(f)} r) + B_n W_n(k_r^{(f)} r)] cos[n(\theta - \theta_0)] e^{i(\omega t - k_z z)} dk_z d\omega \tag{4.1}$$

where k_z and $k_r^{(f)}$ are the axial and radial component of the total fluid wavenumber k_f, and $k_f^2 = \omega^2/v_f^2 = k_z^2 + k_r^{(f)^2}$. ω is the angular frequency and v_f the fluid compressional

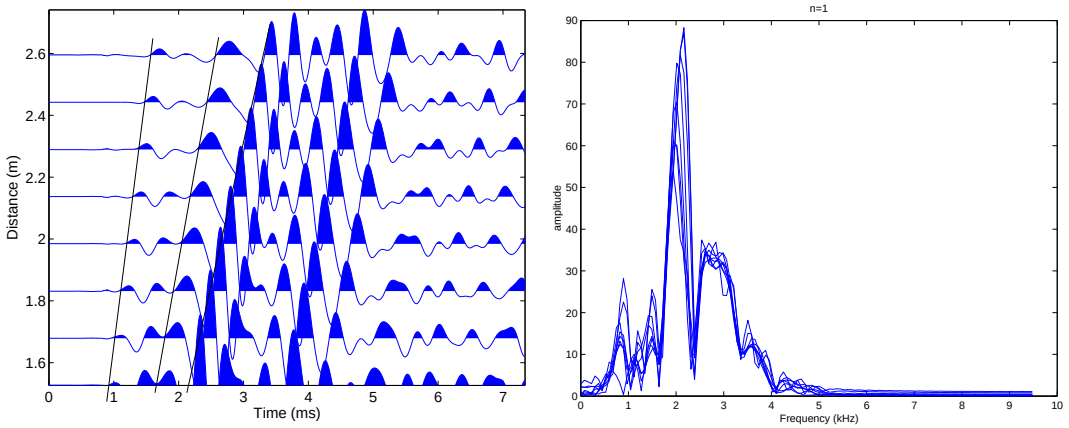

(a) Waveform

(b) Spectra

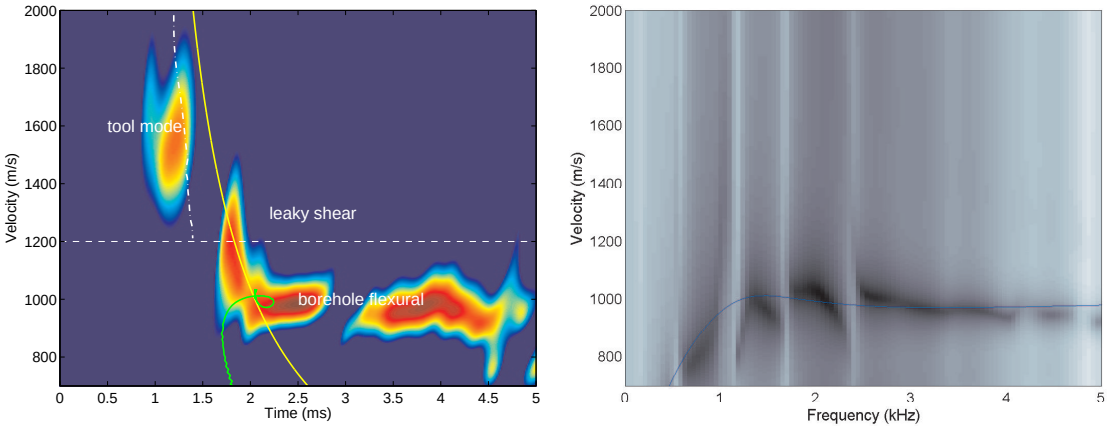

(c) Semblance

(d) Dispersion

Figure 4-13: Dipole results. Source center frequency is 2 kHz. There are three distinctive arrivals (from fast to slow): Tool flexural mode, leaky shear arrival and borehole flexural mode.

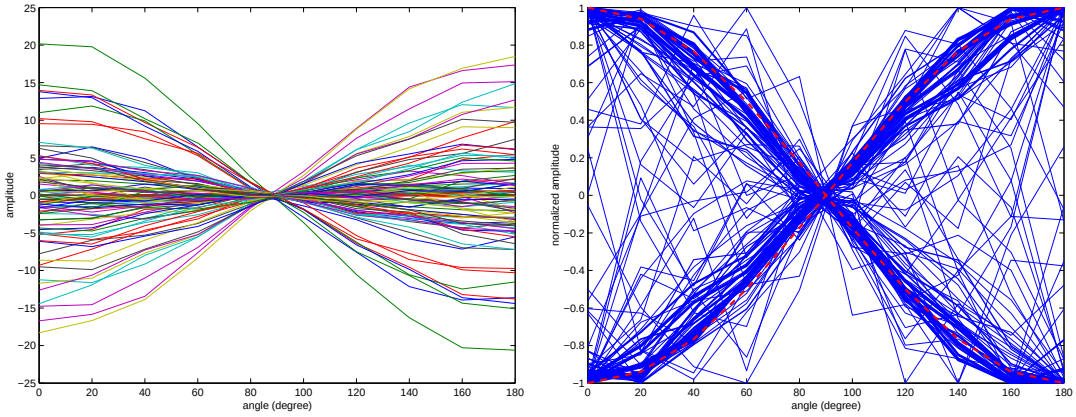

(a) original (b) normalized

Figure 4-14: Waveforms plotted in the θ domain, with each line representing one time sample. a. original waveform; b. amplitude at each time step is normalized by the maximum amplitude along the azimuthal direction, and the line width is proportional to the normalization factor. The dipole characteristic holds in general. The lines that not fall on the $|cos\theta|$ curve are of lower amplitudes.

velocity. θ_0 is the source orientation. In our case, it is zero. Z_n and W_n denote the Bessel and Hankel functions. $S(\omega)$ is the source spectrum. The amplitude of the n-th order mode that is excited in the simulation can be be computed from the waveforms received at the same axial and radial location,

$$p_n(z,t) = \int_{\theta=0}^{2\pi} p(r_0,\theta,z,t)cos(n\theta)d\theta \tag{4.2}$$

We use summation instead of integration as we only have discretized data samples along the azimuthal direction. For an azimuthal resolution of 20^o, the highest mode order that can be estimated without aliasing is n=9. Figure 4-15(a) and 4-15(b) shows the energy of decomposed modes in the time and frequency domain for receivers at $z_{\min}$. Integration over time or frequency for each mode can provide the total energy of the mode. The energy allocation between different modes for all 8 axial locations is shown in figure 4-15(c). It is clear that multipole modes are generated, while the good news is that, the dipole mode is more than 1 order of magnitude larger than

even modes (n=even number), more than 2 orders of magnitude larger than n=0 mode (primarily Stoneley wave), and more than 4 orders of magnitude larger than odd modes (n=odd number). Decomposing waveforms received at all 80 locations (10 azimuthal and 8 axial) into dipole mode (n=1) and conducting the semblance and dispersion analysis, results are the same to those in which waveforms are taken from the receivers at 0^o only or obtained by subtracting two out of phase waveforms. It is then proved that at the frequency range of 0-5 kHz, two out of phase point sources do produce dipole mode with so little contamination from other order modes that neither the semblance nor the dispersion analysis is affected.

Dipole Source – Ring Source

As the dipole mode is proportional to $cos\theta$, it is natural to think of using a ring source with the amplitude also proportional to $cos\theta$ to further suppress other non-dipole modes. A dipole ring source is simulated by 72 point sources around a circle (figure 4-10), with each source magnitude proportional to $cos\theta$. The energy allocation between different modes for all 8 axial locations is shown in figure 4-16. Compared to the two-point-source case 4-15(c), it is clear that non-dipole modes are further suppressed by at least 1 order of magnitude, except for the Stoneley mode. On the other hand, waveforms, semblance and dispersion analysis of the dipole mode (n=1) show results similar to those obtained with two point sources, further indicating that the two-point-source simulates a dipole source very efficiently at low frequencies (0-5 kHz).

Monopole Source (n=0)– Four Point Sources

Four point sources with the same phase are used to mimic a monopole source (figure 4-9(a)). In order to increase the number of azimuthal orders that can be resolved from received waveforms, a dense azimuthal sampling is applied. From $0^o \sim 180^o$, receivers spacing is 2^o, which leads to a total of 728 receivers at all 8 axial locations. The maximum order that can be resolved with this sampling rate is 91.

Figure 4-17(a) and 4-17(b) shows the energy of decomposed modes in the time

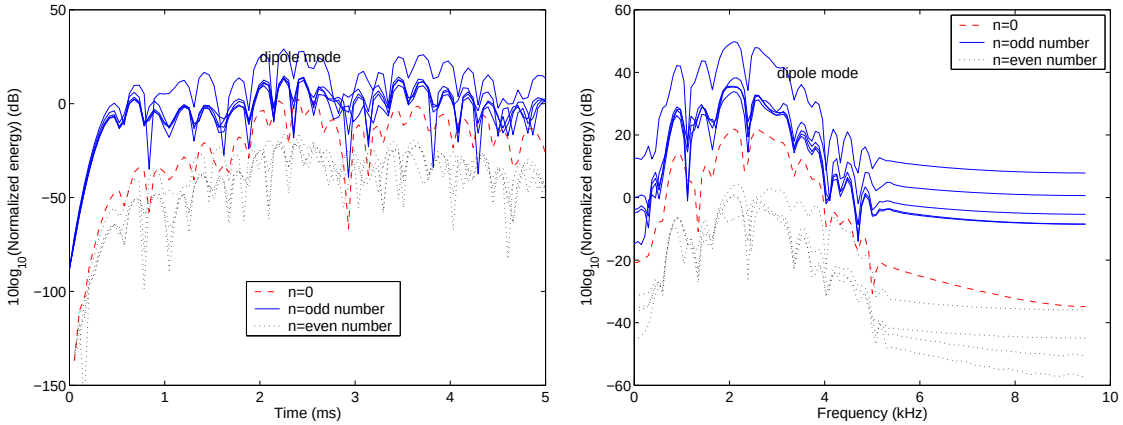

(a) time domain

(b) frequency domain

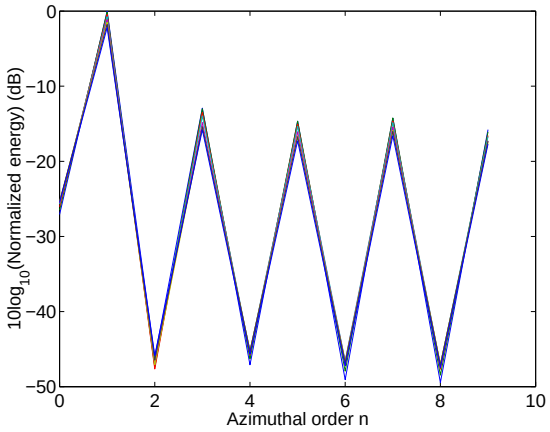

(c) azimuthal order domain

Figure 4-15: Multipole energy at each time step, frequency and azimuthal order, for a dipole source in the borehole with the LWD tool. Source center frequency is 2 kHz. Note that the odd modes are preferentially excited by the dipole source (as expected), with the dipole component (n=1) being the strongest. The next strongest mode n=3 is more than 10 dB lower. Figure a and b show results at the first receiver only. Figure c shows results at all 8 receivers and energy allocation for various modes is very consistent across the receiver array.

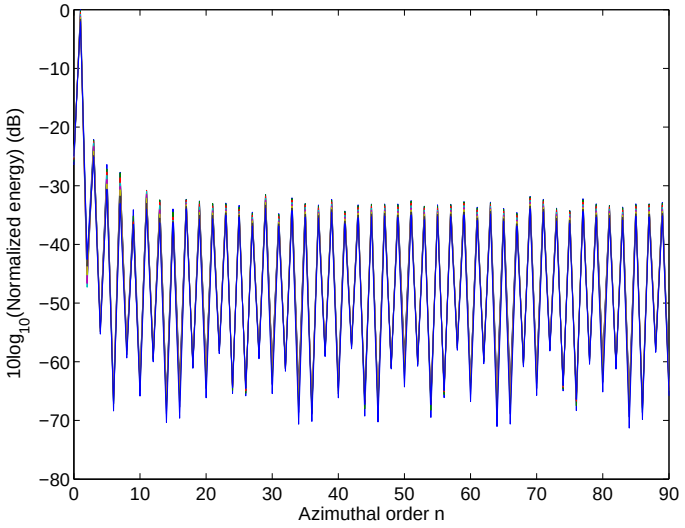

Figure 4-16: Ring source results. Energy allocation between multipole modes at all 8 axial locations. Comparing to the two-point-source case 4-15(c), non-dipole modes are further suppressed by at least 1 order of magnitude, except the Stoneley mode.

and frequency domain for receivers at $z_{\min}$. The energy allocation between different modes for all 8 axial locations is shown in figure 4-17(c). The magnitude of monopole (n=0) mode is more than 2 orders higher than any other modes, indicating that the four point sources excite the monopole mode quite efficiently. In other words, contamination from other modes is very low. Summing up waveforms received at 0^o, 90^o, 180^o and 270^o is normally the practice in real LWD logging. Figure 4-18(a) and 4-18(b) shows the monopole waveforms and their spectra across 8 axial locations. Same waveforms are plotted again in figure 4-19 with early arrivals amplified. Semblance and dispersion analysis results are plotted in figure 4-18(c), and 4-18(d). There are clearly three arrivals: 3000 m/s at around 1 ms, 1200 m/s at around 1.5 ms and 950 m/s at 1.6 ms, corresponding to formation compressional, shear and borehole Stoneley mode. Dispersion of Stoneley mode agrees with analytical solution very well.

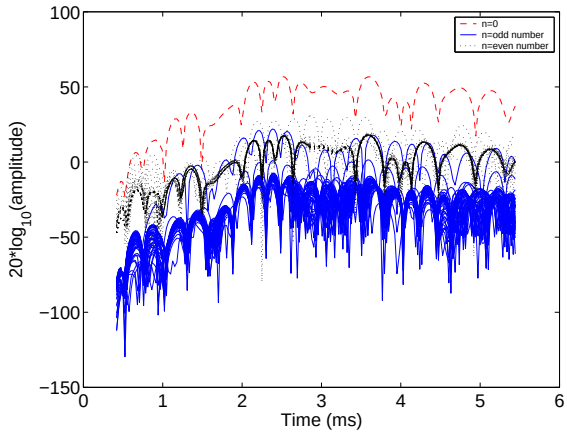

(a) time domain

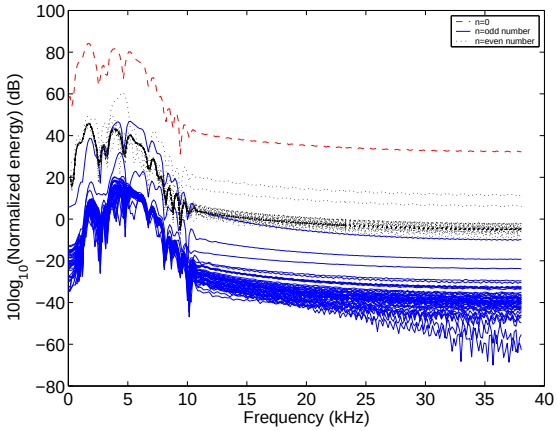

(b) frequency domain

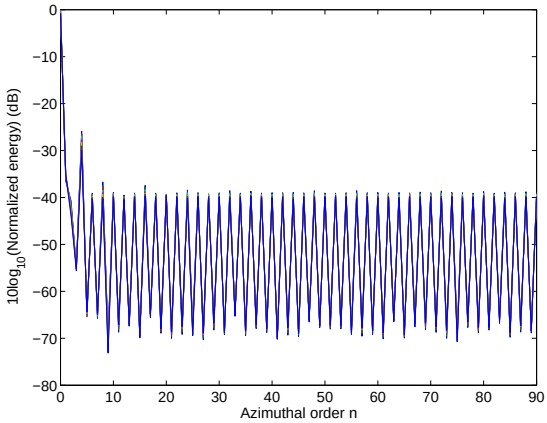

(c) frequency domain

Figure 4-17: Multipole energy at each time step, frequency and azimuthal order, for a monopole source in the borehole with the LWD tool. Source center frequency is 2 kHz. Note that the magnitude of monopole (n=0) mode is more than 2 orders higher than any other modes, indicating that the four point sources excite the monopole mode quite efficiently: contamination from other modes is low.

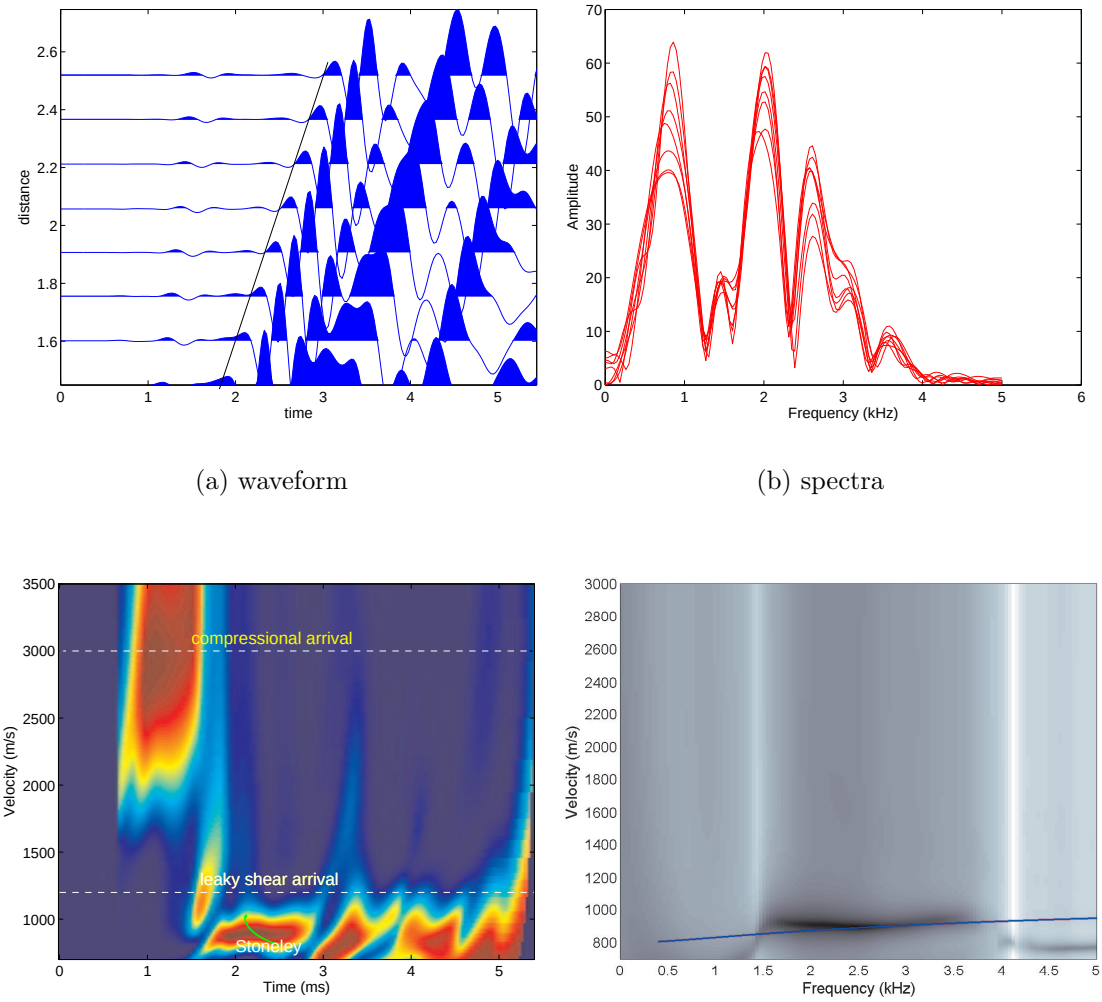

(a) waveform

(b) spectra

(c) semblance

(d) dispersion

Figure 4-18: Monopole results. Waveforms are obtained by adding four receiver arrays at 0^o, 90^o, 180^o and 270^o. Source center frequency is 2 kHz. Large amplitude corresponds to Stoneley mode, which has a signature dispersion behavior: faster at higher frequencies and lower at low frequencies. Formation compressional (3000 m/s), shear (1200 m/s) and borehole Stoneley mode (950 m/s) are observed.

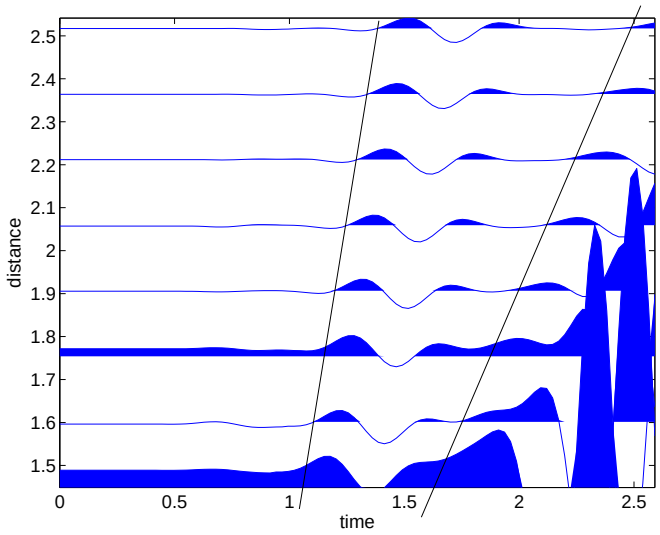

Figure 4-19: Monopole waveforms (same as figure 4-18(a), except arrivals before the Stoneley mode are amplified). Formation compressional and shear arrivals are observed around 1 ms and 1.5 ms.

Quadrupole Source (n=2)– Four Point Sources

Frequency analysis (figure 4-6) predicts that the phase velocity of borehole quadrupole mode approaches to the formation shear at the cut-off frequency. Tang et al. (2002) reported measuring formation shear velocities using a quadrupole ring source. Here the quadrupole is simulated by four point sources (figure 4-9(c)).

Figures 4-20(a) and 4-20(b) show the energy of decomposed modes in the time and frequency domain for receivers at $z_{\min}$. The energy allocation between different modes for all 8 axial locations is shown in figure 4-20(c). The magnitude of quadrupole (n=2) mode is more than 2 orders higher than any other modes, indicating that the four point sources excite the quadrupole mode quite efficiently.

As the model is completely axi-symmetric, waveforms at any two positions with 180^o apart should be exactly the same. Figure 4-21(a) shows the quadrupole waveforms at 0^o and 180^o, confirming the axi-symmetric prediction. Spectra of the waveforms at 0^o is plotted in figure 4-21(b). Their semblance and dispersion analysis results are plotted in figure 4-21(c), and 4-21(d). The quadrupole mode arrives around 1.8

ms. Its phase velocity is close to the formation shear velocity (1200 m/s) at low frequencies, and becomes slower at higher frequencies. Dispersion analysis shows good agreement with theory.

4.4.1 Centered Tool with High Frequency Dipole Source

Figure 4-4 shows at higher frequencies, borehole flexural mode is well separated from the tool flexural. The phase velocity of the borehole flexural mode is about 20% slower than the formation shear. In the current practice, formation shear velocity is computed from borehole flexural velocity using the theoretical dispersion relation. The theoretical dispersion relation of the borehole flexural mode can be completely determined by formation shear, formation compressional, fluid compressional, fluid density, formation density and borehole radius. All informations except formation shear can be obtained from other measurements. As the borehole flexural mode is less dispersive above 8 kHz, the dipole LWD tool is simulated to operate at two higher frequencies: 8 kHz and 15 kHz.

Two out of phase sources are placed at 0^o and 180^o like the low frequency firing case, except now the center frequency of the source is 15 kHz. The frequency band is 0-30 kHz. Compared to previous calculation, the center frequency is increased by more than 7 times. So is $k\delta$. Non-dipole excitation should be more serious. Therefore, energy allocation between multipole modes is investigated first (figure 4-22(c), 4-22(a) and 4-22(b)). Not surprisingly this time, the energy of dipole mode is only 5 dB higher than other odd modes. As major wave energy has not arrived at the last 6 receivers yet (figure 4-23(a)), waveforms at those receivers have significantly lower energy. Thus waveforms at the first 10 axial locations are used in the precessing.

Figure 4-23(a) shows the dipole waveforms obtained by subtracting waveforms received at 180^o from those received at 0^o (current LWD dipole logging practice). Tool mode is weaker than it is in the low frequency case, and it is well ahead of the borehole flexural mode. Figure 4-23(b) shows the spectra of the dipole mode.

Figure 4-23(c) shows semblance results of dipole waveforms. The direct shear is too weak to be visible at this frequency range. Extracted dispersion of the subtracted

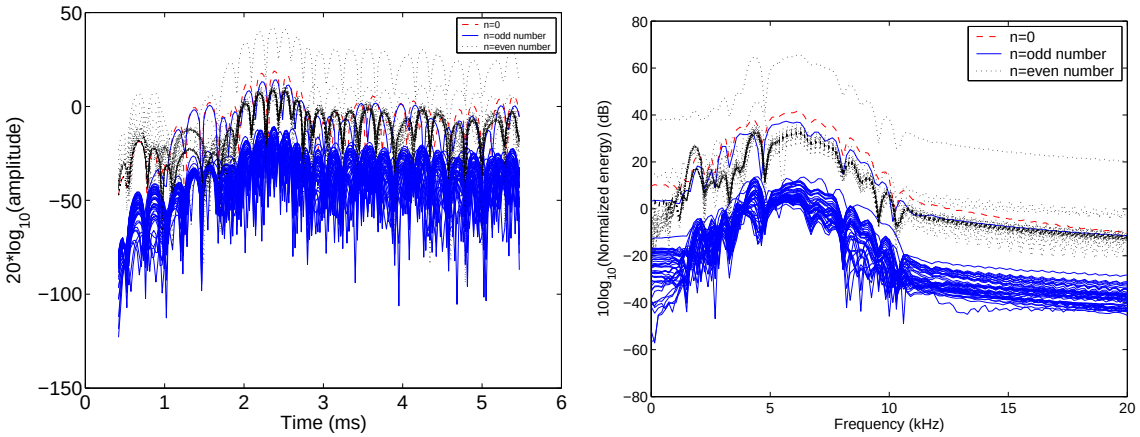

(a) time domain

(b) frequency domain

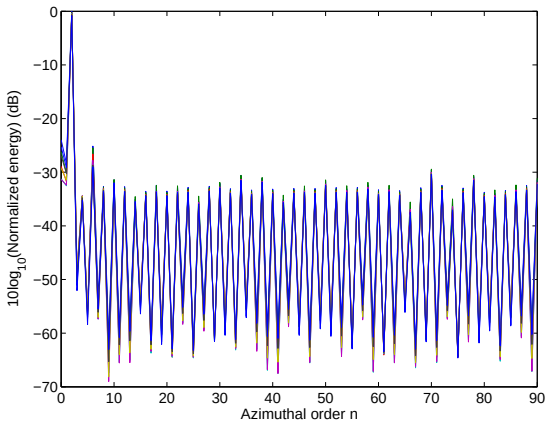

(c) azimuthal order domain

Figure 4-20: Multipole energy at each time step, frequency and azimuthal order, for a quadrupole source in the borehole with the LWD tool. Source center frequency is 2 kHz. Note that the magnitude of quadrupole (n=2) mode is more than 2 orders higher than any other modes, indicating that the four point sources excite the quadrupole mode quite efficiently.

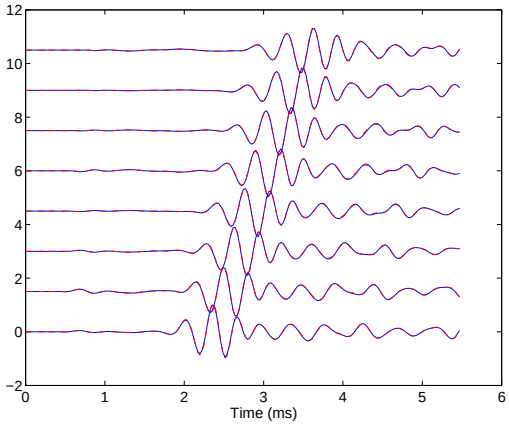

(a) waveform

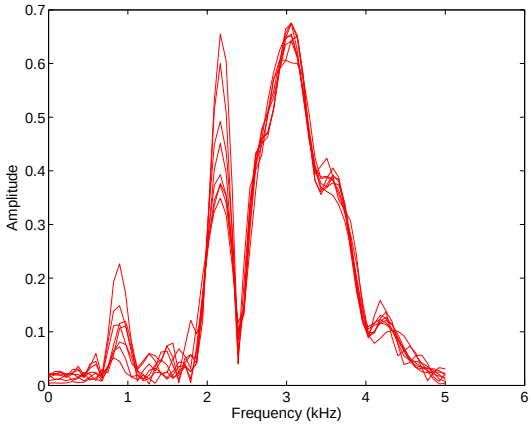

(b) spectra

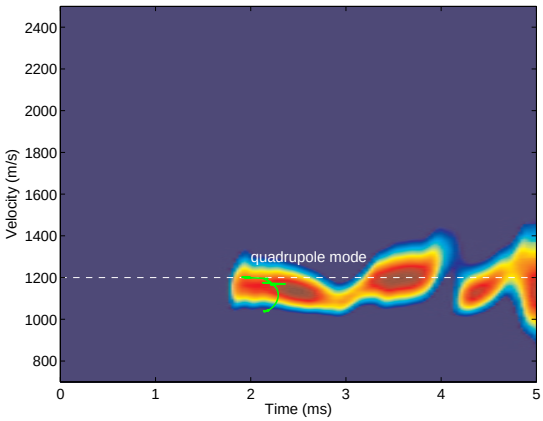

(c) semblance

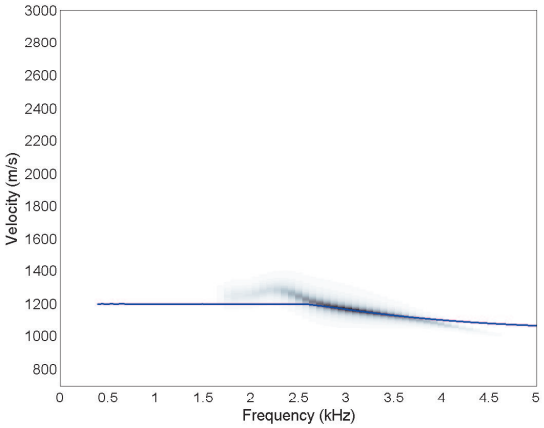

(d) dispersion

Figure 4-21: Quadrupole results. The source center frequency is 2 kHz. Waveforms are obtained by adding receiver arrays at 0^o and 180^o and subtracting receiver arrays at 90^o and 270^o. The quadrupole mode travels at the formation shear velocity at early times, and becomes slower later due to its dispersive behavior.

waveforms shows good agreement with analytical results. Note that at high frequency excitation, the dominant mode (figure 4-23(c) and 4-24) between 800 m/s to 1200 m/s is n=3, with velocity higher than the borehole flexural mode. Note that the theoretical dispersion curve of n=3 mode is above the formation shear at the frequency range of 2.5-6 kHz. At those frequencies, the n=3 is highly leaky. That is clearly shown in the dispersion analysis in figure 4-23(d) and 4-25. The borehole flexural mode is excited in the frequency range of 2.5-6 kHz, corresponding to the first peak in the spectra (figure 4-23(b)). If n=3 mode is taken as the borehole flexural mode, the estimated formation shear velocity will be higher than the actual one. As time domain semblance do not provide frequency dependence directly, it is important to conduct both time domain semblance and frequency dispersion analysis to identity modal arrivals.

When the center frequency is 15 kHz, the borehole flexural responded at lower frequencies (2.5-6 kHz), indicating an inefficient excitation. To make the result even less desirable, higher mode (n=3) is excited which could potentially add complications in data interpretation.

Next we reduce the source frequency to 8 kHz. Results show that although there are some n=3 energy in the dispersion analysis, most coherent semblance energy belongs to the borehole flexural mode. The tool mode remains weak and well separated from the borehole flexural mode. The leaky shear is not observable.

4.4.2 Leaky Shear Arrival

Direct shear arrival is observed in both the monopole and dipole case. It is stronger at low frequencies, consistent with wireline observations (Kurkjian, 1985). While shear arrival in soft formation is too weak in the wireline situation to provide little help in measuring shear velocity, it certainly is strong enough in the LWD to serve as a cross check for modal based measurements, due to the fact that the source and receivers are close to the formation. A numerical experiment is conducted in a two half space fluid-solid model to confirm that direct shear is observable in slow formation (Appendix B).

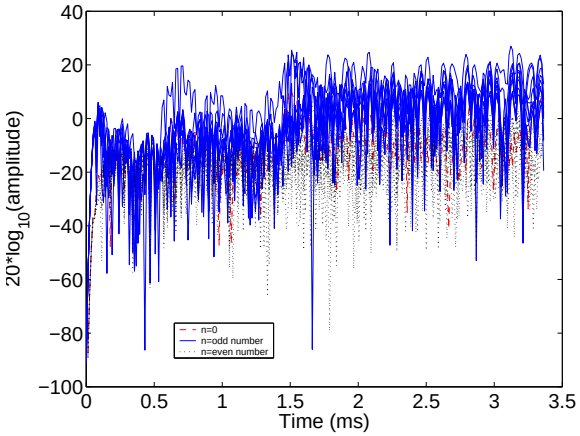

(a) time domain

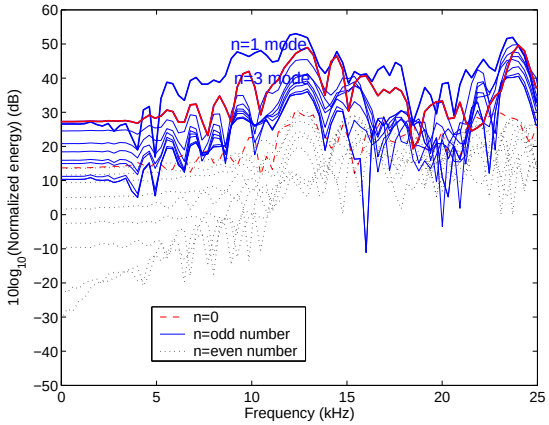

(b) frequency domain

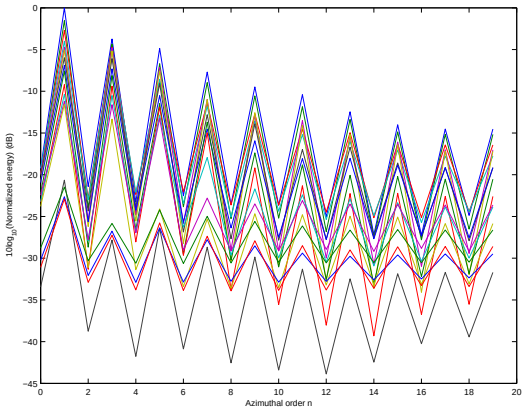

(c) azimuthal order domain

Figure 4-22: Multipole energy at each time step, frequency and azimuthal order, for a dipole source in the borehole with the LWD tool. Source center frequency is 15 kHz. The magnitude of dipole (n=0) mode is 3dB or less higher than n=3 mode, therefore higher modes are likely to be excited. As major wave energy has not arrived at the last 6 receivers yet (figure 4-23(a)), waveforms at those receivers have significantly lower energy in figure (c). Thus waveforms at the first 10 axial locations are used in the precessing.

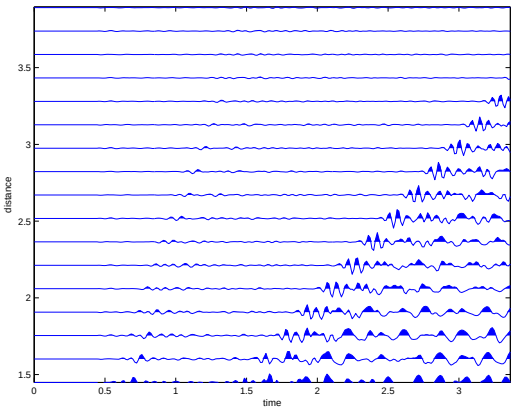

(a) waveforms

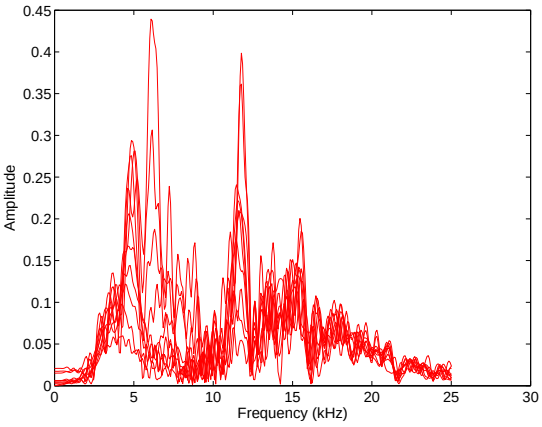

(b) spectra

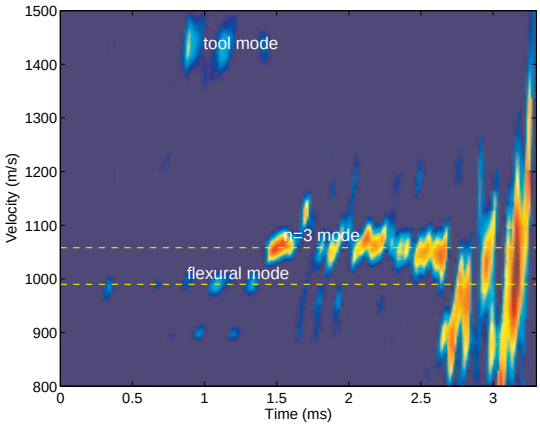

(c) semblance

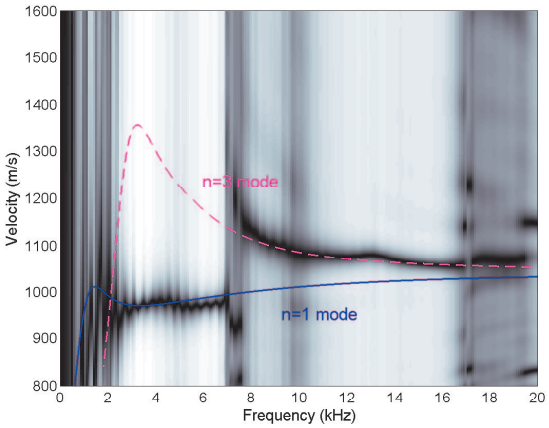

(d) dispersion

Figure 4-23: Dipole results. The source center frequency is 15 kHz. Dipole waveforms are obtained by subtracting those at 180^o from those at 0^o. The tool mode is faster and weaker than the low frequency case. Both n=1 and n=3 modes are excited. n=3 mode shows better coherence in semblance. Note both in the spectra and the dispersion that the borehole dipole mode is excited at 2.5-6 kHz, though the source center frequency is 15 kHz.

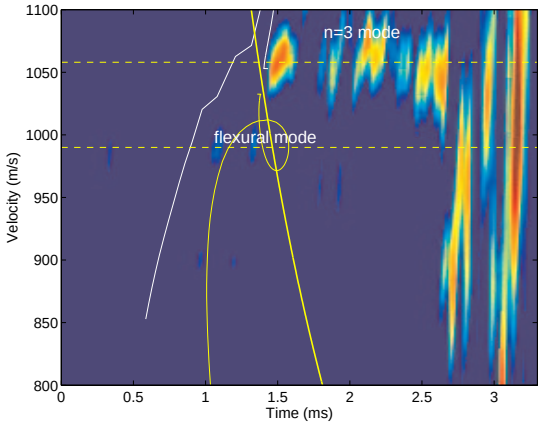

Figure 4-24: A close look of figure 4-23(c).

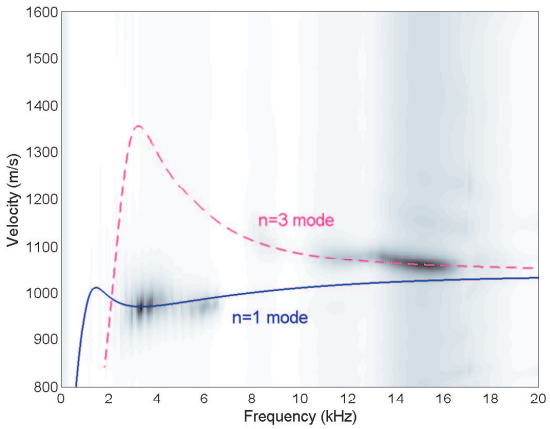

Figure 4-25: The non-normalized version of figure 4-23(d). The borehole flexural mode is mainly at 2.5-6 kHz.

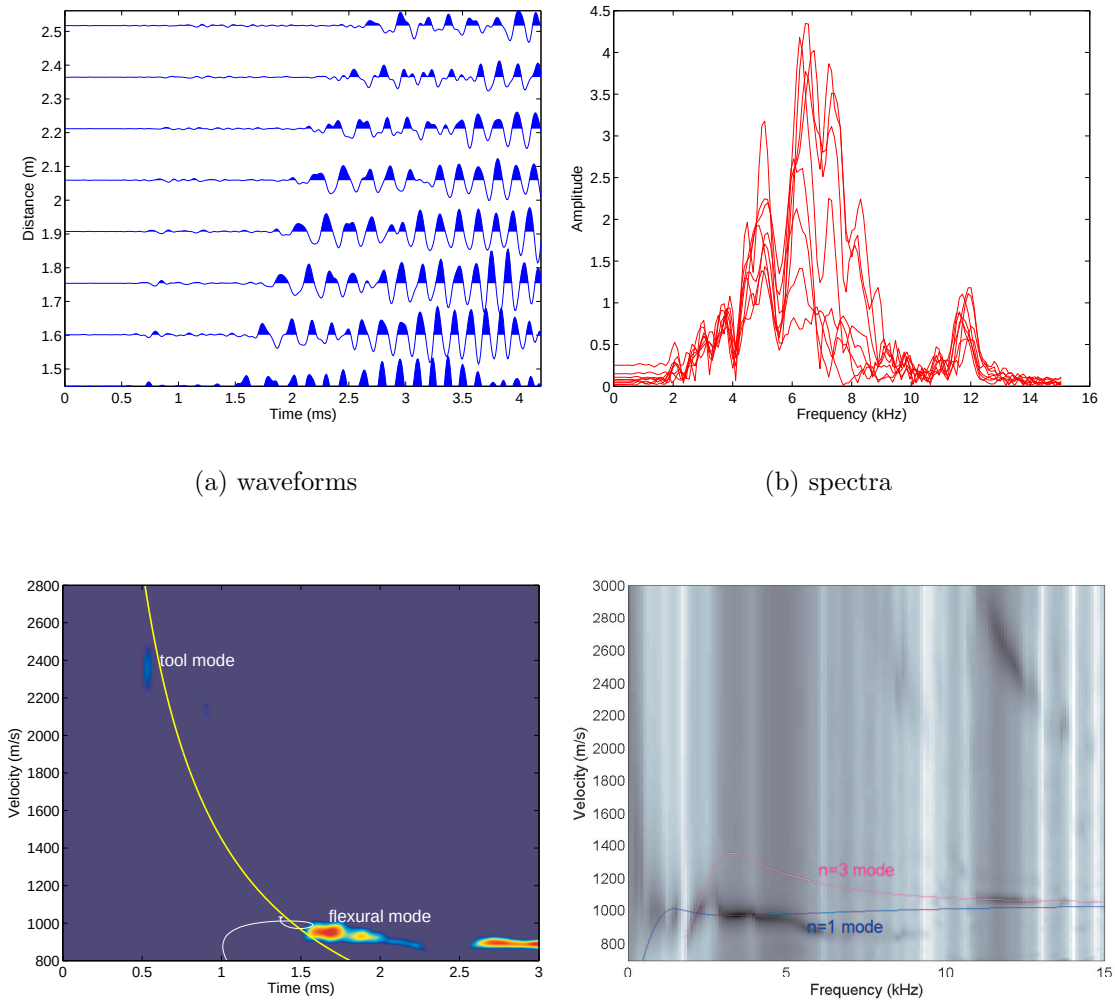

(a) waveforms

(b) spectra

(c) semblance

(d) dispersion

Figure 4-26: Dipole results. The source center frequency is 8 kHz. Dipole waveforms are obtained by subtracting those at 180^o from those at 0^o. The tool mode is faster and weaker than the low frequency case. Both n=1 and n=3 modes are excited. n=1 mode shows better coherence in semblance. n=3 mode is almost not observable in semblance.

4.5 Conclusion

Up to now, characteristics of wave propagations along a fluid-filled borehole in soft formation with a centered LWD tool have been investigated for monopole, dipole and quadrupole sources.

Wireline monopole tools usually operate at high frequencies (around 15 kHz) to obtain formation compressional velocities (Winbow, 1988; Kurkjian, 1985). This study shows that in soft formation, compressional velocity can be logged at low frequencies (0-5 kHz) with LWD tool. In addition, a coherent shear arrival is also observed which can serve as a cross-check for other type of shear measurements, such as wireline dipole logging. The dispersion curves extracted from waveforms agrees with eigenvalue based solution very well at frequencies above 2.5 kHz.

Particular attention is paid to the LWD dipole logging, because dipole logging has been used to measure formation shear velocities in the wireline case for many years. The dipole LWD tool is simulated to operate at three center frequencies: 2 kHz, 8 kHz and 15 kHz. The tool flexural mode is weak in all three cases with the receivers in the fluid annulus. As borehole flexural mode is sensitive to formation shear velocity, measurements of borehole flexural speed can be compensated to the formation shear velocity using the analytical dispersion curve. Good agreement between the numerical and analytical results in all three cases provides confidence in this type of data interpretation. Waveforms at three frequency range show different characteristics. At low frequencies (source center frequency is 2 kHz), a direct shear arrival comes between the weak tool flexural mode and the strong borehole flexural mode, a pattern that can be used to identify borehole flexural mode. At intermediate frequencies (source center frequency is 8 kHz), the direct shear arrival is weak. The tool mode has much higher phase velocity than the borehole flexural mode, so it is well separated from the borehole flexural mode. Compared with the low frequency case, the flexural mode is less dispersive, thus its velocity is more accurately determined. At even high frequencies (source center frequency is 15 kHz), although tool mode remains weak and well separated from borehole modes, higher borehole mode

(n=3) is excited and has better coherence in the semblance image than the flexural mode. Dispersion analysis is then necessary to identify each excited borehole mode. In all three cases, frequency responses of the borehole flexural mode are all at 2-6 kHz. Therefore, operating at lower frequencies is more efficient. Considering both excitation efficiency and the accuracy of velocity analysis, the intermediate frequency range (3 - 8 kHz) is a good choice.

Quadrupole mode asymptotically approaches formation shear velocity at low frequencies, which may serve as a good candidate to measurement formation shear.

Dipole, monopole and quadrupole excitations are efficiently achieved by two out of phase point sources, four identical point sources and four point sources with alternate phases at low frequencies where $k\delta$ is small. At higher frequencies (source center frequency around 8 kHz and 15 kHz), non-dipole modes are excited with relatively higher energy with the two out of phase point sources, now that $k\delta$ is more than 4 or 7 times larger than that of the low frequency case. The dipole mode is only less than 3 dB higher than the next highest mode (n=3), compared with 15 dB in the low frequency case. Those modes affect the quality of velocity analysis. To identify them, frequency domain dispersion analysis is essential.

Chapter 5

Wave Propagation Studies on Acoustic Logging While Drilling Eccentric Tool

Abstract

Effects of eccentric LWD tool on borehole acoustic measurements are investigated using the stretched grid finite difference algorithm (chapter 2 and 3). Monopole, dipole and quadrupole tools are discussed. Eccentric tool generates multipole modes and strong circumferential motions. Appropriate data processing may reduce or eliminate effects of tool eccentricity on the borehole flexural or quadrupole mode. In the dipole logging, for waveforms received at the side where the fluid annulus is the largest, the coupling between the tool flexural mode and the borehole flexural mode is weaker than that in the centered tool case. The phase velocity of the borehole flexural mode is consequently closer to the formation shear velocity at low frequencies, especially when the tool is extremely off-centered. In the monopole case, dipole mode is strong. The direct shear and compressional remain observable in the semblance domain. In the quadrupole case, dipole mode is also strong. The current practice of combining waveforms at four azimuthal locations is necessary to bring up the quadrupole mode.

For the dipole logging at high frequencies (source center frequency of 8 kHz), higher modes (n=2 and 3) are excited. Phase velocities of those multipole modes differ only by several percent, thus identifying the right mode is crucial to measure the shear velocity correctly.

5.1 Introduction

In most studies it is assumed that the LWD tool is at the center of the fluid-filled borehole Rao et al. (1999); Tang et al. (2002). In real LWD situations, however, the tool may be off-centered. With off-centered tool, borehole modes are expected to be different. It is therefore important to understand effects of tool eccentricity on LWD measurements for data interpretation purpose.

The cross-section of the borehole and the tool is shown in figure 5-1. All sources and receivers are shifted together with the tool, or in another word, they do not move relative to the tool. The source center frequency is chosen to be 2 kHz for monopole, dipole and quadrupole sources. For dipole logging, high frequency operation (source center frequency of 8 kHz) is also investigated. Formation and tool properties remain the same as in the centered tool case (Table 4.1).

5.2 Low Frequency Source

5.2.1 Dipole Source – Off Center by 6.3 mm

The center of the tool can be anywhere inside the borehole. The discussion starts with a model of slightly off-centered tool. The tool center is shifted to the negative x direction by 6.3 mm. The resulting fluid annulus is 23.3 mm at 0^o, the largest one, and is labeled with LA. The smallest fluid annulus is 10.7 mm, at 180^o side and labeled with SA. The wave field remains axi-symmetric with respect to x axis. Figure 5-2 and 5-3 shows waveforms received by groups of receivers at various azimuthal locations plotted with common angle gather. The waveforms show motions with opposite phase at most receiver positions 180^o apart, attesting to the dipole characteristics of the

wavefield. This is also evidenced by the wavefield (τ_{xx} component) snapshot at 2.3 ms (figure 5-4).

Waveforms at 0^o (large annulus side), 90^0, 180^o (small annulus side) and those obtained by subtraction waveforms between 0^0 and 180^o are shown in figure 5-5. They are denoted with R_0, R_{90}, R_{180} and $R_0 - R_{180}$. The amplitude of R_{180} is 5 times that of R_0. The tool mode is barely visible in all waveforms. The shear arrival is clearly observed in R_0 and $R_0 - R_{180}$. The borehole flexural mode is the slowest one and the strongest. Studies show that leaky shear is weak (Kurkjian, 1985), the relatively large amplitude in R_0 indicates that shear arrival is due to the trapped mode pole in the vicinity of the practical cutoff, *i.e.*, the phase velocity of borehole flexural approaches the formation shear velocity at low frequencies. The shear arrival in R_{180} is weak, implying a leaky mode. Semblance results of each set of waveforms are shown in figure 5-6. It is clearly shown that the aforementioned three modes exist in all waveforms. As the amplitude of R_{180} is stronger, it is not surprising that the semblance of $R_0 - R_{180}$ resembles more that of R_{180}. Compared to the semblance result of the centered-tool case, tool eccentricity causes the flexural arrival in subtracted waveforms to be slightly dispersive (1.9-2.9 ms, figure 5-6(d)), which may slightly reduce the measurement resolution of the flexural velocity thus the formation shear velocity. However, applying a simple window to cut out semblance energy above 2.3 ms, the resulting shear measurement is little affected by tool eccentricity.

Figure 5-7 shows the same waveforms but in the common z gather. As the azimuthal distribution of pressure field becomes asymmetric, significant energy propagates circumferentially from 180^o, the smaller annulus side to 0^o, the larger annulus side, as the wave field propagates along the borehole axis. This indicates a strong torsional mode. It is more clearly shown in the particle velocity plot (figure 5-8), where strong azimuthal component is observed at angles roughly perpendicularly to the dipole polarization, the interface between the positive and negative pressure field. It can be clearly seen by visualizing the particle motions that at every axial location z, disturbance starts at both 0^o and 180^o, and it is stronger at 180^o. Then a pure circumferential motion follows to mix the uneven disturbance around the borehole

before the radial motion finally kicks in. As long as the borehole fluid is inviscid, as it is assumed in the FDTD computation, there should be no coupling between the tool and borehole through circumferential motion. The coupling mostly happens through radial motions. Borehole flexural mode (dipole) couples with tool flexural mode because they have strong radial motion components.

The existence of the circumferential motion reduces the unevenness around the borehole, it can be predicted that the off-centered tool has little effect on the Schölte fluid-solid interface velocity, thus the higher frequency portion of the borehole flexural mode. Same argument holds for the tool flexural at higher frequencies. At low frequencies on the other hand, the radial motion is stronger at the side where the source is closer to the borehole, and stronger coupling between the borehole flexural and tool flexural is expected than it is in the centered tool situation.

Extracting dispersion curves from the waveforms may reveal more physical information about the waveform characteristics with an off-centered tool. Figure 5-10 and 5-9 shows theoretical dispersion curves of borehole flexural mode with a centered LWD tool when the fluid annulus equals to 10.7 mm and 23.3 mm, in accordance with the smallest and the largest annulus in the off-centered case. The annulus is changed either by reducing (enlarging) the borehole size or by enlarging (reducing) the outer diameter of the steel pipe. Increase in the fluid annulus reduces the coupling between the tool flexural mode and the borehole flexural mode. Therefore the resulting borehole flexural dispersion is closer to that without the tool. A decrease in the fluid annulus enhances the coupling between the tool flexural mode and borehole flexural mode. The resulting borehole flexural dispersion has lower phase velocity at low frequencies where the coupling is the strongest.

Dispersion curves exacted from the four set of waveforms are shown in figure 5-11. Spectra of waveforms are shown in figure 5-12. Dispersion curves at frequencies where the spectra are of low energy or coherence should be read with caution. At 0^o where the fluid annulus is the largest, the extracted dispersion curve is plotted against two theoretical curves. Those curves are computed by assuming a centered tool, one of which uses the original borehole size, and the other uses a bigger borehole

size so that the fluid annulus equals 23.3 mm, the size of the fluid annulus at 0^o with the eccetric tool. The extracted dispersion curve agrees with the theoretical curves. At low frequencies (below 2.5 kHz), it agrees with the one of bigger borehole size and at high frequencies, it agrees with the one of original borehole size. Possible reason for this is that at low frequencies where the tool flexural mode is coupled with the borehole flexural mode, the size of the fluid annulus determines the strength of the coupling thus the resulting dispersion behavior of the borehole flexural mode; at high frequencies where the borehole flexural mode is little affected by the tool flexural mode, tool eccentricity has little effect on the dispersion curve of the borehole flexural mode. At 90^o, dispersion analysis shows the primary energy in the waveforms goes to Stoneley wave (n=0 mode). The extracted dispersion curve agrees with the theoretical one (original borehole size). At 180^o, the radial motion is the strongest, so is the coupling between the tool flexural and the borehole flexural. The dispersion curve of the borehole flexural mode at low frequencies (below 2.5 kHz) is not surprisingly affected by the strength of the coupling, which is determined by the size of the fluid annulus. The extracted dispersion curve therefore agrees with the theoretical curve that is computed by assuming the borehole size is smaller so that the fluid annulus equals to 10.7 mm, the size of the fluid annulus at 180^o with the eccentric tool. The dispersion analysis result of the subtracted waveforms ($R_0 - R_{180}$) shows that the resulting dispersion curve agrees with the theoretical curve of the original borehole size very well. It indicates that the tool eccentricity affects little on the borehole flexural mode in the current practice where the subtracted waveforms ($R_0 - R_{180}$) are used in the data processing.

5.2.2 Dipole Source - Off Center by 10.95 mm

In real LWD situation, the tool can be at any position. It is thus important to understand how the wave properties change as the tool moves at different off-centered locations. In this section, the tool is pushed even further off-center toward the negative x direction, the smallest and largest annulus being 6 mm, and 28 mm, respectively. The coupling between the tool flexural and borehole flexural is expected to be even

stronger at 180^o, while at 0^o and 90^o, everything is expected to be more or less the same as in the less off-centered case.

Figure 5-13 and 5-14 shows waveforms received at receivers at various azimuthal locations plotted with common angle gather. The waveforms show motions with opposite phase at most receiver positions 180^o apart, though the amplitude at the smaller annulus side is even more stronger. The wavefield primarily remains characteristics of dipole(see figure 5-4. Waveforms at 0^o (large annulus side), 90^0, 180^o (small annulus side) and subtraction between 0^0 and 180^o are shown in figure 5-15.

The tool flexural is stronger at 180^o then at 0^o as the source is much closer to the borehole. The azimuthal pressure distribution shown by waveforms plotted in common z gathers (figure 5-16), indicates even more asymmetry and stronger circumferential motions.

Semblance and dispersion analysis results are shown in figure 5-17 and 5-18 for waveforms, R_0, , R_{90}, R_{180} and R_0 and R_{180}. Compared with the case of slightly off-centered tool, they show little change at 0^o, except that the phase velocity of the borehole flexural mode is even closer to the formation shear velocity at low frequencies due to a further weaken coupling with the tool flexural mode. At 90^o, in addition to the Stoneley mode, the borehole flexural mode is recorded due to higher asymmetry of the wavefield. At 180^o where the coupling between the tool flexural mode and the borehole flexural mode is even stronger, the phase velocity of the borehole flexural mode is even slower at low frequencies (below 2.5 kHz). The extracted dispersion curve agrees with the theoretical one (centered tool model) that is computed by assuming a reduced borehole size (the fluid annulus equals to the smallest annulus in this eccentric tool case). Dispersion analysis of $R_0 - R_{180}$ shows that those waveforms contain multipole modes. Applying a time window to the waveforms in figure 5-15(d) to keep the first large amplitude ripple for each receivers (*e.g.* in receiver 1, keeping signals before 2.6 ms) before the dispersion analysis, the resulting dispersion curve of $R_0 - R_{180}$ is shown in figure 5-19. It agrees with the theoretical dispersion curve of the model with centered tool and original borehole size. This result implies that through appropriate data processing, the effect of tool eccentricity may be reduced

or eliminated in dipole logging even when the tool is extremely off-centered.

5.2.3 Monopole Source - Off Center by 10.95 mm

Monopole logging traditionally provides formation compressional velocity and Stoneley mode for permeability analysis. In chapter 4, direct shear in the soft formation is clearly shown in the monopole data. It is of interest to investigate how that changes with off-centered tool.

Figures 5-20 and 5-14 show waveforms received at various azimuthal locations plotted with common angle gather. Unlike in the centered tool case where waveforms are of the same phase at locations 180^o apart, torsional motion is introduced by the off-centered tool. The snapshot of the wavefield at 2.3 ms shows both dipole and monopole characteristics. Strong dipole motion indicates a weak monopole excitation. Waveforms plotted in common z gather shows asymmetric azimuthal pressure distribution and torsional motions (figure 5-23).

Figure 5-24 shows waveforms, R_0, R_{90}, R_{180} and $R_0 + R_{180} + R_{90} + R_{270}$. They exhibit complicated patterns due to the excitation of multipole modes. Semblance results show clear compressional arrivals at all angles, which is a good news, as compressional velocity is mainly measured by monopole tools (figure 5-26). With the help of dispersion analysis (figure 5-27, strong borehole flexural mode is observed at 0^o, 90^o and 180^o, except the coupling between the tool and the borehole flexural is strong at 90^o and 180^o, while little coupling happens at 0^o. Dispersion curve of $R_0 + R_{180} + R_{90} + R_{270}$ resembles that of R_{180}. That is not surprising because the amplitude of R_{180} is more than 7 times and 3 times larger than that of R_0 and R_{90}, respectively. The remaining shear arrival in the summation waveforms is the leaky refracted shear.

The monopole LWD tool in both the centered and off-centered case show it can provide shear measurement as a cross-check for modal based measurements.

5.2.4 Quadrupole Source - Off Center by 10.95 mm

In the centered tool case, quadrupole mode appeared to be a good candidates for measuring shear velocity in soft formation. It is important to evaluate its behavior when the tool is off centered.

Figure 5-28 $\sim$ 5-29 shows waveforms received at various azimuthal locations plotted with common angle gather. The waveforms at 0^o and 180^o are not completely in phase. Snapshots of the wavefield at 2.1 ms (figure 5-30) shows monopole, dipole, quadrupole and higher order modes are excited when the tool is off-centered. Strong tortional motion exists due to strong azimuthal pressure gradient (figure 5-31). As many modes co-exists in the borehole, waveforms, semblance and dispersion results are complex(figures 5-32, 5-33 and 5-34). At 0^o (large annulus side), Stoneley, borehole flexural and quadrupole modes are excited. The borehole flexural mode is strong. Its dispersion curve agrees with the theoretical one with bigger borehole. Dispersion curves of Stoneley and the quadrupole mode agree with their theoretical counterparts with original borehole size. At 90^o, the quadrupole mode is stronger. The dispersion curve of the borehole flexural mode agrees with the theoretical one with a smaller borehole. At 180^o, the borehole flexural mode is stronger, again its dispersion curve agrees the theoretical one of smaller borehole size. The quadrupole mode is observable. When summing waveforms at 0^o and 180^o and subtracting those at 90^o and 270^o, the flexural mode energy is suppressed and the quadrupole mode is brought up very clearly (figure 5-33(d) and 5-34(d)). Its phase velocity is exactly the formation shear velocity at low frequencies.

So for the quadrupole LWD logging, the current practice of summing up waveforms at 0^o and 180^o is a good way to enhance the quadrupole mode in both the centered and off-centered tool cases.

5.3 High Frequency Dipole Source Off Center by 10.95 mm (f_c= 8 kHz)

It was pointed out in chapter 4 that LWD tools working at higher frequencies have some engineering advantage. There are interests of using high frequency sources for measuring formation shear velocity. It is then of importance to discuss wave propagation behavior when the tool is off-centered at high frequency. The frequency spectra of the source with a center frequency of 8 kHz is shown in figure 4-11(c).

Figure 5-35 and 5-36 shows waveforms at various azimuthal angles. Waveforms maintains out of phase motion when being 180^o apart. Magnitudes are substantially higher at places with smaller annulus for all major arrivals. It is not surprising that the azimuthal pressure distribution now is more polarized than the low frequency (figure 5-37). There still exists torsional motion.

It was established previously that the off-centered LWD tool affects modal dispersions only at low frequencies where borehole modes couples with tool modes. At high frequencies, all modes are localized and approaches to the fluid-solid interface velocity. It then can be expected that the off-centered tool at high frequency firing has little effect on the shape of dispersion curves.

Figure 5-38 shows waveforms R_0, R_{90}, R_{180} and $R_0 - R_{180}$. The corresponding spectra are shown in figure 5-39(c). At 0^o where the annulus is the largest, in addition to the borehole flexural mode (n=1), n=3 mode is excited (figures 5-40(a), 5-41 and 5-43(a)). As its phase velocity approaches the shear velocity at low frequencies, n=3 mode has an arrival close to the formation shear in the semblance domain (figure 5-40). It is not direct shear because the frequency is too high to have strong leaky shear. At 90^o, n=3 mode is not as strong as it is at 0^o. More higher modes are excited (*e.g.* n=2 mode), but the borehole flexural is the strongest and show the best coherence in the time domain semblance(figure 5-40(b) and 5-43(b)). At 180^o where the fluid annulus is the smallest, there are two distinct arrivals with phase velocities between

800 m/s and 1200 m/s (figure 5-40(c)). The theoretical dispersion curves that fit the two arrivals best in both dispersion and semblance domain is the borehole flexural mode with the original borehole size and the borehole quadrupole mode with smaller borehole size (figures 5-42, 5-43(c) and 5-44). Note that n=3 mode shown at 180^o is weaker. Subtracting waveforms at 180^o from 0^o, all three modes, the borehole flexural mode, the n=3 mode and borehole quadrupole mode show up in the semblance and dispersion curves (figures 5-40(d), 5-43(d) and 5-45). Note that at low frequencies (below 5 kHz), there is a rather pure borehole flexural mode (see figure 5-45(a)). The phase velocity of the borehole flexural mode is between the n=3 mode and quadrupole mode. In field operation, shear velocity is computed from the phase velocity borehole flexural mode. It is then important to identify the right arrivals.

5.4 Conclusions

Effects of eccentric LWD tool on borehole acoustic measurements are investigated. For all source types, when the LWD tool works at low frequencies (center frequency is 2 kHz), substantial torsional or circumferential motions are observed and asymmetric or odd numbered order modes are more efficiently excited, regardless of the source type. The eccentric tool affects dispersion behaviors of asymmetric modes through tool-borehole mode coupling at the frequency range of 0-2 kHz for an 8.5 inch borehole. For dipole logging, waveforms at the side with the largest fluid annulus, where the coupling between the tool and the borehole modes becomes weak, shear arrival is strong. The large shear arrival amplitude indicates the shear arrival is due to the trapped mode pole in the vicinity of the practical cutoff. It means that the phase velocity of borehole flexural mode approaches to the formation shear at low frequency limit. At the side where the fluid annulus is the smallest, waveforms are strongly affected by the tool through borehole and tool flexural mode coupling, causing phase velocities of the borehole flexural mode at low frequencies to be even slower at lower frequencies (below 2.5 kHz). The closer the tool is to the borehole wall, the stronger the coupling is at the side with small fluid annulus. Appropriate data processing may

reduce or eliminate the effect of tool eccentricity on the dipole waveforms ($R_0 - R_{180}$.

For the monopole logging, eccentric tool generates strong flexural modes. Both direct compressional and shear arrivals of the formation appear in the semblance. For quadrupole logging, strong odd numbered modes (n=1,3) are generated, it is necessary to sum up waveforms at 0^o and 180^o and subtracting waveforms at 90^o and 270^o to eliminate odd numbered modes and bring up the quadrupole. Altogether, for the low frequency source case, tool eccentricity has little effect on shear measurement.

When the dipole LWD tool is designed to work at a center frequency of 8 kHz, besides the borehole flexural mode, n=3 and quadrupole mode are excited. The phase velocity of the flexural mode is between that of the n=3 mode and the quadrupole mode. With multipole modes having phase velocities different by several percent, identifying the right mode is crucial to obtain the right shear velocity. Cross-check between the semblance and dispersion results is an effective way to locate the borehole flexural mode.

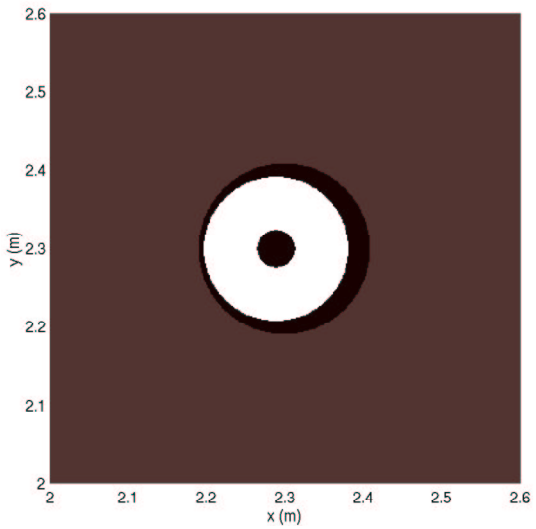

Figure 5-1: The reconstructed borehole cross-section with an off-centered tool. The mesh is not shown for a better view of the model. the borehole diameter is around 20 cm, the outer diameter of the tool is about 18 cm. The fluid annulus could be as small as 6 millimeters.

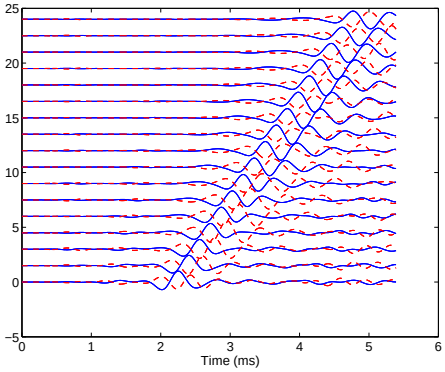

(a) 0^o and 180^o

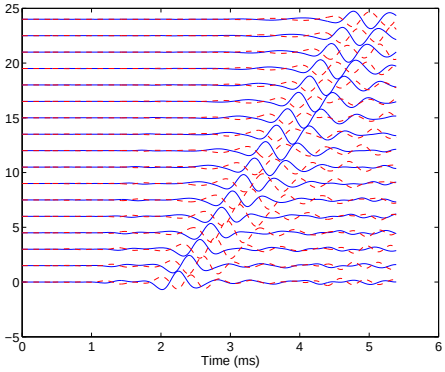

(b) 10^o and 190^o

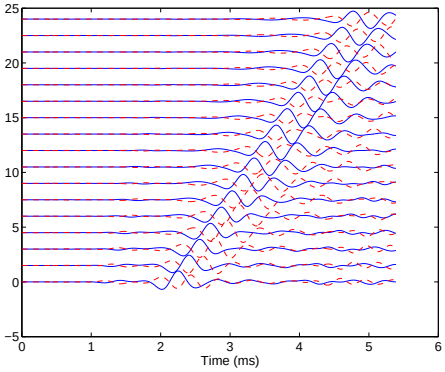

(c) 20^o and 200^o

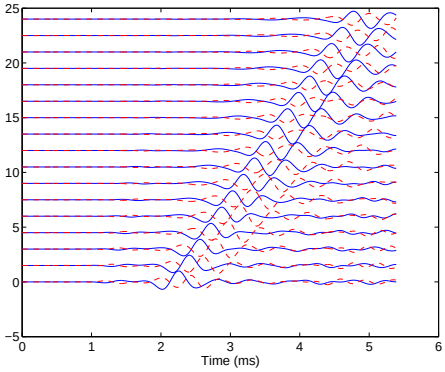

(d) 30^o and 210^o

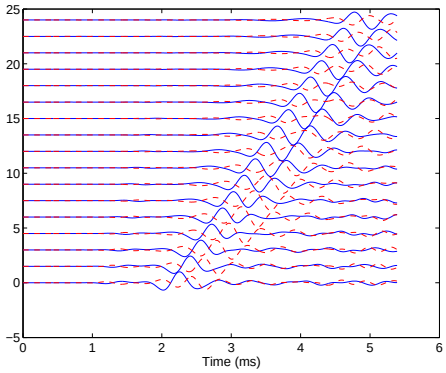

(e) 40^o and 220^o

Figure 5-2: Dipole source with the tool slightly off-centered (6.3 mm). The source center frequency is 2 kHz. Waveforms received by groups of receivers at various azimuthal locations plotted with common angle gather. Dash line: receivers in the second quadrant; Solid line: receivers in the first quadrant. Compared to the centered tool case in figure 4-12, waveforms at locations being 180^o apart are no longer perfectly out of phase because of wavefield asymmetry.

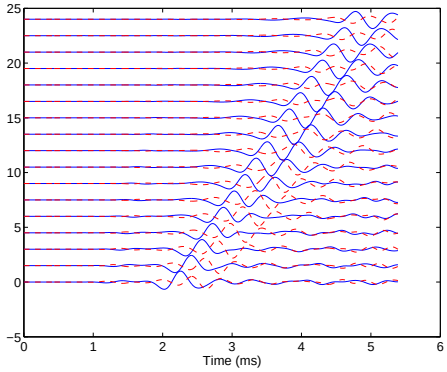

(a) 50^o and 230^o

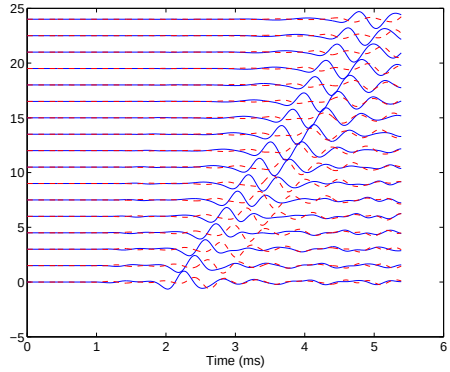

(b) 60^o and 1240^o

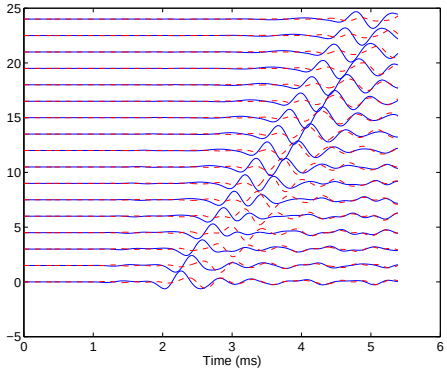

(c) 70^o and 250^o

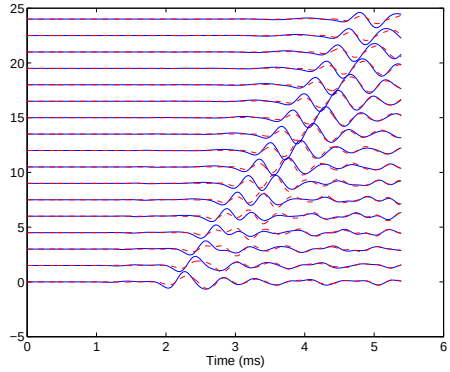

(d) 80^o and 260^o

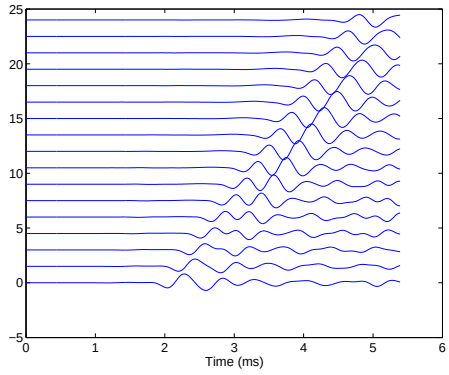

(e) 90^o

Figure 5-3: Dipole source (low frequency) slightly off-centered (6.3 mm). Waveforms received by groups of receivers at various azimuthal locations plotted with common angle gather. Dash line: receivers in the second quadrant; Solid line: receivers in the first quadrant. Compared to the centered tool case in figure 4-12, waveforms at locations being 180^o apart are no longer perfectly out of phase because of wavefield asymmetry.

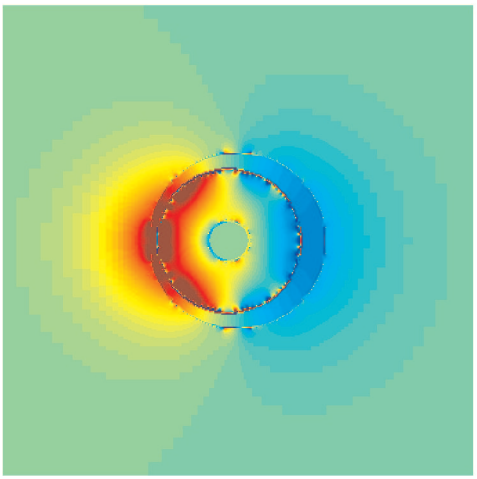

Figure 5-4: Dipole source (low frequency) off-centered (10.95 mm). Snapshot of wavefield (τ_{xx} component) at the first receiver location (t=2.3 ms). The wavefield remains dipole characteristics, though not symmetric.

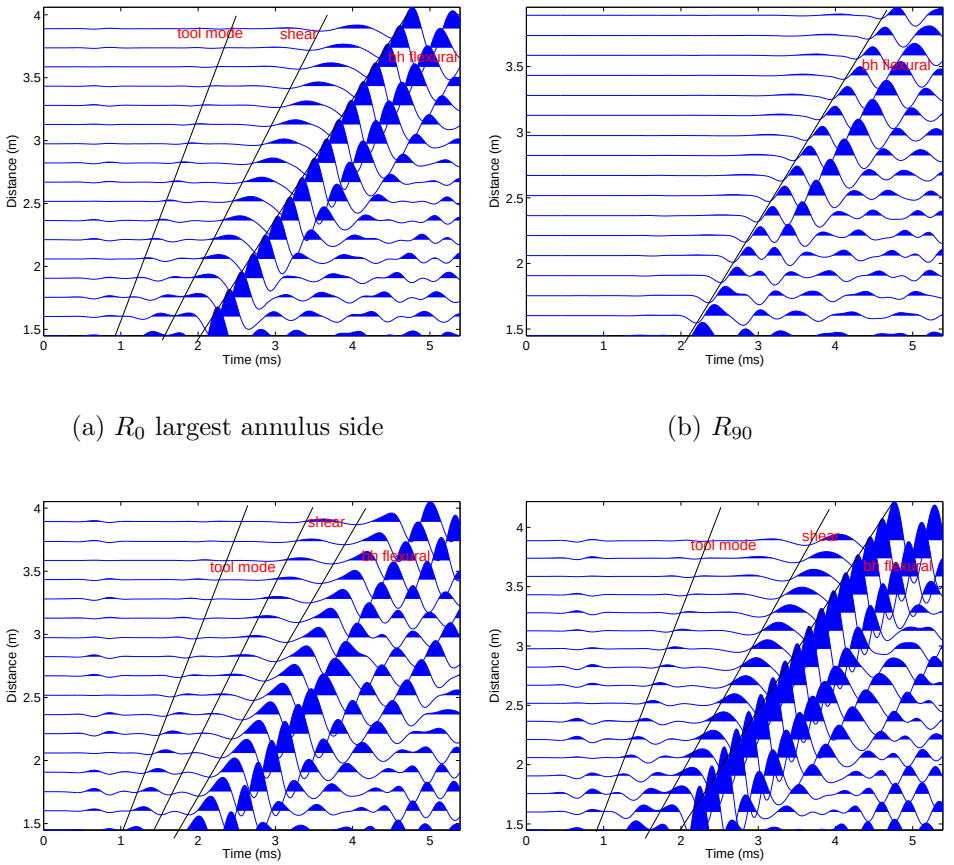

(a) R_0 largest annulus side

(b) R_{90}

(c) R_{180} smallest annulus side

(d) $R_0 - R_{180}$

Figure 5-5: Dipole results with slightly off-centered tool (6.3 mm). The source center frequency is 2 kHz. Waveforms at 0^o, 90^0 and those obtained from waveform subtraction are normalized by the maximum amplitude at 0^o. They are denoted with R_0, R_{90}, R_{180} and $R_0 - R_{180}$. R_{180} is normalized by its maximum amplitude. The maximum amplitude of R_{180} is 5 times larger than R_0. The tool mode is weak in all waveforms. The shear arrival is clearly observable in R_0 and $R_0 - R_{180}$. The borehole flexural mode is the slowest one and the strongest in amplitude. It is very dispersive at 180^o. As the leaky shear is weak, the relatively large amplitude in R_0 indicates that shear arrival is due to the trapped mode pole in the vicinity of the practical cutoff, *i.e.*, the phase velocity of borehole flexural approaches the formation shear velocity at low frequencies.

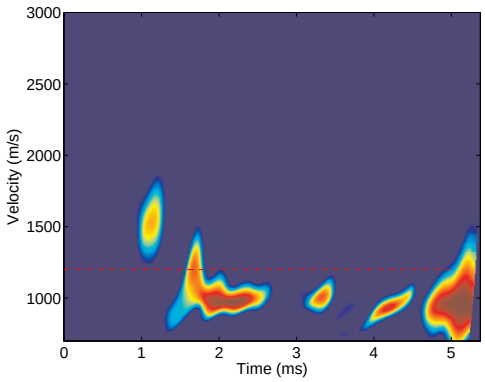

(a) R_0 large annulus side

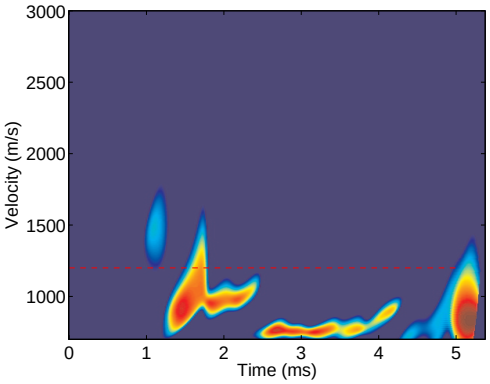

(b) R_{90}

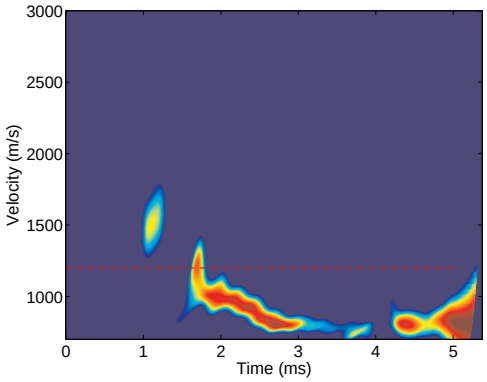

(c) R_{180} small annulus side

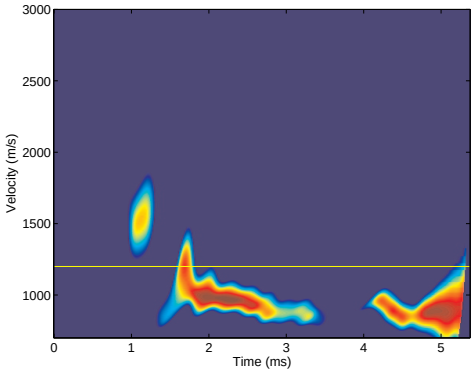

(d) $R_0 - R_{180}$

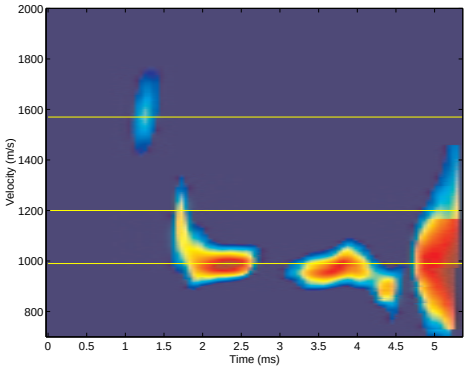

(e) centered tool

Figure 5-6: Dipole results with slightly off-centered (6.3 mm) tool. Semblance result of waveforms R_0, R_{90}, R_{180} and $R_0 - R_{180}$. Figure e shows the semblance of the dipole waveforms when the tool is at the center.

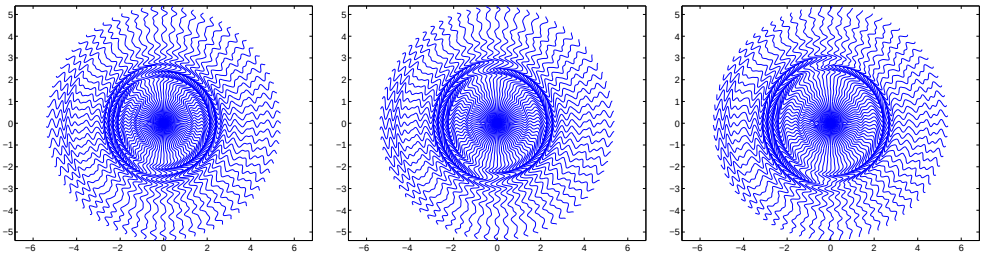

(a) R_1 (b) R_2 (c) R_3

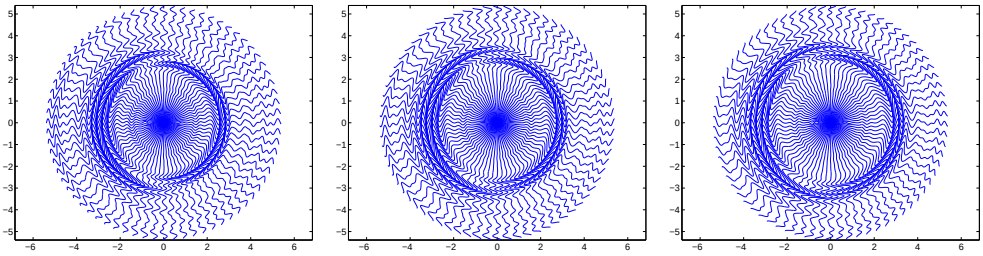

(d) R_4 (e) R_5 (f) R_6

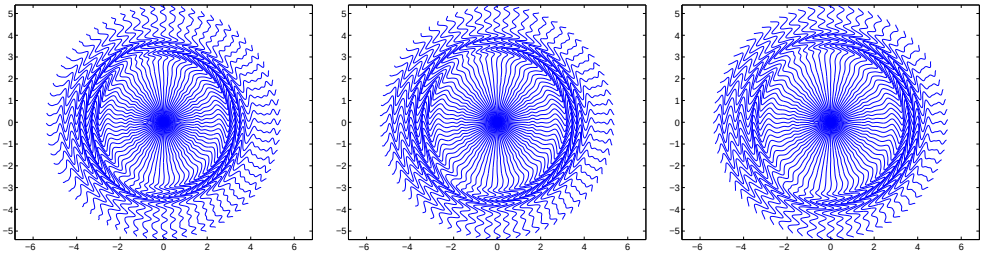

(g) R_7 (h) R_8 (i) R_9

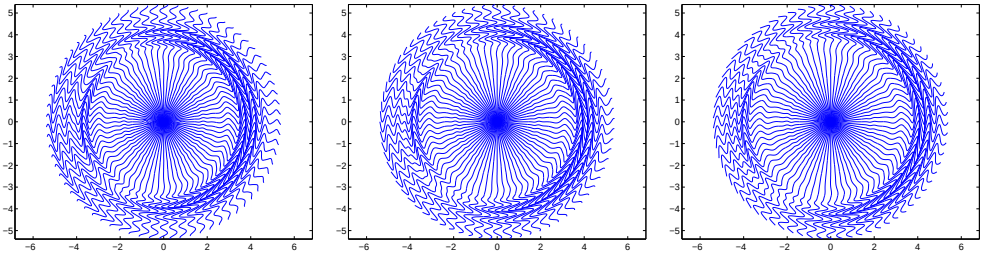

(j) R_{10} (k) R_{11} (l) R_{12}

Figure 5-7: Dipole tool (low frequency) slightly off-centered (6.3 mm). Pressure waveforms received at groups of receivers at various azimuthal locations plotted at common z gather (normalized by the same amplitude). The smallest annulus side is at 0^o, the right side (SA) and the largest annulus side is at 180^o, the left side (LA). As the radiation pattern becomes asymmetric, significant energy propagates circumferentially from SA to LA, as wave propagating along the borehole axis, indicating a strong torsional mode.

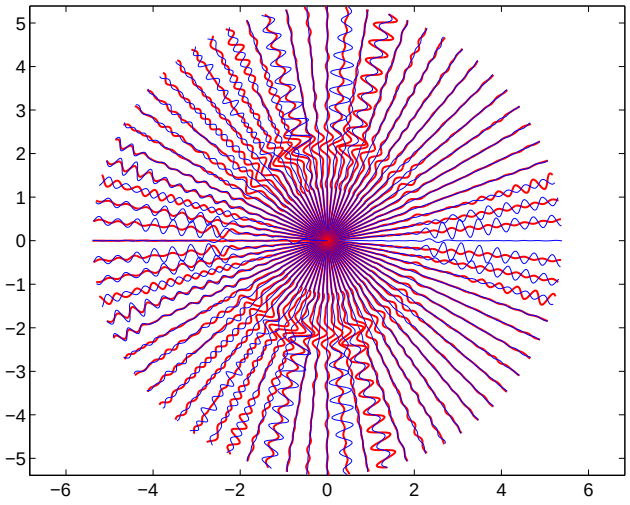

(a) R_1

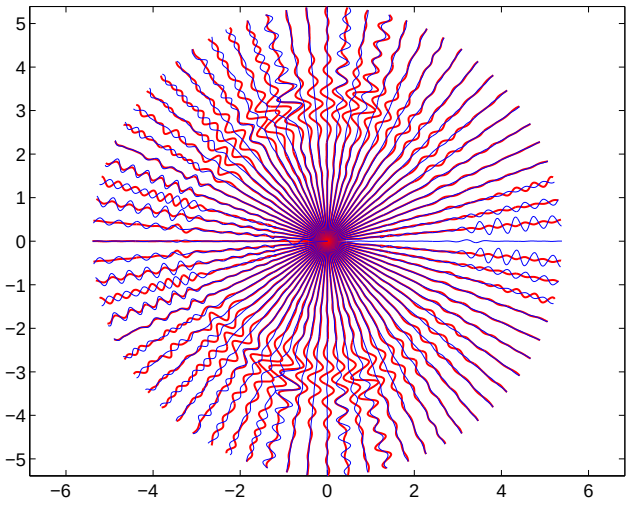

(b) R_6

Figure 5-8: Dipole tool (low frequency) slightly off-centered (6.3 mm). Radial (thin line) and azimuthal (thick line) particle velocities at all angles. Strong azimuthal component is observed at angles roughly perpendicularly to the dipole polarization, the interface between the positive and negative pressure field. At every axial location z, disturbance starts at both SA and LA, while it is stronger as the source is closer to the borehole at SA. Then a pure circumferential motion follows to mix the uneven disturbance around the borehole before the radial motion finally kicks in.

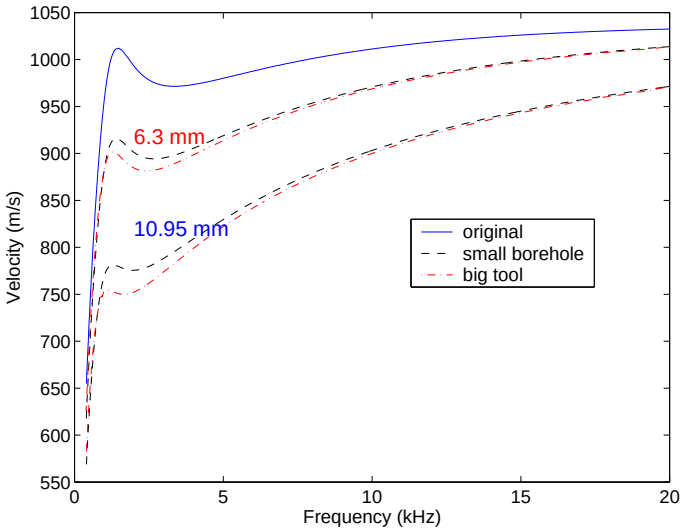

Figure 5-9: Dispersion curves of borehole flexural mode. Decreasing in the fluid annulus enhances the coupling between the tool flexural mode and borehole flexural mode. The resulting borehole flexural dispersion has much lower phase velocity at low frequencies where the coupling is the strongest.

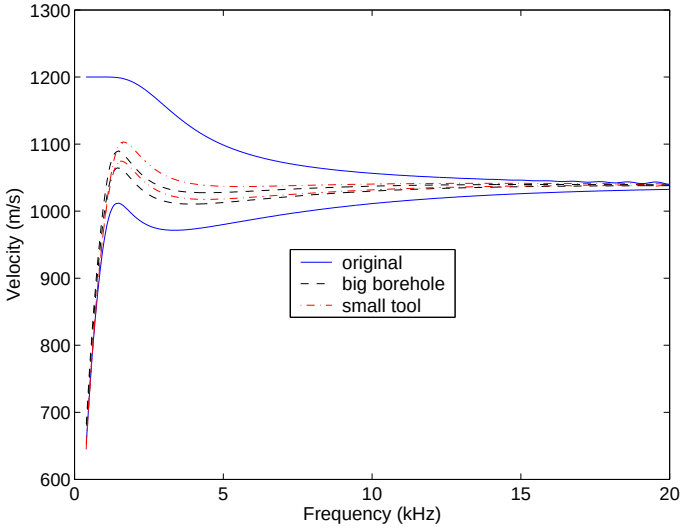

Figure 5-10: Dispersion curves of borehole flexural mode. Increment in the fluid annulus reduces the coupling between the tool flexural mode and the borehole flexural mode. Therefore the resulting borehole flexural dispersion is closer to that without the tool.

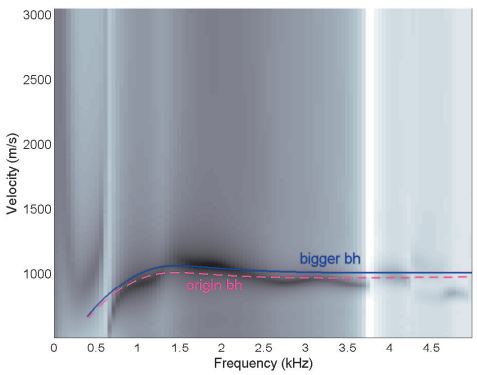

(a) R_0 smallest annulus side

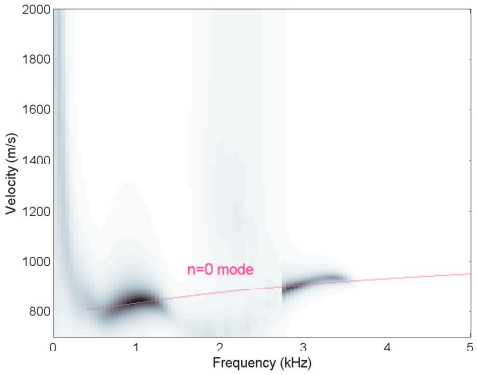

(b) R_{90}

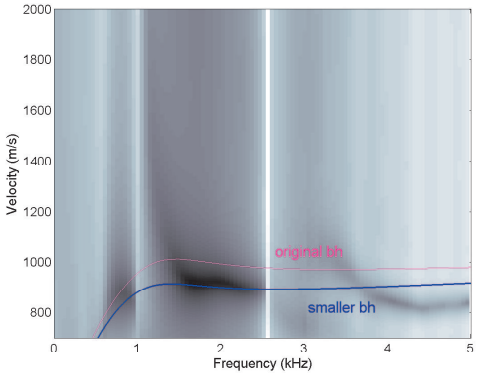

(c) R_{180} largest annulus side

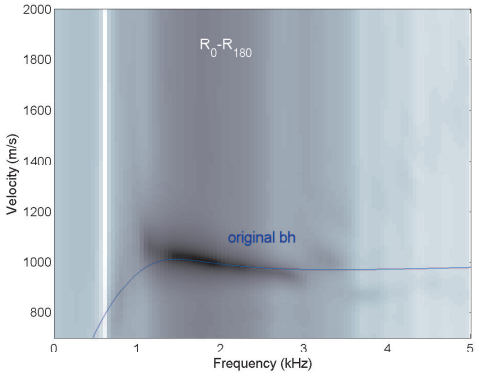

(d) $R_0 - R_{180}$

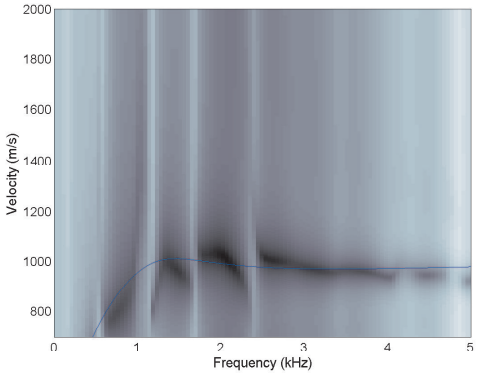

(e) centered tool

Figure 5-11: Dipole results with slightly off-centered (6.3 mm) tool. Dispersion analysis result of waveforms at 0^o, , 90^0, 180^o and subtraction between 0^0 and 180^o. Figure e shows the dispersion of the dipole waveforms when the tool is at the center. Solid lines represent theoretical dispersion curves of models with centered LWD tool.

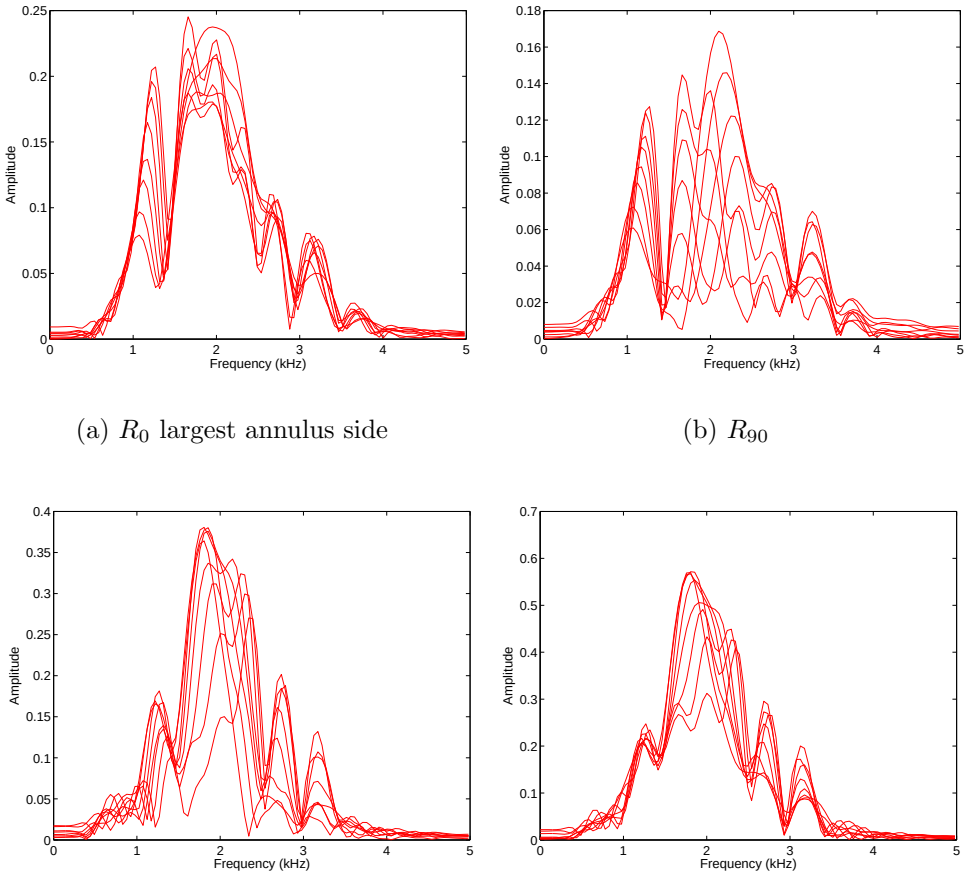

(a) R_0 largest annulus side

(b) R_{90}

(c) R_{180} smallest annulus side

(d) $R_0 - R_{180}$

Figure 5-12: Dipole results with slightly off-centered (6.3 mm) tool. The source center frequency is 2 kHz. Spectra of waveforms at 0^o, 90^0, 180^o and subtraction between 0^0 and 180^o.

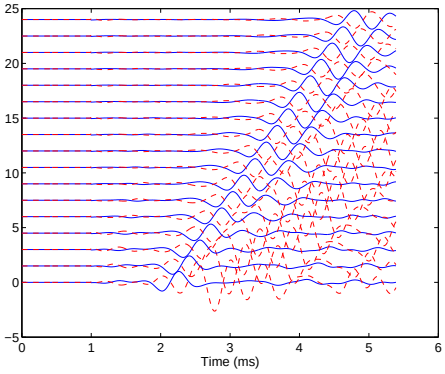

(a) 0^o and 180^o

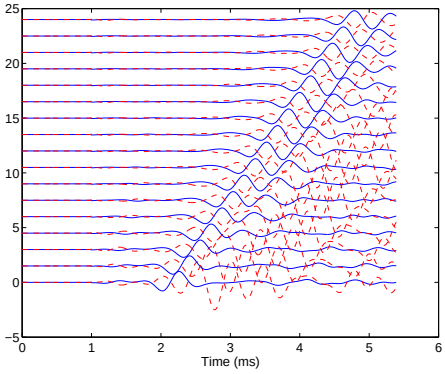

(b) 10^o and 190^o

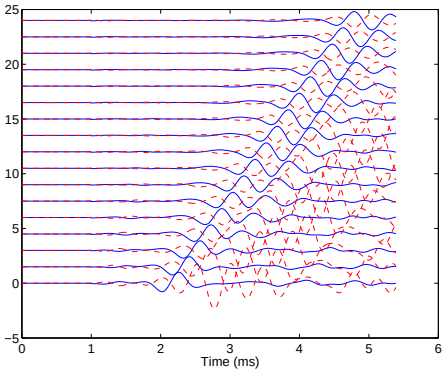

(c) 20^o and 200^o

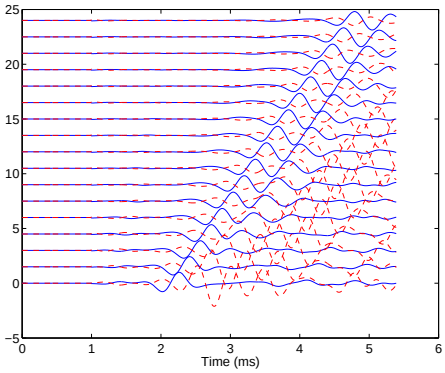

(d) 30^o and 210^o

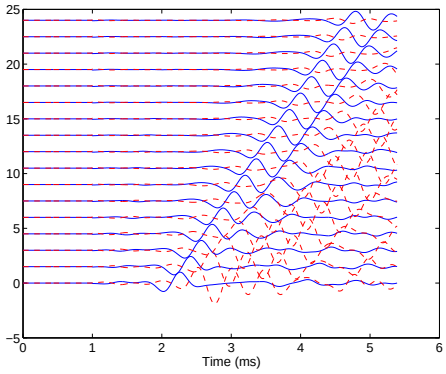

(e) 40^o and 220^o

Figure 5-13: Dipole tool (low frequency) off-centered (10.95 mm). Waveforms received by groups of receivers at various azimuthal locations plotted with common angle gather. Dash line: receivers in the second quadrant; Solid line: receivers in the first quadrant.

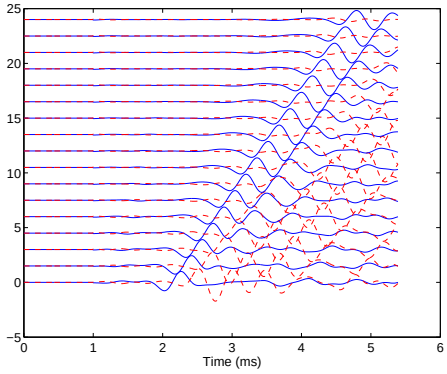

(a) 50^o and 230^o

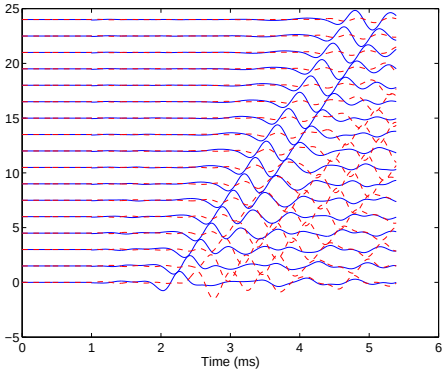

(b) 60^o and 240^o

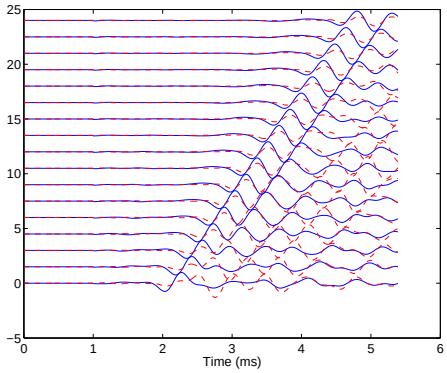

(c) 70^o and 250^o

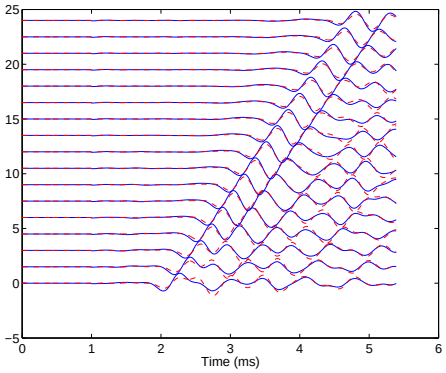

(d) 80^o and 260^o

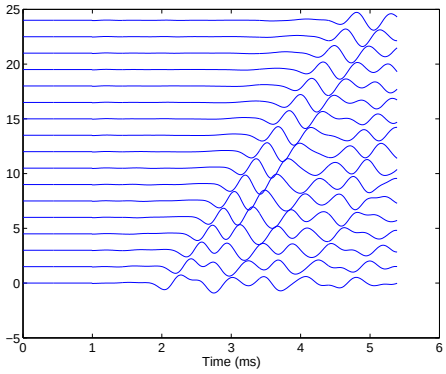

(e) 90^o

Figure 5-14: Dipole tool (low frequency) off-centered (10.95 mm). Waveforms received by groups of receivers at various azimuthal locations plotted with common angle gather. Dash line: receivers in the second quadrant; Solid line: receivers in the first quadrant.

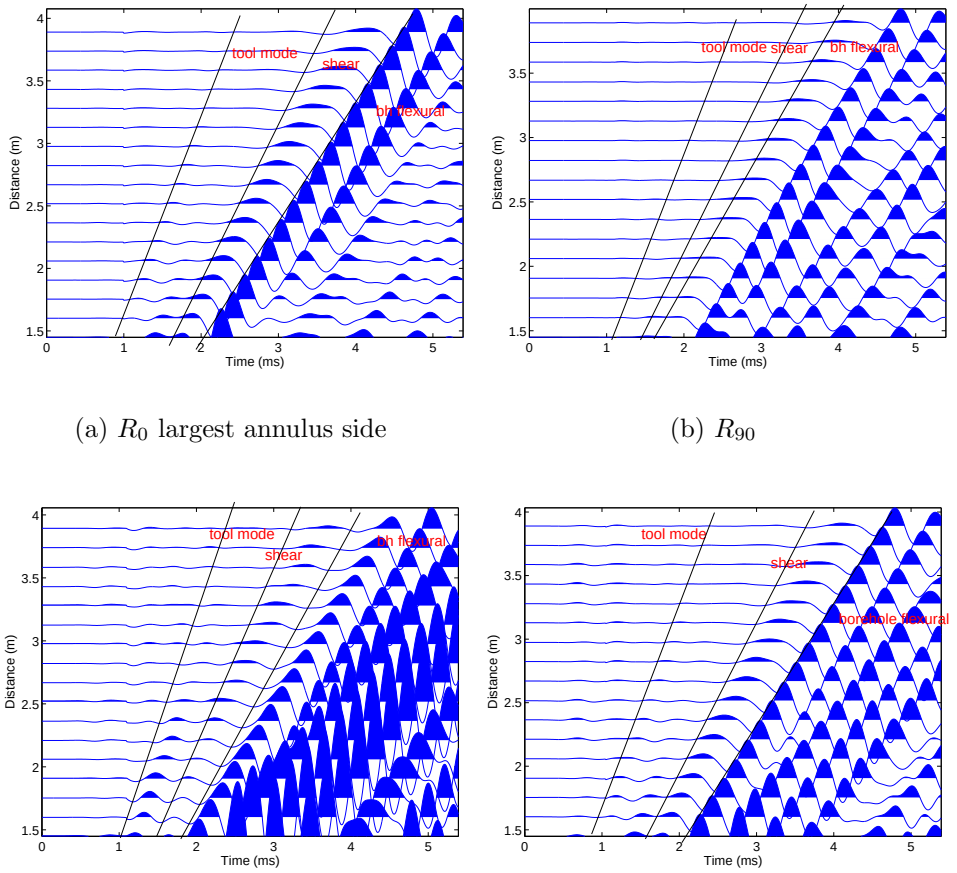

(a) R_0 largest annulus side

(b) R_{90}

(c) R_{180} smallest annulus side

(d) $R_0 - R_{180}$

Figure 5-15: Dipole results with off-centered tool (10.95 mm). Source center frequency is 2 kHz. Waveforms at all locations are normalized by the maximum amplitude at 0^o. The tool mode is weak at all locations. Shear arrival is clearly observable in waveforms at 0^o and from subtraction. The borehole flexural mode is the slowest one and the strongest in amplitude. At the largest annulus side, the phase velocity of borehole flexural approaches the formation shear velocity at low frequencies.

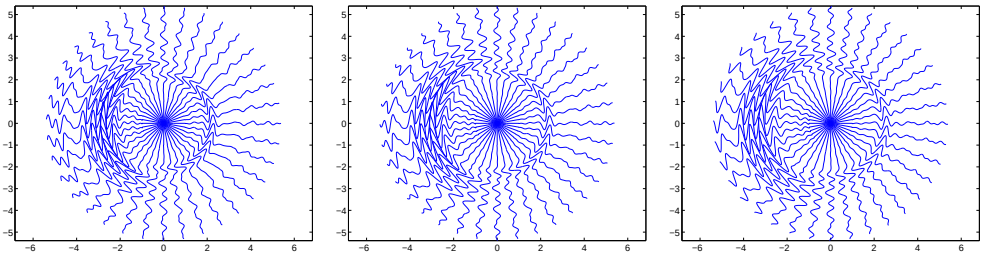

(a) R_1 (b) R_2 (c) R_3

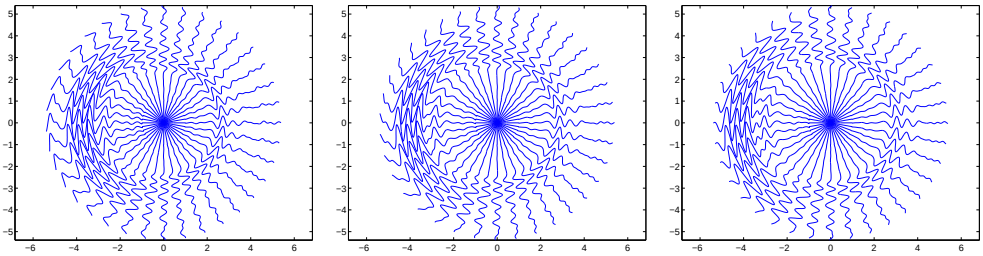

(d) R_4 (e) R_5 (f) R_6

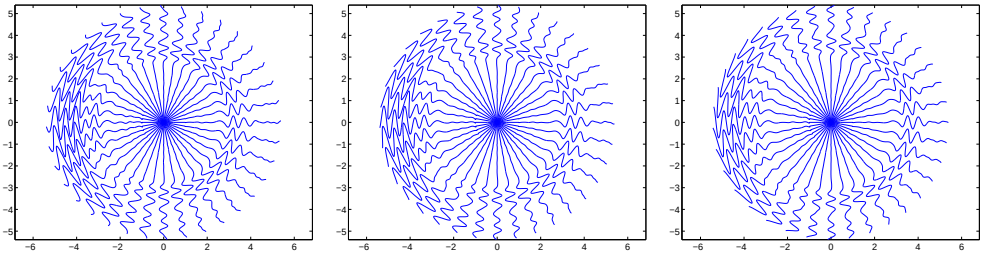

(g) R_7 (h) R_8 (i) R_9

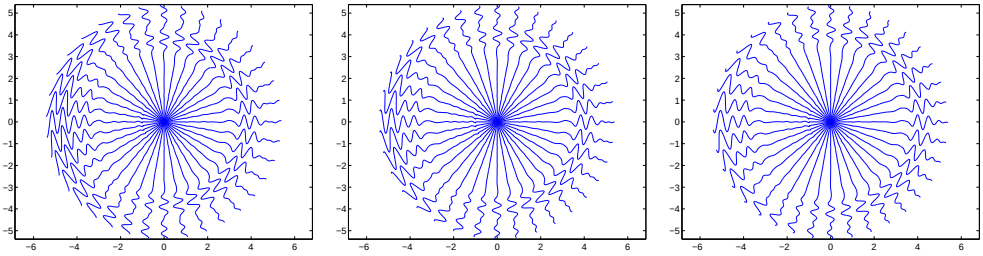

(j) R_{10} (k) R_{11} (l) R_{12}

Figure 5-16: Dipole source (low frequency) off-centered (10.95 mm). Waveforms received at receivers at various azimuthal locations plotted as common z gather.

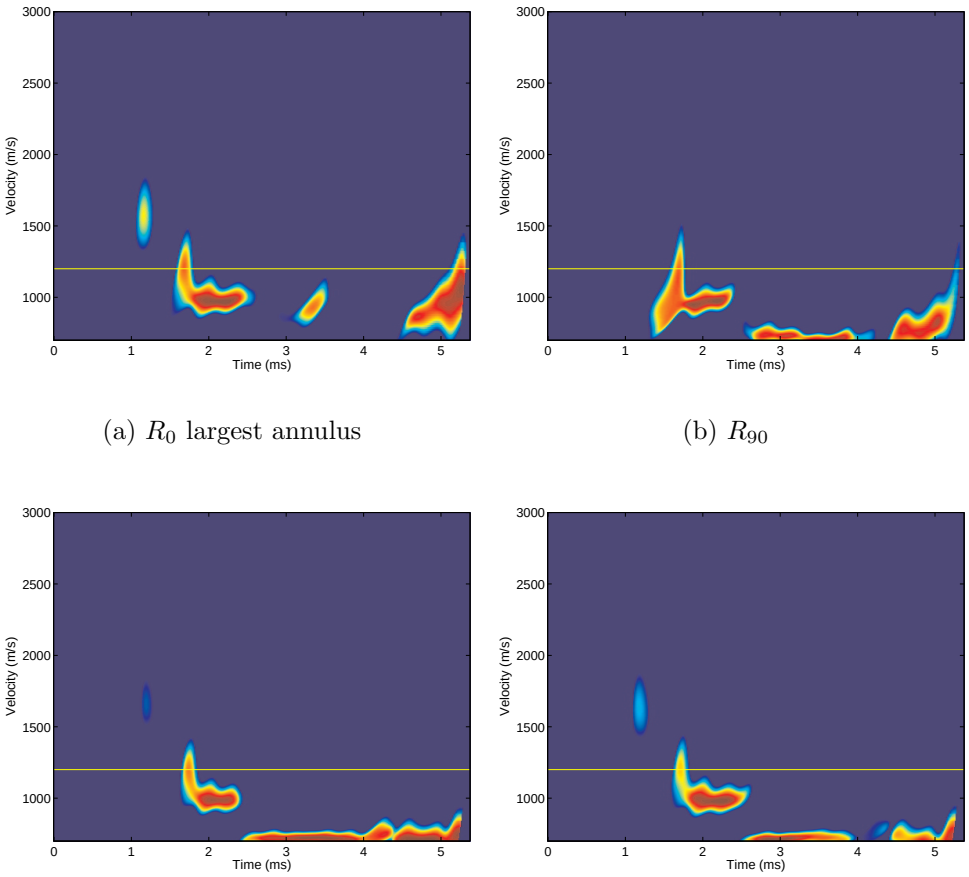

(a) R_0 largest annulus

(b) R_{90}

(c) R_{180} smallest annulus

(d) $R_0 - R_{180}$

Figure 5-17: Dipole tool (low frequency) off-centered (10.95 mm). Semblance result of waveforms at 0^o, 90^0, 180^o and subtraction between 0^0 and 180^o.

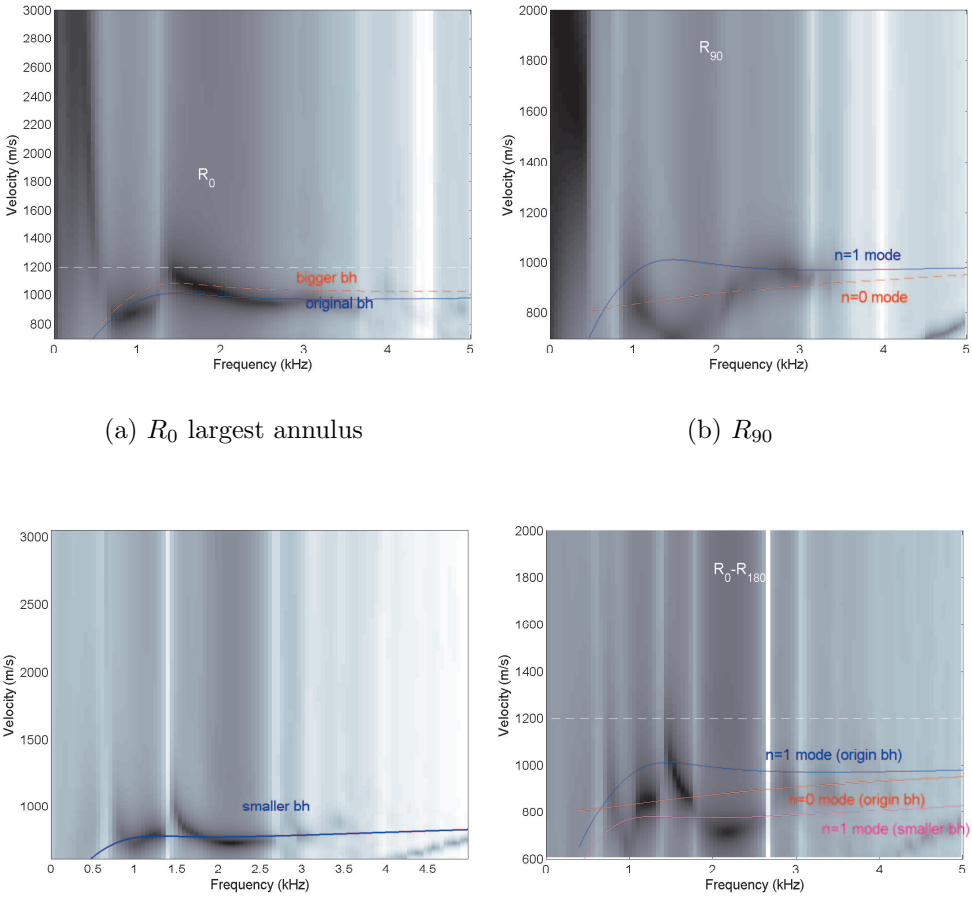

(a) R_0 largest annulus

(b) R_{90}

(c) R_{180} smallest annulus

(d) $R_0 - R_{180}$

Figure 5-18: Dipole tool (low frequency) off-centered (10.95 mm). Dispersion analysis result of waveforms at 0^o, , 90^0, 180^o and subtraction between 0^0 and 180^o. Solid lines represent theoretical dispersion curves of centered tool case.

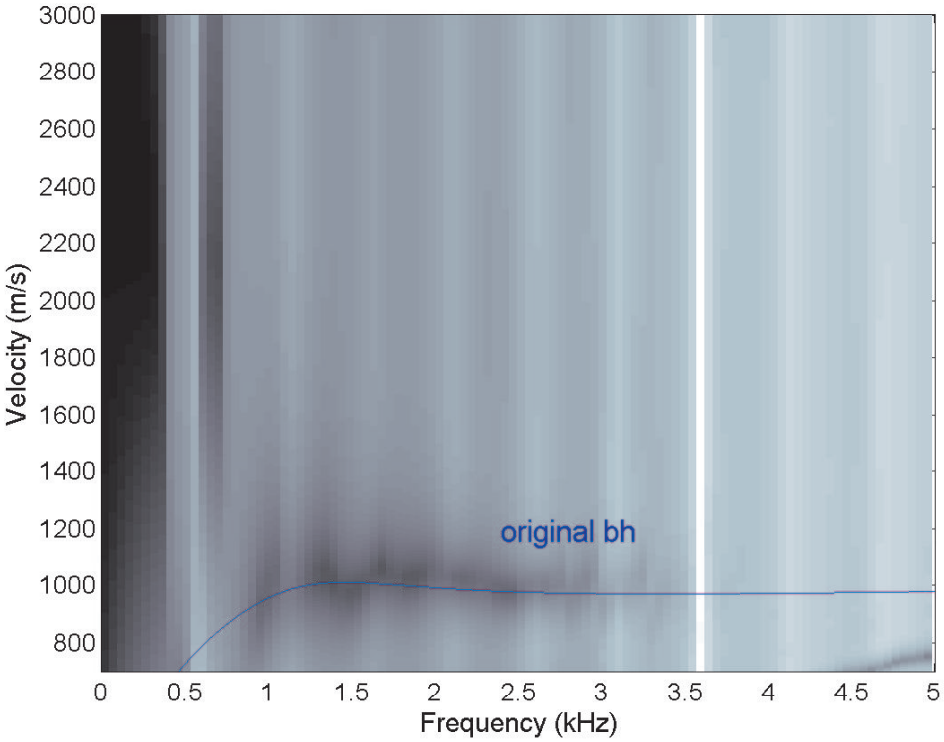

Figure 5-19: The dispersion curve of $R_0 - R_{180}$. Before the dispersion analysis, a time window is applied to the waveforms in figure 5-15(d) to keep the first large amplitude ripple for each receivers (*e.g.* in receiver 1, keeping signals before 2.6 ms). The solid line is the theoretical dispersion curve of the borehole flexural mode with centered tool and original borehole size.

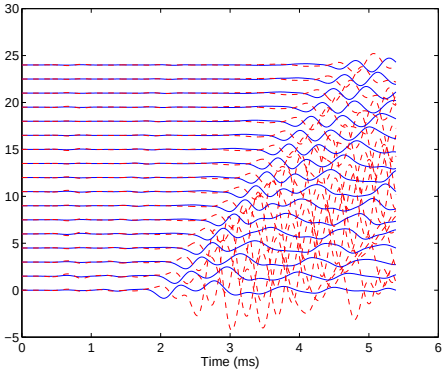

(a) 0^o and 180^o

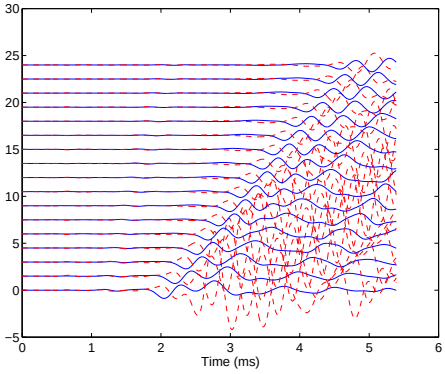

(b) 10^o and 190^o

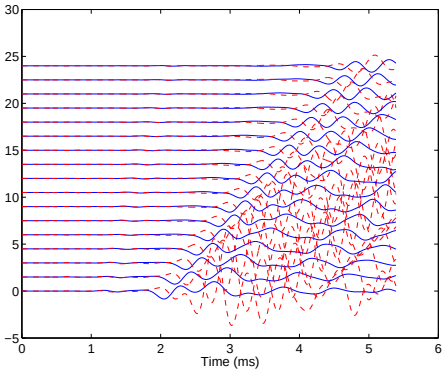

(c) 20^o and 200^o

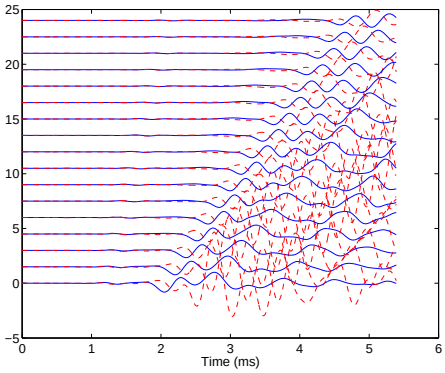

(d) 30^o and 210^o

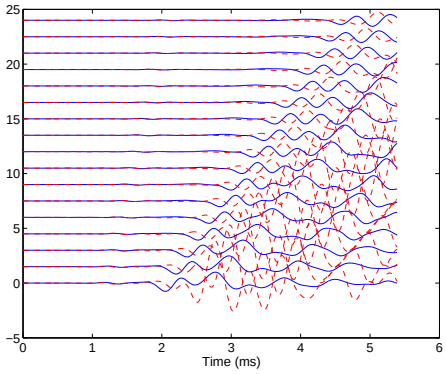

(e) 40^o and 220^o

Figure 5-20: Monopole source (low frequency) off-centered (10.95 mm). Waveforms received by groups of receivers at various azimuthal locations plotted with common angle gather. Dash line: receivers in the second quadrant; Solid line: receivers in the first quadrant.

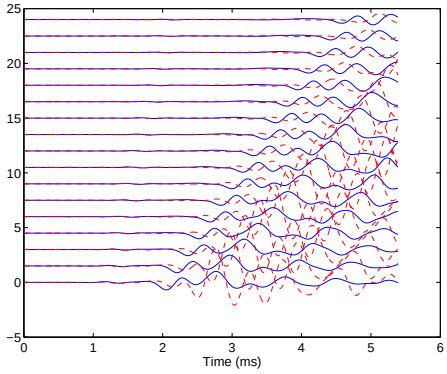

(a) 50^o and 230^o

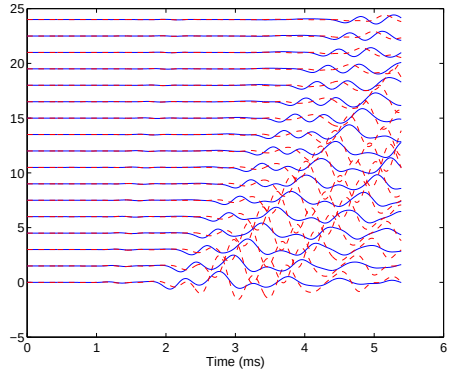

(b) 60^o and 240^o

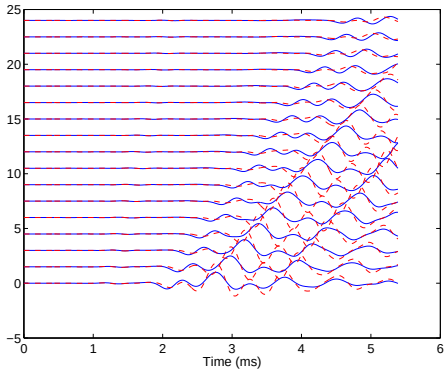

(c) 70^o and 250^o

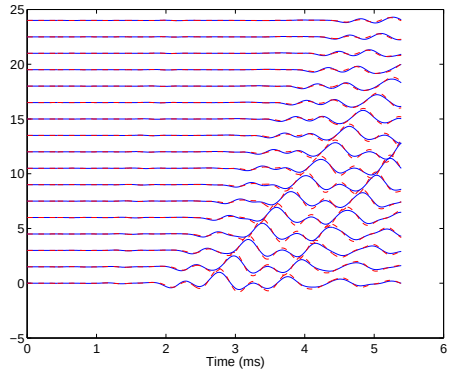

(d) 80^o and 260^o

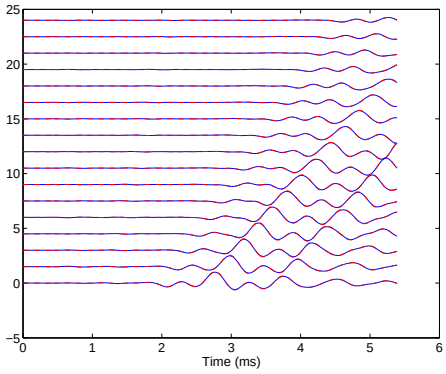

(e) 90^o

Figure 5-21: Monopole source (low frequency) off-centered (10.95 mm). Waveforms received by groups of receivers at various azimuthal locations plotted with common angle gather. Dash line: receivers in the second quadrant; Solid line: receivers in the first quadrant.

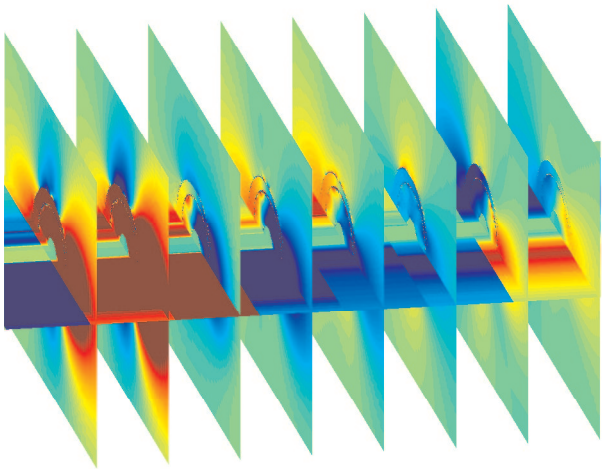

(a) 3D snapshot

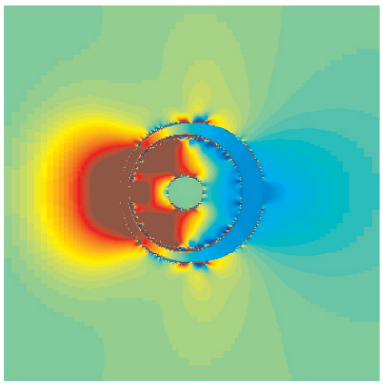

(b) cross section slice z_1

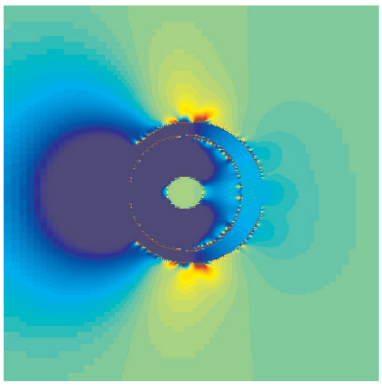

(c) cross section slice z_2

Figure 5-22: Monopole source (low frequency) off-centered (10.95 mm). Snapshot of wavefield (τ_{xx} component) at 2.3 ms. In figure a, each slice is at the receiver position.

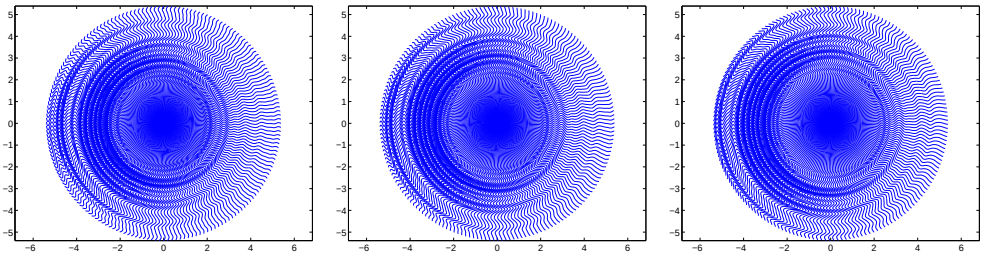

(a) R_1 (b) R_2 (c) R_3

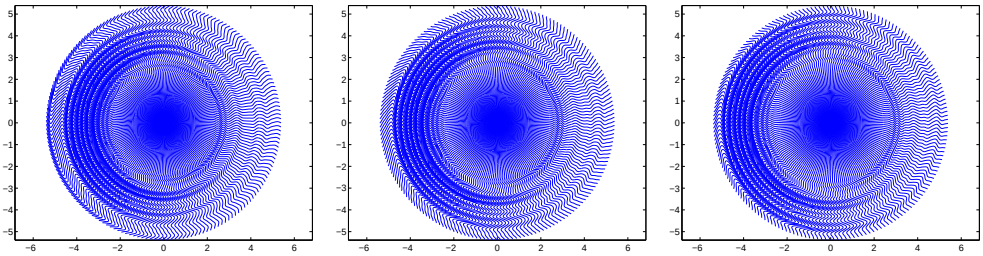

(d) R_4 (e) R_5 (f) R_6

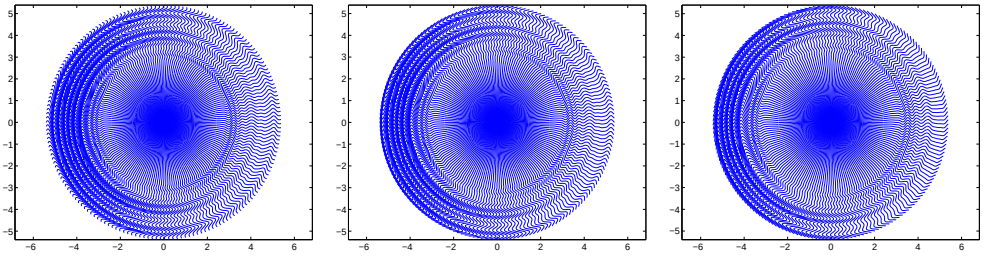

(g) R_7 (h) R_8 (i) R_9

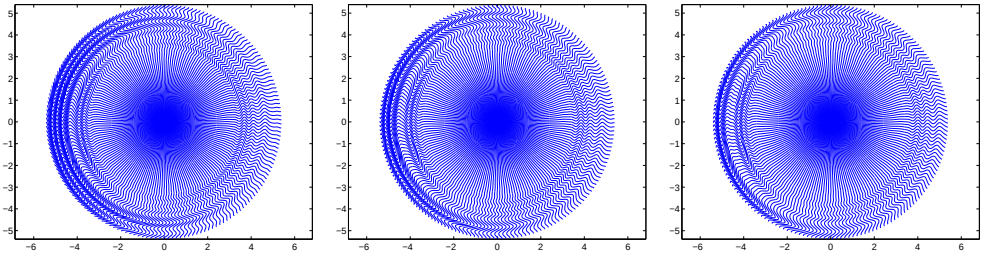

(j) R_{10} (k) R_{11} (l) R_{12}

Figure 5-23: Monopole source (low frequency) off-centered (10.95 mm). Waveforms received at groups of receivers at various azimuthal locations plotted as common z gather.

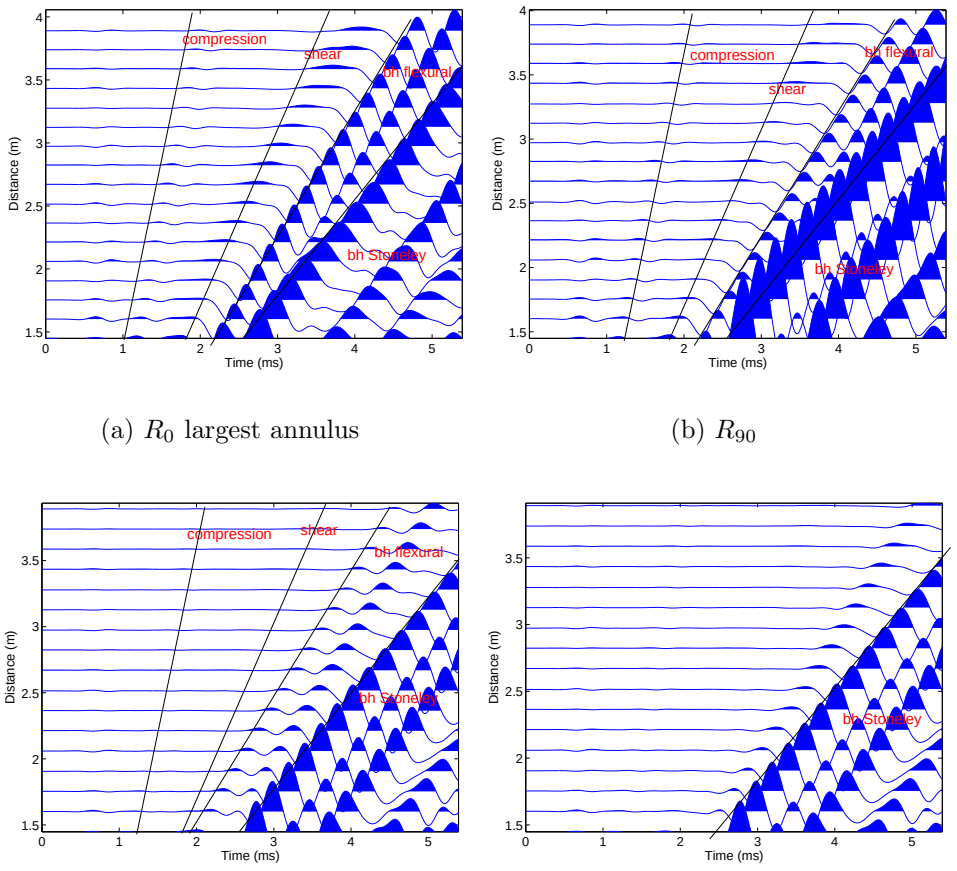

(a) R_0 largest annulus

(b) R_{90}

(c) R_{180} smallest annulus

(d) $R_0 + R_{180} + R_{90} + R_{270}$

Figure 5-24: Monopole source (low frequency) off-centered (10.95 mm). Waveforms at 0^o, 90^o, 180^o and summation of waveforms at 0^o, 180^o, 90^o and 270^o.

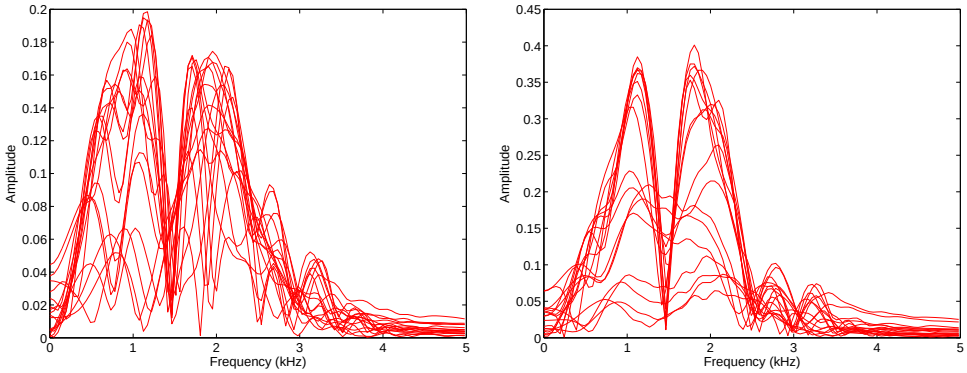

(a) R_0 largest annulus

(b) R_{90}

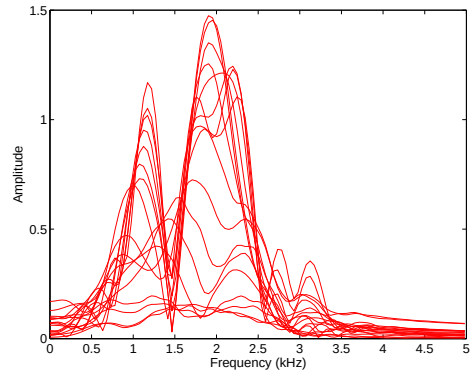

(c) R_{180} smallest annulus

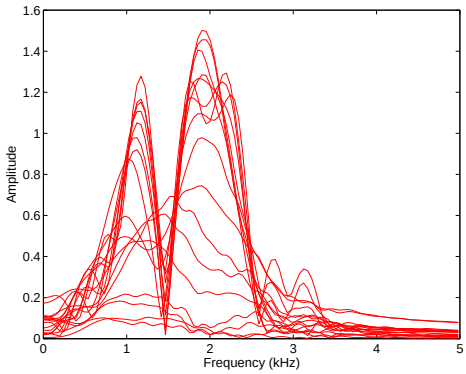

(d) $R_0 + R_{180} + R_{90} + R_{270}$

Figure 5-25: Monopole source (low frequency) off-centered (10.95 mm). Spectra of waveforms R_0, R_{90}, R_{180} and $R_0 + R_{180} + R_{90} + R_{270}$.

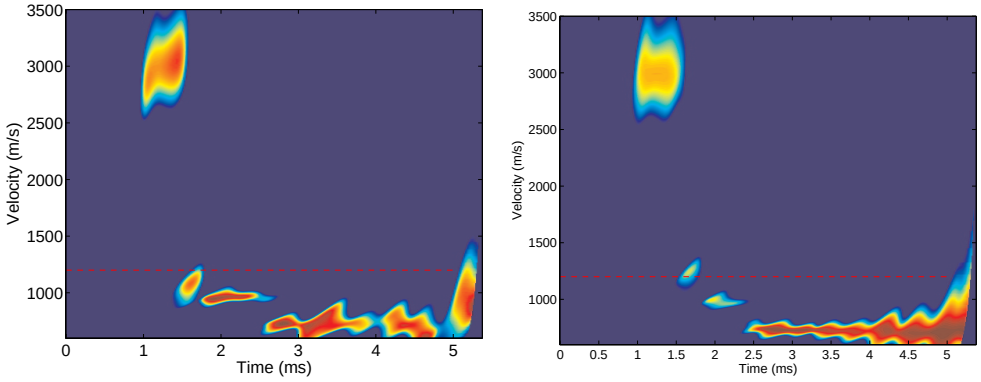

(a) R_0 largest annulus

(b) R_{90}

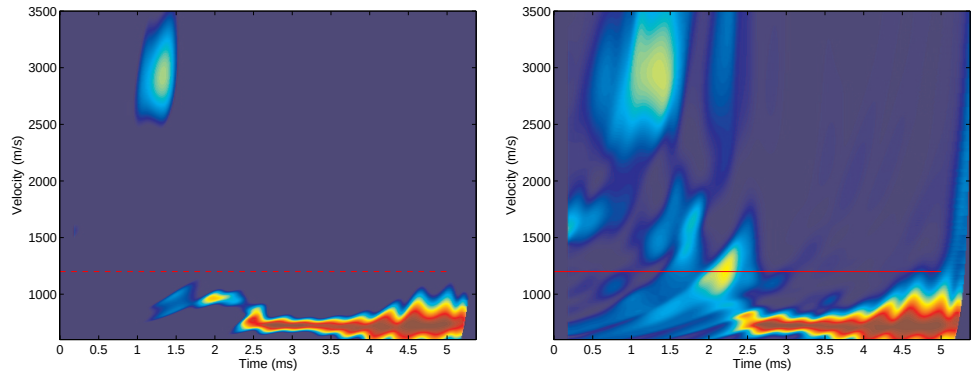

(c) R_{180} smallest annulus

(d) $R_0 + R_{180} + R_{90} + R_{270}$

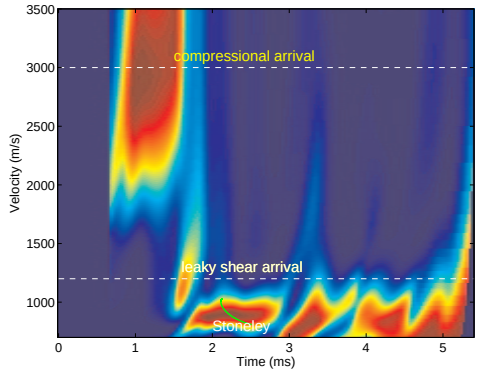

(e) centered tool

Figure 5-26: Monopole source (low frequency) off-centered (10.95 mm). Semblance results of waveforms at 0^o, 90^o, 180^o and summation of waveforms at 0^o and 180^o, as well as the semblance result from the centered tool case.

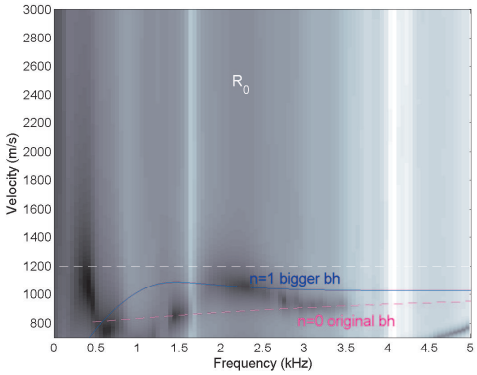

(a) R_0 largest annulus

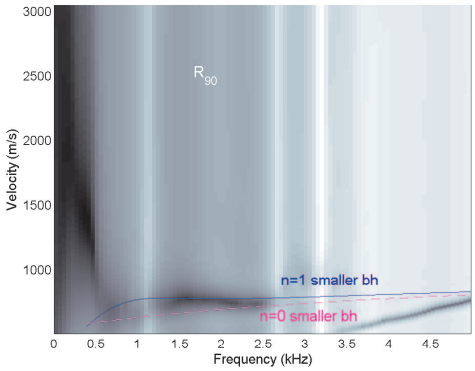

(b) R_{90}

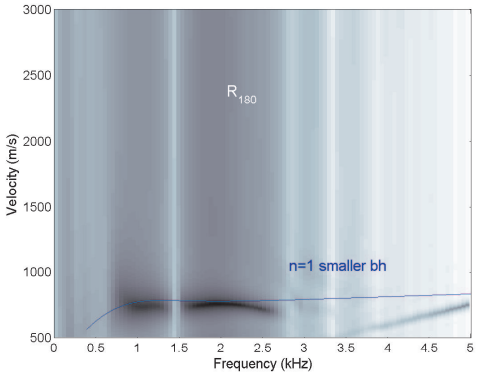

(c) R_{180} smallest annulus

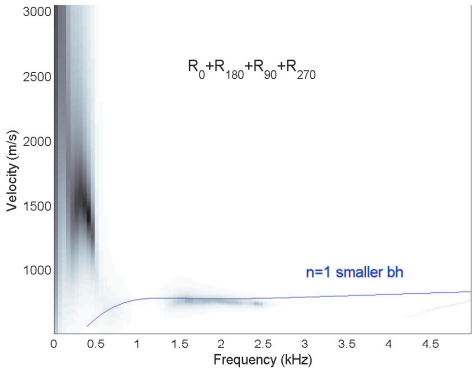

(d) $R_0 + R_{180} + R_{90} + R_{270}$

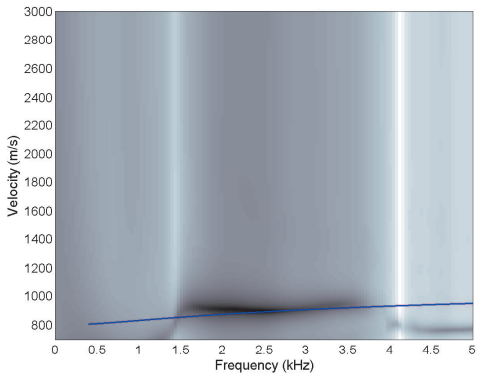

(e) centered tool

Figure 5-27: Monopole source (low frequency) off-centered (10.95 mm). Dispersion results of waveforms at 0^o, 90^o, 180^o and summation of waveforms at 0^o and 180^o, as well as dispersion result from the centered tool case. Solid lines represent borehole Stoneley (n=0) and the flexural mode (n=1) from analytical solutions with a centered LWD tool.

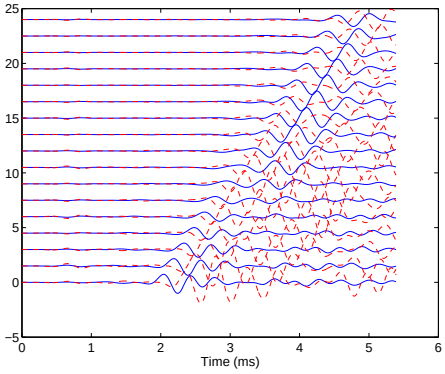

(a) 0^o and 180^o

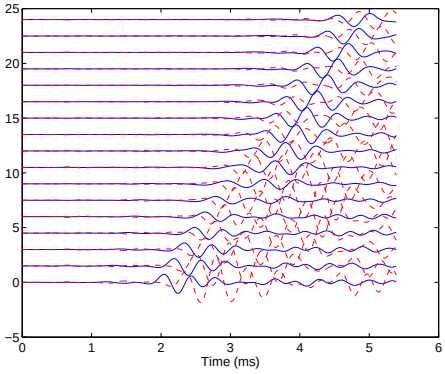

(b) 10^o and 190^o

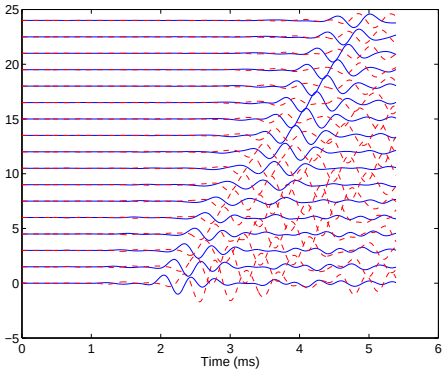

(c) 20^o and 200^o

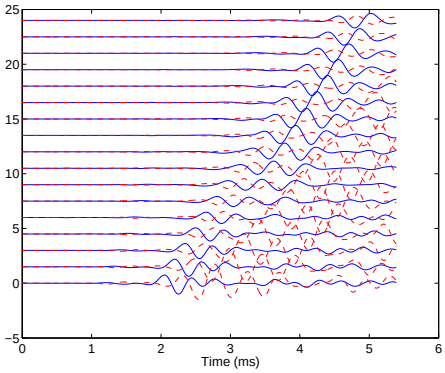

(d) 30^o and 210^o

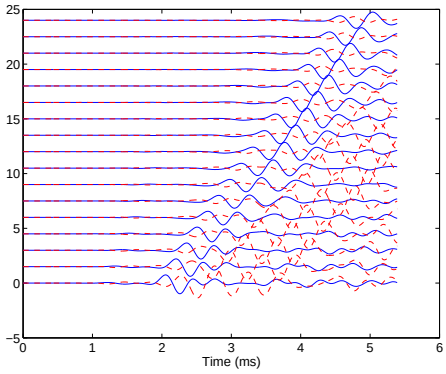

(e) 40^o and 220^o

Figure 5-28: Quadrupole source (low frequency) off-centered (10.95 mm). Waveforms received by groups of receivers at various azimuthal locations plotted with common angle gather. Dash line: receivers in the second quadrant; Solid line: receivers in the first quadrant.

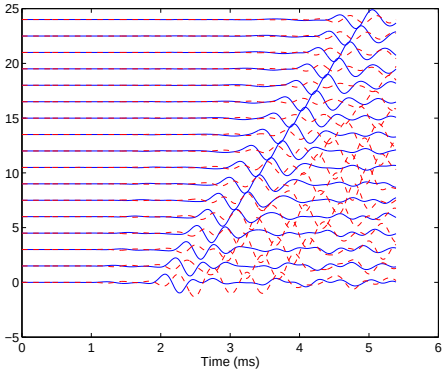

(a) 50^o and 230^o

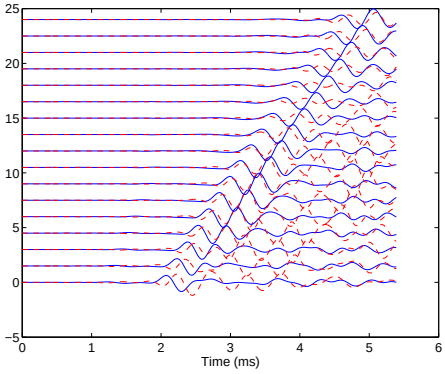

(b) 60^o and 240^o

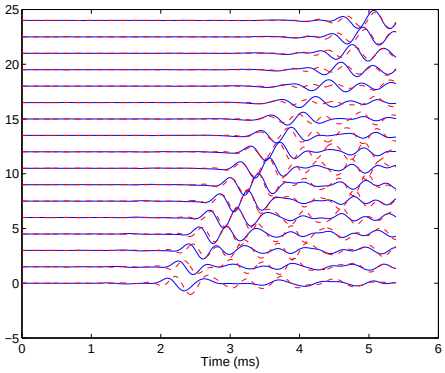

(c) 70^o and 250^o

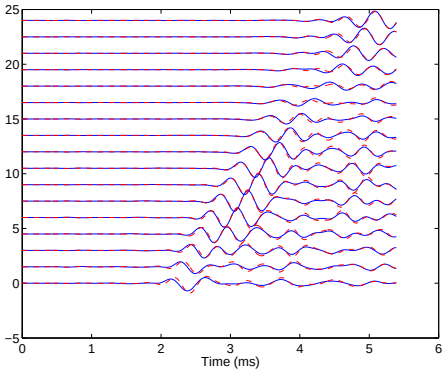

(d) 80^o and 260^o

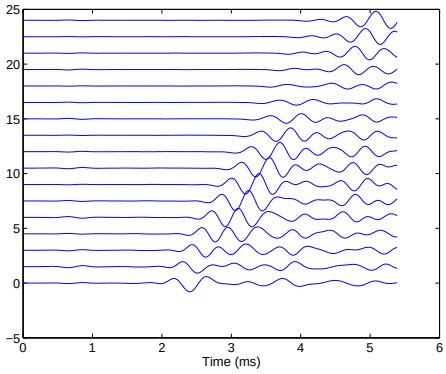

(e) 90^o

Figure 5-29: Quadrupole source (low frequency) off-centered (10.95 mm). Waveforms received by groups of receivers at various azimuthal locations plotted with common angle gather. Dash line: receivers in the second quadrant; Solid line: receivers in the first quadrant.

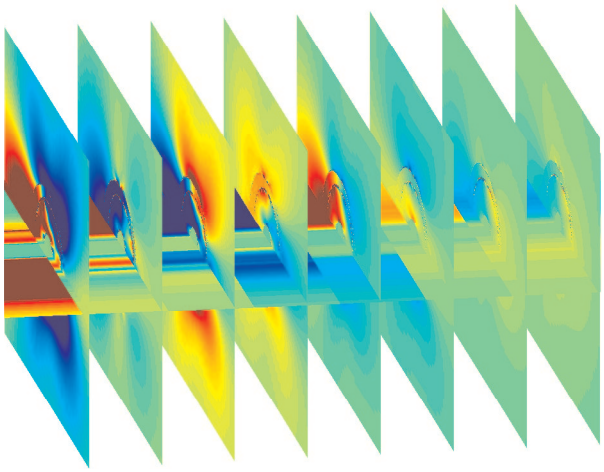

(a) 3D snapshot

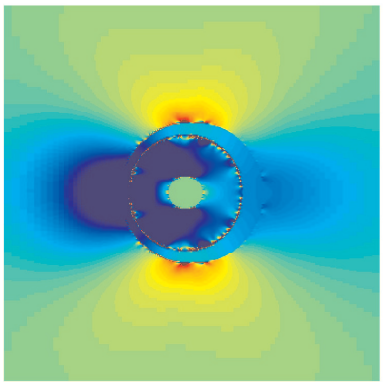

(b) cross section slice z_1

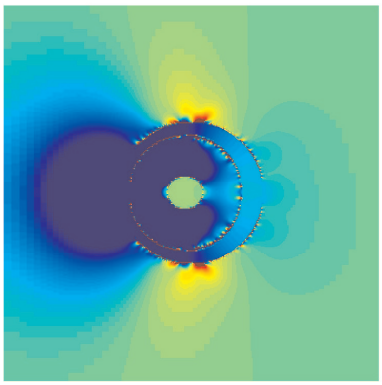

(c) cross section slice z_2

Figure 5-30: Quadrupole source (low frequency) off-centered (10.95 mm). Snapshot of wavefield (τ_{xx} component) at 2.3 ms. In figure a, each slice is at the receiver position.

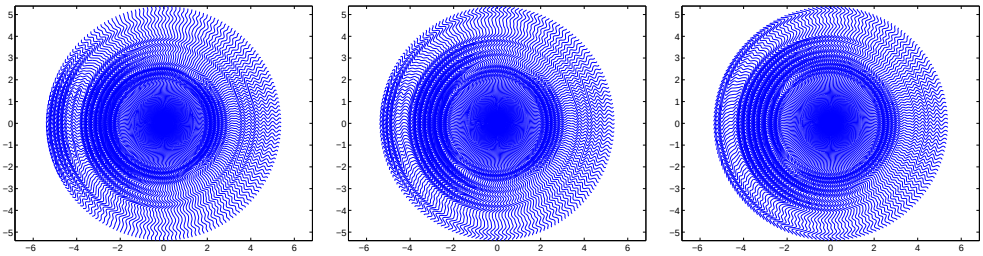

(a) R_1 (b) R_2 (c) R_3

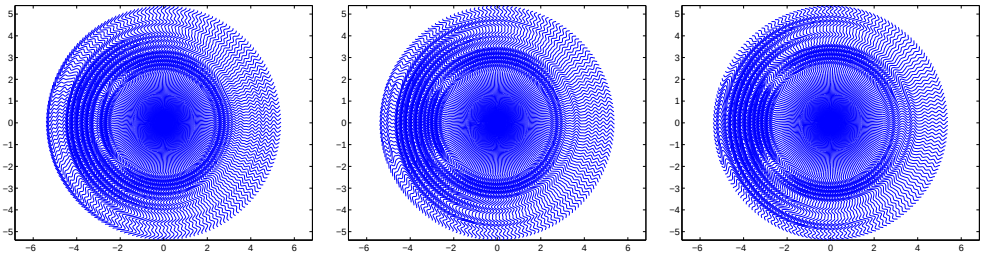

(d) R_4 (e) R_5 (f) R_6

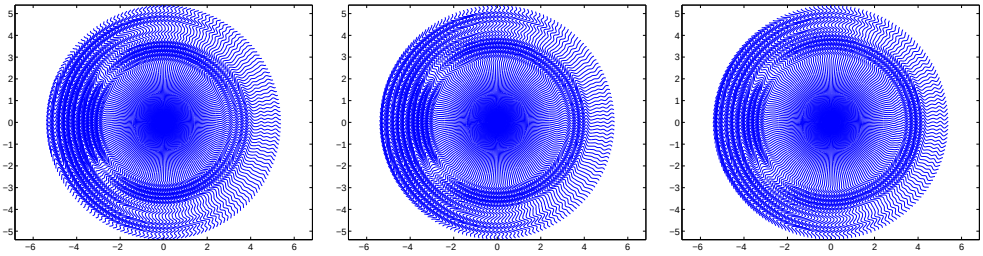

(g) R_7 (h) R_8 (i) R_9

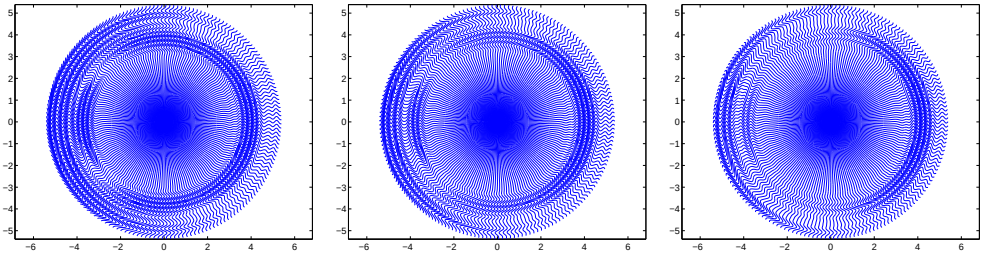

(j) R_{10} (k) R_{11} (l) R_{12}

Figure 5-31: Quadrupole source (low frequency) off-centered (10.95 mm). Waveforms received at groups of receivers at various azimuthal locations plotted as common z gather.

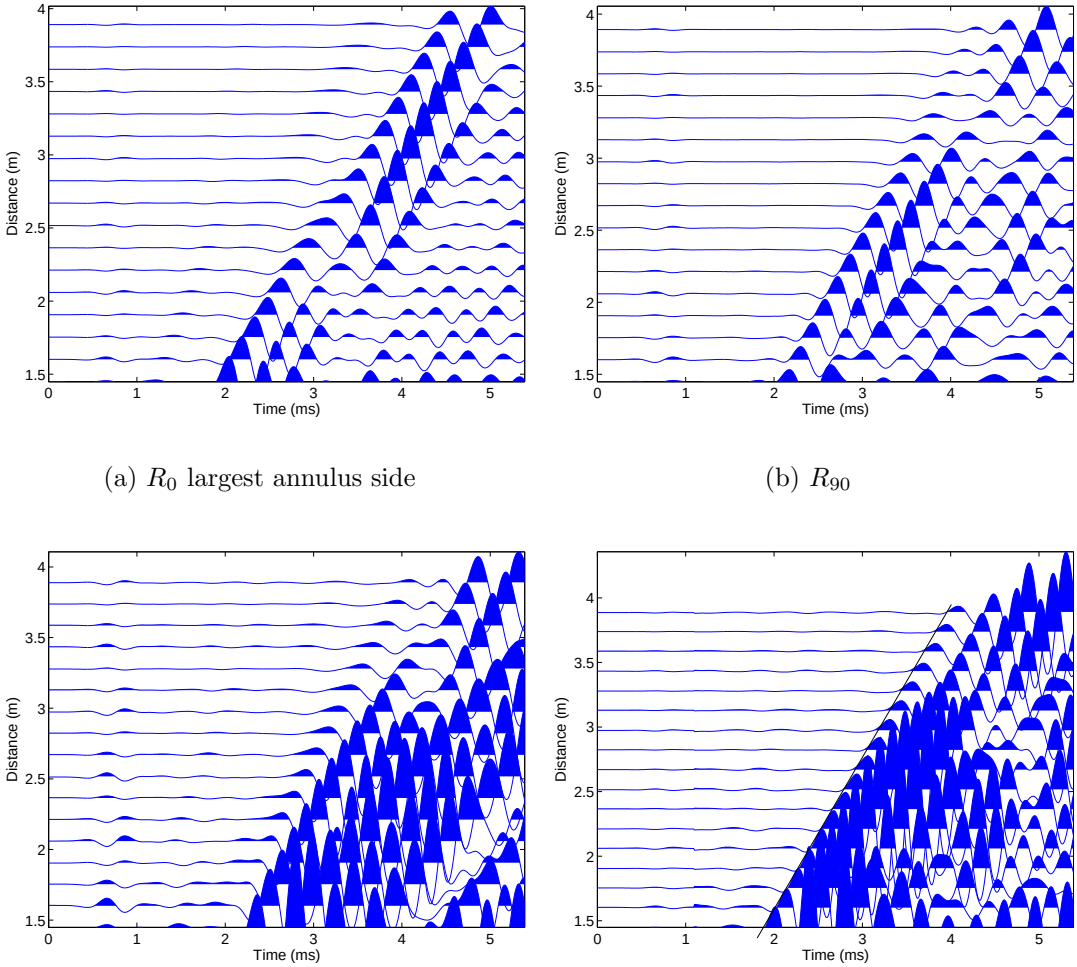

(a) R_0 largest annulus side

(b) R_{90}

(c) R_{180} smallest annulus side

(d) $R_0 + R_{180} - R_{90} - R_{270}$

Figure 5-32: Quadrupole source (low frequency) off-centered (10.95 mm). Waveforms at 0^o, 90^0, 180^o and summation of waveforms at 0^o and 180^o that subtracts waveforms at 90^o and 270^o.

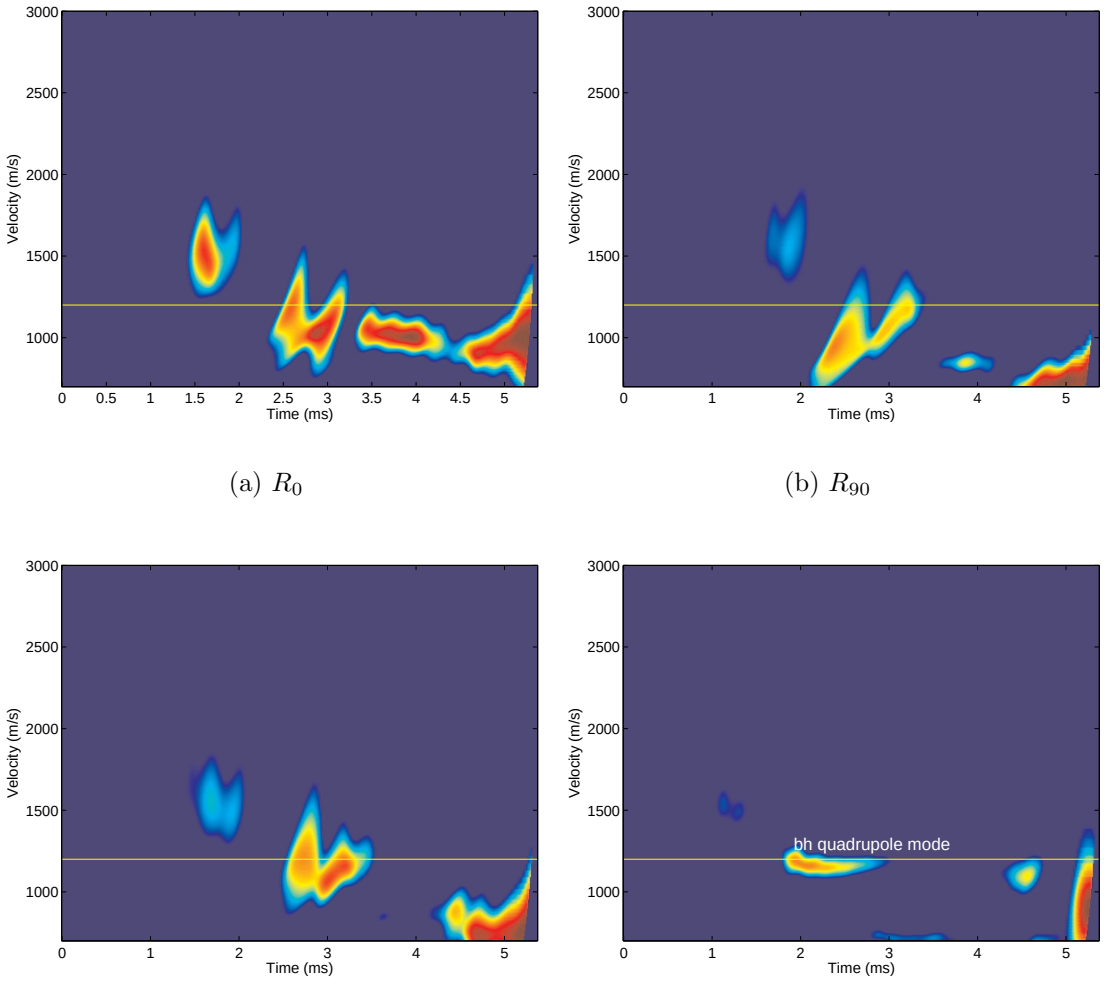

(a) R_0

(b) R_{90}

(c) R_{180}

(d) $R_0 + R_{180} - R_{90} - R_{270}$

Figure 5-33: Quadrupole source (low frequency) off-centered (10.95 mm). Semblance result of waveforms at 0^o, 90^0, 180^o and summation of waveforms at 0^o and 180^o. The quadrupole mode is brought up by summation and subtraction. Its phase velocity is at the formation shear velocity.

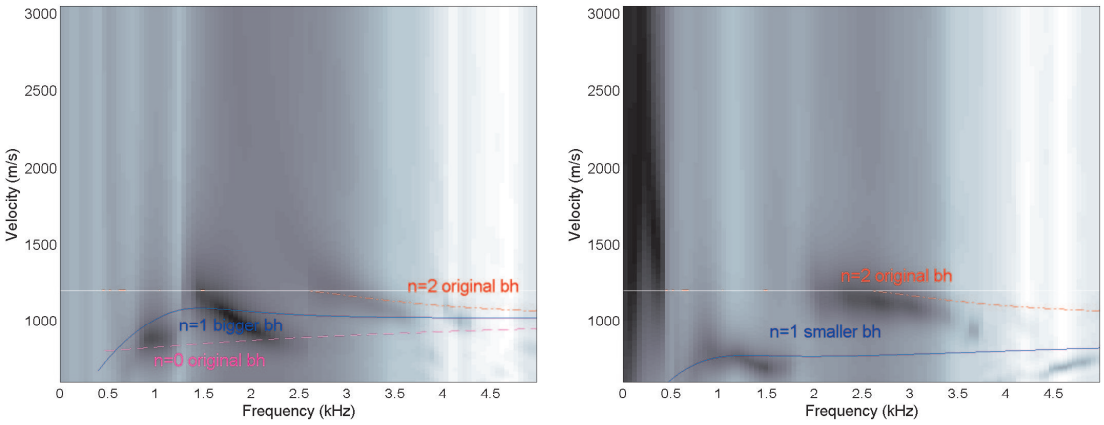

(a) R_0 large annulus side

(b) R_{90}

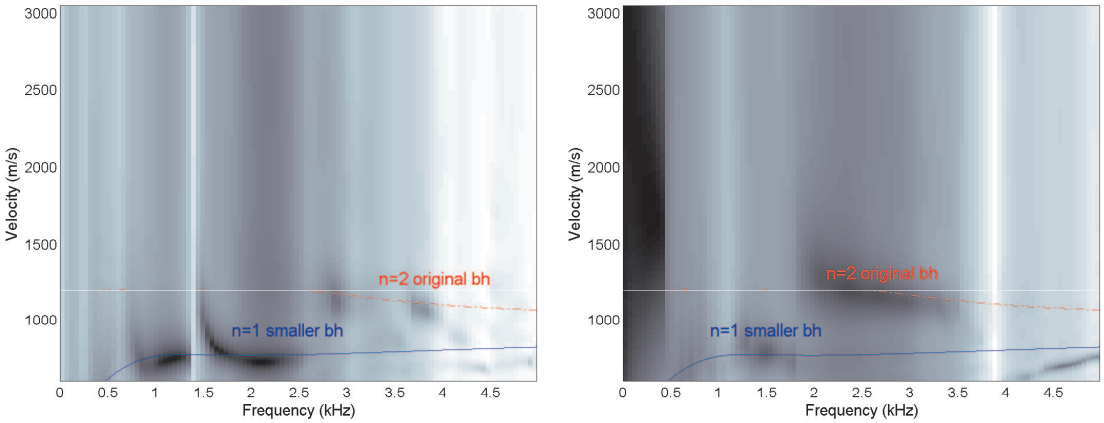

(c) R_{180} small annulus side

(d) $R_0 + R_{180} - R_{90} - R_{270}$

Figure 5-34: Quadrupole source (low frequency) off-centered (10.95 mm). Dispersion analysis result of waveforms at 0^o, 90^0, 180^o and summation of waveforms at 0^o and 180^o. Solid lines represent borehole Stoneley, flexural and quadrupole mode from analytical solutions with a centered LWD tool.

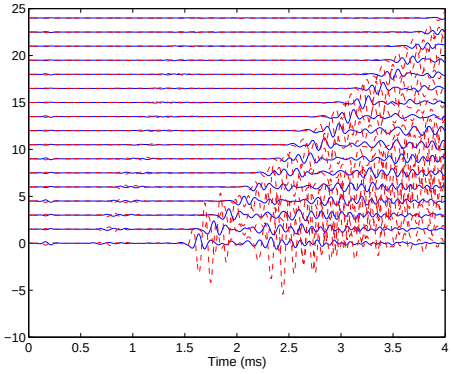

(a) 0^o and 180^o

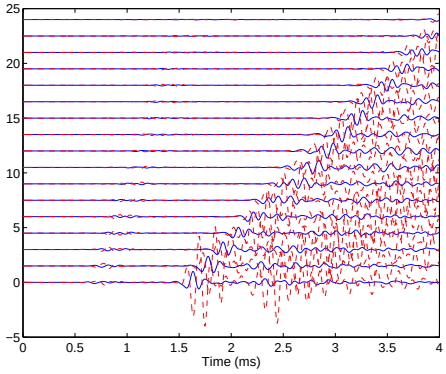

(b) 10^o and 190^o

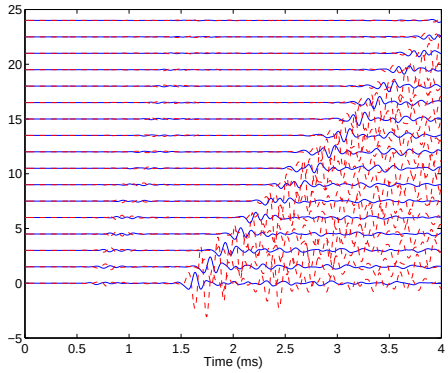

(c) 20^o and 200^o

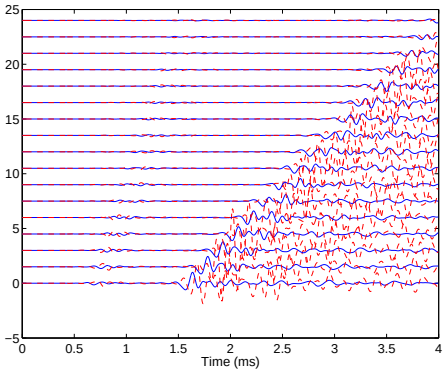

(d) 30^o and 210^o

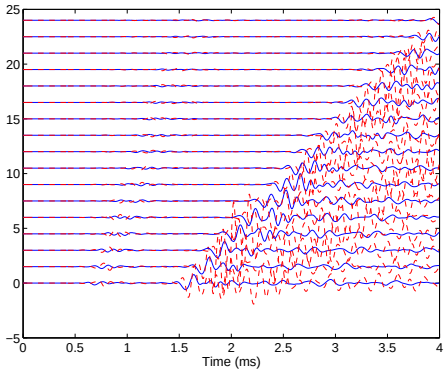

(e) 40^o and 220^o

Figure 5-35: Dipole source (high frequency) off-centered (10.95 mm). Waveforms received by groups of receivers at various azimuthal locations plotted with common angle gather. Dash line: receivers in the second quadrant; Solid line: receivers in the first quadrant.

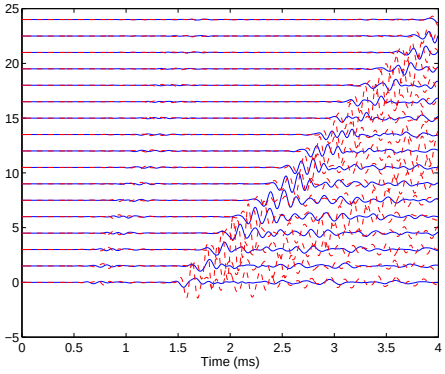

(a) 50^o and 230^o

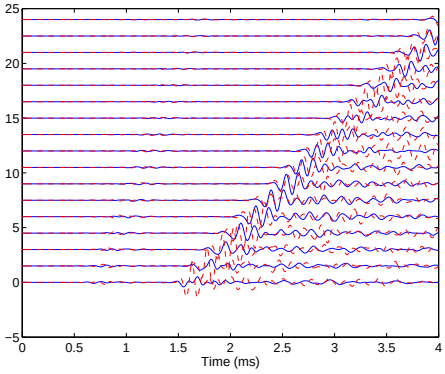

(b) 60^o and 240^o

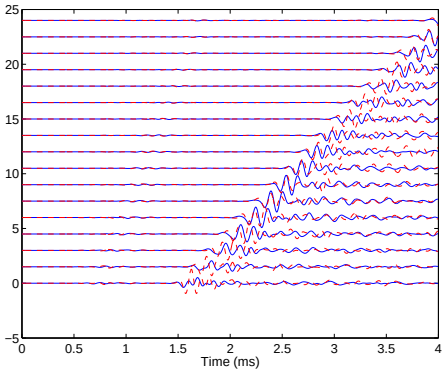

(c) 70^o and 250^o

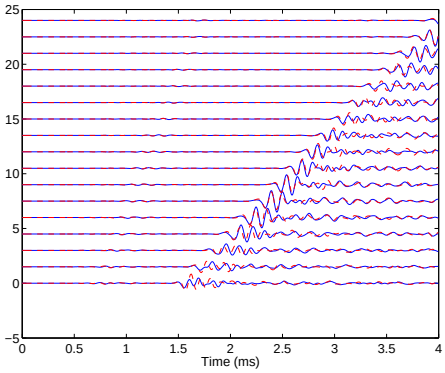

(d) 80^o and 260^o

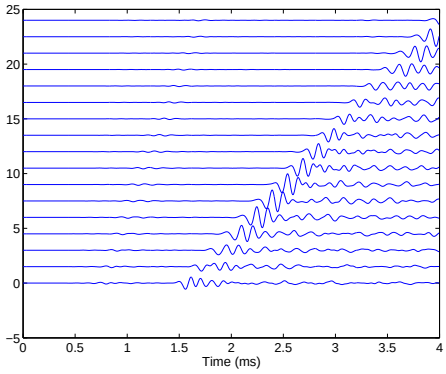

(e) 90^o

Figure 5-36: Dipole source (high frequency) off-centered (10.95 mm). Waveforms received by groups of receivers at various azimuthal locations plotted with common angle gather. Dash line: receivers in the second quadrant; Solid line: receivers in the first quadrant.

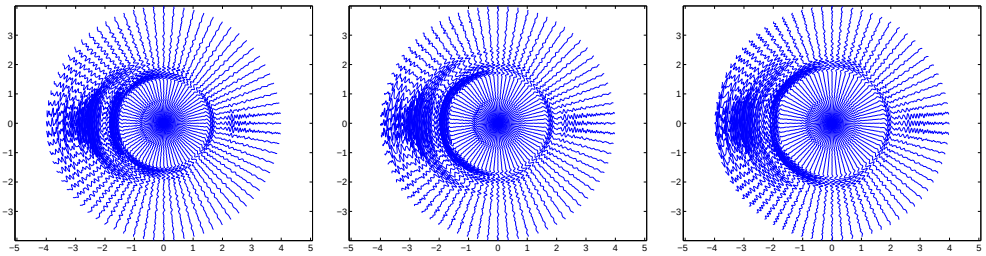

(a) R_1 (b) R_2 (c) R_3

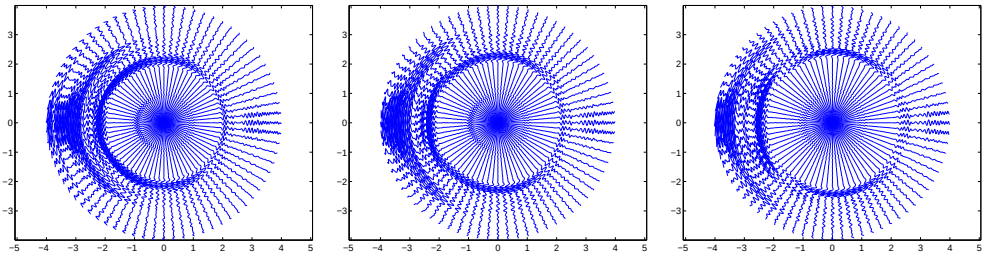

(d) R_4 (e) R_5 (f) R_6

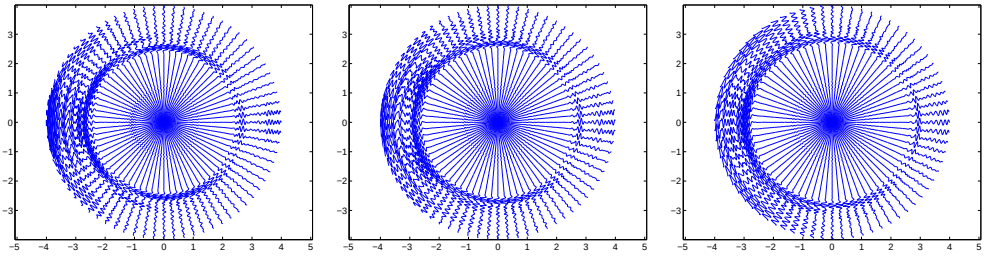

(g) R_7 (h) R_8 (i) R_9

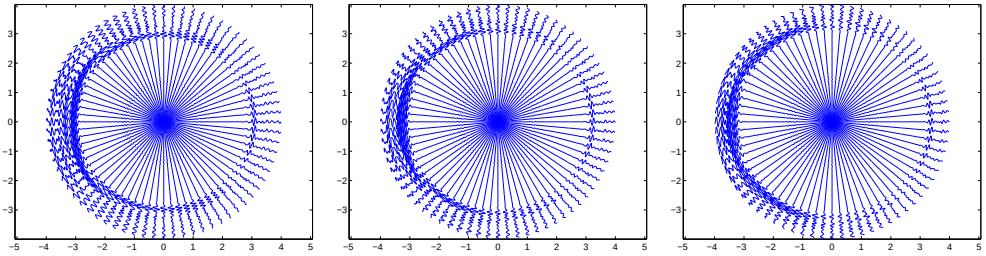

(j) R_{10} (k) R_{11} (l) R_{12}

Figure 5-37: Dipole source (high frequency) off-centered (10.95 mm). Waveforms received at groups of receivers at various azimuthal locations plotted as common z gather.

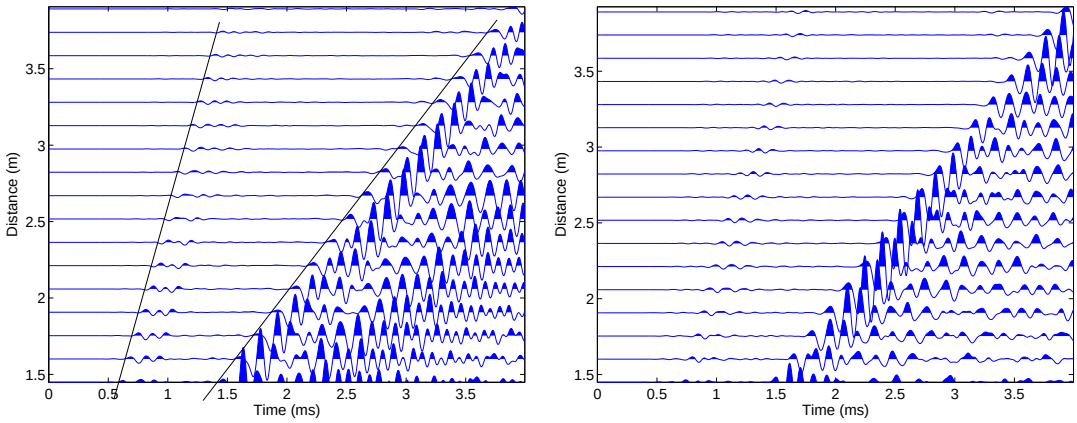

(a) R_0 large annulus side

(b) R_{90}

(c) R_{180} small annulus side

(d) $R_0 - R_{180}$

Figure 5-38: Dipole source (high frequency) off-centered (10.95 mm). Waveforms at 0^o, 90^0, 180^o and subtraction of waveforms at 0^o and 180^o.

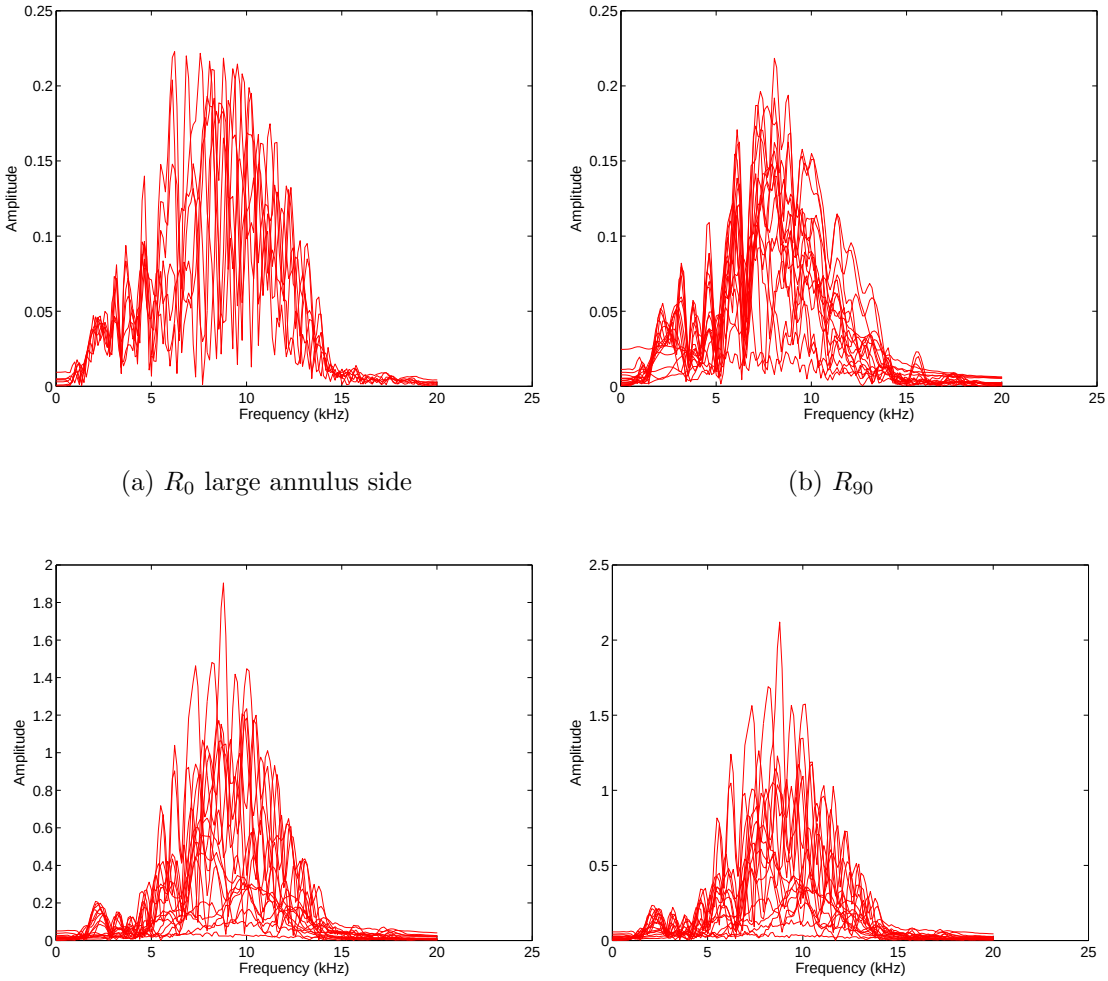

(a) R_0 large annulus side

(b) R_{90}

(c) R_{180} small annulus side

(d) $R_0 - R_{180}$

Figure 5-39: Dipole source (high frequency) off-centered (10.95 mm). Spectra of waveforms at 0^o, 90^0, 180^o and subtraction of waveforms at 0^o and 180^o.

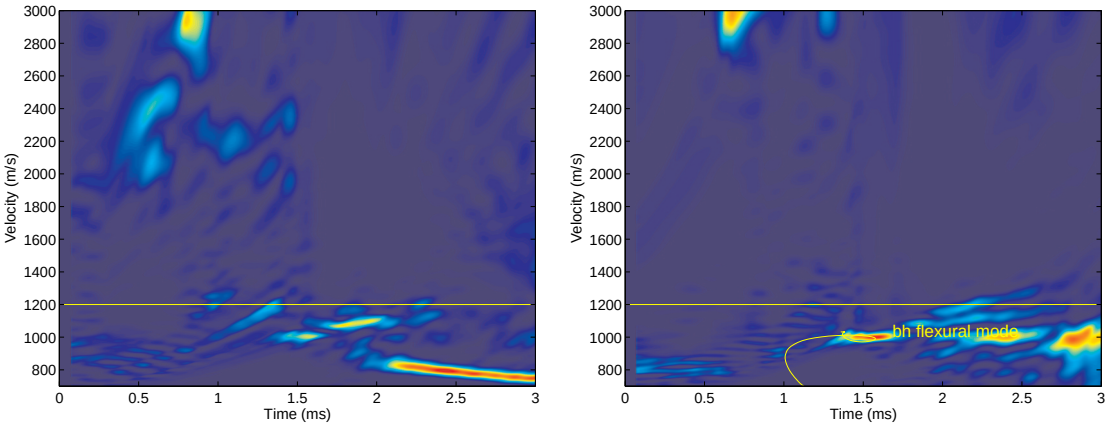

(a) R_0 large annulus side

(b) R_{90}

(c) R_{180} smallest annulus side

(d) $R_0 - R_{180}$

Figure 5-40: Dipole source (high frequency) off-centered (10.95 mm). Semblance of waveforms at 0^o, 90^0, 180^o and subtraction of waveforms at 0^o and 180^o.

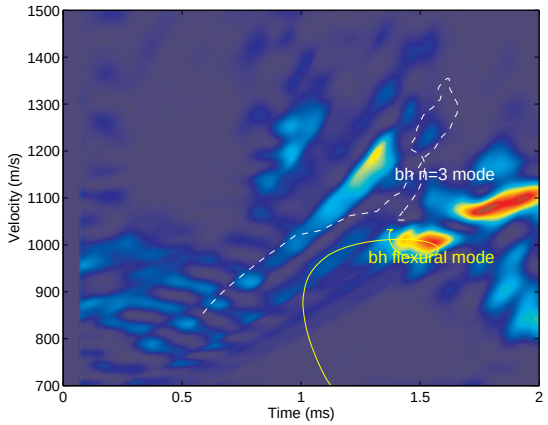

Figure 5-41: Dipole source (high frequency) off-centered (10.95 mm). Zoom-in results of waveforms at 0^o, the large annulus side. They are plotted against theoretical phase velocity *v.s* group delay curves of borehole flexural mode and borehole n=3 mode. These two modes fit the arrivals the best both in semblance and dispersion.

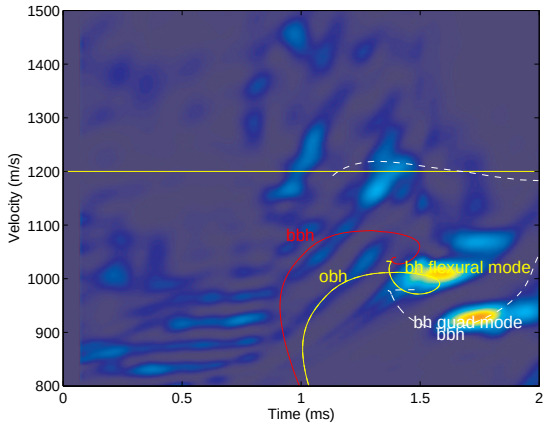

Figure 5-42: Dipole source (high frequency) off-centered (10.95 mm). Zoom-in results of waveforms at 180^o, the small annulus side. They are piloted against theoretical phase velocity *v.s* group delay curves of borehole flexural mode and borehole n=2 mode with enlarged borehole size. These modes fit the arrivals the best both in semblance and dispersion.

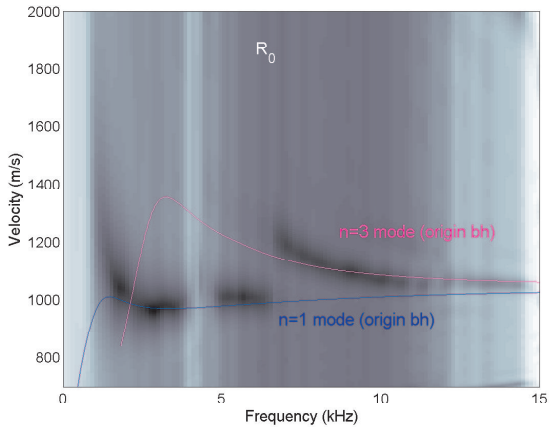

(a) R_0 large annulus side

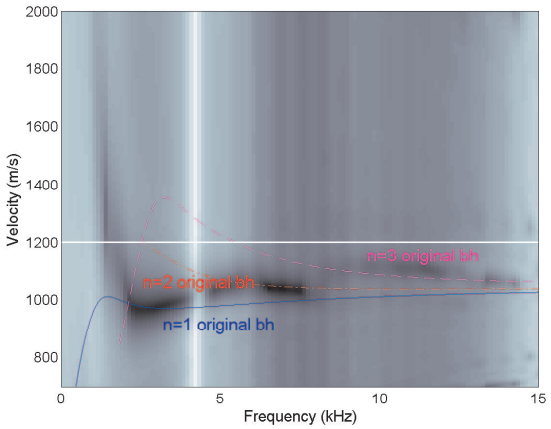

(b) R_{90}

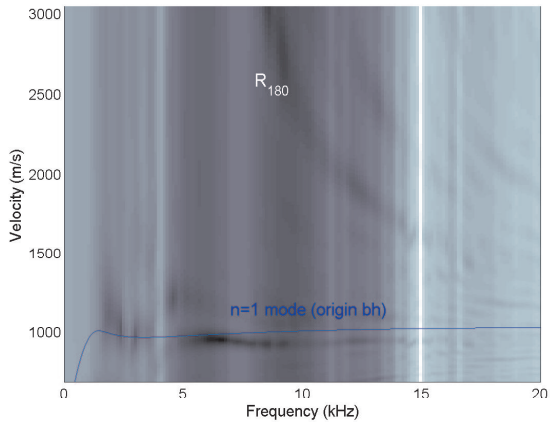

(c) R_{180} small annulus side

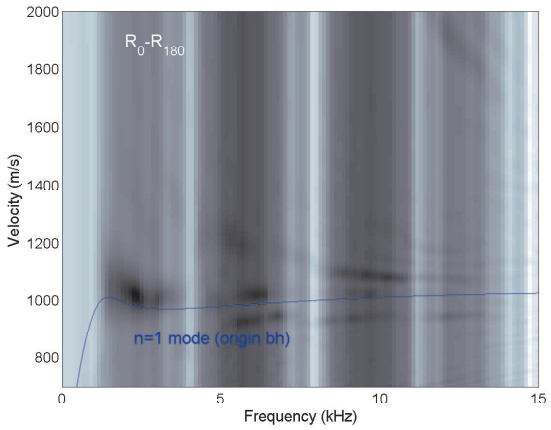

(d) $R_0 - R_{180}$

Figure 5-43: Dipole source (high frequency) off-centered (10.95 mm). Dispersion result of waveforms at 0^o, 90^0, 180^o and subtraction of waveforms at 0^o and 180^o, plotted against analytical solutions with original borehole size.

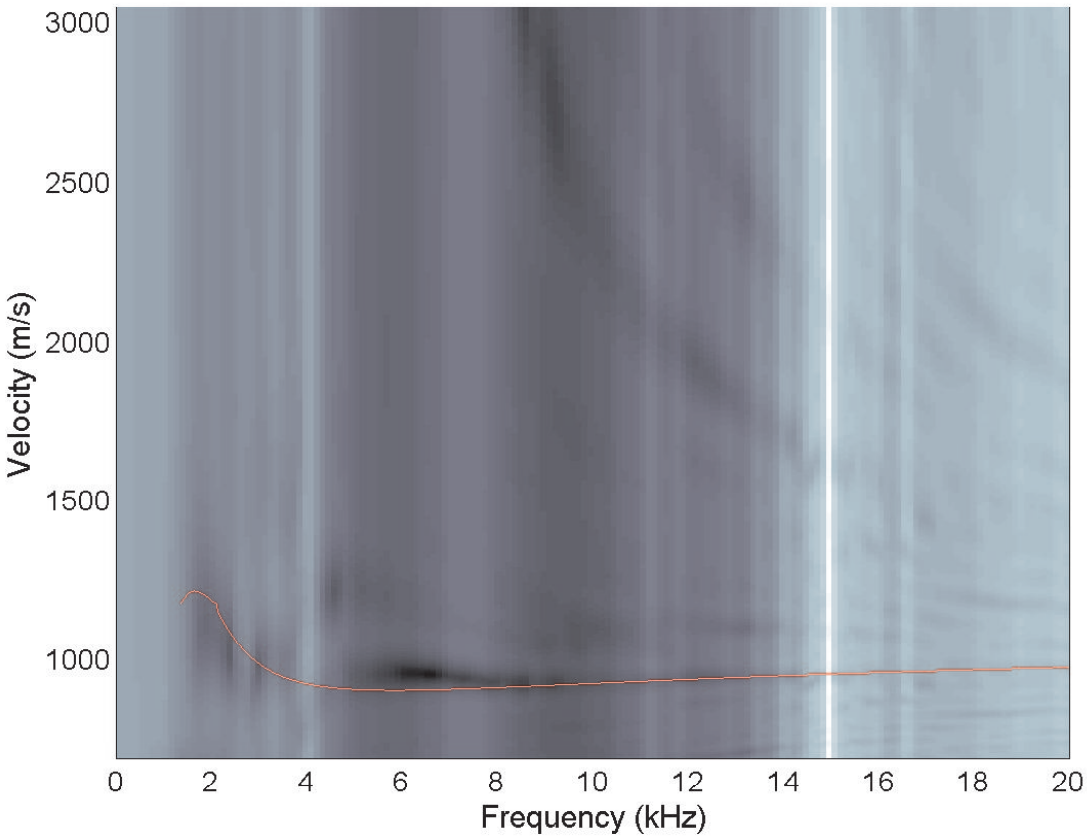

Figure 5-44: The same extracted dispersion as figure 5-43(c). The solid line is the quadrupole mode with centered LWD tool and smaller borehole size.

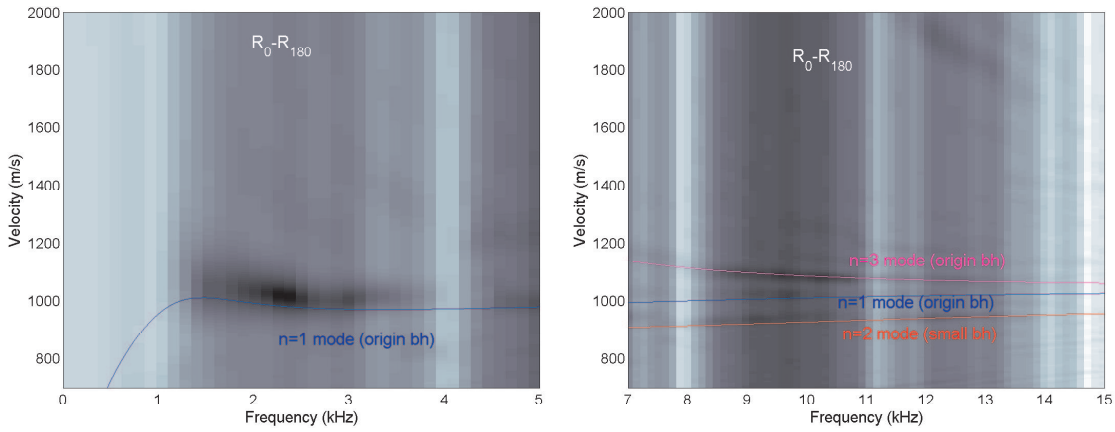

(a) Low Frequency (0 - 5 kHz)

(b) High Frequency (7 - 15 kHz)

Figure 5-45: Dipole source (high frequency) off-centered (10.95 mm). Same dispersion curves extracted from the subtracted waveforms as in figure 5-43(d). a. A closer look at low frequencies. The extracted curve agrees with the theoretical curve of the borehole flexural mode of original borehole size; b. A closer look at high frequencies. There are three modes and each is plotted against with theoretical curves that fit them the best: borehole flexural mode with original borehole size, borehole n=3 mode with original borehole size and borehole quadrupole mode (n=2) with smaller borehole size.

Chapter 6

Estimating Formation Stress Profiles from Acoustic Measurements

Abstract

In-situ formation stress directions and magnitudes are estimated by inverting the borehole flexural and Stoneley dispersions obtained from standard acoustic logging data (dipole and monopole logs). The underlying procedure consists of the following steps: first, we locate stressed zones in the formation by searching for crossovers in flexural dispersions. Second, the fast shear direction is estimated from the cross-dipole waveforms. It corresponds to the direction of the maximum horizontal stress (S_H). Finally, a multi-frequency inversion of both the Stoneley and flexural dispersions yields the maximum (S_H) and minimum (S_h) horizontal stress magnitudes together with the three formation third-order elastic (TOE) constants, c_{111}, c_{112} and c_{123}, defined about the selected reference (isotropic) state. The inversion method is based on equations that relate S_H and S_h with variations in phase velocities of the borehole flexural and Stoneley waves in the stressed state from those in the assumed reference state, the state that is hydrostatically loaded and isotropic. Phase velocities of the

flexural and Stoneley modes as a function of frequency can be obtained from processing the cross-dipole and monopole waveforms, respectively. The borehole flexural and Stoneley dispersions in the assumed reference (isotropic) state are obtained from the solution of a standard boundary-value problem. The sensitivity functions for the inversion model are obtained from the eigenfunctions of the boundary-value problem in the reference state. Results for the stress directions and magnitudes obtained from the inversion of the Stoneley and flexural dispersions over a selected bandwidth are consistent with focal mechanism and borehole breakout data present in the world map database Zoback (1992).

6.1 Introduction

As lithospheric plates interact with each other, complicated stresses patterns develop within each plate. Knowledge of formation stresses would aid in enhanced recovery of hydrocarbons, prevention of sand production and borehole instability (Gaarenstroom et al., 1993; Dore and Lundin, 1996; Finkbeiner et al., 1998; Wiprut, 2001). The formation stress state at a given location can be completely characterized by magnitudes and directions of three principal stresses, S_v, S_H, and S_h, denoting the vertical, maximum horizontal and minimum horizontal stresses, respectively (Zoback and Zoback, 1980; Zoback, 1992). Currently, large scale stress orientations are estimated from geological or geophysical data including earthquake focal mechanisms, fault slips and volcanic alignments (Zoback, 1992). For exploration and engineering purposes, earthquake and volcanic data lack the necessary resolution, not mentioning the fact that they may not occur over the desired area. At local scale, techniques like borehole breakouts and *in-situ* stress measurements, such as hydraulic fracturing and overcoring, are commonly used. In vertical boreholes, breakouts represent shear failure of the borehole wall centered in the S_h direction, the azimuth of the maximum circumferential compressive or the hoop stress (Gough and Bell, 1982; Zoback et al., 1985). They may help locate horizontal stress orientations fairly accurately, but provide little information for estimating stress magnitudes (Zoback et al., 1985). By

far the most accurate, also the most expensive, technique to measure the formation stress is hydraulic fracturing, where the formation stress is assumed to be completely balanced by a controlled fluid pressure when a shear failure happens to the borehole wall. However, that assumption often breaks down in realistic measurements (Haimson, 1988). Besides, controlled fracturing is a costly and destructive process.

In this paper a non-destructive technique is developed to estimate *in-situ* stresses indirectly from borehole acoustic measurements. Stresses induce anisotropy and velocity changes in a formation (Nur and Simmons, 1969; Lo et al., 1986). While it may be difficult in seismic data to differentiate stress induced anisotropy from intrinsic anisotropy caused by such things like depositional patterns and thin-layered bedding, this is not the case for borehole acoustic data. To satisfy the boundary conditions at the circular wall, an originally uniform stress field deforms and concentrates around a borehole. For example, in a vertical borehole, the maximum compressional stress around the borehole aligns with the direction of the minimum regional horizontal stress. Borehole flexural mode is sensitive to the far-field stress at low frequencies and to the near-field stress at high frequencies. As a result, a crossover occurs in borehole flexural dispersion, indicating stress-induced anisotropy dominating over other sources of intrinsic anisotropy. This behavior was theoretically predicted by Sinha and Kostek (1996). The prediction was subsequently verified in a laboratory scaled-borehole experiment (Winkler et al., 1998).

This study is the first example that show the flexural dispersion crossover in field data. Using the flexural crossover as a stress signature in the borehole acoustic data, we are able to isolate stressed zones. In a stressed zone, the polarization direction of fast shear wave, estimated from cross-dipole waveforms, corresponds to the direction of the maximum horizontal stress. The direction of minimum horizontal stress is perpendicular to the fast shear direction.

In the presence of horizontal stresses, S_H and S_h, changes in the Stoneley and flexural dispersions from a nearby reference state can be described by a linear perturbation model (Sinha and Kostek, 1996). This perturbation model is used as the basis for the inversion of borehole dispersions for the stress magnitudes. Following

the theorem of linear superposition, we derive equations that relate S_H, S_h, and the formation non-linear elastic constants c_{111}, c_{112} and c_{123} to variations in flexural and Stoneley dispersions. A multi-frequency inversion technique based on these equations yields the deviatoric stress magnitudes (S_H and S_h) from those assumed in the reference state.

6.2 Stress Magnitude Estimation

In order to evaluate magnitudes of horizontal stresses, a perturbation model is applied that quantitatively describes how the magnitude of horizontal stresses is related to borehole flexural dispersions (Tiersten, 1978; Norris et al., 1994; Sinha and Kostek, 1996).

Before we outline the perturbation derivation for a small dynamic field superimposed on a pres-tress, we briefly introduce some preliminary terminology and notation. A detailed version of the underlining theoretical framework and the test of its applicability to real rocks in described in Appendix C. The kinematics of deformation of a material point associated with a propagating wave in a stressed medium can be described in terms of three different configurations of the solid: the *reference*, *intermediate*, and *current* configurations of material points. These configurations denote the undeformed state, statically deformed biasing state, and the state of elastic wave-induced deformation superimposed on the bias, respectively. We first note that under the static bias the material points move from the *reference* coordinates X_L to the *intermediate* coordinates ξ_α, and we can map points from the *reference* coordinates to the *intermediate* coordinates by

$$\xi_\alpha = \xi_\alpha(X_L). \tag{6.1}$$

Then, for the superposed small dynamic motion, the material points move from the *intermediate* coordinates ξ_α to the *present* coordinates y_i, and we have

$$y_i = y_i(\xi_\alpha, t) = \hat{y}_i(X_L, t). \tag{6.2}$$

All notations follow the convention that capital Latin indices, lower-case Greek indices, and lower-case Latin indices, refer to the Cartesian components of the *reference* coordinates, *intermediate* coordinates, and *present* coordinates of material points, respectively. A comma followed by an index denotes partial differentiation with respect to a geometric coordinate. Also, the summation convention for repeated tensor indices and the dot notation for differentiation with respect to time hold. The coordinate system is set up as X_1 along borehole axis, and X_2 and X_3 in the plane perpendicular to X_1. Equations 6.1 and 6.2 are mapping functions that relate three configurations of the solid. In this paper, the density, linear moduli and third-order moduli of the material refer to a specific *reference* state.

In a reference state, the equations of motion for a borehole mode can be expressed as

$$K^{Lm}_{L\gamma,L} + \rho_o \omega_m^2 u^m_\gamma = 0 \tag{6.3}$$

where $K^{Lm}_{L\gamma}$ is the Piola-Kirchhoff stress tensor in linear elasticity that defines stresses in the *intermediate* and *reference* configurations (Truesdell and Noll, 1992), ρ_0 is the density in the reference configuration, and u^m_γ denotes a small amplitude dynamic solution to the wave equation of a fluid-filled borehole surrounded by an isotropic and homogeneous formation (*reference* state) at an eigen-frequency, ω_m (Biot, 1952).

Referring to the *reference* state, the equation of motion in the presence of initial stresses in the medium (i.e., a static bias) may be written in terms of Piola-Kirchhoff stress tensor as

$$K^L_{L\gamma,L} + K^{NL}_{L\gamma,L} + \rho_0 \omega^2 u_\gamma = 0 \tag{6.4}$$

where $K^{NL}_{L\gamma}$ is the nonlinear portion of the Piola-Kirchhoff stress tensor that denotes the perturbation from the linear portion, $K^L_{L\gamma}$. $K^L_{L\gamma}$ and $K^{NL}_{L\gamma}$ may be expressed as

$$K^L_{L\gamma} = c_{L\gamma M\nu} u_{\nu,M} \tag{6.5}$$

and

$$K^{NL}_{L\gamma} = \hat{c}_{L\gamma M\nu} u_{\nu,M} \tag{6.6}$$

where

$$\hat{c}_{L\gamma M\nu} = T_{LM}\delta_{\gamma\nu} + c_{L\gamma M\nu AB}E_{AB} + c_{L\gamma KM}w_{\nu,K} + c_{LKM\nu}w_{\gamma,K} \tag{6.7}$$

with

$$T_{LM} = c_{LMRS}w_{R,S} \tag{6.8}$$

and

$$E_{AB} = \frac{1}{2}(w_{A,B} + w_{B,A}). \tag{6.9}$$

In equation 6.4, u_γ denotes the small-amplitude dynamic solution at a frequency of ω in the presence of a static bias. $c_{L\gamma M\nu}$ and $c_{L\gamma M\nu AB}$ are the second and third-order elastic constants, respectively (Thurston and Brugger, 1964). In equations 6.7, 6.8 and 6.9, T_{LM}, E_{AB} and $w_{\gamma,K}$ denote the biasing stresses, strains and (static) displacement gradients, respectively. Note that the biasing stresses, strains and displacement gradients are spatially varying due to borehole stress concentration. Therefore, $K^L_{L\gamma,L}$ and $K^{NL}_{L\gamma,L}$ are position dependent and a direct solution of the boundary-value problem is not possible.

Equations 6.3 and 6.4 can be combined to form an integral equation valid for a continuum of arbitrary volume V_0 in the reference configuration:

$$\int_{V_0} dV_0[(K^L_{L\gamma,L} + K^{NL}_{L\gamma,L} + \rho_0\omega^2 u_\gamma)u^{m*}_\gamma - (K^{Lm}_{L\gamma,L} + \rho_0\omega^2_m u^m_\gamma)u^*_\gamma] = 0 \tag{6.10}$$

where * denotes complex conjugate. According to Gauss's theorem of divergence, equation 6.10 can be re-cast into a form that is convenient for calculating a small perturbation at the frequency ω_m:

$$\begin{aligned}\int_{V_0} dV_0\rho_0(\omega^2 u_\gamma u^{m*}_\gamma - \omega^2_m u^m_\gamma u^*_\gamma) &= \oint_{S_0} N_L[K^{Lm}_{L\gamma}u^*_\gamma - K^L_{L\gamma}u^{m*}_\gamma] \\ &- \int_{V_0} dV_0 K^{NL}_{L\gamma,L}u^{m*}_\gamma \end{aligned} \tag{6.11}$$

where N_L is the outward unit normal in the reference or undeformed configuration. S_0 is the surface surrounding V_0. The quantities in the perturbed state (i.e. in the presence of biasing stresses and strains) are related to those in the unperturbed state

by assuming the linear relationships

$$u_\gamma = u_\gamma^m + \epsilon u_\gamma, \tag{6.12}$$

$$u_\gamma^* = u_\gamma^* + \epsilon u_\gamma^* \tag{6.13}$$

and

$$\omega = \omega_m + \Delta\omega_m \tag{6.14}$$

where ϵ is an arbitrary small number. Substituting equation 6.12, 6.13 and 6.14 into equation 6.11 and neglecting quadratic or higher terms of ϵ and $\Delta\omega_m$ yields a general form of the perturbation integral for calculating changes in the eigen frequency ω_m caused by the biasing stresses and strains:

$$\Delta\omega_m = \frac{\oint_{S_0} dS_0 N_L [K_{L\gamma}^{Lm} u_\gamma^* - K_{L\gamma}^L u_\gamma^{m*}] - \int_{V_0} dV_0 K_{L\gamma,L}^{NL} u_\gamma^{m*}}{2\omega_m \int_{V_0} \rho_0 u_\gamma^m u_\gamma^{m*} dV_0}. \tag{6.15}$$

The boundary surface S_0 is at the borehole wall; therefore, N_L denotes the negative radial direction, and $N_L K_{L\gamma} u_\gamma^*$ represents the energy flux in the negative radial direction. There is no energy flow in the radial direction for any guided mode that decays away from the borehole in both the unperturbed and perturbed states. Consequently, we have

$$N_L K_{L\gamma}^{Lm} u_\gamma^{m*} = 0, \tag{6.16}$$

and in the perturbed state we have

$$N_L (K_{L\gamma}^L + K_{L\gamma}^{NL}) u_\gamma^* = 0. \tag{6.17}$$

Applying Gauss's theorem of divergence to the volume integral in the numerator of equation 6.15 and incorporating equations 6.16 and 6.17, the first-order perturbation in the eigen-frequency ω_m is obtained as

$$\Delta\omega_m = \frac{\int_{V_0} K_{L\gamma}^{NL} u_{\gamma,L}^{m*} dV_0}{2\omega_m \int_{V_0} \rho_0 u_\gamma^m u_\gamma^{m*} dV_0}. \tag{6.18}$$

Note that elements of the nonlinear part of the Piola-Kirchhoff stress tensor $K_{L\gamma}^{NL}$ in equation 6.18 are known in terms of the second- and third-order elastic constants and biasing stresses in the statically deformed state as given by equations 6.7, 6.8 and 6.9. The index m refers to the family of normal modes for a borehole in the reference state. Eigen-frequencies of each normal mode, ω_m are solved previously (Biot, 1952; Peterson, 1974; Tsang and Rader, 1979; Cheng and Toksoz, 1981). For each of the modes that are sensitive to stress application, such as the flexural mode and Stoneley mode, at a given wavenumber k_z, the first-order perturbation in the eigen-frequency ω_m at each wavenumber k_z, is obtained by $\omega_m + \Delta\omega_m$.

Without reducing generality, let us assume S_H is applied in the X_2-direction while S_h is applied in the X_3-direction. First, let us take $S_h = 0$. Thus, the borehole is subject to a uniaxial stress S_H. For a given wavenumber k_z, the first-order perturbation in eigen-frequencies of the Stoneley and flexural modes, ω_2, ω_3 and ω_{St}, may be given by (Sinha, 1997)

$$\begin{aligned} \frac{\Delta\omega_2^H}{k_z} &= C_1^0 S_H + C_2^0 S_H \frac{c_{111}}{c_{66}} + C_3^0 S_H \frac{c_{112}}{c_{66}} \\ &+ C_4^0 S_H \frac{c_{123}}{c_{66}}, \end{aligned} \tag{6.19}$$

$$\begin{aligned} \frac{\Delta\omega_3^H}{k_z} &= C_1^{90} S_H + C_2^{90} S_H \frac{c_{111}}{c_{66}} + C_3^{90} S_H \frac{c_{112}}{c_{66}} \\ &+ C_4^{90} S_H \frac{c_{123}}{c_{66}}, \end{aligned} \tag{6.20}$$

and

$$\begin{aligned} \frac{\Delta\omega_{St}}{k_z} &= C_1 S_H + C_2 S_H \frac{c_{111}}{c_{66}} + C_3 S_H \frac{c_{112}}{c_{66}} \\ &+ C_4 S_H \frac{c_{123}}{c_{66}}, \end{aligned} \tag{6.21}$$

where $\Delta\omega_{St}^H$, $\Delta\omega_2^H$ and $\Delta\omega_3^H$ denote first-order frequency perturbations for the Stoneley wave and flexural waves polarized in the X_2- and X_3-directions, respectively. Coefficients C_i^0, C_i^{90}, and C_i, with i = 1, 2, 3 and 4, are frequency dependent integrals

that can be evaluated in terms of the known flexural wave solution in the reference state and biasing stresses of unit-magnitude and corresponding strains in the formation (see Appendix D). The superscript 0 denotes flexural wave polarization along the far-field uniaxial stress direction, while 90 denotes flexural wave polarization in the perpendicular direction.

Similarly, if S_H=0 and only S_h is applied, the corresponding first-order perturbations in respective eigen-frequencies ω_2, ω_3 and ω_{St} are

$$\begin{aligned}\frac{\Delta\omega_2^h}{k_z} &= C_1^{90}S_h + C_2^{90}S_h\frac{c_{111}}{c_{66}} + C_3^{90}S_h\frac{c_{112}}{c_{66}} \\ &+ C_4^{90}S_h\frac{c_{123}}{c_{66}},\end{aligned} \tag{6.22}$$

$$\begin{aligned}\frac{\Delta\omega_3^h}{k_z} &= C_1^{0}S_h + C_2^{0}S_h\frac{c_{111}}{c_{66}} + C_3^{0}S_h\frac{c_{112}}{c_{66}} \\ &+ C_4^{0}S_h\frac{c_{123}}{c_{66}},\end{aligned} \tag{6.23}$$

and

$$\begin{aligned}\frac{\Delta\omega_{St}^h}{k_z} &= C_1S_h + C_2S_h\frac{c_{111}}{c_{66}} + C_3S_h\frac{c_{112}}{c_{66}} \\ &+ C_4S_h\frac{c_{123}}{c_{66}}.\end{aligned} \tag{6.24}$$

Note that S_h is in the X_3-direction; thus flexural wave polarization oriented in the X_2-direction is perpendicular to the far-field uniaxial stress direction. Also first-order perturbations of the respective eigen-frequencies are function of stress magnitude. The total first-order frequency perturbations due to the application of the two uniaxial stresses of S_H and S_h are linear combinations of $\Delta\omega_m^H$ and $\Delta\omega_m^h$, *i.e.*, $\Delta\omega_m = \Delta\omega_m^H + \Delta\omega_m^h$, with $m = 2, 3$ and St, respectively. Frequency perturbations $\Delta\omega_m$ are added to their respective eigen-frequencies ω_m for various values of the wavenumber along the borehole axis, k_z, to obtain changes in phase velocities of two principal flexural

waves and the Stoneley wave at a given frequency,

$$\begin{aligned}\frac{v_2 - v_R}{v_R} = \; & S_H(C_1^0 + C_2^0\frac{c_{111}}{c_{66}} + C_3^0\frac{c_{112}}{c_{66}} + C_4^0\frac{c_{123}}{c_{66}}) \\ & + S_h(C_1^{90} + C_2^{90}\frac{c_{111}}{c_{66}} + C_3^{90}\frac{c_{112}}{c_{66}} + C_4^{90}\frac{c_{123}}{c_{66}}),\end{aligned} \tag{6.25}$$

$$\begin{aligned}\frac{v_3 - v_R}{v_R} = \; & S_h(C_1^0 + C_2^0\frac{c_{111}}{c_{66}} + C_3^0\frac{c_{112}}{c_{66}} + C_4^0\frac{c_{123}}{c_{66}}) \\ & + S_H(C_1^{90} + C_2^{90}\frac{c_{111}}{c_{66}} + C_3^{90}\frac{c_{112}}{c_{66}} + C_4^{90}\frac{c_{123}}{c_{66}}),\end{aligned} \tag{6.26}$$

and

$$\frac{v^{St} - v_R^{St}}{v_R^{St}} = (S_H + S_h)(C_1 + C_2\frac{c_{111}}{c_{66}} + C_3\frac{c_{112}}{c_{66}} + C_4\frac{c_{123}}{c_{66}}), \tag{6.27}$$

where v_R and v_R^{St} are the flexural and Stoneley phase velocities in the reference state. Equations 6.25, 6.26 and 6.27 are used as the the forward modeling in the inversion for S_H, S_h, c_{111}, c_{112}, and c_{123}. Phase velocities of the Stoneley wave, v^{St}, and flexural waves, v_2 and v_3 in equations 6.25, 6.26 and 6.27, are determined from the monopole and cross-dipole waveforms, respectively. Phase velocities in the reference state can be computed numerically by solving an eigenvalue problem of a fluid-filled borehole surrounded by an isotropic formation. Note that except for the five unknowns S_H, S_h, c_{111}, c_{112}, and c_{123}, and the formation elastic constant in the reference state c_{66}, all quantities in equations 6.25, 6.26 and 6.27 are frequency dependent. Consequently, phase velocities of v_2, v_3, v^{St}, v_R and v_R^{St} at multipole wavenumbers (k_z) are selected to construct the inversion scheme. Nonlinear lest square approach is used for the inversion.

6.3 Results from Cross-dipole and Monopole Logs in California

We analyze a set of cross-dipole and monopole waveforms acquired by a wireline acoustic tool in a vertical well for the estimation of stress directions and magnitudes.

The well is located in the southwestern San Joaquin basin in California, about 60 km from the San Andreas fault(figure 6-1).

The data were acquired every 15 cm (6 inches) from 479 m (1571.5 feet) in depth up to 131.5 m (431.5 feet). The cross-dipole tool consists of one pair of dipole sources with orthogonal polarizations and eight pairs of dipole receivers polarized in the same directions with the dipole sources. Figure 6-2 shows a diagram of a cross-dipole logging tool. The receiver pairs are 15 cm (6.0 inches) apart. The nearest receiver pair is 3.35 m (11 ft) away from the sources. Each receiver records waveforms that are excited by both sources, resulting 8 four-component waveforms. Denoting one dipole orientation as x and the other as y, the four-component waveforms can be labeled as d_{xx}, d_{xy}, d_{yx} and d_{yy}. d_{xy} represents waveforms excited by the dipole source polarized in the x direction and received by the dipole receiver polarized in the y direction. Monopole data, containing both the compressional headwave and the borehole Stoneley mode were acquired with a monopole tool that consists of one monopole source and eight monopole receivers with 15 cm (6 inches spacing). The four-component crossdipole waveforms and monopole waveforms at 1370.5 feet are plotted in figure 6-3. Tectonic stresses can cause stress-induced shear anisotropy in such vertical wells. Our investigation of formation stresses consists of the following steps:

1. *Low-pass filtering and time windowing of cross-dipole waveforms.* First, we use a short Fourier transform, a technique that estimates time-localized frequency contents of a waveform and generates a time-frequency domain figure that is called a spectrogram, to analyze various wave modes generated in the borehole by dipole sources. Figure 6-4a shows a typical spectrogram of waveforms recorded by a cross-dipole log. Note the earliest arrival around 15 kHz is the tool mode followed by a compressional headwave around 5 kHz. The flexural mode is a high amplitude signal around 1.5 kHz with the lowest velocity around 600 m/s. Figure 6-4b shows velocities of all the modes in their respective frequency ranges. These results show the presence of a weak compressional mode around 5 kHz; a borehole flexural mode around 1.5 kHz; and a tool arrival around 15

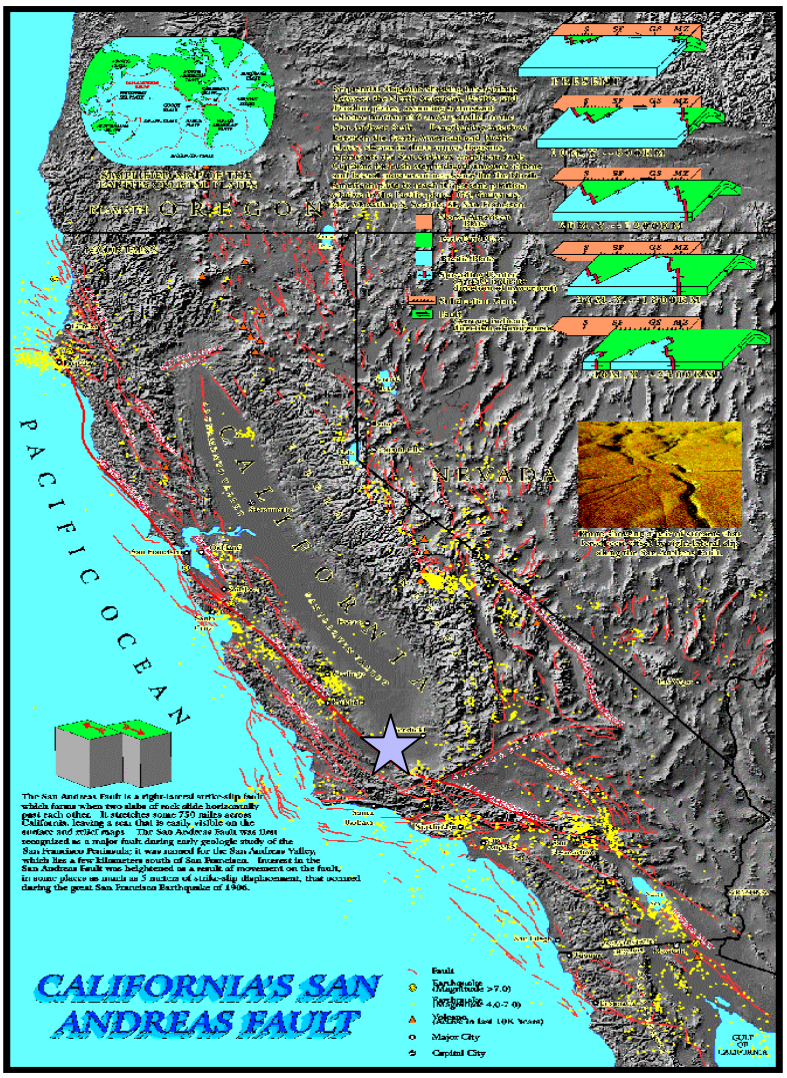

Figure 6-1: The field data is acquired in a well located in the southwestern San Joaquin basin in California, about 60 km from the San Andreas fault, as shown on a topographic map obtained from the USGS web site.

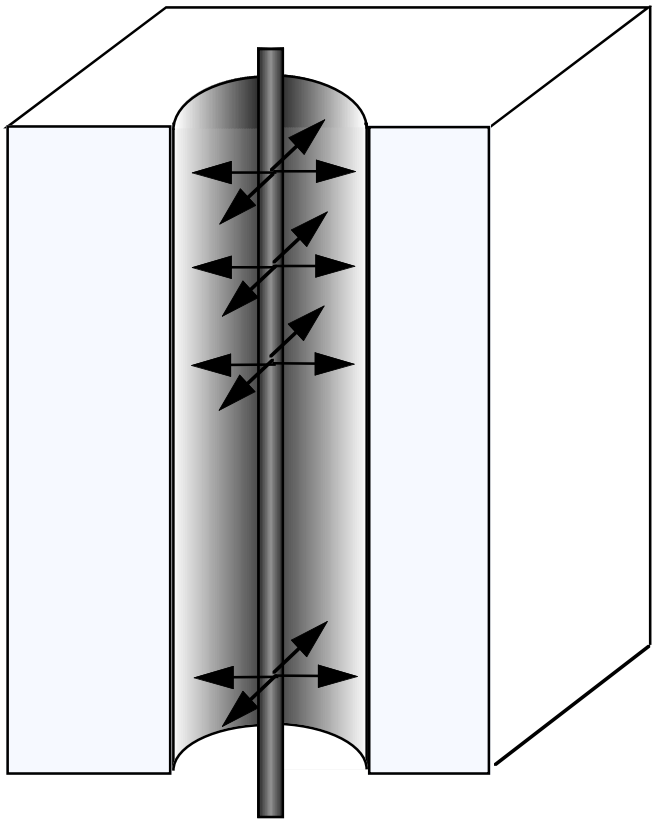

Figure 6-2: Diagram of a cross-dipole logging tool. It consists of one pair of dipole source with orthogonal polarizations and eight pairs of dipole receivers polarized in the same direction with one of the dipole sources.

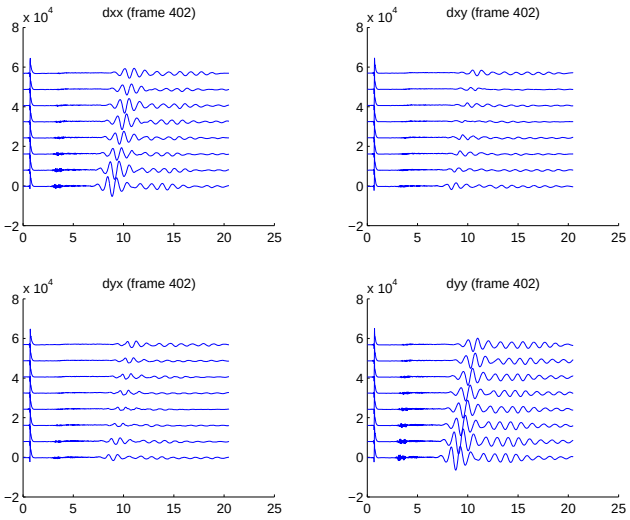

(a) cross-dipole

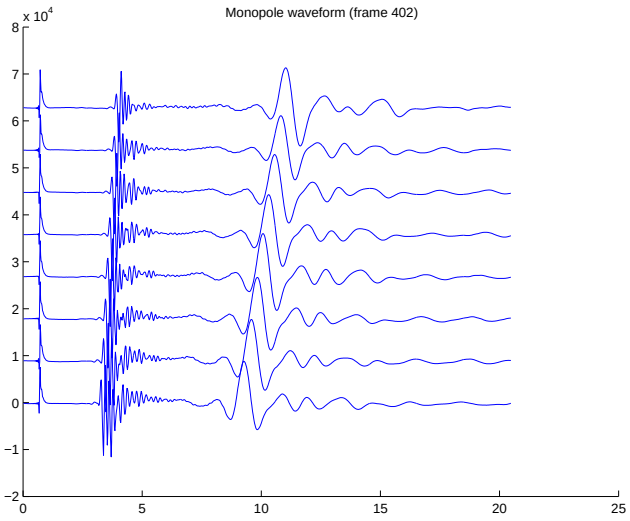

(b) monopole

Figure 6-3: Waveforms recorded in the field at depth 1370.5 feet. a. four-component cross-dipole data. b. monopole data.

kHz. Since a borehole flexural wave consists of low-frequency components and propagates the slowest among all the generated waves, low-pass filtering and time windowing the recorded waveforms help to obtain relatively pure flexural waves.

2. *Fast shear azimuth estimation and rotation of recorded dipole waveforms to the fast and slow shear directions.* The orientation of the fast shear or flexural wave polarization in the far field is obtained by using the low frequency part of cross-dipole flexural waveforms with the modified Alford rotation technique that takes into account the signature mismatch of sources and receivers (Huang et al., 1998). Waveforms at each depth are then rotated so that the sources and receivers are aligned with the principal flexural wave polarizations. As a result, the rotated waveforms contain largely pure principal flexural waves and are ready for further processing.

3. *Dispersion analysis.* In order to locate depths where crossovers in flexural dispersions or stress-induced anisotropy occurs, flexural dispersions are extracted from the data using one mode method (Nolte et al., 1997), which is outlined in Appendix A. Dipole dispersion crossover is continuously observed in the depth range of 390 m to 430 m (1279.5 ft to 1411 ft). Figure 6-5A presents a typical dispersion crossover for the two principal flexural waves in the stressed zone. Figure 6-5B shows the compressional headwave and the dispersive Stoneley wave from monopole logging data in the same well at the same depth. The compressional wave velocity is around 1600 m/s, the same value as in figure 6-4. The presence of crossovers indicates horizontal formation stresses on a weakly anisotropic or isotropic formation at those depths where the polarization direction of the fast flexural wave corresponds to the direction of formation maximum horizontal stress. Figure 6-6 shows the maximum horizontal formation stress directions in the stressed zone. By computing the cross-correlation of the low-frequency part of the fast and slow flexural waveforms, we obtain the group delays between the slow and fast flexural waves (Figure 6-6). The delays in-

dicate the amount of stress-induced anisotropy in the formation. The shear velocity anisotropy can be expressed as

$$\frac{V_2 - V_3}{V_3} = \frac{V_2 \Delta t}{L}, \tag{6.28}$$

where V_2 and V_3 are the fast and slow shear velocities, respectively; and Δt is the group delay at a given depth as shown in the second panel of Figure 6-6. Typically, we observe a group delay Δt=1 ms, and an average shear velocity V_2=620 m/s (2034 ft/s) in this depth interval. These values yield an average shear anisotropy of about 16%. Note that the entire depth interval in Figure 6-6 shows dipole dispersion crossovers and a significant amount of stress-induced shear anisotropy. The maximum horizontal formation stress direction is oriented at 30^o to 50^o east from north.

4. *Stress magnitude estimation.* The dotted lines in Figure 6-8 represent dispersions measured from logs. From each of the dispersion curves of flexural waves and the Stoneley wave, five frequency points from the frequency band 1 kHz to 2 kHz with 250 Hz spacing are selected for inversion. Borehole parameters and the reference state in the inversion are listed below.

$$\begin{aligned}
\text{Formation compressional velocity} &: V_1 = 1693 m/s, \\
\text{Formation shear velocity} &: V_2 = 570 m/s, \\
\text{Formation mass density} &: \rho = 2400 kg/m^3, \\
\text{Borehole radius} &: R = 0.2 m, \\
\text{Fluid compressional velocity} &: V_f = 1500 m/s, \\
\text{Fluid mass density} &: \rho_f = 1000 kg/m^3.
\end{aligned}$$

Magnitudes of the maximum and minimum horizontal formation stresses as well as three formation nonlinear elastic constants are obtained by inverting phase velocity changes in the fast and slow borehole flexural wave as well as the

Stoneley wave using equations 6.25, 6.26 and 6.27. The results are as follows:

$$S_H = -40MPa, \quad S_h = -12MPa,$$
$$c_{111} = -608.6GPa, \quad c_{112} = 25.4GPa,$$
$$c_{123} = 201.2GPa.$$

Theoretical dispersion curves are calculated by substituting the above results into equations 6.25, 6.26 and 6.27. Good agreement between measured and theoretical dispersion curves indicates that the mean-square errors of the inversion are small.

From the dispersion curves of flexural waves (Figure 6-8), it is obvious that the formation is very "soft", i.e., has very low shear velocity, around 610 m/s. Formation overburden can be a good approximation of the vertical stress, S_v. Assuming that the average formation density from the surface to the depth of 400 m is 2300 kg/m^3, the vertical stress in the depth range of the stressed zone is on the order of 8.8 to 9.7 MPa. This value is slightly smaller than S_h. The stress field of the area of this study is of the form $S_H \gg S_h \approx S_v$, producing a combination of strike-slip and thrust faulting. These results are consistent with results from borehole breakout studies (Mount and Suppe, 1992) and with focal mechanism and borehole breakout data presented in the world stress map database (Zoback, 1992), shown in figure 6-7.

6.4 Discussion

The existence of a borehole alters the stress field in the formation. The stress field distribution around a borehole caused by a far-field compressive stress S is given by

Timoshenko and Goodier (1982)

$$
\begin{aligned}
T_{RR} &= \frac{S}{2}(1-\frac{a^2}{R^2})+\frac{S}{2}(1+\frac{3a^4}{R^4}-\frac{4a^2}{R^2})cos2\Phi, \\
T_{\Phi\Phi} &= \frac{S}{2}(1+\frac{a^2}{R^2})-\frac{S}{2}(1+\frac{3a^4}{R^4})cos2\Phi, \\
T_{R\Phi} &= -\frac{S}{2}(1-\frac{3a^4}{R^4}+\frac{2a^2}{R^2})sin2\Phi, \\
T_{ZZ} &= \mu(T_{RR}+T_{\Phi\Phi}), \\
T_{ZR} &= 0, \\
T_{Z\Phi} &= 0
\end{aligned}
\tag{6.29}
$$

where a is borehole radius, μ is the formation Poisson's ratio, R is the radial distance from the borehole axis, and Φ is the azimuth angle that is measured relative to the far-field uniaxial stress direction. Figure 6-9 shows radial (T_{RR}), circumferential($T_{\Phi\Phi}$) and radial-azimuthal shear ($T_{R\Phi}$) stress variations away from the borehole surface along various azimuthal directions from the stress axis ($\Phi = 0^o, 30^o, 60^o$, and 90^o). All stresses are normalized with respect to the far-field stress, S. When the radial distance, R is over 2 to 3 times the borehole radius, the stress field is very close to that of the far-field. Borehole guided waves can penetrate the formation up to a radial distance of about one wavelength (Cheng and Toksoz, 1981). The center frequency of Stoneley and borehole flexural waves that are used in the stress magnitude inversion is 1 kHz. Velocities of Stoneley wave and both flexural waves are over 600 m/s. Therefore, Stoneley wave and flexural waves are sensitive to formation properties up to 60 cm from the center of the borehole, or over 3 times of the borehole radius. Therefore, the estimated stress magnitudes represent the far-field formation stress quite well.

6.5 Conclusions

Techniques presented in this paper for studying *in-situ* formation stresses are non-destructive using the standard acoustic logging data, and are reasonably reliable in

estimating absolute stress magnitudes. Inversions for stress directions and magnitudes are simple, efficient and well-conditioned.

Anisotropy in rocks can be characterized as either intrinsic or stress-induced. It is possible to have a mixture of these two types of anisotropy in the earth. The stress magnitude inversion scheme presented in this paper requires observations of stress-induced anisotropy dominating intrinsic anisotropy. In general, the azimuthal anisotropy in the shallow crust is due to differences in horizontal stresses. The method developed in this study can determine the directions and magnitudes of maximum and minimum horizontal stresses.

6.6 Acknowledgments

Special thanks to Chevron Petroleum Technology Company for providing us with well logs. This research was supported by the Borehole Acoustic Logging Consortium at the Earth Resources Laboratory.

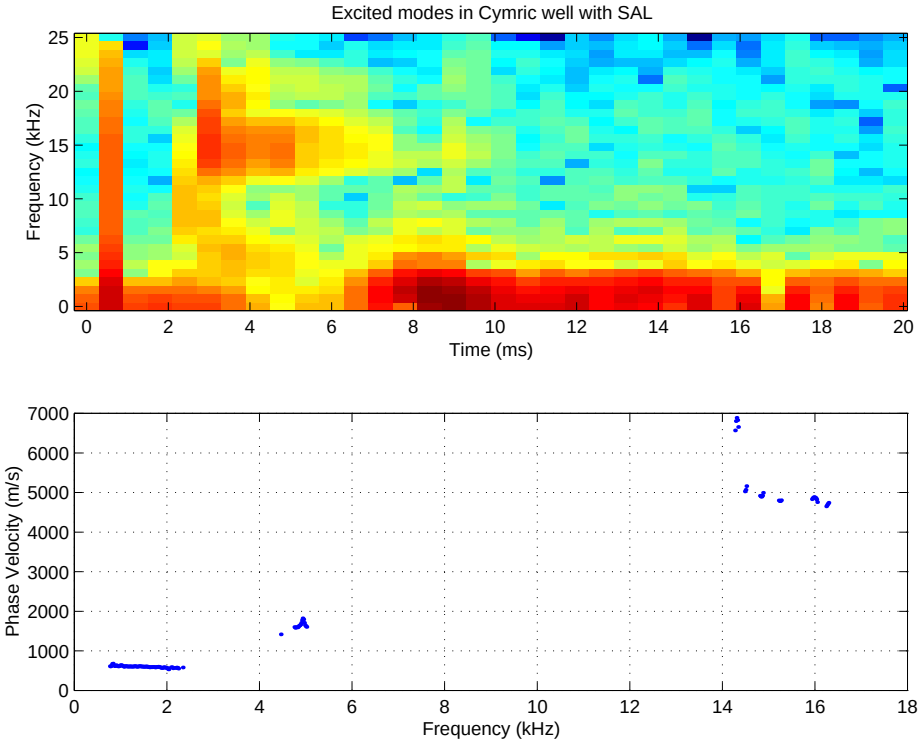

Figure 6-4: Separation of all borehole modes that are generated by the acoustic tool. a (Top): A typical spectrogram of recorded waveforms. Red and blue colors indicate high and low amplitudes of signals in the measurement frequency band of approximately 1 to 20 kHz. b (bottom): Velocities and frequency band of the flexural mode, compressional headwave, and a first-order tool mode.

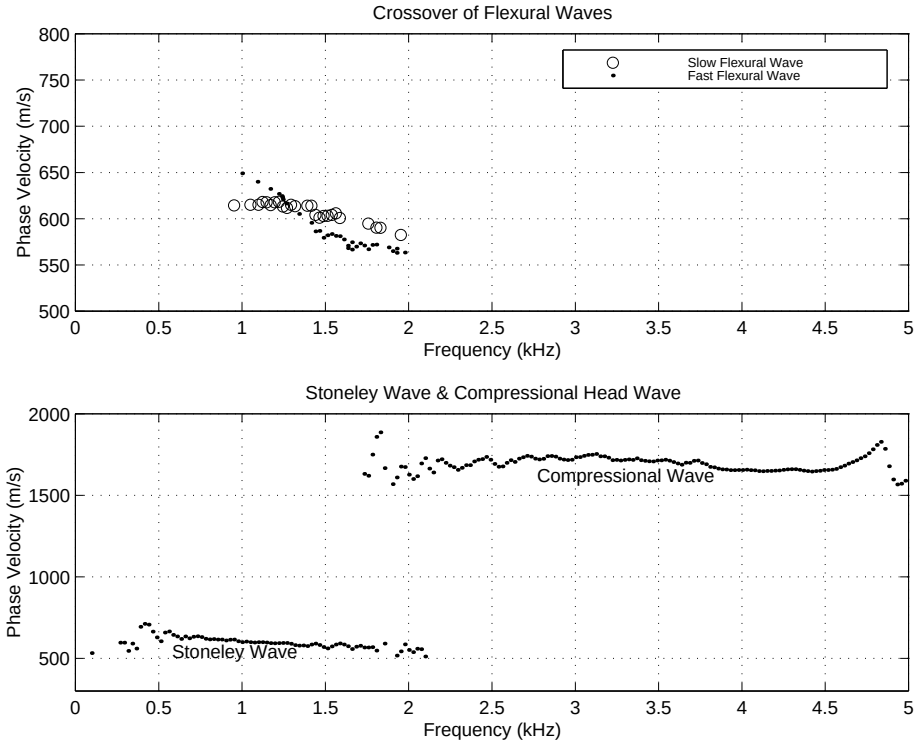

Figure 6-5: Typical dispersion curves of borehole modes in the stressed zone extracted from the acoustic logging data. A (Top): Flexural waves from cross-dipole logging; B (Bottom): Compressional headwave and Stoneley wave from monopole logging.

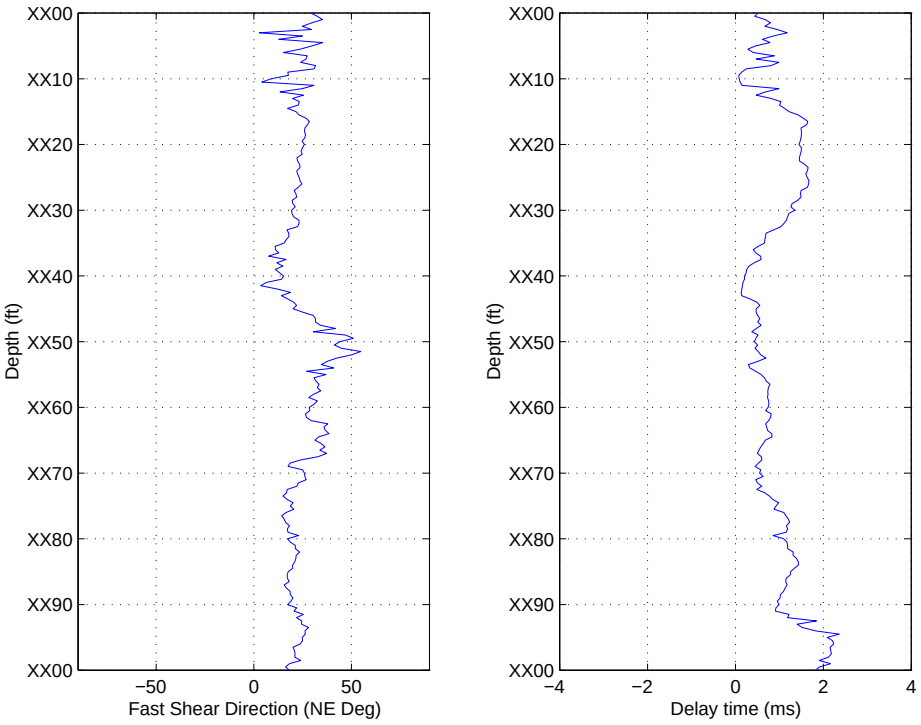

Figure 6-6: Maximum stress direction in the stressed zone where crossovers in flexural dispersions are continuously observed. The maximum horizontal stress is oriented $30^o \sim 40^o$ northeast. The result agrees with the world stress map (figure 6-7). The second panel shows the group delay of the slow flexural wave from the fast one obtained by cross-correlating the low-frequency part of the fast and slow flexural waveforms.

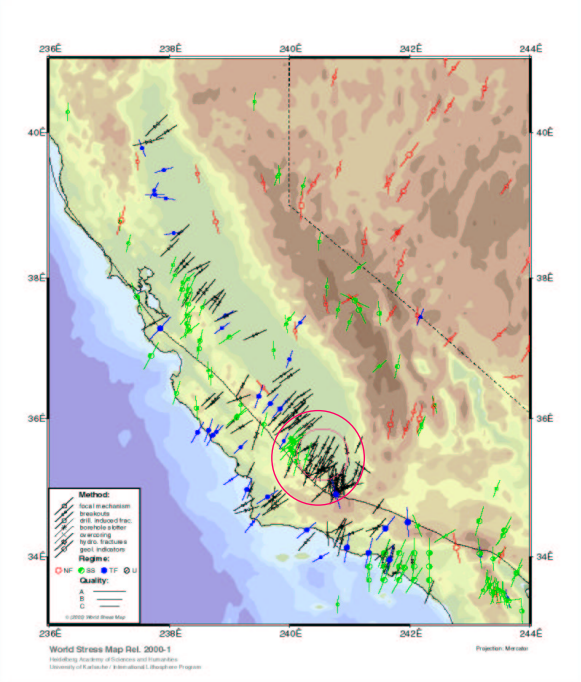

Figure 6-7: Orientation of the maximum horizontal stress in the world stress map (Zoback, 1992). The circled area is where the field data were acquired.

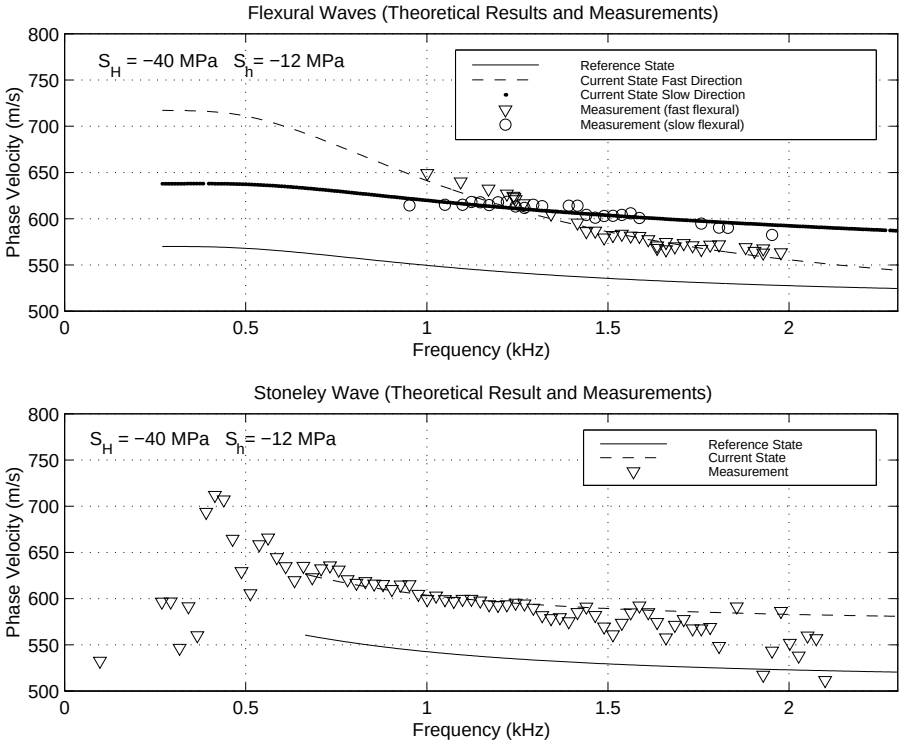

Figure 6-8: Dispersion curves that are estimated from data as well as calculated by the perturbation theory with inverted tectonic stresses and nonlinear elastic constants as inputs. The heavy line in the first figure is the theoretical dispersion curve of the slow flexural wave.

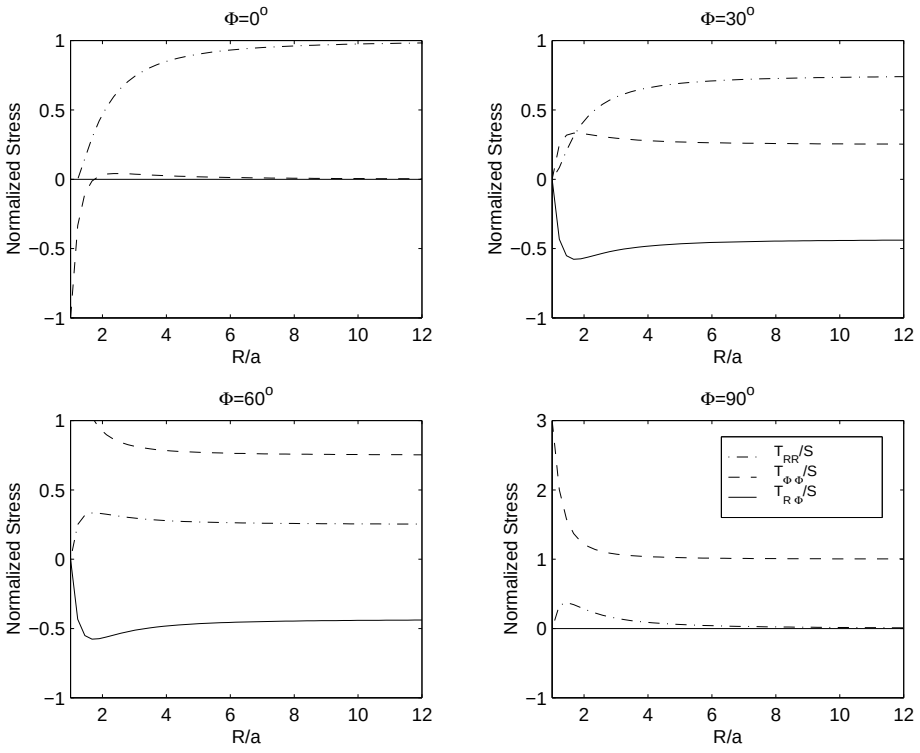

Figure 6-9: Radial (T_{RR}), circumferential($T_{\Phi\Phi}$) and radial-azimuthal shear ($T_{R\Phi}$) stress variations away from the borehole surface along various azimuthal directions from the stress axis ($\Phi = 0^o, 30^o, 60^o,$ and 90^o). All stresses are normalized with respect to the far-field stress S.

Chapter 7

Conclusions and Future Work

Making measurements of formation properties while drilling (LWD) is becoming an important procedure in the petroleum industry. In LWD, the drill collar serves as the "logging tool". This in turn introduces a large diameter mandrel into the borehole and it produces a thin annulus of fluid between the tool and the formation. Numerical modeling of seismic waves in such systems, with highly contrasting material properties and layers pose a challenge that traditional finite difference and finite element algorithm become computationally costly. A novel finite difference time domain algorithm has been developed that features non-uniform grid, wavelet-based difference operator and anisotropic perfectly matched layer. This algorithm reduces numerical reflections and wave distortions introduced by grid change to a minimum. Using coordinate stretching, the algorithm discretizes the physical space with variable grid, while solving the wave equation on a uniform mesh. That approach helps to retain the advantages of an uniform mesh. Further improvement in efficiency was achieved through the development of a wavelet-based difference operator. Unlike the conventional Taylor's expansion based method, the wavelet-based by using a family of compactly supported wavelet function represents the derivative operator without truncation and allows less grid point per wavelength. The wavelet-based scheme also yields more accurate reflection and transmission coefficients at sharp boundaries, especially when combined with finer grids in the neighborhood of a discontinuity. Coordinate stretching is also employed in deriving an anisotropic perfectly matched

layer, superior to the currently available perfectly matched layer formulation which requires field splitting, a process that requires more computer memory for the storage of extra variables. When the medium is homogeneous in z direction, further saving in computational cost is obtained since the finite difference algorithm solves the wave equation in (x,y,k_z,t) domain before taking inverse Fourier transformation of the solution back to (x,y,z,t) domain. The main objective of this thesis was to calculate the response of an LWD acoustic tool by developing an appropriate finite difference algorithm. The overall saving in computer memory for most LWD models could be in the order of several hundred times.

The stretched grid finite difference algorithm is used for a comprehensive investigation of wave propagations in the logging while drilling. The investigation is focused on soft formations where formation shear velocity is slower than borehole fluid velocity, because shear velocity measurement, one of the key measurements that acoustic logging is designed to acquire, is the most problematic in soft formations. The key questions include: What are the best source type and frequency range for measuring shear velocity? What is the influence of LWD tool position (centered or off-centered) on the received waveforms? Do monopole, dipole and quadrupole sources, made of point sources, produce pure mode? If not, what is the resulting effect is on velocity analysis. In answering these questions, the following conclusions were reached for measurements in soft formation:

- Frequency range is the key factor to obtain reliable shear velocity measurement. The system should be designed at low frequencies to make measurements in slow formation (below 6 kHz). For a broadband or high frequency system, multipole modes are excited. To identify borehole modes, it is necessary to combine time domain semblance and frequency dispersion analysis.

- Shear waves are observed in dipole logging and monopole logging at low frequencies. These are “leaky” refracted waves. They can be used as a cross-check for shear velocity measurements.

- All these sources, monopole, dipole and quadrupole sources are suitable for

shear velocity measurement. The monopole source produces direct shear when the tool is centered, and strong flexural mode that approaches to the formation shear velocity at low frequency limit when the tool is off-centered. The dipole source produces a weak yet visible shear arrival when the tool is centered, and a much stronger one when the tool is off-centered. The shear arrival in the off-centered case is believed to be associated with the flexural mode. The phase velocity of the flexural mode is slower at low frequencies (0-2.5 kHz) when the tool is centered. The quadrupole source produces a clean quadrupole mode. Its phase velocity approaches the formation shear velocity at low frequency limit for both centered and off-centered tool.

- In addition to modes decribed above, a torsional mode is generated when the tool is off-centered.

- Dipole, monopole and quadruple excitations are efficiently achieved by two point sources with opposite phase, four point sources all in phase, and four point sources at with alternate phases.

Cross-dipole logs (wireline) can be used to determine azimuthal anisotropy and to estimate stress magnitudes and directions from borehole acoustic measurements. We developed an inversion method to obtain the directions and magnitude of formation stresses. We applied this method to data from California. The estimated stress directions are consistent with those obtained from earthquake focal mechanism and borehole breakout data given in the world stress map database (Zoback, 1992).

7.1 Future Work

The FDTD algorithm developed in this dissertation is a stand alone tool able to handle a variety of models from fluid-filled borehole to layered media. Besides efficient mesh and low numerical reflection from the absorbing layer, it produces the most accurate reflection and transmission at sharp boundaries by using wavelet-based difference operator. There are several directions to further the functionality of the

FDTD algorithm. Currently the algorithm is in 2.5D, requiring homogeneous property in one of the dimensions. For broader applications, the next step is to extend it from 2.5D to 3D and add message passing interface (MPI) for parallel computing. Another direction is to add intrinsic attenuation to the wave equation by introducing viscoelasticity to the algorithm (Robertsson et al., 1994; Hestholm, 1999). The wavelet-based difference operator in the current FDTD algorithm only uses the scale functions. Higher accuracy may be obtained by incorporate the wavelet functions.

The stress inversion scheme discussed in the dissertation is successful in obtaining stress information from the particular acoustic logging data and consistent to previous investigations. Because *in-situ* stresses are at the average level of 20 to 80 MPa, some rocks may undergo plastic deformations. At those stress levels, elastic moduli may no longer be a linear function of formation stresses as assumed in the dissertation. The key step to further the study of stress inversion is therefore to build realistic constitutive relationship into the calculation.

Appendix A

Extracting Dispersion Curve From Waveforms: A Back Propagation Based Formula

Under the assumption that the formation properties do not vary axially over the receiver array, the propagation of a borehole wave along the axis of a fluid-filled borehole can be described by the equation (Biot, 1952; Tsang and Rader, 1979)

$$u(z,t) = \int_{-\infty}^{\infty}\int_{-\infty}^{\infty} S(\omega)R(\omega)\tilde{G}(k,\omega)e^{-j\omega t}e^{jkz}dkd\omega, \tag{A.1}$$

where $u(z,t)$ denotes the pressure variation on the borehole axis as a function of distance z and time t. $\tilde{G}(k,\omega)$ denotes the spatial and time Fourier transform of the borehole excitation function. k is the vertical wavenumber. The excitation function of borehole waves can be expressed by an unique linear combination of a group of orthogonal functions with each function representing a single borehole mode. Equation A.1 works well for a single borehole mode. $S(\omega)$ and $R(\omega)$ denote the Fourier transform of the source signature and the receiver response, respectively. As our interest is in the frequency dependence of the phase velocities, or the dispersion of one

borehole mode, we can take the Fourier transform of $u(z,t)$ over time,

$$U(z,\omega) = S(\omega)R(\omega)\int_{-\infty}^{\infty}\tilde{G}(k,\omega)e^{jkz}dk. \tag{A.2}$$

Elementary concepts from complex-variable analysis can be used to rewrite the continuous integral in equation A.2 as a sum of contributions from the singularities of $\tilde{G}$ (Roever et al., 1974; Peterson, 1974; Tsang and Rader, 1979; Kurkjian, 1985). Generally, if $U(z,\omega)$ is the recorded waveform that includes all types of borehole waves (guided and head waves), two types of singularities will contribute to the integral in equation A.2: poles and branch points. The pole contributions are associated with guided modes, while the branch points are due to body waves in the formation (Lang *et al.*, 1987). In our case, $U(z,\omega)$ represents the waveform of a single pure borehole guided wave mode, thus only one pole contributes to the integral in equation A.2. For a pole located at $k = k_p(\omega)$, the residue of the pole will be of the form $1/(2\pi j)g_p(\omega)e^{jk_p(\omega)z}$. Thus an alternative representation, which is exact, of equation A.2 is

$$U(z,\omega) = S(\omega)R(\omega)g_p(\omega)e^{jk_p(\omega)z}. \tag{A.3}$$

The waveform at each receiver, $u(z,t)$, containing one single borehole mode is obtained by filtering and time-windowing the recorded full waveform. In the dipole case, we rotate the filtered and time-windowed waveforms. For convenience, we denote $u(z,t)$ at i-th receiver as $u_i(t)$ and Fourier transform $u_i(t)$ to $U_i(\omega)$. The first receiver is the one that is the closest to the source. According to equation A.3, $U_i(\omega)$ can be represented as

$$U_i(\omega) = S(\omega)R(\omega)g_p(\omega)e^{-k_p^i[z_0+(i-1)\Delta z]}e^{j\frac{\omega}{v_z^0(\omega)}[(i-1)\Delta z+z_0]} \tag{A.4}$$

where k_p^i is the imaginary part of k_p, representing the attenuation coefficient of the borehole mode, and $k_p^r = \omega/v_z^0(\omega)$ is the real part of k_p, denoting the vertical wavenumber of the borehole mode. z_0 is the distance from the source to the first receiver, and Δz is receiver spacing. We now rewrite equation A.4 in terms of $U_1(\omega)$,

the wave spectrum at the first receiver:

$$U_i(\omega) = U_1(\omega)e^{-k_p^i(i-1)\Delta z}e^{j\frac{\omega}{v_z^0(\omega)}(i-1)\Delta z}. \tag{A.5}$$

For each frequency ω, we define a vector, $\underline{U}(\omega)$, as

$$\underline{U}(\omega) = \begin{bmatrix} U_1(\omega) \\ U_2(\omega) \\ U_3(\omega) \\ \vdots \\ U_N(\omega) \end{bmatrix} \tag{A.6}$$

where N denotes number of receivers. Waves at each receiver are propagated back to the location of the first receiver by compensating the phase changes from the first receiver location to their current location. As for small amplitude waves, the attenuation term is not dependent on velocity; therefore, there is no need to adjust the attenuation term during the back propagation. We then sum up the back propagated waves as

$$e(\omega, v_z) = \frac{|\underline{U}^*(\omega)\underline{\Phi}(\omega, v_z)|}{\sqrt{\underline{U}^*(\omega)\underline{U}(\omega)}}. \tag{A.7}$$

$e(\omega, v_z)$ is the amplitude of the normalized summation of waves that are back propagated to the position of the first receiver. $\underline{\Phi}(\omega)$ denotes the phase term that propagates N waves back to the first receiver.

$$\underline{\Phi}(\omega) = \begin{bmatrix} \phi_1(\omega, v_z) \\ \phi_2(\omega, v_z) \\ \phi_3(\omega, v_z) \\ \vdots \\ \phi_N(\omega, v_z) \end{bmatrix} \tag{A.8}$$

where

$$\phi_i(\omega, v_z) = e^{j\frac{\omega}{v_z}(i-1)\Delta z}. \tag{A.9}$$

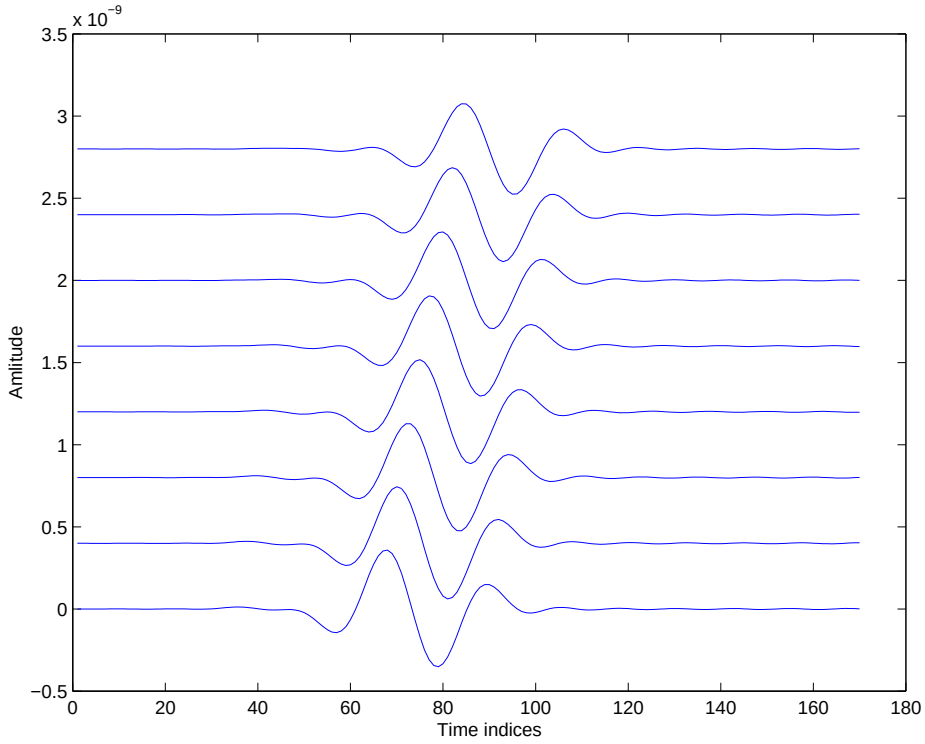

Figure A-1: Synthetic borehole flexural waveforms obtained by a Finite Difference algorithm.

At each frequency, if the phase velocity v_z, that we use to back propagate waves at N receivers, equals the true phase velocity, $e(\omega, v_z)$ reaches its maximum. Ideally, if there is no noise, $e(\omega, v_z)$ will be 1 at its maximum.

Figure A-1 shows a set of synthetic borehole flexural waves at eight receivers obtained by a finite difference algorithm. Figure A-2A shows the dispersion curve estimated using one mode method and the analytical dispersion curve for the same formation properties. They agree very well. To show that both the dispersion extraction technique and the FDTD algorithm developed in this thesis is accurate for the frequency domain analysis, dispersions curves are extracted from the waveforms computed in chapter 2, where the model is a fluid-filled borehole without the LWD tool. Figure A-3 shows the resulting dispersion curves that are plotted against theoretical solutions. They agree with each other very well.

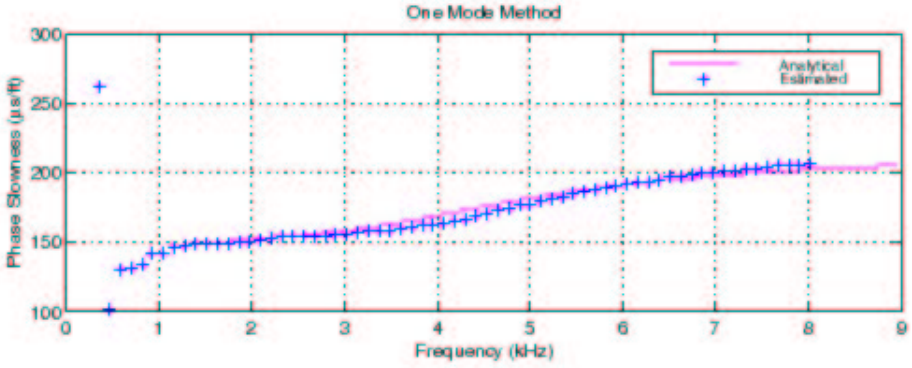

Figure A-2: Estimated dispersion curves of the flexural wave in Figure A-1 and analytical dispersion curve for same formation properties.

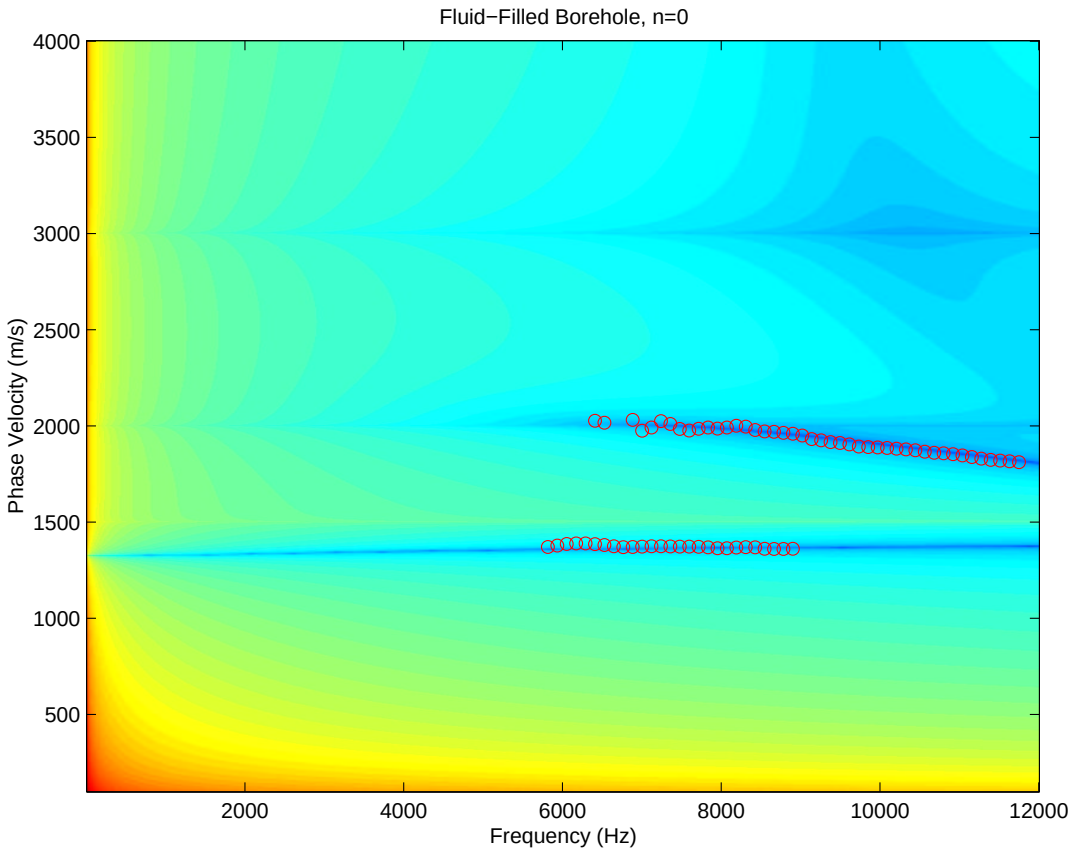

Figure A-3: Dispersion curves in a fluid-filled borehole with monopole source without the LWD tool. circle: extracted from waveforms computed in chapter 2; colormap: zero map of the analytical eigenvalue equations, dark lines representing analytical solutions of borehole modes. The numerical results agree with the analytical solution very well.

Appendix B

Leaky Shear

Direct shear arrival is observed in both the monopole and dipole case in chapter 4 and 5. It is stronger at low frequencies. While the shear arrival in soft formation is too weak in the wireline situation to provide little help in measuring shear velocity, it certainly is strong enough in the LWD to serve as a cross check for modal based measurements, due to the fact that the source and receivers are close to the formation. To confirm it is the direct shear, a numerical experiment is conducted in a two half space fluid-solid model. The fluid is water and the solid has the same property as the soft formation. The source is 6 mm away from the interface in the water and receiver arrays are placed according to figure B-1. The center frequency of the source is 2 kHz. Figure B-2 and B-4 shows waveforms and spectra recorded by the receiver array that is 6 mm away from the interface. CA closer look at the waveforms are shown in figure B-3. Semblance and dispersion analysis results are shown in figure B-5 and B-6.

Although the Stoneley wave is strong, the leaky shear is strong enough to show in the waveform as the first arrival. Its energy decays as a function of $1/R^3$, where R is the receiver offset. It is of higher frequency content than the Stoneley wave. The leaky shear dies out 9 cm away from the interface.

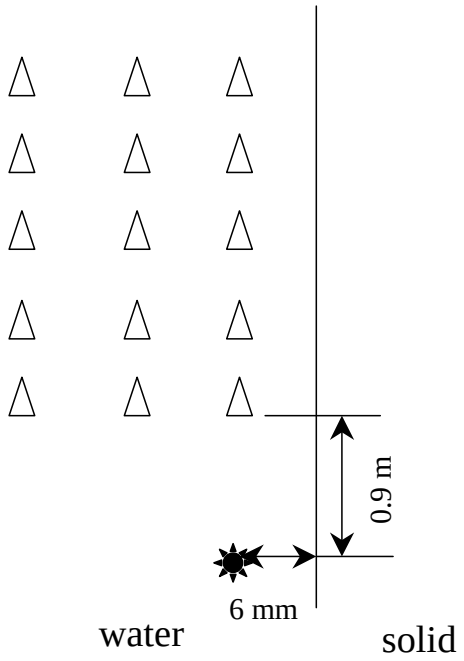

Figure B-1: Schematic illustration of source and receiver positions. The FDTD computation is conducted in 3D.

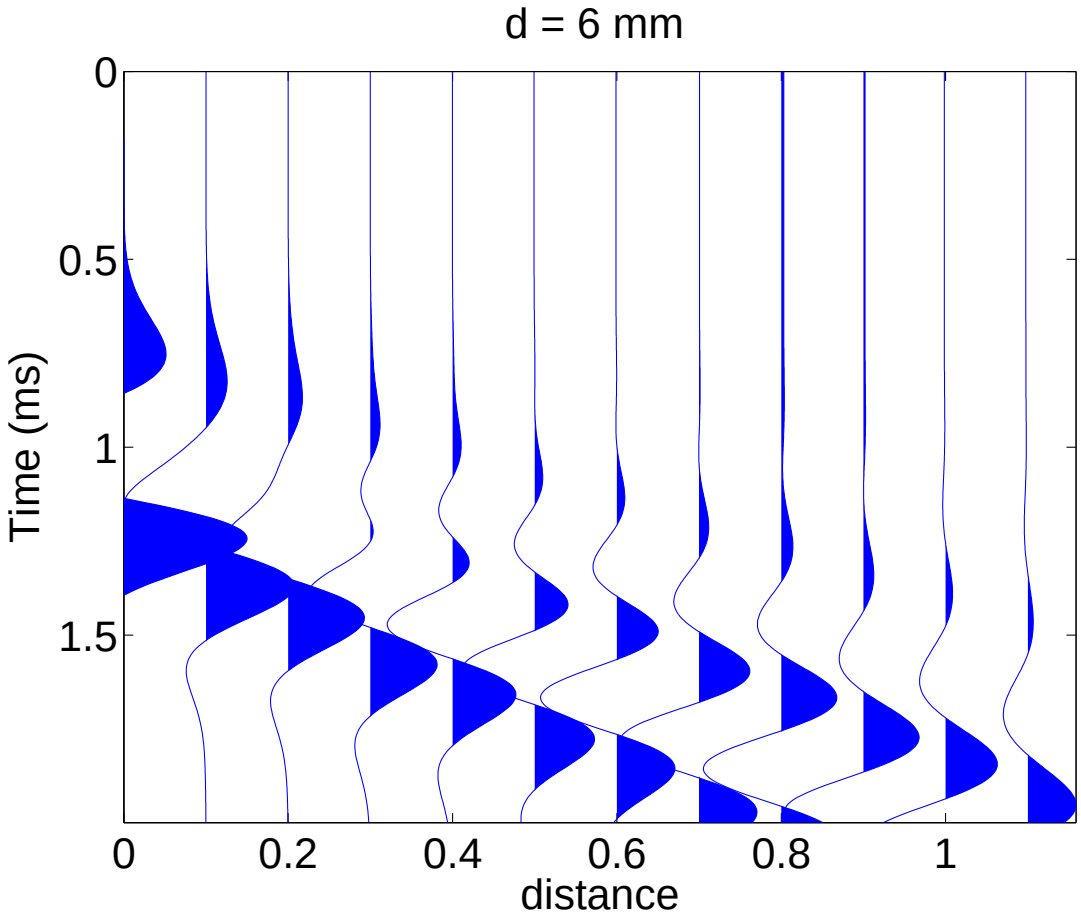

Figure B-2: Waveforms recorded by the receiver array that is 6 mm away from the interface.

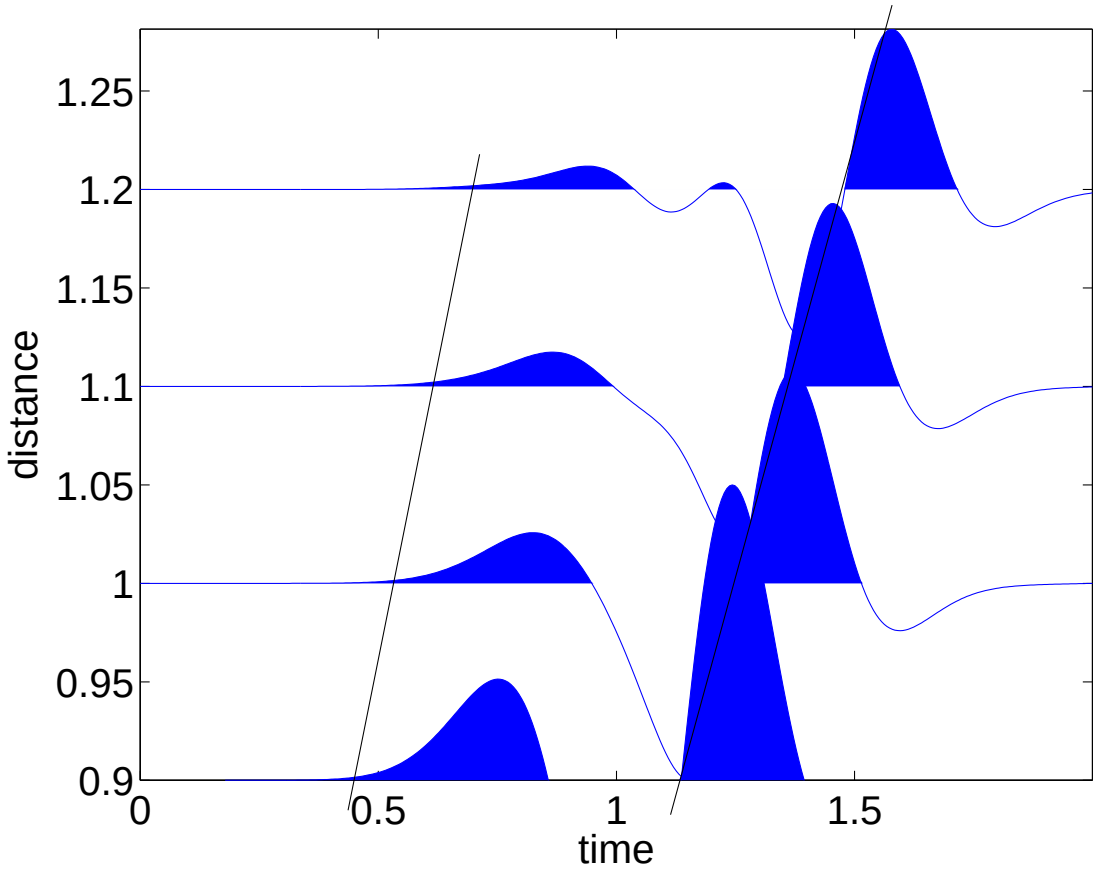

Figure B-3: A closer look at waveforms in figure B-2.

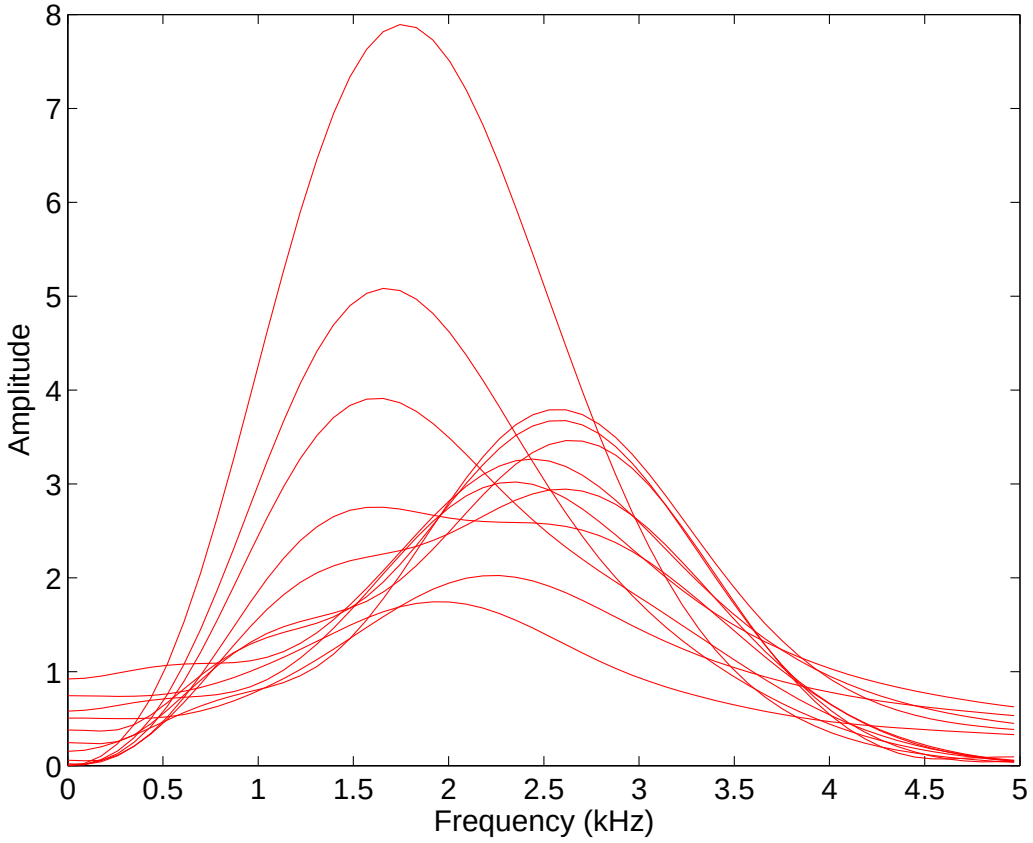

Figure B-4: Spectra of waveforms in figure B-2.

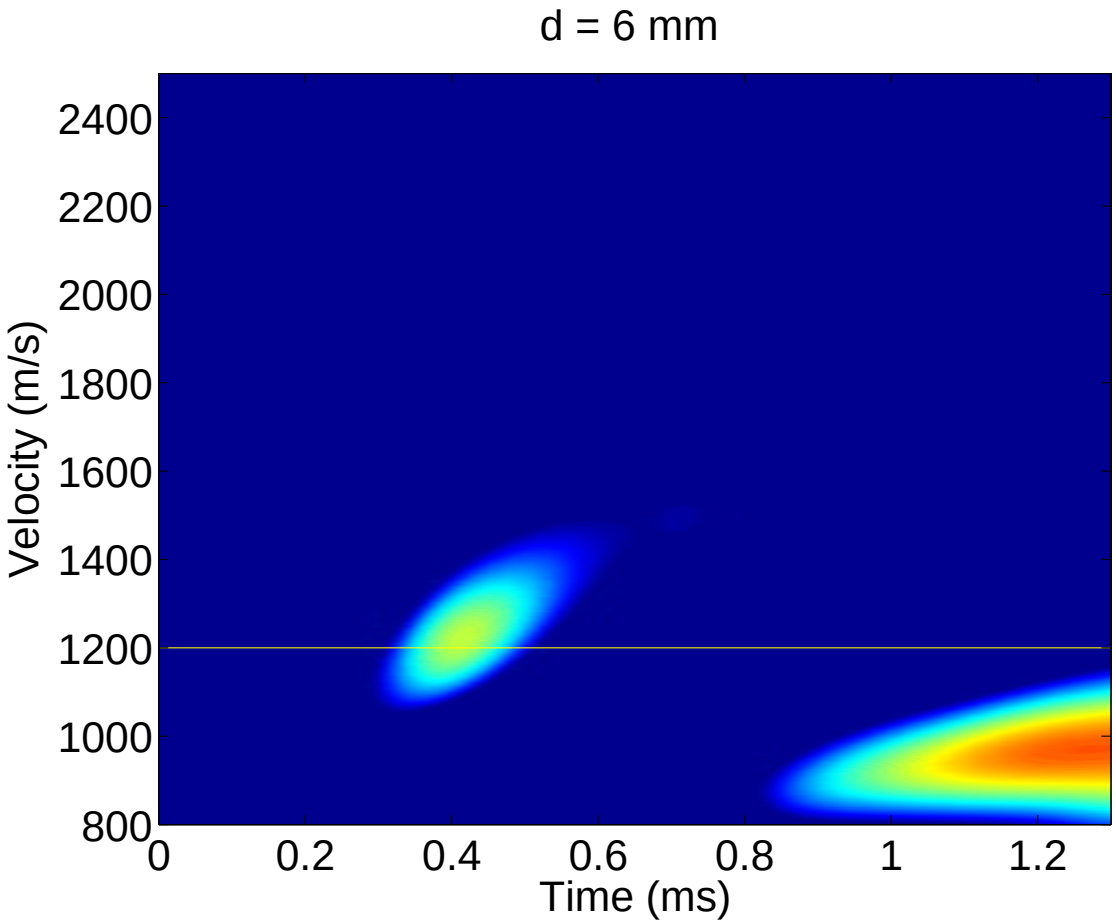

Figure B-5: Semblance result of waveforms in figure B-2.

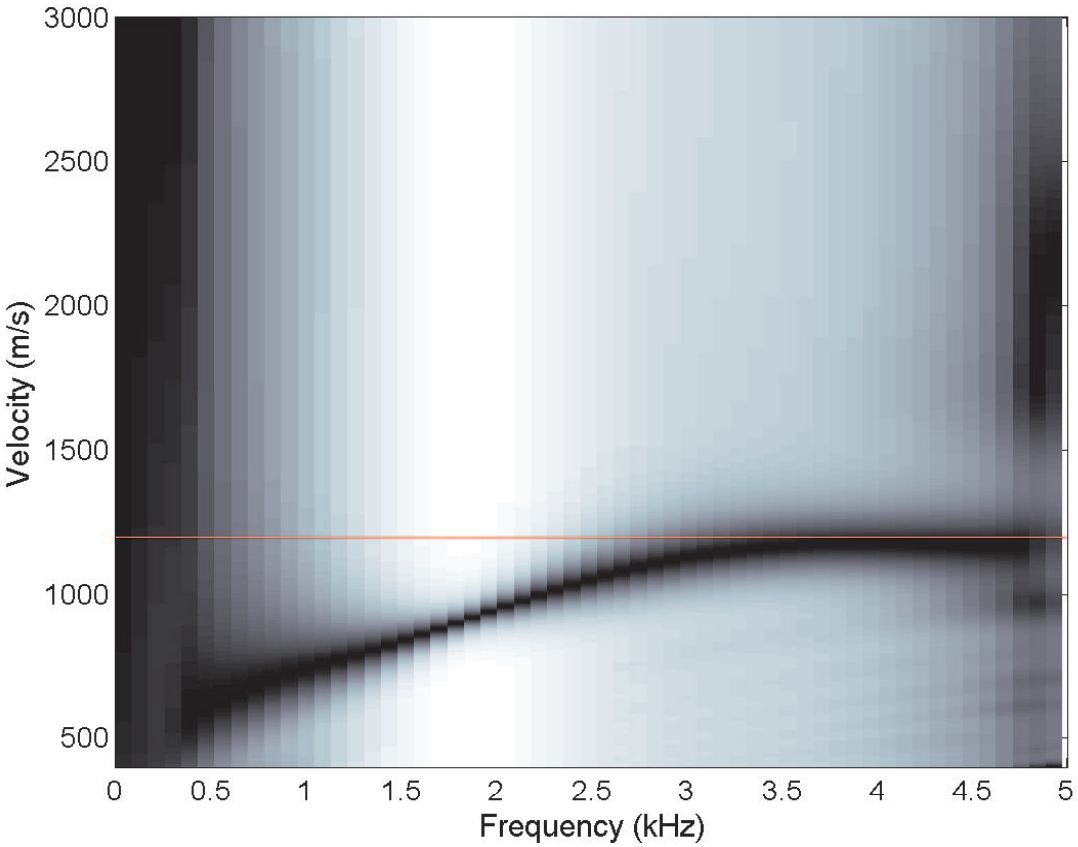

Figure B-6: Dispersion analysis result of waveforms in figure B-2.

Appendix C

Effects of Stresses on Elastic Velocities of Rocks: Theory of Acoustoelasticity and Experimental Measurements

ABSTRACT

The theory of acoustoelasticity, having been developed for polycrystalline materials, provides direct link between the change of elastic wave velocities and static stresses in solids. It is the theoretical foundation for studying stress effects on wave propagation along a fluid-filled borehole in the rest of the thesis. The objective of this appendix is to review the theory and its applicability to rocks.

C.1 Introduction

The phenomenon of stress-induced velocity change in rocks, referred as acoustoelasticity, is a well-established observation (Nur and Simmons, 1969; Lo et al., 1986; Johnson and Christensen, 1993). It is classically modeled by a change in alignments and density of cracks or any other alignment of micro-structural flaws or defects, caused by

a changing stress(*e.g.* Sayers et al. (1990)). Theory of acoustoelasticity, having been developed under the framework of continuum mechanics, describes a small dynamic perturbation superimposed on a predeformed medium due to the presence of a static stress.

The theory of acoustoelasticity invokes third-order elastic (TOE) constants to account for the nonlinear strain response to stresses of finite magnitude (Thurston and Brugger, 1964). Note that the nonlinearity is referred to the fact that wave velocity is a function of applied stresses, not that the dynamic field is nonlinear. On the contrary, the dynamic motion is infinitesimally small thus linear. A full review of the derivation of this theory can be found in (Pao et al., 1984)

Development of the theory has been stimulated by the interest of measuring applied or residual stresses in polycrystalline materials. Due to the presence of compliant mechanical defects (cracks, micro-fractures, grain joints, *etc*), rocks in general show stronger nonlinear elastic behavior, *i.e.* stronger dependency of compressional and shear velocities on static stresses, than crystals or polycrystalline materials (Meegan et al., 1993; Johnson et al., 1993; Johnson and McCall, 1994). The theory of acoustoelasticity had not been popular in the geophysical community until recently when it is employed in estimating *in-situ* stresses, for it provides efficient and direct quantitative links of the change of velocities to static stresses, both to their directions and magnitudes. Recently a number of studies have been reported using the acoustoelasticity theory to compute TOE constants of various types of rocks from laboratory measurements (Johnson and Rasolofosaon, 1996; Winkler and Liu, 1996; Sarkar et al., 2002).

In this appendix, I shall first review the general theory of acoustoelasticity, and derive formulae of velocity change as a function of static stresses. I then apply those formulae to several published experimental measurements of various types of rocks. A connection between Sayer's microcrack model and the theory of acoustoelasticity is made afterwords. Note that the micro-crack model, relating velocity changes with static stresses through opens and closes of micro-cracks, does not establish the direct quantitative dependency of velocities on stress magnitudes. The goal here is not to

present an exhaustive analysis of the experimental data available from the literature, but to illustrate the applicability of the theory of acoustoelasticity to rocks. First I shall analyze a set of high precision velocity *v.s.* stress data of dry Colton Sandstone Dillen (2000), then investigate velocity changes with confining pressures on Chelmsford Granite, Chicopee Shale and Berea Sandstone (Johnson et al., 1993; Lo et al., 1986). Velocity change as a function of uniaxial stresses is also investigated (Nur and Simmons, 1969).

C.2 Theory of Acoustoelasticity

The theory of acoustoelasticity was developed in the 1960s by introducing third-order elastic constants and separating dynamic motions from the large, static deformation caused by static stresses (Pao et al., 1984).

To understand the theory, it is essential to know three material configurations: the natural, the initial and the final states. The natural and initial configurations refer to states when the material is free of stresses and statically deformed, respectively. The final configuration denotes the material state with wave-induced dynamic deformation superimposed on the static load (Fig C-1). A physical variable in the natural, initial, or final state is designated by a superscript label 0, i, or f, respectively. The positions of a particle in the body at natural, initial, and final states are measured by position vectors ξ, X, and x, respectively, all directed from the origin of a common Cartesian coordinate system. The components of ξ and other physical quantities which refer to the natural configuration are denoted by Greek subscripts; those of X and others refer to the initial configuration by upper case Roman subscripts; and those of x and others refer to the final configuration by lower case Roman subscripts. Thus ξ_α, X_J, and x_j (α, J, $j = 1, 2, 3$) are the components of position vectors in three respective configurations (Fig C-1).

The static deformation and the driven stress, which can be denoted with the initial Kirchhoff (the second Piola-Kirchhoff) stress tensor referring to the natural configuration $\mathbf{T^i}$ or the Cauchy stress tensor referring the initial state $\mathbf{t_i}$, must satisfy

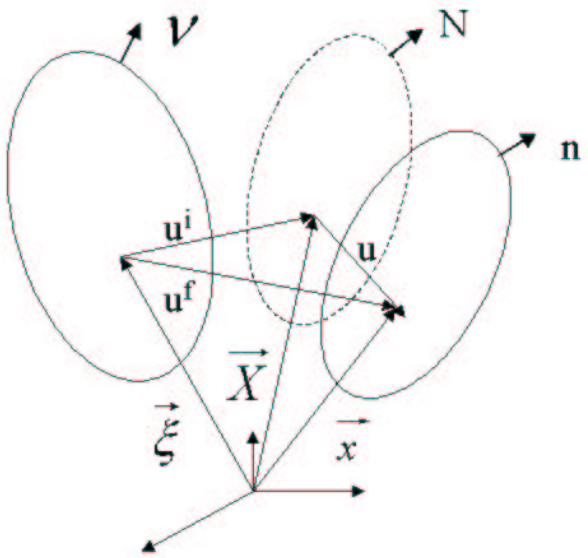

Figure C-1: Coordinates for a material point at the natural (ξ), initial (X) and final (x) configurations of a statically deformed body subject to a dynamics wave field (Pao et al., 1984).

the equations of equilibrium, *i.e.*

$$\frac{\partial}{\partial \xi_\beta}[T^i_{\beta\gamma}(\delta_{\alpha\gamma} + \frac{\partial u^i_\alpha}{\partial \xi_\gamma})] = 0,$$
$$\frac{\partial t^i_{JK}}{\partial X_K} = 0. \tag{C.1}$$

The dynamic wave propagating across the statically deformed body is governed by the following equation of motion referring to the natural and initial states, respectively,

$$\frac{\partial}{\partial \xi_\beta}(T^f_{\beta\alpha} + T^f_{\beta\gamma}\frac{\partial u^f_\alpha}{\partial \xi_\gamma}) = \rho^0 \frac{\partial^2 u^f_\alpha}{\partial t^2},$$
$$\frac{\partial}{\partial X_K}(T^f_{KJ} + T^f_{KL}\frac{\partial u^f_J}{\partial X_L}) = \rho^i \frac{\partial^2 u^f_J}{\partial t^2}. \tag{C.2}$$

where $\mathbf{T^f}$ and $\mathbf{t^i}$ are stress tensors at the final state referring to the natural and the initial configurations, respectively. ρ^0 and ρ^i are the corresponding mass densities. Subtracting equation C.1 from equation C.2, the equation of motion is obtained for the incremental displacement in natural coordinates $u(\xi, t)$ and in the initial coordinate $u(X, t)$,

$$\frac{\partial}{\partial \xi_\beta}[T_{\alpha\beta} + T^i_{\beta\gamma}\frac{\partial u_\alpha}{\partial \xi_\gamma} + T_{\beta\gamma}\frac{\partial u^i_\alpha}{\partial \xi_\gamma}] = \rho^0 \frac{\partial^2 u_\alpha}{\partial t^2}, \tag{C.3}$$
$$\frac{\partial}{\partial X_J}[T_{IJ} + t^i_{JK}\frac{\partial u_I}{\partial X_K}] = \rho^i \frac{\partial^2 u_I}{\partial t^2}. \tag{C.4}$$

So far the only assumptions made in the derivation are that the initial deformation is static and that the dynamic disturbance is small. We have not asked how the particles are carried from the position ξ to X, nor have we imposed restrictions on the constitutive property of the material. Thus the equations of motion equation C.2 are applicable to waves propagating in a medium undergone general form of static deformation, finite or infinitesimal, elastic or inelastic.

Now we introduce the constitutive relationship in the context of acoustoelasticity. One basic assumption in the theory is that the material is hyperelastic, i.e. the material remains elastic throughout the deformation without going into plasticity. A

deformation in a medium is accompanied with a change of internal energy W (per unit mass) or free energy F (per unit mass). The law of energy conservation states:

$$dW = \theta dS + T_{\alpha\beta} dE_{\alpha\beta}/\rho^0, dF = -Sd\theta + T_{\alpha\beta} dE_{\alpha\beta}/\rho^0, \tag{C.5}$$

where θ is the temperature, S the entropy, and $F = W - \theta S$. For a hyperelastic body, W is a function of strain E and S, and F is a function of E and θ. Therefore, we have

$$T_{\alpha\beta} = \rho^0 (\frac{\partial W}{\partial E_{\alpha\beta}})_S = \rho^0 (\frac{\partial F}{\partial E_{\alpha\beta}})_\theta. \tag{C.6}$$

The subscript S indicates an adiabatic thermodynamic process, and θ an isothermal process.

The function $W(E)$ may be expanded about the state of zero strain,

$$\rho^0 W(E) = \frac{1}{2} c_{\alpha\beta\gamma\delta} E_{\alpha\beta} E_{\gamma\delta} + \frac{1}{6} c_{\alpha\beta\gamma\delta\epsilon\eta} E_{\alpha\beta} E_{\gamma\delta} E_{\epsilon\eta} + \cdots . \tag{C.7}$$

Combining equations C.6 and C.7, a constitutive equation for $T^i_{\alpha\beta}$ or $T^f_{\alpha\beta}$ is thus obtained by neglecting the higher order terms:

$$T^i_{\alpha\beta} = c_{\alpha\beta\gamma\delta} E^i_{\gamma\delta} + \frac{1}{2} c_{\alpha\beta\gamma\delta\epsilon\eta} E^i_{\gamma\delta} E^i_{\epsilon\eta}, \tag{C.8}$$

$$T^f_{\alpha\beta} = c_{\alpha\beta\gamma\delta} E^f_{\gamma\delta} + \frac{1}{2} c_{\alpha\beta\gamma\delta\epsilon\eta} E^f_{\gamma\delta} E^f_{\epsilon\eta}. \tag{C.9}$$

From the difference of these two equations, a constitutive equation for the incremental stress tensor $T_{\alpha\beta}$ is derived,

$$T_{\alpha\beta} = c_{\alpha\beta\gamma\delta} E_{\gamma\delta} + c_{\alpha\beta\gamma\delta\epsilon\eta} e^i_{\gamma\delta} e_{\epsilon\eta}, \tag{C.10}$$

where the infinitesimal strain tensor e^i and e are used. $e_{\alpha\beta} = (\frac{\partial u_\alpha}{\partial \xi_\beta} + \frac{\partial u_\beta}{\partial \xi_\alpha})/2$ and $e^i_{\alpha\beta} = (\frac{\partial u^i_\alpha}{\partial \xi_\beta} + \frac{\partial u^i_\beta}{\partial \xi_\alpha})/2$.

The difference of the Lagrangian strain tensor in the final and initial states $E^f_{\alpha\beta}$

and $E^i_{\alpha\beta}$, is given approximately by

$$E_{\alpha\beta} = E^f_{\alpha\beta} - E^i_{\alpha\beta} = \frac{1}{2}(\frac{\partial u_\alpha}{\partial \xi_\beta} + \frac{\partial u_\beta}{\partial \xi_\alpha} + \frac{\partial u^i_\lambda}{\partial \xi_\alpha}\frac{\partial u_\lambda}{\partial \xi_\beta} + \frac{\partial u^i_\lambda}{\partial \xi_\beta}\frac{\partial u_\lambda}{\partial \xi_\alpha}). \tag{C.11}$$

In terms of displacement gradients, the constitutive equation is

$$T_{\alpha\beta} = c_{\alpha\beta\gamma\delta}(\delta_{\rho\gamma} + \frac{\partial u^i_\rho}{\partial \xi_\gamma})\frac{\partial u_\rho}{\partial \xi_\delta} + c_{\alpha\beta\gamma\delta\epsilon\eta}\frac{\partial u^i_\gamma}{\partial \xi_\delta}\frac{\partial u_\epsilon}{\partial \xi_\eta}. \tag{C.12}$$

where only terms linear in $\frac{\partial u}{\partial \xi}$ or $\frac{\partial u^i}{\partial \xi}$ are retained. Substituting the constitutive equations for $T_{\alpha\beta}$ into equation C.3, we obtain the equation of motion in term of $u(\xi, t)$, the incremental displacement introduced by the dynamic field,

$$\frac{\partial}{\partial \xi_\beta}[T^i_{\gamma\beta}\frac{\partial u_\alpha}{\partial \xi_\gamma} + \Gamma_{\alpha\beta\gamma\delta}\frac{\partial u_\gamma}{\partial \xi_\delta}] = \rho^0\frac{\partial^2 u_\alpha}{\partial t^2}. \tag{C.13}$$

This is the equation describing the dynamic field with reference to the natural coordinates. The initial stress can be arbitrarily distributed and the material can have intrinsic anisotropy. The coefficient $\Gamma_{\alpha\beta\gamma\delta} = \Gamma_{\gamma\delta\alpha\beta}$ is of lower order symmetry than $c_{\alpha\beta\gamma\delta}$. It is the effective elastic moduli of the material after static deformation.

$$\Gamma_{\alpha\beta\gamma\delta} = c_{\alpha\beta\gamma\delta} + c_{\alpha\beta\rho\delta}\frac{\partial u^i_\gamma}{\partial \xi_\rho} + c_{\rho\beta\gamma\delta}\frac{\partial u^i_\alpha}{\partial \xi_\rho} + c_{\alpha\beta\gamma\delta\epsilon\eta}e^i_{\epsilon\eta} \tag{C.14}$$

Einstein summation convention applies in all derivations.

For a homogeneously predeformed medium, i.e. T^i and $\partial u^i/\partial \xi$ are constant throughout the body, the equation of motion [equation C.13] is reduced to

$$A_{\alpha\beta\gamma\delta}\frac{\partial^2 u_\gamma}{\partial \xi_\beta \partial \xi_\delta} = \rho^0\frac{\partial^2 u_\alpha}{\partial t^2}, \tag{C.15}$$

where

$$A_{\alpha\beta\gamma\delta} = T^i_{\beta\delta}\delta_{\alpha\gamma} + \Gamma_{\alpha\beta\gamma\delta} \tag{C.16}$$

are constant coefficients.

A plane sinusoidal wave is represented by

$$u_\alpha = U_\alpha exp[i(\kappa\nu_\beta\xi_\beta - \omega t)], \tag{C.17}$$

where **U** is a constant complex vector, ω the angular frequency, $\kappa(= 2\pi/\text{wavelength})$ the wave number, and ν (a unit vector) the wave normal. The wave speed is given by $v = \omega/\kappa$. On substituting equation C.17 into equation C.15, we obtain a system of equations for the amplitude vector **U**:

$$[A_{\alpha\beta\gamma\delta}\nu_\beta\nu_\delta - \rho^0 v^2\delta_{\alpha\gamma}]U_\gamma = 0. \tag{C.18}$$

The associated characteristic equation is

$$|A_{\alpha\beta\gamma\delta}\nu_\beta\nu_\delta - \rho^0 v^2\delta_{\alpha\gamma}| = 0. \tag{C.19}$$

Once the initial stress and initial displacement gradients are specified, and the values of ρ^0, $c_{\alpha\beta\gamma\delta}$, and $c_{\alpha\beta\gamma\delta\epsilon\eta}$ in a medium are given, the eigenvalues (wave velocities) and eigenvectors (polarization directions) of equation C.18 can be solved for each direction ν of propagation.

The above equation of motion refers to the natural state, the state without static deformations. It is appropriate to apply those equations to laboratory measurements where the rock is initially unstressed. However, to describe wave propagations in the solid earth, it is more appropriate to work with formulae referring to the statically loaded state, *i.e.* the initial state, as all measured properties are made after the earth is stressed by tectonic movements.

The constitutive equation for the incremental stress with reference to the initial state, T_{JK}, is obtained by transforming $T_{\alpha\beta}$ by equation C.21.

$$T_{IJ} = C_{IJKL}\frac{\partial u_K}{\partial X_L} \tag{C.20}$$

$$T_{JK} = |\frac{\partial X}{\partial \xi}|^{-1}\frac{\partial X_J}{\partial \xi_\alpha}\frac{\partial X_K}{\partial \xi_\beta}T_{\alpha\beta}. \tag{C.21}$$

The equation of motion in terms of the displacement referring to the initial state, $u(X,t)$, is derived by substituting the constitutive equation C.20 into equation C.4,

$$\frac{\partial}{\partial X_J}[(\delta_{IJ}t^i_{JL} + C_{IJKL})\frac{\partial u_K}{\partial X_L}] = \rho^i \frac{\partial^2 u_I}{\partial t^2}. \tag{C.22}$$

where

$$\begin{aligned} C_{IJKL} &= c_{IJKL}(1 - e^i_{NN}) + c_{IJKLMN}e^i_{MN} + c_{MJKL}\frac{\partial u^i_I}{\partial X_M} \\ &+ c_{IMKL}\frac{\partial u^i_J}{\partial X_M} + c_{IJML}\frac{\partial u^i_K}{\partial X_M} + c_{IJKM}\frac{\partial u^i_L}{\partial X_M} \end{aligned} \tag{C.23}$$

where e_{NN} is the bulk dilation. For consistency of first-order approximation, the mass density in the initial state ρ^i is converted to ρ^0 by the following approximation:

$$\rho^i \approxeq \rho^0(1 + e^i_{11} + e^i_{22} + e^i_{33}). \tag{C.24}$$

Within the framework of the aforementioned theory, the assumptions that lead to equations C.3 and C.4 are

- The initial deformation is static and the body is at equilibrium in the initial state.
- The superposed dynamic motion is small.

C.3 Colton Sandstone

In his study, Dillen (2000) carried out series of ultrasonic experiment on a cubic block of Colton sandstone. The sample consists of lithic quartz and feldspar. It is fairly homogeneous and has a porosity of about 3%. At zero stress state, the measured P-wave velocities in the $X-$ and $Z-$directions are approximately equal and differ by 5% from the velocity in the $Y-$direction. We assume that the Colton sandstone is transversely isotropic with the symmetry axis in the $Y-$direction. Figure C-2 shows the load cycle ABCD as a function of experiment time. The entire ABCD stress path

has equal normal stresses in the $X-$ and $Z-$directions.

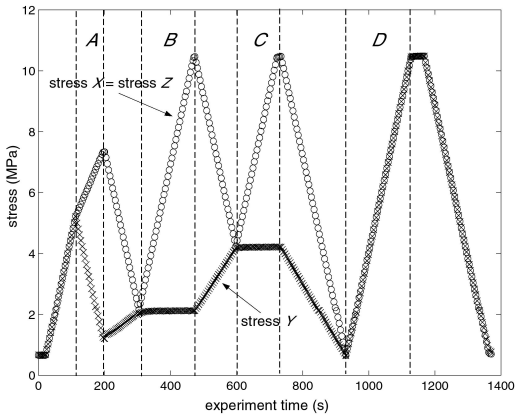

Figure C-2: Loading cycle ABCD of the tri-axial pressure machine. To preserve the intrinsic transverse isotropy of the sample, the stress in the $X-$direction is equal to the stress in the $Z-$direction (Dillen, 2000).

According to the characteristic equation (Eq C.19), when a plane wave is propagating in the $X-$direction, $\nu_1 = 1$, $\nu_2 = 0$ and $\nu_3 = 0$; therefore, Eq C.19 becomes

$$|A_{\alpha 1 \gamma 1} - \rho^0 v^2 \delta_{\alpha\gamma}| = 0. \tag{C.25}$$

In matrix form, it is

$$\begin{vmatrix} A_{11} - \rho^0 v^2 & A_{16} & A_{15} \\ A_{61} & A_{66} - \rho^0 v^2 & A_{65} \\ A_{51} & A_{56} & A_{55} - \rho^0 v^2 \end{vmatrix} = 0, \tag{C.26}$$

where

$$A_{11} = c_{11} + T^i_{11} + (2c_{11} + c_{111})e^i_{11} + c_{112}e^i_{22} + c_{113}e^i_{33}, \tag{C.27}$$

$$A_{55} = c_{55} + T^i_{33} + (2c_{55} + c_{155})e^i_{11} + c_{144}e^i_{22} + c_{344}e^i_{33}, \tag{C.28}$$

$$A_{66} = c_{66} + T^i_{22} + (2c_{66} + c_{166})e^i_{11} + c_{266}e^i_{22} + c_{366}e^i_{33}. \tag{C.29}$$

In Dillen's experiment, one of the principal initial strains is in the $X-$direction; therefore, $e^i_{31} = e^i_{21} = 0$, thus $A_{51} = A_{15} = A_{16} = A_{61} = 0$. From Eq C.26 we may obtain the compressional velocity propagating in $X-$direction as follows

$$v^2_{p_x} = \frac{A_{11}}{\rho^0}. \tag{C.30}$$

A_{11} is determined in Eq C.27. According to the acoustoelasticity theory, initial strains e^i_{11}, e^i_{22} and e^i_{33} are linearly related with applied stresses T^i_{11}, T^i_{22} and T^i_{33} through Hook's Law. Let $\mathbf{E} = [\mathbf{e^i_{11} e^i_{22} e^i_{33}}]^{\mathbf{T}}$ and $\mathbf{T} = [\mathbf{T^i_{11} T^i_{11} T^i_{33}}]^{\mathbf{T}}$, we have $\mathbf{E} = \mathbf{C^{-1}T}$. Note that $T^i_{11} = T^i_{22}$ in the experiment. $\mathbf{C}$ is the matrix of elastic stiffnesses,

$$\mathbf{C} = \begin{vmatrix} c_{11} & c_{12} & c_{13} \\ c_{12} & c_{22} & c_{12} \\ c_{13} & c_{12} & c_{11} \end{vmatrix} \tag{C.31}$$

Substituting the initial strains as a function of applied stresses into Eq C.27 and then substituting Eq C.27 into Eq C.30, we find that the square of compressional velocity propagating in $X-$direction is a linear function of applied stresses T_{11} and T_{22}:

$$v^2_{p_x} = (v_{p_x})^2_0 + AT^i_{11} + BT^i_{22}, \tag{C.32}$$

where $(v_{p_x})_0$ denotes the compressional wave propagating in the $X-$direction in the natural state. A and B are constants that are completely determined by elastic moduli and TOE constants of the rock.

T^i_{22} is constant in loading period B and C, thus $v^2_{p_x}$ is a linear function of T^i_{11}. In period A, the normal stresses in the X and $Z-$directions T^i_{11} raise from 5 MPa to 7 MPa, and for the same period of time, T^i_{22} decreases from 5 MPa to 1 MPa. We may work out the relation between T^i_{11} and T^i_{22} in period A as

$$T^i_{22} = 5 - 2T^i_{11}. \tag{C.33}$$

Substituting Eq C.33 into Eq C.32, we may also find that $v^2_{p_x}$ is a linear function of

T_{11}^i in loading period A, only with a different slope from that in periods B and C. Similar dependence of $v_{p_x}^2$ on T_{11}^i is found in load period D with yet another slope.

Similar analysis holds for dependence of P wave propagating in the $Y-$direction and for shear waves.

Figures C-3, C-4, C-5 and C-6 show both experimental and theoretical results of compressional and shear velocities versus the normal stress in the $X-$direction during cycle ABCD. The fact that very small root mean square errors between theory and experiments suggests that the theory of acoustoelasticity holds for rocks in the stress range of the experiment. We may infer that in the regime of small stresses which is below 10 MPa in the above experiment, there is no permanent deformation in the rock, i.e., cracks will reopen when stresses are removed. This satisfied the assumption associated with the theory of acoustoelasticity which requires the rock to be elastic.

C.4 Chelmsford Granite, Chicopee Shale and Berea Sandstone

A second experimental data set is analyzed for the following reason. The stress range up to 10 MPa to which the Colton sandstone was subjected, as described above, is too low to encompass *in-situ* stresses that occur in a hydrocarbon reservoir. An exception is overpressured reservoirs, showing anomalously high pore fluid pressures, resulting in correspondingly low effective stresses. Therefore, Johnson and Christensen (1993) and Lo's (1986) experimental data with confining pressures up to 200 MPa on Millboro and Braillier shales and up to 100 MPa on Berea sandstone, Chicopee shale and Chelmsford granite are analyzed in the following.

In both Johnson and Lo's experiments, three compressional and six shear velocities are measured for each of the rock samples under vacuum dry condition (Johnson et al., 1993) and Lo et al. (1986). Figure C-7 illustrates velocities measured and symmetry planes of rock samples each of which is measured transversely isotropic in the natural

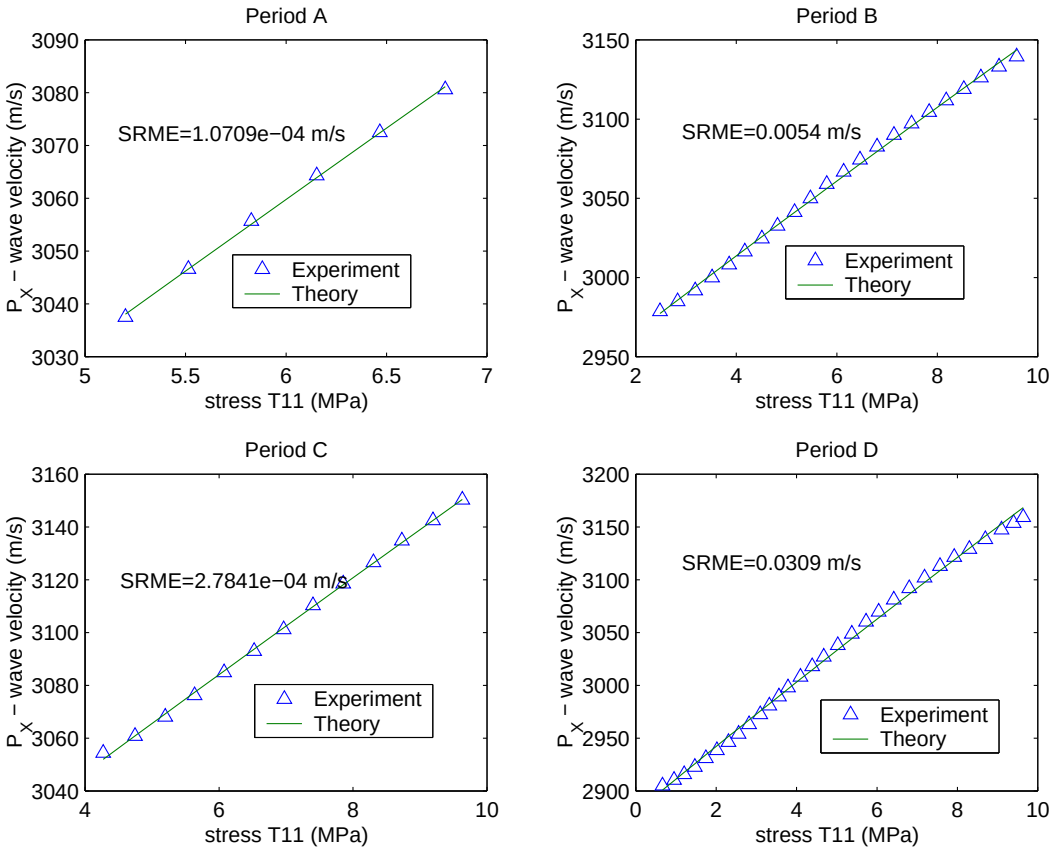

Figure C-3: Theoretical and experimental results of velocity of the compressional wave propagating in the $X-$direction versus the normal stress in the $X-$direction during the cycle ABCD (Dillen, 2000).

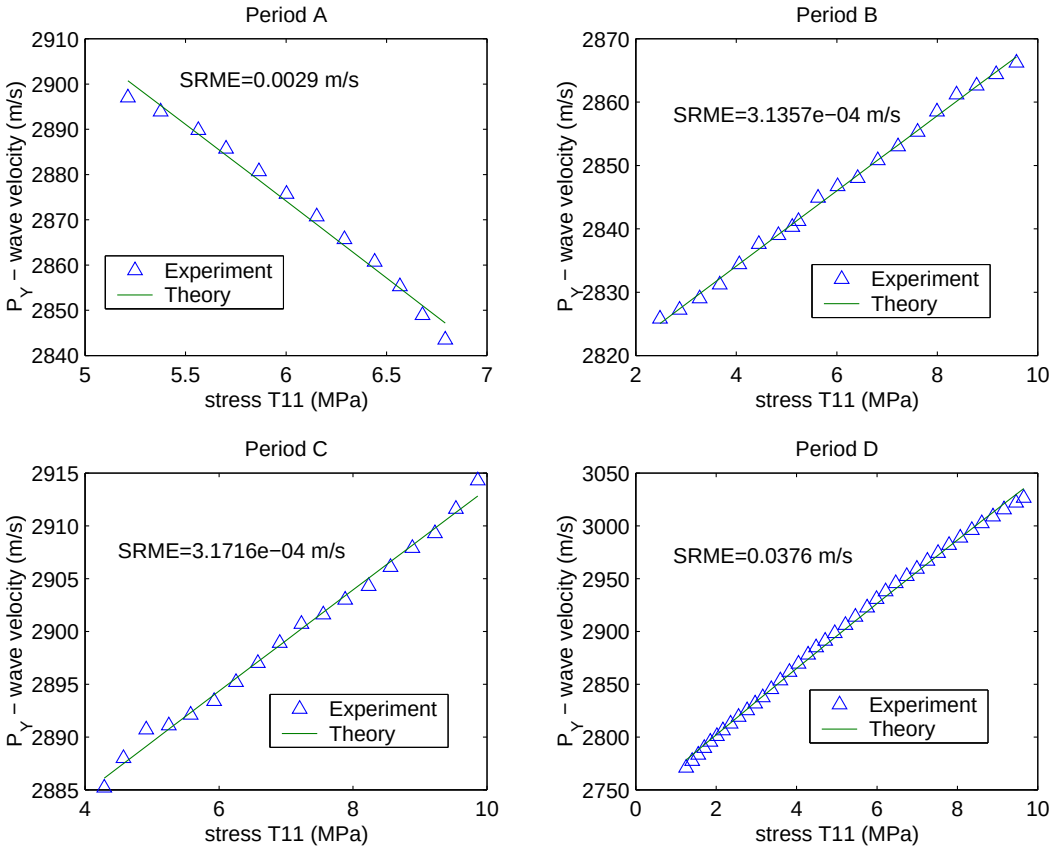

Figure C-4: Theoretical and experimental results of velocity of the compressional wave propagating in the $Y-$direction versus the normal stress in the $X-$direction during the cycle ABCD.

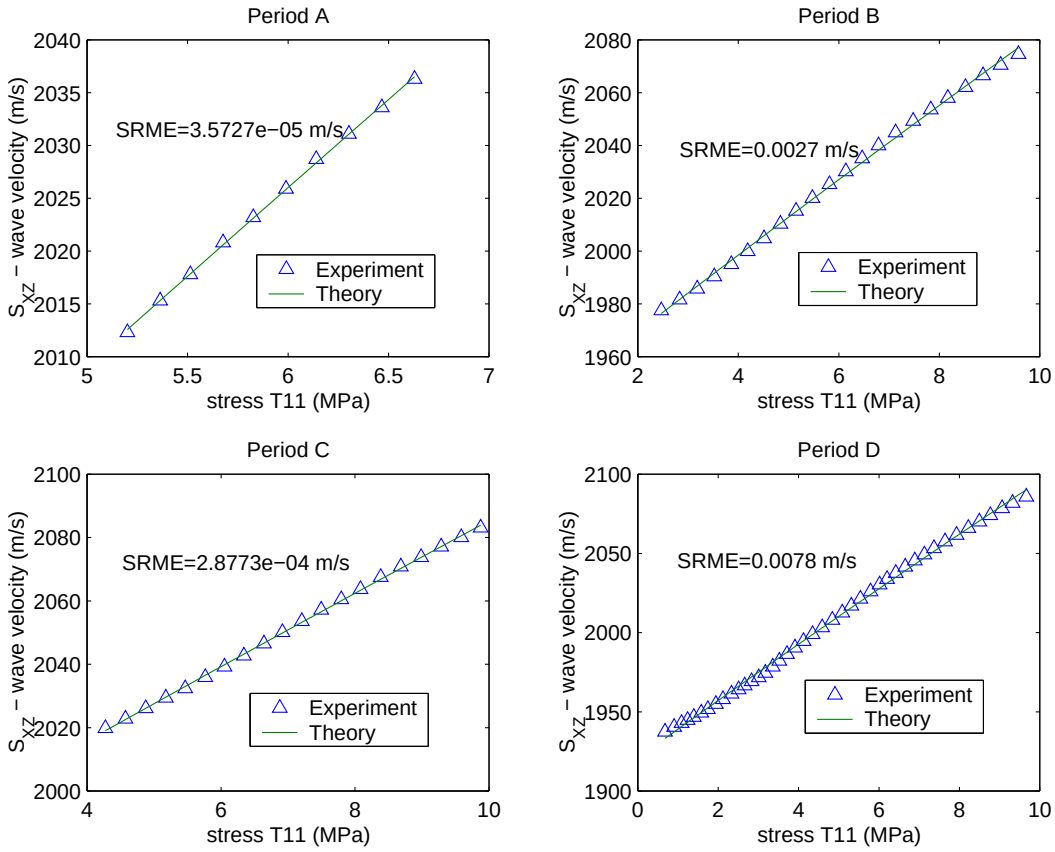

Figure C-5: Theoretical and experimental results of velocity of the shear wave propagating in the $X-$direction and polarizing in the $Z-$direction versus the normal in the $X-$direction during the cycle ABCD (experiment by Dillen).

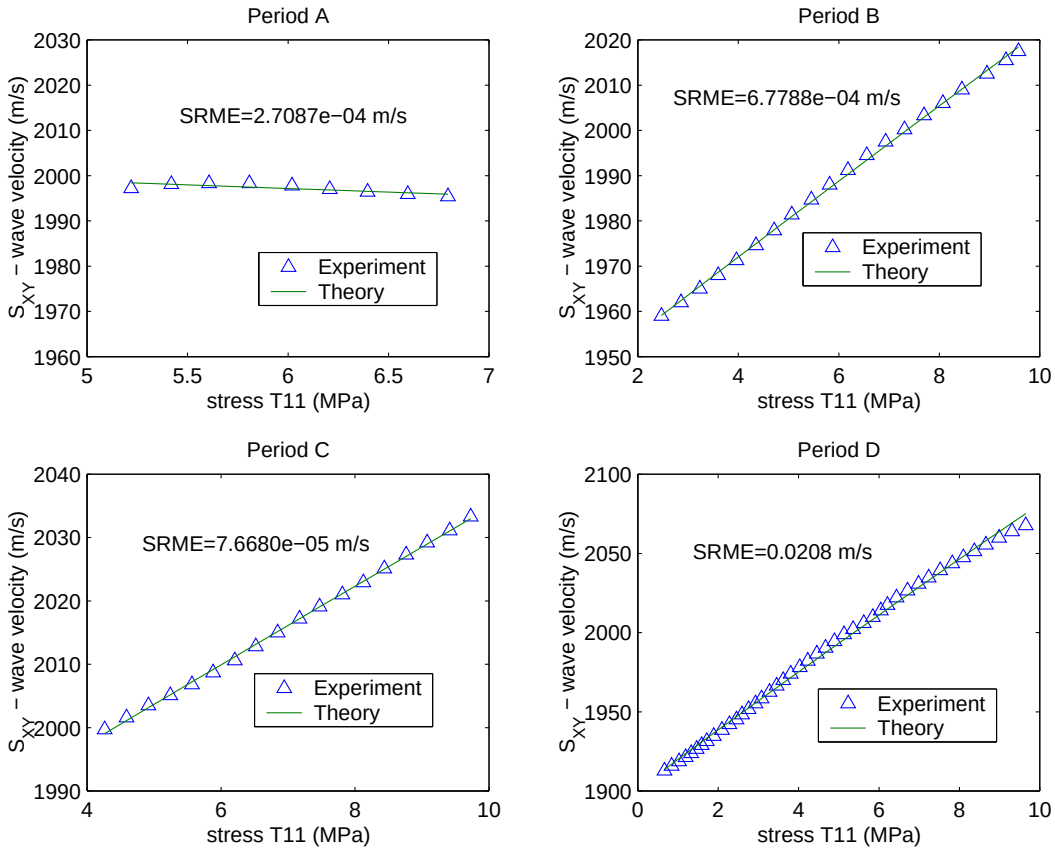

Figure C-6: Theoretical and experimental results of velocity of the shear wave propagating in the $X-$direction and polarizing in the $Y-$direction versus the normal in the $X-$direction during the cycle ABCD (experiment by Dillen).

state.

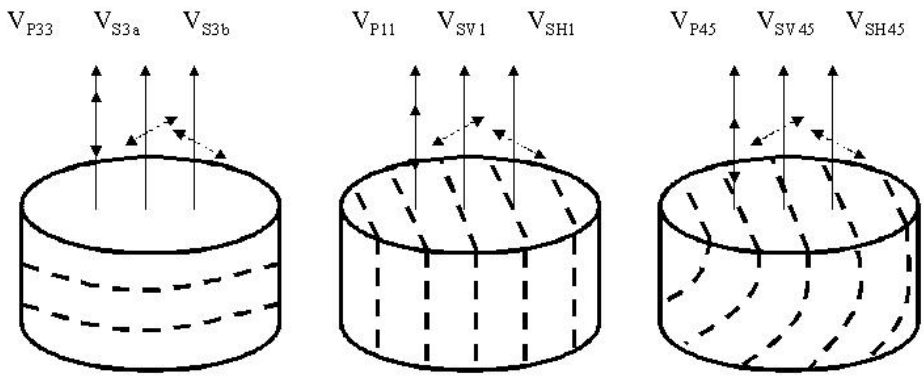

Figure C-7: Velocities measured and symmetry planes of rock samples each of which is measured transversely isotropic in the natural state (both Johnson and Lo's experiments).

Figures C-8, C-9 and C-10 show that root mean square errors between experiments and theoretical predictions are below 1% for every shale sample at all confining pressures. The excellent agreement between theory and experiment is not surprising, for all shale samples have very low porosities thus crack growth and coalescence, primary factors attributing to the highly nonlinear and inelastic behavior in rocks, are very inactive. For the Berea sandstone sample, experiments and theory show sound agreement at confining pressure levels that are higher than 30 MPa (Figure C-12). A significant portion of cracks in this rock are closed at the confining pressure of 30 MPa therefore the rock starts to have a similiar behavior to shales. The corresponding error between experiments and theory is also winthin 1%. For the granite sample, the required confining pressure to close the majority of cracks is 40 MPa (Figure C-11). When stresses are applied to a rock, elastic and inelastic deformations are competing with each other. The inelastic deformation includes permenant closure of cracks, development of new cracks that results from local failures and permenant relative movement between rock grains. In order to account for inelastic deformation, the theory of acoustoelasticity has to be modified. From the above analysis, we find

that the theory of acoustoelasticity applies to all shale samples of low porosity. For the sandstone and granite samples, in the intermediate stress regime which is about 10 MPa to 30 or 40 PMa, they undergo primarily inelastic deformations. When the stress level is 30 or 40 MPa higher, the theory of acoustoelasticity works well with all types of rocks that are studied in this paper, because most cracks are closed at that confining pressure level and thus elastic deformation becomes primary. Rocks are under high confining pressures when they are kilometers beneath the surface of the earth where we are interested to measure *in-situ* stresses. So for the purpose of estimating *in-situ* stresses, the theory of acoustoelasticity is applicable to all types of rocks.

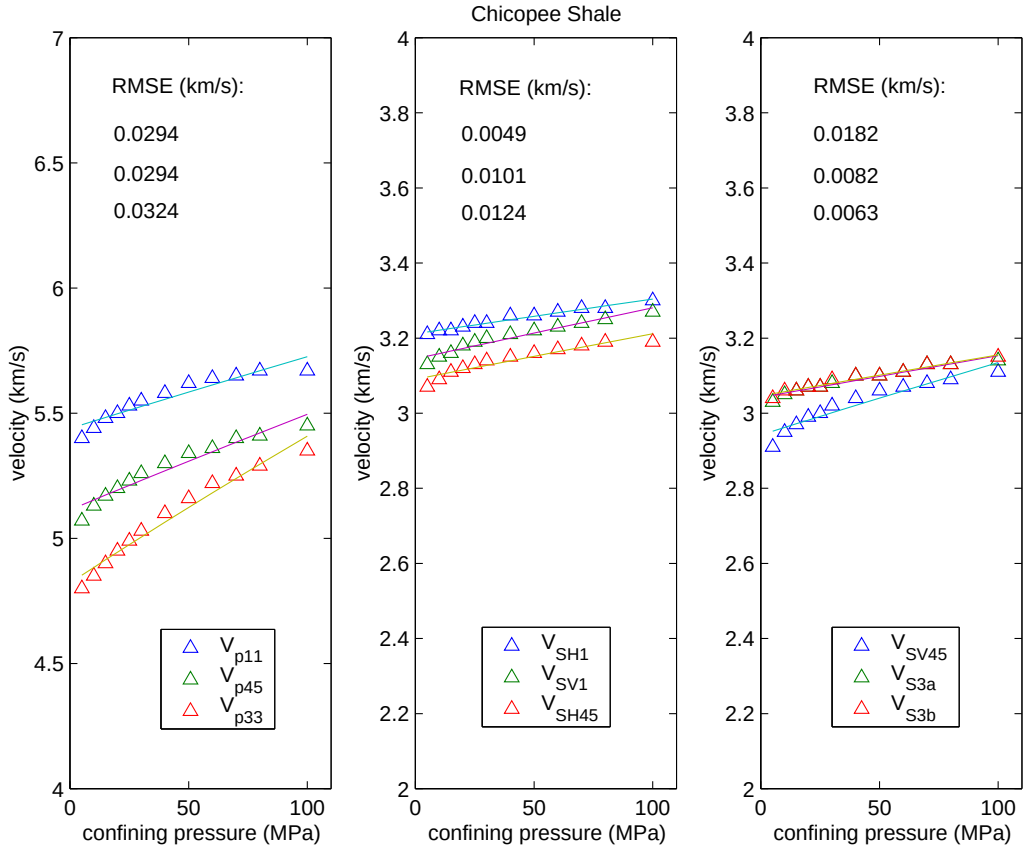

Figure C-8: Theoretical and experimental results for Braillier shale (experiment by Johnson and Christensen (1993). Δ: experiment; solid line: theory. RMSE denotes root mean square error between theory and experiment.

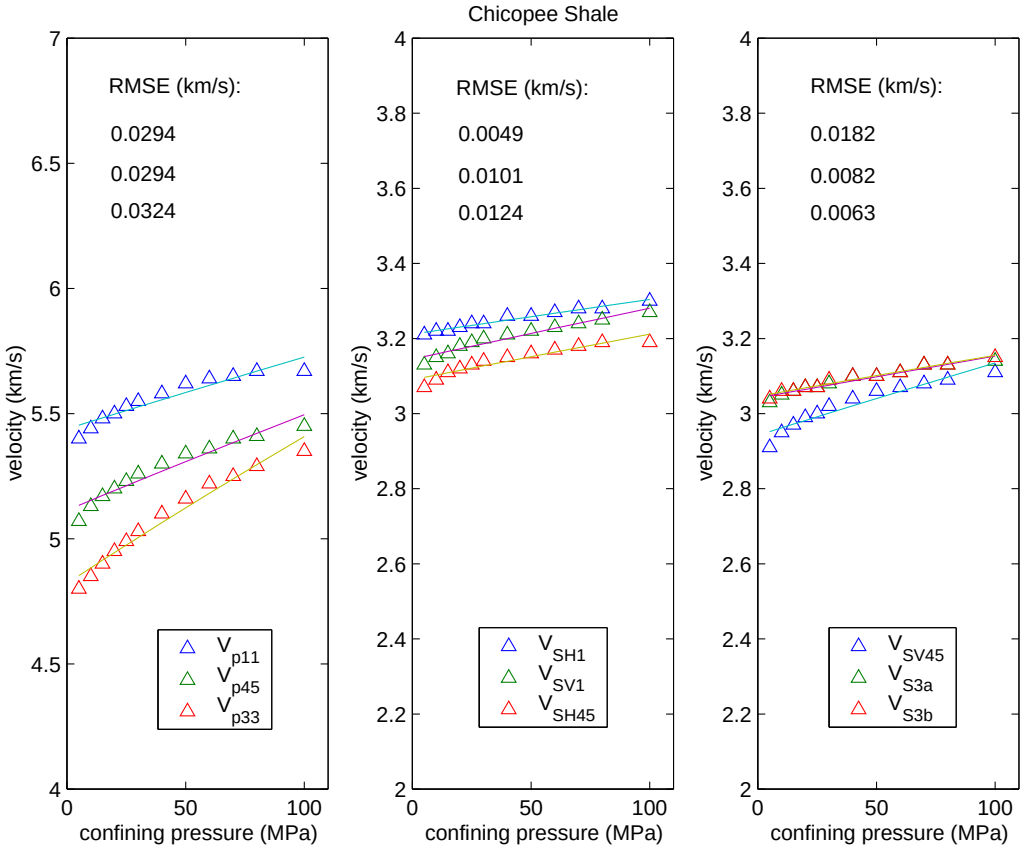

Figure C-9: Theoretical and experimental results for Millboro shale (experiment by Johnson and Christensen (1993). Δ: experiment; solid line: theory.

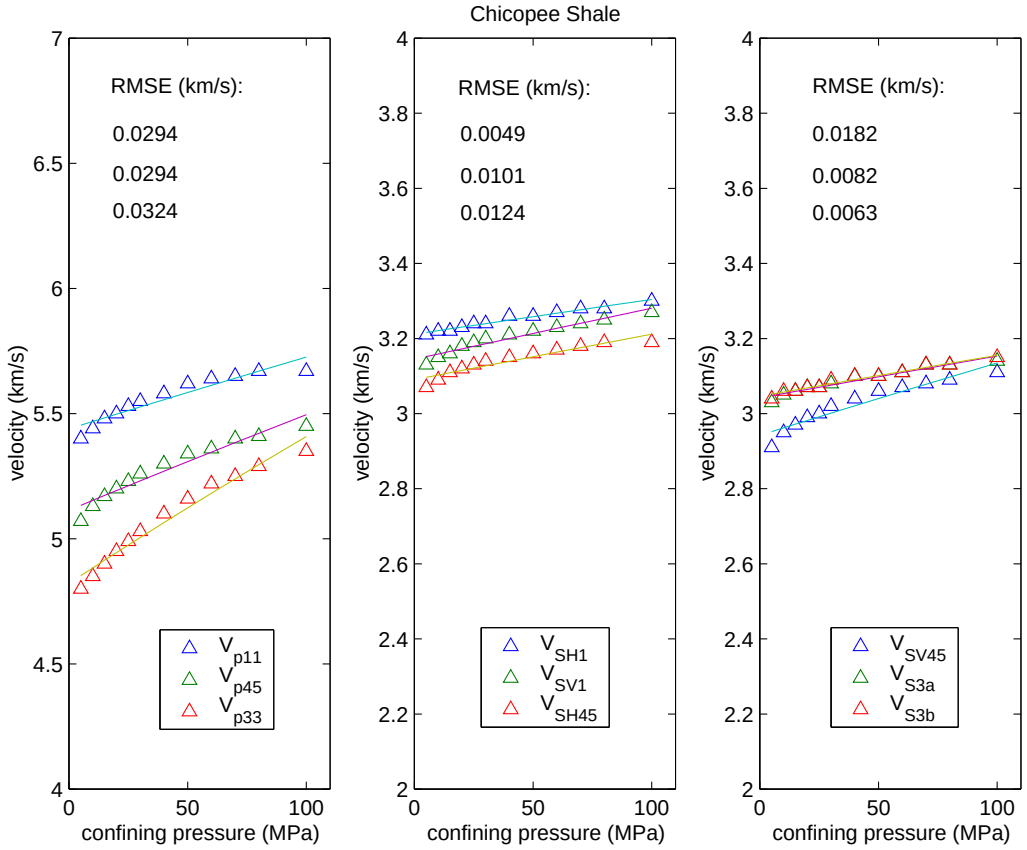

Figure C-10: Theoretical and experimental results for Chicopee Shale (experiment by Lo *et al* (1986). Δ: experiment; solid line: theory.

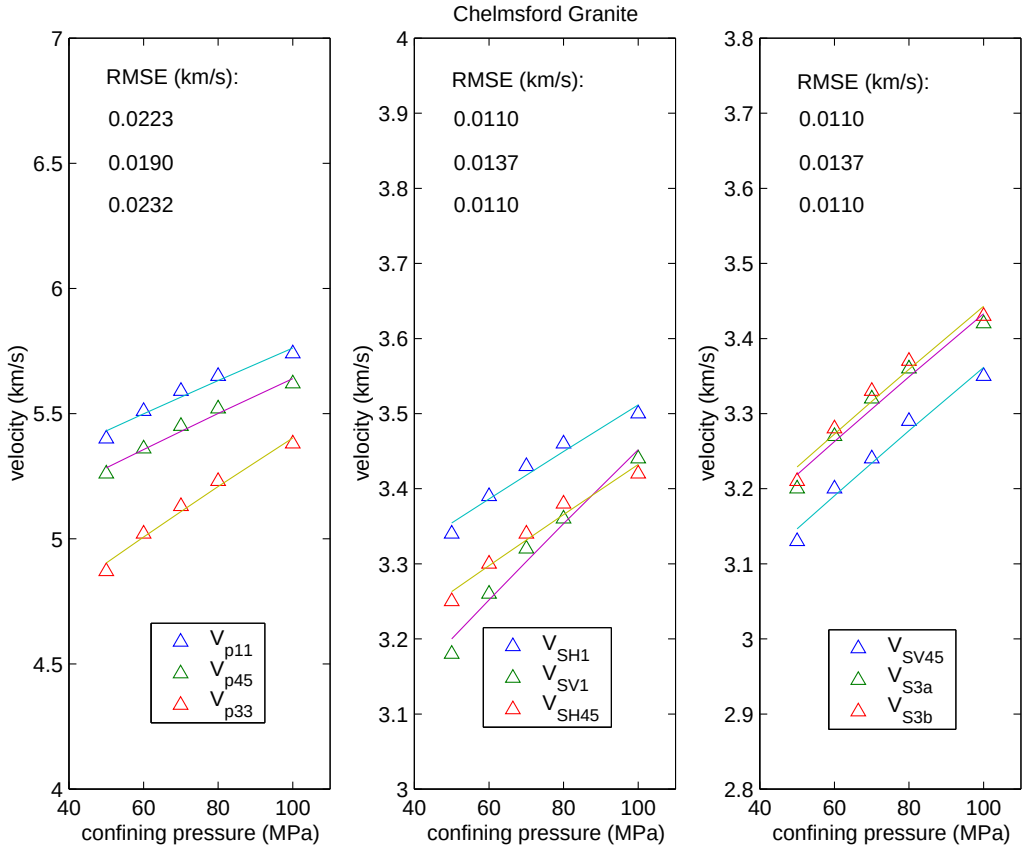

Figure C-11: Theoretical and experimental results and their relative errors for Chelmsford granite (experiment by Lo *et al* (1986). Δ: experiment; solid line: theory.

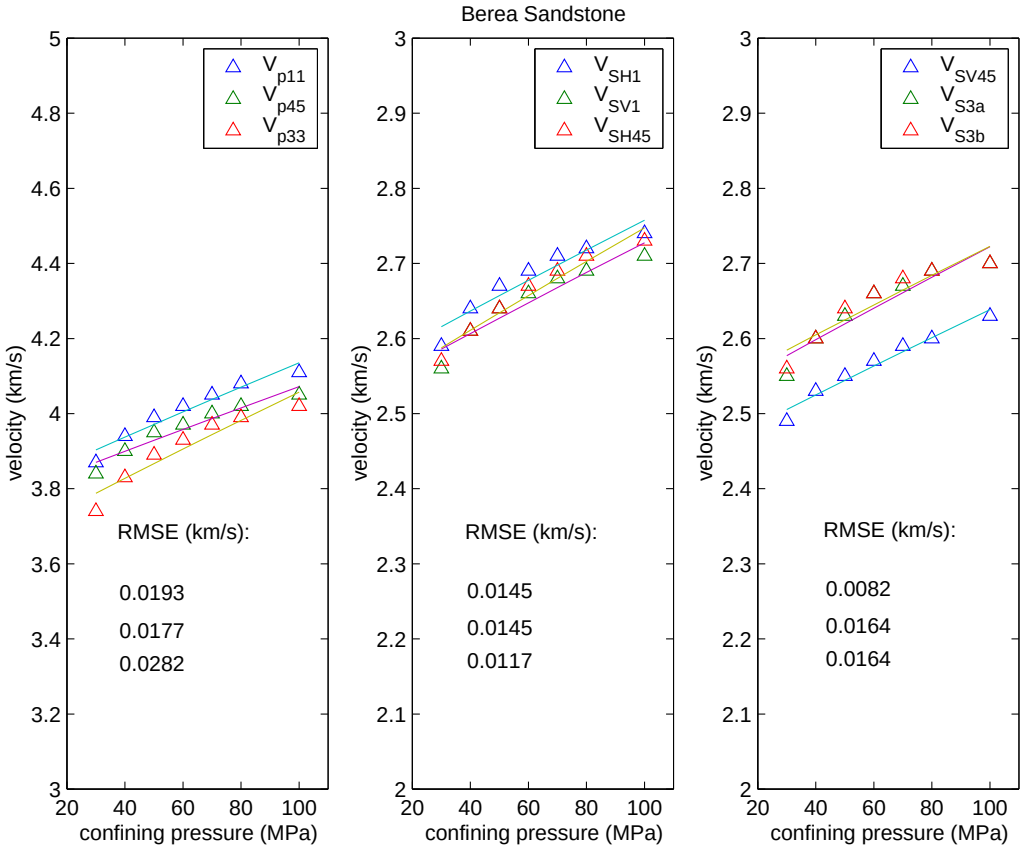

Figure C-12: Theoretical and experimental results and their relative errors for Berea sandstone (experiment by Lo *et al* (1986). Δ: experiment; solid line: theory.

C.5 Barre Granite

Nur and Simmons (1969) measured compressional velocities at various radial directions of a cylindrical sample of Barre granite subject to an uniaxial compressive stress normal to the axis of the cylinder.

It is more convenient to work with cylindrical coordinates given the geometry of the experimental setup. Note that in cylindrical coordinates, the stress tensor $\mathbf{T} = [\mathbf{T^i_{11}T^i_{22}T^i_{33}}]^{\mathbf{T}} = [\mathbf{T^i_{rr}T^i_{\beta\beta}T^i_{zz}}]^{\mathbf{T}}$, and the strain tensor $\mathbf{E} = [\mathbf{e^i_{11}e^i_{22}e^i_{33}}]^{\mathbf{T}} = [\mathbf{e^i_{rr}e^i_{\beta\beta}e^i_{zz}}]^{\mathbf{T}}$. The initial strain $\mathbf{E}$ is linearly related to the initial stress $\mathbf{T}$ through elastic moduli as mentioned previously. Components of $\mathbf{E}$ and $\mathbf{T}$ in equation C.27 can be those in cylindrical coordinates as defined above. Suppose the applied uniaxial stress, σ, coincides with $\beta = 0^o$; therefore, at angle β, the three normal stresses components of $\mathbf{T}$ in cylindrical coordinates are

$$\mathbf{T} = \begin{bmatrix} \sigma cos^2\beta \\ \sigma sin^2\beta \\ 0 \end{bmatrix}. \tag{C.34}$$

Substituting the radial component in equation C.34 into equation C.30, we obtain the compressional wave velocity as a function of applied stress σ and the angle β,

$$v_p^2 = (v_p)_0^2 + A\sigma + B\sigma cos^2\beta, \tag{C.35}$$

where A and B are constants determined by elastic moduli and TOE constants of the rock. $(v_p)_0$ is the compressional velocity in the natural state. We choose the average stress-free velocity $(v_p)_0$ at all angles to be 3.79 km/s, and then invert Nur's data (10 MPa, 20 MPa and 30 MPa) for constants A and B. The results are $A = 0.008$ and $B = 0.0225$.

An alternative way of analyzing stress-induced velocity changes in rocks is to think microscopically which has long been well received in geophysical community(e.g.Sayers (1988a), Sayers et al. (1990)). Because the theory of acoustoelasticity, using a macro-

scopic approach, also works reasonably well with rocks, as shown in (Johnson and Rasolofosaon, 1996; Winkler and Liu, 1996), we shall make comparison between the two approaches.

Sayers applied the micro-crack theory to the measurements of Nur and Simmons (Sayers, 1988b). His formula for the compressional velocity at angle β is

$$v_p = A + Bcos2\beta, \tag{C.36}$$

where A and B are unknown variables that depend not only on the elastic properties of the rock, but also the applied stress. He evaluated A and B by fitting the measurements of Nur and Simmons with the following results:

Stress (MPa)	A	B
10	4.052	0.199
20	4.271	0.301
30	4.414	0.322

Figure C-13 exhibits compressional wave velocity measurements of Nur and Simmons for Barre granite compared with the acoustoelastic theory and micro-crack model prediction. An error analysis shows errors between experiment measurements and both models are mostly below 2% (Figure C-14). Relative errors between the two models also suggest the two models agree with each other quite well (Figure C-15).

The micro-crack model implicitly deals with the velocity dependence on the applied stress. A and B are inverted for each applied stress level and thus are dependents of applied stress. On the other hand, in the acoustoelastic approach, A and B are constants that depend only on the elastic properties of the rock. So it is not surprising that micro-crack model fits the experiments slightly better than acoustoelastic model. However, for the ultimate purpose of inverting measured velocity changes for formation stresses, it is a disadvantage of the micro-crack model not to work explicitly with the velocity dependence on the applied stress.

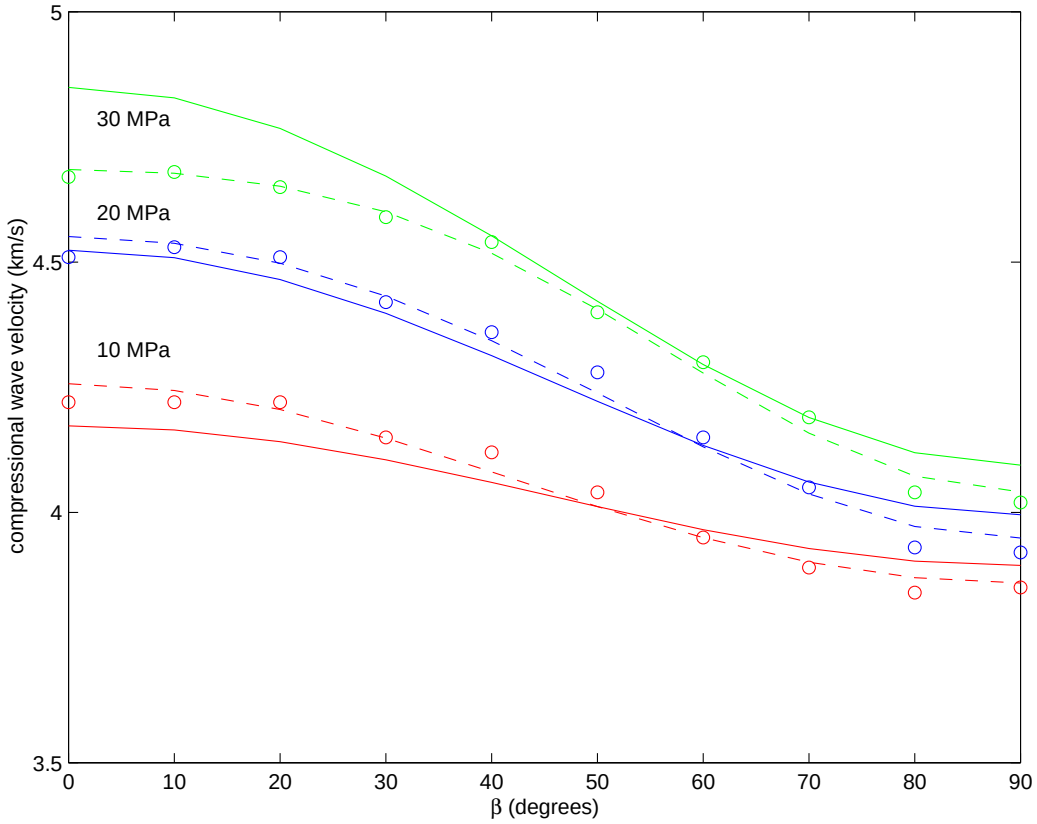

Figure C-13: Compressional wave velocity measurements of Nur and Simmons (Nur and Simmons, 1969) for Barre granite compared with the acoustoelastic theory and micro-crack model prediction (Sayers, 1988b). Solid line: acoustoelasticity, Dash line: micro-crack model.

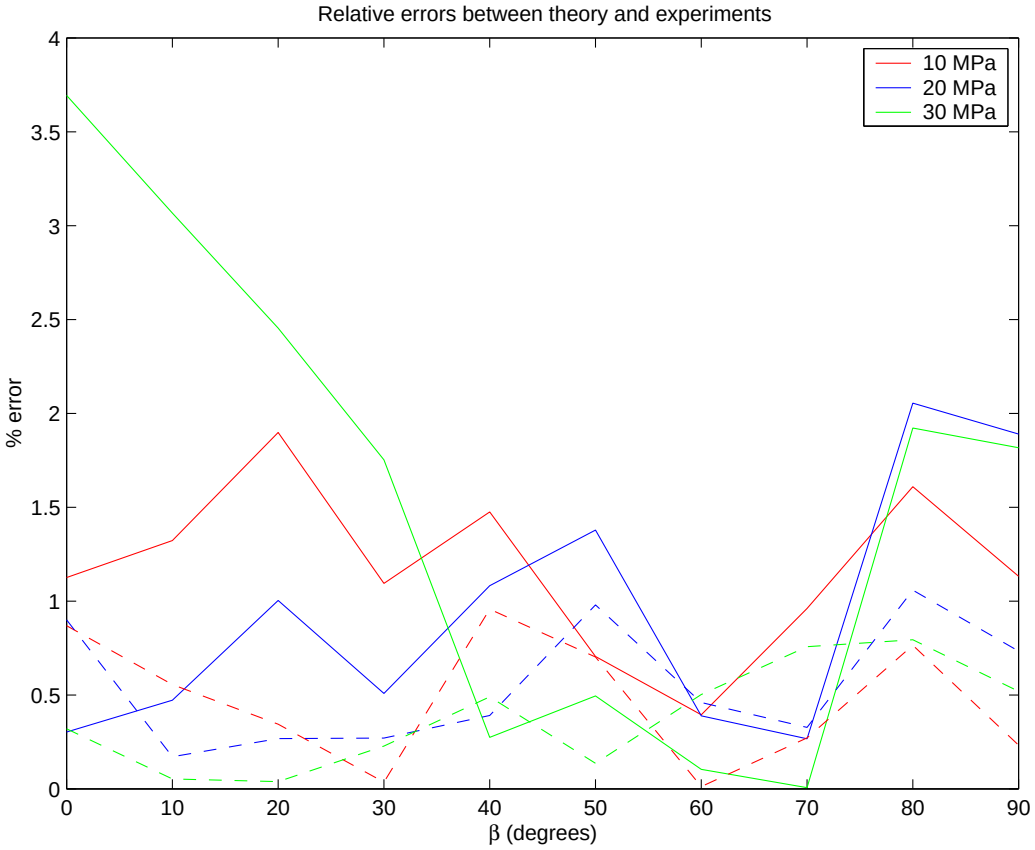

Figure C-14: Relative error between experiment measurements and theory for Barre granite. Solid line: acoustoelasticity, Dash line: micro-crack model.

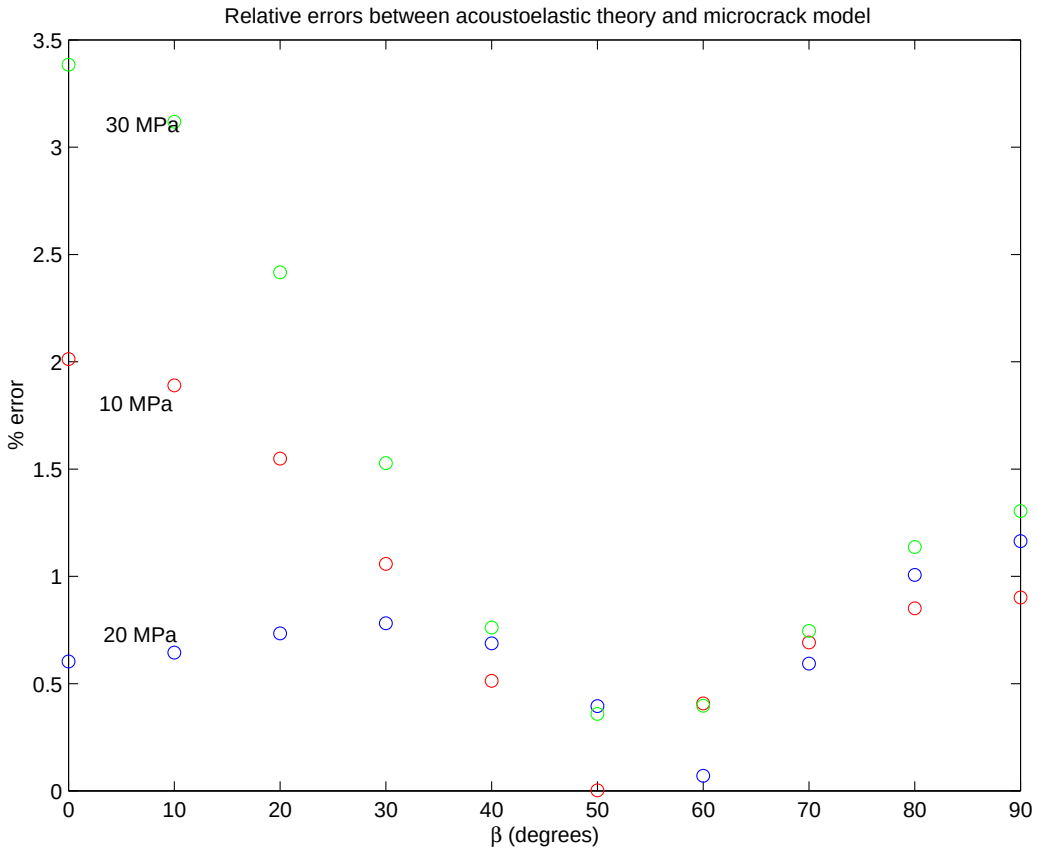

Figure C-15: Relative error between acoustoelastic theory and micro-crack model for Barre granite.

C.6 Conclusion

Rocks in general exhibit strong nonlinear stress-strain behavior. As a result, applied or residual stresses in rocks affect sound velocity considerably. The micro-crack model explains this phenomenon from a microscopic point view, *i.e.*, relating velocity changes to crack closures and reopenings caused by applied stresses. However the direct dependence of velocity changes on stresses, the relationship necessary to invert sound velocity change for formation stresses, is not established in this model whereas it is in theory of acoustoelasticity, a model that explains the nonlinear behavior from a macroscopic point of view. In the past 40 years, the theory of acoustoelasticity has been confirmed and widely employed to evaluate applied or residual stresses in polycrystalline materials. It is only in recent years that the theory is applied to rock measurements. Its applicability to rocks have been confirmed by two independent research efforts (Johnson and Rasolofosaon, 1996; Winkler and Liu, 1996). Using the various measurements on different types of rocks by various people, we compared acoustoelastic theory with the micrography model and found they agree with each other within 2% of error.

It is also worth of noting that the current theory of acoustoelasticity is based on the first two none zero terms of the Taylor's expansion of the internal energy, which leads to the second order elastic and TOE constants. Dry rocks however show stronger nonlinearity than polycrystalline materials. That means higher order terms are needed to account for the stronger nonlinearity. In the situation of *in-situ* borehole measurement, the rocks are subjected to some amount of confining pressure, the nonlinear behavior in the rock is reduced greatly. So for wave propagation in a fluid-filled borehole for logging, the current theory of acoustoelasticity is able to account for the dominant characteristics of the statically stressed formation.

Appendix D

Sensitivity coefficients for borehole guided wave dispersions to the formation stress and third-order elastic constants

In chapter 6, details about coefficients C_i^0, C_i^{90}, and C_i, with $i = 1$, 2, 3 and 4, are left out. Those coefficients are computed from the perturbation theory outlined in chapter 6. They frequency dependent integrals that can be evaluated in terms of the known flexural wave solution in the reference state and biasing stresses of unit-magnitude and corresponding strains in the formation. The superscript 0 denotes flexural wave polarization along the far-field uniaxial stress direction, while 90 denotes flexural wave polarization in the perpendicular direction.

D.1 Flexural Mode

The sensitivity coefficients C_1^0, C_2^0, C_3^0, C_4^0, are given by the following integrals

$$C_1^0 = \frac{I_1}{2\omega_m^2 I_N}, \tag{D.1}$$

$$C_2^0 = \frac{c_{66} I_2}{2\omega_m^2 I_N}, \tag{D.2}$$

$$C_3^0 = \frac{c_{66} I_3}{2\omega_m^2 I_N}, \tag{D.3}$$

$$C_4^0 = \frac{c_{66} I_4}{2\omega_m^2 I_N}. \tag{D.4}$$

Since the integral I_1 consists of several lengthy expressions, we express this integral as a sum of 9 terms as shown below:

$$I_1 = \sum_{Q=1}^{9} I_{1Q}, \tag{D.5}$$

where

$$\begin{aligned} I_{11} &= \int_a^\infty r dr \int_0^{2\pi} d\phi [T_{ZZ} u_{z,z} + c_{12}[E_{RR} u_{r,r} + E_{\Phi\Phi}(\frac{u_{\phi,\phi}}{r} + \frac{u_r}{r})] \\ &+ c_{12} E_{R\Phi}(\frac{u_{r,\phi}}{r} - \frac{u_\phi}{r} + u_{\phi,r})] u^*_{z,z}, \end{aligned} \tag{D.6}$$

$$\begin{aligned} I_{12} &= \int_a^\infty r dr \int_0^{2\pi} d\phi [c_{12} E_{RR} u_{z,z} + 2c_{11} E_{RR} u_{r,r} + T_{RR} u_{r,r} \\ &+ c_{12}(E_{RR} + E_{\Phi\Phi})(\frac{u_{\phi,\phi}}{r} + \frac{u_r}{r}) + c_{66} E_{RZ}(\frac{u_{r,\phi}}{r} - \frac{u_\phi}{r} + u_{\phi,r}) \\ &+ (T_{R\Phi} + c_{12} E_{R\Phi}) u_{r,\phi} + c_{11} E_{R\Phi} u_{\phi,r}] u^*_{r,r}, \end{aligned} \tag{D.7}$$

$$\begin{aligned} I_{13} &= \int_a^\infty r dr \int_0^{2\pi} d\phi [c_{12} E_{\Phi\Phi} u_{z,z} + c_{12}(E_{RR} + E_{\Phi\Phi}) u_{r,r} \\ &+ (2c_{11} E_{\Phi\Phi} + T_{\Phi\Phi})(\frac{u_{\phi,\phi}}{r} + \frac{u_r}{r}) + c_{66} E_{R\Phi}(\frac{u_{r,\phi}}{r} - \frac{u_\phi}{r} + u_{\phi,r}) \\ &+ (T_{R\Phi} + c_{12} E_{R\Phi}) u_{\phi,r} + c_{11} E_{R\Phi}(\frac{u_{r,\phi}}{r} - \frac{u_\phi}{r})](\frac{u^*_{\phi,\phi}}{r} + \frac{u^*_r}{r}), \end{aligned} \tag{D.8}$$

$$I_{14} = \int_a^\infty r dr \int_0^{2\pi} d\phi [T_{RR} u_{z,r} + T_{R\Phi} \frac{u_{z,\phi}}{r} + c_{66}(E_{RR} u_{r,z} + E_{R\Phi} u_{\phi,z})] u^*_{z,r}, \tag{D.9}$$

$$
\begin{aligned}
I_{15} &= \int_a^\infty r dr \int_0^{2\pi} d\phi [c_{66} E_{RR}(u_{z,r} + u_{r,z}) + c_{66} E_{R\Phi}(\frac{u_{z,\phi}}{r} + u_{\phi,z}) \\
&+ (T_{ZZ} + c_{66} E_{RR}) u_{r,z} + c_{66} E_{R\Phi} u_{\phi,z}] u^*_{r,z}, \qquad \text{(D.10)}
\end{aligned}
$$

$$
\begin{aligned}
I_{16} &= \int_a^\infty r dr \int_0^{2\pi} d\phi [T_{ZZ} u_{\phi,z} + c_{66}(E_{R\Phi} u_{r,z} + E_{\Phi\Phi} u_{\phi,z}) \\
&+ c_{66} E_{R\Phi}(u_{z,r} + u_{r,z}) + c_{66} E_{\Phi\Phi}(\frac{u_{z,\phi}}{r} + u_{\phi,z})] u^*_{\phi,z}, \qquad \text{(D.11)}
\end{aligned}
$$

$$
I_{17} = \int_a^\infty r dr \int_0^{2\pi} d\phi [T_{R\Phi} u_{z,r} + T_{\Phi\Phi} \frac{u_{z,\phi}}{r} + c_{66}(E_{R\Phi} u_{r,z} + E_{\Phi\Phi} u_{\phi,z})] \frac{u^*_{z,\phi}}{r}, \quad \text{(D.12)}
$$

$$
\begin{aligned}
I_{18} &= \int_a^\infty r dr \int_0^{2\pi} d\phi [c_{12} E_{R\Phi} u_{z,z} + (c_{11} + c_{66}) E_{R\Phi} u_{r,r} + c_{66} E_{RR}(\frac{u_{r,\phi}}{r} - \frac{u_\phi}{r}) \\
&+ (T_{R\Phi} + (c_{66} + c_{12}) E_{R\Phi})(\frac{u_{\phi,\phi}}{r} + \frac{u_r}{r}) \\
&+ (T_{RR} + c_{66} E_{\Phi\Phi}) u_{\phi,r} + c_{66} E_{\Phi\Phi}(\frac{u_{r,\phi}}{r} - \frac{u_\phi}{r} + u_{\phi,r})] u^*_{\phi,r}, \qquad \text{(D.13)}
\end{aligned}
$$

$$
\begin{aligned}
I_{19} &= \int_a^\infty r dr \int_0^{2\pi} d\phi [c_{12} E_{R\Phi} u_{z,z} + (c_{11} + c_{66}) E_{R\Phi}(\frac{u_{\phi,\phi}}{r} + \frac{u_r}{r}) + c_{66} E_{\Phi\Phi} u_{\phi,r} \\
&+ (T_{R\Phi} + (c_{66} + c_{12}) E_{R\Phi}) u_{r,r} \\
&+ (T_{\Phi\Phi} + c_{66} E_{RR})(\frac{u_{r,\phi}}{r} - \frac{u_\phi}{r}) \\
&+ c_{66} E_{RR}(\frac{u_{r,\phi}}{r} - \frac{u_\phi}{r} + u_{\phi,r})](\frac{u^*_{r,\phi}}{r} - \frac{u^*_\phi}{r}). \qquad \text{(D.14)}
\end{aligned}
$$

The remaining integrals I_2, I_3, I_4 and I_N take the following forms

$$\begin{aligned}
I_2 &= \int_a^\infty rdr \int_0^{2\pi} d\phi [[E_{RR}u_{r,r} + \frac{1}{2}E_{R\Phi}(\frac{u_{r,\phi}}{r} - \frac{u_\phi}{r} + u_{\phi,r})]u^*_{r,r} \\
&+ [E_{\Phi\Phi}u_{\phi,\phi} + \frac{1}{2}E_{R\Phi}(\frac{u_{r,\phi}}{r} - \frac{u_\phi}{r} + u_{\phi,r})](\frac{u^*_{\phi,\phi}}{r} + \frac{u^*_r}{r}) \\
&+ \frac{1}{4}[E_{RR}(u_{r,z} + u_{z,r}) + E_{R\Phi}(\frac{u_{z,\phi}}{r} + u_{\phi,z})](u^*_{z,r} + u^*_{r,z}) \\
&+ \frac{1}{4}[E_{R\Phi}(u_{r,z} + u_{z,r}) + E_{\Phi\Phi}(\frac{u_{z,\phi}}{r} + u_{\phi,z})](u^*_{\phi,z} + \frac{u^*_{z,\phi}}{r}) \\
&+ \frac{1}{4}[(E_{RR} + E_{\Phi\Phi})(\frac{u_{r,\phi}}{r} - \frac{u_\phi}{r} + u_{\phi,r}) \\
&+ 2E_{R\Phi}(u_{r,r} + \frac{u_{\phi,\phi}}{r} + \frac{u_r}{r})](u^*_{\phi,r} + u^*_{r,\phi})], \qquad \text{(D.15)}
\end{aligned}$$

$$\begin{aligned}
I_3 &= \int_a^\infty rdr \int_0^{2\pi} d\phi [[(E_{RR} + E_{\Phi\Phi})u_{z,z} \\
&+ E_{RR}u_{r,r} + E_{\Phi\Phi}(\frac{u_{\phi,\phi}}{r} + \frac{u_r}{r}) + E_{R\Phi}(\frac{u_{r,\phi}}{r} - \frac{u_\phi}{r} + u_{\phi,r})]u^*_{z,z} \\
&+ [E_{RR}u_{z,z} + E_{\Phi\Phi}u_{r,r} + (E_{RR} + E_{\Phi\Phi})(\frac{u_{\phi,\phi}}{r} + \frac{u_r}{r}) - \frac{1}{2}E_{R\Phi}(\frac{u_{r,\phi}}{r} - \frac{u_\phi}{r} + u_{\phi,r})]u^*_{r,r} \\
&+ [E_{\Phi\Phi}u_{z,z} + (E_{RR} + E_{\Phi\Phi})u_{r,r} + E_{RR}(\frac{u_{\phi,\phi}}{r} + \frac{u_r}{r}) - \frac{1}{2}E_{R\Phi}(\frac{u_{r,\phi}}{r} - \frac{u_\phi}{r} + u_{\phi,r})](\frac{u^*_{\phi,\phi}}{r} + \frac{u^*_r}{r}) \\
&+ \frac{1}{4}[(2E_{\Phi\Phi} - E_{RR})(u_{r,z} + u_{z,r}) - 3E_{R\Phi}(\frac{u_{z,\phi}}{r} + u_{\phi,z})](u^*_{z,r} + u^*_{r,z}) \\
&+ \frac{1}{4}[(2E_{RR} - E_{\Phi\Phi})(\frac{u_{z,\phi}}{r} + u_{\phi,z}) - 3E_{R\Phi}(u_{z,r} + u_{r,z})](u^*_{\phi,z} + u^*_{z,\phi}) \\
&+ \frac{1}{2}(2E_{R\Phi}u_{z,z} - E_{R\Phi})(u_{r,r} + \frac{u_{\phi,\phi}}{r} + \frac{u_r}{r})(u^*_{\phi,r} + u^*_{r,\phi}) \\
&- \frac{1}{2}(E_{RR} + E_{\Phi\Phi})(\frac{u_{r,\phi}}{r} - \frac{u_\phi}{r} + u_{\phi,r})(u^*_{\phi,r} + u^*_{r,\phi})], \qquad \text{(D.16)}
\end{aligned}$$

$$\begin{aligned}
I_4 &= \int_a^\infty rdr \int_0^{2\pi} d\phi [[E_{\Phi\Phi}u_{r,r} + E_{RR}(\frac{u_{\phi,\phi}}{r} + \frac{u_r}{r}) - E_{R\Phi}(\frac{u_{r,\phi}}{r} - \frac{u_\phi}{r} + u_{\phi,r})]u^*_{z,z} \\
&+ E_{\Phi\Phi}u_{z,z}u^*_{r,r} + E_{RR}u_{z,z}(\frac{u^*_{\phi,\phi}}{r} + \frac{u^*_r}{r}) \\
&+ \frac{1}{2}[E_{R\Phi}(\frac{u_{z,\phi}}{r} + u_{\phi,z}) - E_{\Phi\Phi}(u_{z,r} + u_{r,z})](u^*_{z,r} + u^*_{r,z}) \\
&+ \frac{1}{2}[E_{R\Phi}(u_{r,z} + u_{z,r}) - E_{RR}(\frac{u_{z,\phi}}{r} + u_{\phi,z})](u^*_{\phi,z} + u^*_{z,\phi}) \\
&- E_{R\Phi}u_{z,z}(u^*_{\phi,r} + \frac{u^*_{r,\phi}}{r} - \frac{u^*_\phi}{r})], \qquad \text{(D.17)}
\end{aligned}$$

$$
\begin{aligned}
I_N &= \int_0^a r dr \int_0^{2\pi} d\phi \rho_f [u_r^f u_r^{f*} + u_\phi^f u_\phi^{f*} + u_z^f u_z^{f*}] \\
&+ \int_a^\infty r dr \int_0^{2\pi} d\phi \rho_s [u_r u_r^* + u_\phi u_\phi^* + u_z u_z^*], \qquad \text{(D.18)}
\end{aligned}
$$

where T_{ZZ} is the axial stress in the formation; E_{RR}, $E_{\Phi\Phi}$ and $E_{R\Phi}$ are the static strains in the formation written in cylindrical-polar coordinates; c_{11}, c_{12} and c_{66} are the linear elastic constants of the formation in the reference state; u_r^f, u_ϕ^f and u_z^f denote flexural wave solutions in the fluid; and, u_r, u_ϕ and u_z are flexural wave solutions in the formation with radial polarization parallel to the far-field stress direction.

The sensitivity coefficients C_1^{90}, C_2^{90}, C_3^{90} and C_4^{90} are given by the same expressions as for C_1^0, C_2^0, C_3^0 and C_4^0, except for the important difference that all of the biasing stresses and strains are rotated by 90^o from before so that the far-field stress direction is now perpendicular to the flexural wave radial polarization direction.

D.2 Stoneley Mode

The sensitivity coefficients C_1, C_2, C_3 and C_4 are given by the following integrals

$$C_1 = \frac{J_1}{2\omega_m^2 J_N}, \qquad \text{(D.19)}$$

$$C_2 = \frac{c_{66} J_2}{2\omega_m^2 J_N}, \qquad \text{(D.20)}$$

$$C_3 = \frac{c_{66} J_3}{2\omega_m^2 J_N}, \qquad \text{(D.21)}$$

$$C_4 = \frac{c_{66} J_4}{2\omega_m^2 J_N} \qquad \text{(D.22)}$$

where J_1, J_2, J_3 and J_4 are expressed in terms of surface integrals as shown below:

$$\begin{aligned} J_1 &= \int_a^\infty r dr \int_0^{2\pi} d\phi [[T_{ZZ} u_{z,z} + c_{12}(E_{RR} u_{r,r} + E_{\Phi\Phi}\frac{u_r}{r})] u^*_{z,z} \\ &+ [c_{12} E_{RR} u_{z,z} + (T_{RR} + 2c_{11} E_{RR}) u_{r,r} + c_{12}(E_{RR} + E_{\Phi\Phi})\frac{u_r}{r}] u^*_{r,r} \\ &+ [c_{12} E_{\Phi\Phi} u_{z,z} + (T_{\Phi\Phi} + 2c_{11} E_{\Phi\Phi})\frac{u_r}{r} + c_{12}(E_{RR} + E_{\Phi\Phi}) u_{r,r}]\frac{u^*_r}{r} \\ &+ [T_{RR} u_{z,r} + c_{66} E_{RR} u_{r,z}] u^*_{z,r} \\ &+ [c_{66} E_{RR}(u_{z,r} + u_{r,z}) + (T_{ZZ} + c_{66} E_{RR}) u_{r,z}] u^*_{r,z}], \end{aligned} \tag{D.23}$$

$$\begin{aligned} J_2 &= \int_a^\infty r dr \int_0^{2\pi} d\phi [[E_{RR} u_{r,r}] u^*_{r,r} + [E_{\Phi\Phi}\frac{u_r}{r}]\frac{u^*_r}{r} \\ &+ \frac{1}{4}[E_{RR}(u_{z,r} + u_{r,z})](u^*_{z,r} + u^*_{r,z})], \end{aligned} \tag{D.24}$$

$$\begin{aligned} J_3 &= \int_a^\infty r dr \int_0^{2\pi} d\phi [[E_{RR} + E_{\Phi\Phi}) u_{z,z} + E_{\Phi\Phi}\frac{u_r}{r} + E_{RR} u_{r,r}] u^*_{z,z} \\ &+ [E_{RR} u_{z,z} + E_{\Phi\Phi} u_{r,r} + (E_{RR} + E_{\Phi\Phi})\frac{u_r}{r}] u^*_{r,r} \\ &+ [E_{\Phi\Phi} u_{z,z} + E_{RR}\frac{u_r}{r} + (E_{RR} + E_{\Phi\Phi}) u_{r,r}]\frac{u^*_r}{r} \\ &+ \frac{1}{4}[(2E_{\Phi\Phi} - E_{RR})(u_{z,r} + u_{r,z})](u^*_{z,r} + u^*_{r,z})], \end{aligned} \tag{D.25}$$

$$\begin{aligned} J_4 &= \int_a^\infty r dr \int_0^{2\pi} d\phi [[E_{\Phi\Phi} u_{r,r} + E_{RR}\frac{u_r}{r}] u^*_{z,z} \\ &+ E_{\Phi\Phi} u_{z,z} u^*_{r,r} + E_{RR} u_{z,z}\frac{u^*_r}{r} \\ &- \frac{1}{2}[E_{\Phi\Phi}(u_{z,r} + u_{r,z})](u^*_{z,r} + u^*_{r,z})], \end{aligned} \tag{D.26}$$

$$\begin{aligned} J_N &= \int_0^a r dr \int_0^{2\pi} d\phi \rho_f (u^f_r u^{f*}_r + u^f_z u^{f*}_z) \\ &+ \int_a^\infty r dr \int_0^{2\pi} d\phi \rho_s (u_r u^*_r + u_z u^*_z), \end{aligned} \tag{D.27}$$

where u_r^f and u_z^f denote the Stoneley wave solution in the borehole fluid; and, u_r and u_z are the corresponding solution in the formation.

Bibliography

Aron, J., Chang, S., Dworak, R., Hsu, K., Lau, T., masson, J., Mayes, J., McDaniel, G., Randall, C., Kostek, S., and Plona, T. (1994). Sonic compressional measurements while drilling. *SPWLA 35th Annual Logging Symposium*.

Berenger, J. P. (1994). A perfectly matched layer for the absorption of electromagnetic-waves. *J. Comput. Phys.*, 114:185–200.

Biot, M. A. (1952). Propagation of elastic waves in a cylindrical bore containing a fluid. *J. Appl. Phys.*, 23:997–1005.

Bouchon, M. and Schmitt, D. (1989). Full-wave acoustic logging in an irregular borehole. *Geophysics*, 54:758–765.

Browning, G., Kreiss, H. O., and Oliger, J. (1973). Mesh refinement. *Mathematics of Computation*, 27:29–39.

Chen, N. (1994). *Borehole wave propagation in isotropic and anisotropic media : three-dimensional finite difference approach*. PhD dissertation, Massachusetts Institute of Technology, Department of Earth, Atmospheric and Planetary Sciences. This is a full PHDTHESIS entry.

Cheng, C. H. and Toksoz, M. N. (1981). Elastic wave propagation in a fluid-filled borehole and synthetic acoustic logs. *Geophysics*, 46:1042–1053.

Crowder, H. J. and Dalton, C. (1971). Erros in the use of nonuniform mesh systems. *Journal of Computational Physics*, 7:32–45.

Cunha, C. A. (1993). Elastic modeling in discontinuous media. *Geophysics*, 59:1840–1851.

Dablain, M. A. (1986). The application of high-order differencing to the scalar wave equation. *Geophysics*, 51:54–66.

Daubechies, I. (1988). Orthogonal bases of compactly supported wavelets. *Commun. Pure and Appl. Math*, 41:909–996.

Deslauriers, G. and Dubuc, S. (1989). Symmetric iterative interpolation processes. *Constr. Approx.*, 5:49–68.

Dillen, M. (2000). *Time-lapse seismic monitoring of subsurface stress dynamics*. PhD dissertation, Technische Universiteit Delft, Department of Geophysics. This is a full PHDTHESIS entry.

Dore, A. G. and Lundin, E. R. (1996). Cenozoic compressional structures on the ne atlantic margin: nature, origin and potential significance for hydrocarbon exploration. *Petroleum Geoscience*, 2:299–311.

Dubuc, S. (1986). Interpolation through an iterative scheme. *J. Math. Anal. Appl.*, 114:185–204.

Ellefsen, K. J., Burns, D. R., and Cheng, C. H. (1993). Homomorphic processing of the tube wave generated during acoustic logging. *Geophysics*, 58:1400–1407.

Ellefsen, K. L. (1990). *Elastic wave propagation along a borehole in an anisotropic medium*. PhD dissertation, Massachusetts Institute of Technology, Department of Earth, Atmospheric and Planetary Sciences. This is a full PHDTHESIS entry.

Finkbeiner, T., Zoback, M. D., Stump, B., and Flemings, P. (1998). In situ stress, pore pressure, and hydrocarbon migration in the south eugene island filed. *Overpressures in petroleum exploration, workshop proceedings: Elf Aquitaine Memoir 72, Pau, France*, pages 103–110.

Fujii, M. and Hoefer, W. J. (2001). A wavelet formulation of the finite-difference method: Full-vector analysis of optical waveguid junctions. *IEEE Journal of Quantum Electronics*, 37(8):1015–1029.

Gaarenstroom, L., Tromp, R. A. J., de Jong, M. C., and M., B. A. (1993). Overpressures in the central north sea: implications for trap integrity and drilling safety. *Geology of Northwest Europe: Proceedings of the 4th Conference (J. R. Parker, ed)*, pages 1305–1313.

Gough, D. I. and Bell, R. S. (1982). Stress orientations from borehole wall fractures with examples from Colorado, east Texas, and northern Canada. *Can. J. Earth Sci.*, 19:1358–1370.

Haimson, B. (1988). Preface. *Proc. 2nd International Workshops on Hydraulic Fracturing Stress Measurements*, pages 1–4.

Harrington, R. F. (1993). *Field computation by moment methods*. IEEE Press series on electromagnetic waves. Piscataway, NJ : IEEE Press.

Hayashi, K. (1999). Variable grid finite-difference modeling including surface topography. Master's thesis, Massachusetts Institute of Technology.

Hestholm, S. (1999). Three-dimensional finite-difference viscoelastic wave modeling including surface topography. *Geophysics Journal International*, 139:852–878.

Heysse, D., Robbins, C., and Minear, J. (1996). Field tests of an acoustic logging-while-drilling tool in various borehole environments. *SPWLA 37th Annual Logging Symposium, New Orleans*.

Huang, X., Burns, D. R., and Toksoz, N. M. (1998). Dispersion analysis of cross-dipole data. *Borehole Acoustics and Logging/Reservoir Delineation Consortia Annual Report, MIT*.

Huang, X., Sinha, B. K., Burns, D. R., and Toksoz, N. M. (1999). Formation stress estimation using standard acoustic logging. *Soc. Explor. Geophys. Expanded Abstracts*, pages BG2.6(53–56).

Johnson, J. E. and Christensen, N. I. (1993). Compressional to shear velocity ratios in sedimentary rocks. *Int. J. Rock Mech. Min. Sci. and Geomech. Abstr.*, 30:751–754.

Johnson, P. and McCall, K. R. (1994). Observation and implications of nonlinear elastic wave response in rock. *Geophys. Res. Lett.*, 21:165–168.

Johnson, P. A. and Rasolofosaon, P. N. J. (1996). Nonlinear elasticity and stress-induced anisotropy in rock. *J. Geophys. Res.*, 101:3113–3124.

Johnson, P. A., Rasolofosaon, P. N. J., and Zinszner, B. E. (1993). *Advances in Nonlinear Acoustics*, chapter Measurement of nonlinear elastic response in rock by the resonant bar method, pages 531–536. World Science, Singpore.

Krumpholz, M. and Katehi, L. P. B. (1996). Mrtd: New time-domain schemes based on multiresolution analysis. *IEEE Transactions on Microwave Theory and Techniques*, 44(4):555–571.

Krumpholz, M. and Russer, P. (1993). Two-dimensional fdtd and tlm. *Int. J. Num. Modeling*, 7(2):141–153.

Krumpholz, M. and Russer, P. (1994). A field theoretical derivation of tlm. *IEEE Trans. Microwave Theory Tech.*, 42(9):1660–1668.

Kurkjian, A. L. (1985). Numerical computation of individual far-field arrivals excited by an acoustic source in a borehole. *Geophysics*, 50:852–866.

Kurkjian, A. L. and Chang, S. K. (1986). Acoustic multipole sources in fluid-filled boreholes. *Geophysics*, 51:148–163.

Lang, S. S., Kurkjian, A. L., McClellan, J. H., Orris, C. F., and Parks, T. W. (1987). Esimating slowness dispersion from arrays of sonic logging data. *Geophysics*, 52:530–544.

Liu, Q. and Sinha, B. K. (2000). Multipole acoustic waveforms in fluid-filled boreholes in biaxially stressed formations: A finite difference method. *Geophysics*, 65(1):190–201.

Liu, Q. H. (1999). Perfectly matched layers for elastic waves in cylindrical and spherical coordinates. *J. Acoust. Soc. Am.*, 105:2075–2084.

Lo, T. W., Coyner, K. B., and Toksoz, M. N. (1986). Experimental determination of elastic anisotropy of Berea sandstone, Chicopee shale, and Chelmsford granite. *Geophysics*, 51(1):164–171.

Mallat, S. G. (1997). *A Wavelet Tour of Signal Processing*. San Diego, CA:Academic.

Market, J., Althoff, G., Barnett, C., and Deady, R. (2002). Processing and quality control of lwd dipole sonic measurements. *SPWLA 43rd Annual Logging Symposium, Oiso, Japan*.

Meegan, G. D. J., Hohnson, P. A., Guyer, R. A., and McCall, K. R. (1993). Observations of nonlinear elastic wave behavior in sandstones. *J. Acoust. Soc. Am.*, 94:3387–3391.

Minear, J., Birchak, R., Robbins, C., Linyaev, E., and Mackie, B. (1995). Compressional wave slowness measurement while drilling. *SPWLA 36th Annual Logging Symposium, Paris*.

Minear, J., Heysse, D., and Boonen, P. (1996). Initial results from an acoustic logging while drilling tool. *SPE Annual Technical Conference and Exhibition, Denver*.

Mount, V. S. and Suppe, J. (1992). Present-day stress orientations adjacent to active strike-slip faults: California and Sumatra. *J. Geophys. Res.*, 97:11,995–12,013.

Nolte, B., Rao, R., and Huang, X. (1997). Dispersion analysis of split flexural waves. *Borehole Acoustics and Logging/Reservoir Delineation Consortia Annual Report, MIT*.

Norris, A. N., Bikash, K. S., and Kostek, S. (1994). Acoustoelasticity of solid/fluid composite systems. *Geophys. J. Int.*, 118:439–446.

Norris, A. N. and Sinha, B. K. (1993). Weak elastic anisotropy and the tube wave. *Geophysics*, 58:1091–1098.

Nur, A. and Simmons, G. (1969). Stress-induced velocity anisotropy in rock:an experimental study. *J. Geophys. Res.*, 74:6667–6674.

Paillet, F. L. and Cheng, C. H. (1991). *Acoustic Waves In Boreholes*. CRC Press.

Pao, Y.-H., Sachse, W., and Fukuoka, H. (1984). *Physical Acoustics*, volume 17, chapter Acoustoelasticity and Ultrasonic Measurements of Residual Stresses, pages 61–143. Academic Press, Inc.

Peterson, E. W. (1974). Acoustic wave propagation along a fluid-filled cylinder. *J. Acoust. Soc. Am.*, 45:3340–3350.

Pitarka, A. (1999). 3d elastic finite-difference modeling of seismic motion using staggered grids with nonuniform spacing. *Bulletin of the Seismological Society of America*, 89:54–69.

Randall, C. J. (1990). Eccentric dipole sources in fluid-filled boreholes: Numerical and experimental results. *J. Acoust. Soc. Am.*, 87:2405–2420.

Randall, C. J. (1991a). Modes of noncircular fluid-filled borehole in elastic formations. *J. Acoust. Soc. Am.*, 89:1002–1016.

Randall, C. J. (1991b). Multipole acoustic waveforms in nonaxisymmetric boreholes and formations. *J. Acoust. Soc. Am.*, 90:1620–1631.

Rao, V. N. R., Burns, D. R., and Toksoz, M. N. (1999). Models in LWD applications. *Borehole Acoustics and Logging/Reservoir Delineation Consortia Annual Report, MIT*.

Robertsson, J., Blanch, J., and Symes, W. (1994). Viscoelastic finite difference modeling. *Geophysics*, 59:1444–1456.

Roever, W., Rosenbaum, J., and Vining, T. (1974). Acoustic waves from am impulsive source in a fluid-filled borehole. *J. Acoust. Soc. Am.*, 55:1144–1157.

Sarkar, D., Bakkulin, A., and Kranz, B. (2002). Anisotropic inversion of seismic data for stressed media: theory and a physical modeling study on berea sandstone. *Soc. Explor. Geophys. Expanded Abstracts*.

Sayers, C. M. (1988a). Inversion of ultrasonic wave velocity measurements to obtain the microcrack orientation distribution function in rocks. *Ultrasonics*, 26:73–77.

Sayers, C. M. (1988b). Stress-induced elastic wave anisotropy in fractured rock. *Ultrasonics*, 26:311–317.

Sayers, C. M., Van Munster, J. G., and King, M. S. (1990). Stress-induced ultrasonic anisotropy in Berea sandstone. *J. Rock Mech. Min. Sci. & Geomech. Abstr.*, 27(5):429–436.

Schmitt, D. P. (1988). Shear wave logging in elastic formations. *J. Acoust. Soc. Am*, 84:2215–2229.

Shlager, K. L. and Schneider, J. B. (1998). A survey of the finite-difference time-domain literature. In Taflove, A., editor, *Adnvaces in Computational Electrodynamics: The Finite-Difference Time-Domain Method*, chapter 1, pages 1–62. Artech House, Boston, MA.

Sinha, B. K. (1997). Inversion of borehole dispersions for formation stresses. *Proc. 1997 IEEE Internation Ultrasonic Symposium , October 5-8 , IEEE Catalog No. 97CH36118*, pages 781–786. October 5-8 , IEEE Catalog No. 97CH36118.

Sinha, B. K. and Kostek, S. (1996). Stress-induced azimuthal anisotropy in borehole flexural waves. *Geophysics*, 61:1899–1907.

Stephen, R. A., Casas, C., and Cheng, C. H. (1985). Finite difference synthetic acoustic logs. *Geophysics*, 50:1588–1609.

Summers, G. C. and Broding, R. A. (1952). Continuous velocity logging. *Geophysics*, 17:598.

Taflove, A. (1998). *Advances in Computational Electrodynamics: The Finite-Difference Time-Domain Method*, chapter 1. Artech House.

Tang, X. M., Wang, T., and Patterson, D. (2002). Multipole acoustic logging while-drilling. In *Expanded Abstracts of SEG International Exposition and 72nd Annual Meeting, Salt Lake City, Utah.*

Thurston, R. N. and Brugger, K. (1964). Third-order elastic constants and the velocity of small amplitude elastic waves in homogeneously stressed media. *Phys. Rev.*, 33:A1604–1610.

Tiersten, H. F. (1978). Perturbation theory for linear electroelastic equations for small fields superposed on a bias. *J. Acoust. Soc. Am.*, 64:832–837.

Timoshenko, S. P. and Goodier, J. N. (1982). *Theory of elasticity.* McGraw Hill Book Co., New York.

Truesdell, C. and Noll, W. (1992). *The non-linear field theories of mechanics.* Springer-Verlag, New York.

Tsang, L. and Rader, D. (1979). Numerical evaluation of the transient acoustic waveform due to a point source in a fluid-filled borehole. *Geophysics*, 44:1706–1720.

Virieux, J. (1986). P-sv wave propagation in heterogeneous media: Velocity-stress finite difference method. *Geophysics*, 51:345–369.

Vossen, R. V., Robertsson, J., and Chapman, C. (2002). Finite-difference modeling of wave propagation in a fluid-solid configuration. *Geophysics*, 67:618–624.

White, J. E. (1967). The hula log - a proposed acoustic tool. *Trans. Soc. Professional Well Log Analysts 8th Ann. Logging Symposium.*

Willis, M. and Toksoz, M. N. (1983). Automatic p and s velocity determination from full waveform acoustic logs. *Geophysics*, 48:1631.

Winbow, G. A. (1988). A theoretical study of acoustic s-wave and p-wave velocity logging with conventional and dipole sources in soft formations. *Geophysics*, 53:1334–1342.

Winkler, K. W. and Liu, X. (1996). Measurements of third-order elastic constants in rocks. *J. Acoust. Soc. Am*, 100(3):1392–1398.

Winkler, K. W., Sinha, B. K., and Plona, T. J. (1998). Effects of borehole stress concentrations on dipole anisotropy measurements. *Geophysics*, 63:11–17.

Wiprut, D. (2001). *Stress, Borehole Stability, and Hydrocarbon Leakage in the Northern North Sea*. PhD dissertation, Stanford University, Department of Geophysics. This is a full PHDTHESIS entry.

Yilmaz, O. (1987). *Seismic Data Processing*. Society of Exploration Geophysics.

Zheng, Y. (2002). *Acousto-electric Leviation for Particle and Drop Array Studies: Instrument Characterization and Its Application*. PhD dissertation, Yale University, Department of Mechanical Engineering. This is a full PHDTHESIS entry.

Zheng, Y., Huang, X., and Apfel, R. E. (2002). New anisotropic perfectly matched layer boundary conditions for elastic waves in solids. *J. Acoust. Soc. Am.*, 111:2450.

Zheng, Y., Huang, X., and M. N., T. (2003). A new non-splitting anisotropic perfectly matched layer for elastic finite difference time domain method. *prepared for submission*.

Zoback, M. D., Moos, D., and Anderson, R. N. (1985). Wellbore breakouts and *in-situ* stress. *J. Geophys. Res.*, 90:5523–5530.

Zoback, M. L. (1992). First- and second-order patterns of stress in the lithosphere: the world stress map project. *J. Geophys. Res.*, 97:11,703–11,728.

Zoback, M. L. and Zoback, M. D. (1980). State of stress of the conterminous United States. *J. Geophys. Res.*, 85:6113–6156.